TESTING SMALL-SCALE AND FULL-SCALE LIQUID-TO-AIR MEMBRANE

ENERGY EXCHANGERS (LAMEEs)

A Thesis Submitted to the College of

Graduate Studies and Research

In Partial Fulfillment of the Requirements

For the Degree of Doctor of Philosophy

In the Department of Mechanical Engineering

University of Saskatchewan

Saskatoon

By

Davood Ghadiri Moghaddam

PERMISSION TO USE

In presenting this thesis in partial fulfilment of the requirements for a Postgraduate degree from the University of Saskatchewan, I agree that the Libraries of this University may make it freely available for inspection. I further agree that permission for copying of this thesis in any manner, in whole or in part, for scholarly purposes may be granted by the professors who supervised my thesis work or, in their absence, by the Head of the Department or the Dean of the College in which my thesis work was done. It is understood that any copying or publication or use of this thesis or parts thereof for financial gain shall not be allowed without my written permission. It is also understood that due recognition shall be given to me and to the University of Saskatchewan in any scholarly use which may be made of any material in my thesis.

Requests for permission to copy or to make other use of material in this thesis in whole or part should be addressed to:

Head of the Department of Mechanical Engineering

University of Saskatchewan

Saskatoon, Saskatchewan (S7N 5A9)

ABSTRACT

A liquid-to-air membrane energy exchanger (LAMEE) is a novel flat-plate membrane-based energy exchanger where heat and moisture transfer between air and solution streams occurs through a semi-permeable membrane. The LAMEE consists of many air and solution flow channels, each separated by a membrane. A small-scale single-panel LAMEE consists of a single pair of neighboring air and solution channels. This PhD thesis focuses on developing, testing and modeling the small-scale single-panel LAMEE, and investigating the similarity between the small-scale LAMEE and a full-scale LAMEE. This PhD thesis presents a methodology to investigate similarity between small-scale and full-scale energy exchangers.

A single-panel energy exchanger test (SPEET) facility is developed and built to measure the performance of the small-scale single-panel LAMEE under different test conditions. Also, the small-scale LAMEE is numerically modeled by solving coupled heat and mass transfer equations for the air, solution and membrane of the LAMEE. The effects of membrane vapor diffusion resistance and enhanced air side convective heat transfer coefficient are numerically investigated. The numerical model of the small-scale LAMEE is validated with the experimental data for summer test conditions, and effectiveness values agree within ±4% in most cases. Moreover, the effects of different heat and mass transfer directions, and salt solution types and concentrations are experimentally and numerically investigated. The results show that the LAMEE effectiveness is strongly affected by the heat and mass transfer directions but negligibly affected by salt solution type and concentration.

The solution-side effectiveness for liquid-to-air membrane energy exchangers is introduced in this thesis for the first time. The results show that the solution-side effectiveness should be used to evaluate the sensible and total effectiveness of LAMEE regenerators. Finally, the similarity between the small-scale and full-scale LAMEEs is investigated experimentally and numerically. The results show that the small-scale LAMEE effectiveness results can be used to predict the performance of a full-scale LAMEE within ±2% to ±4% in most cases.

ACKNOWLEDGEMENTS

DEDICATION

I dedicate this thesis to my wife, my parents, my brother and my sister.

Thank you very much for your love and encouragement throughout my life.

TABLE OF CONTENTS

LIST OF TABLES

LIST OF FIGURES

NOMENCLATURE

Acronyms

AHRI   Air-Conditioning, Heating and Refrigeration Institute

ASHRAE   American Society of Heating, Refrigerating and Air-Conditioning Engineers

ASME   American Society of Mechanical Engineers

ER   Energy Recovery

GHG   Green-House Gas

HACS   Hybrid Air-Conditioning System

HVAC   Heating, Ventilating and Air-conditioning

LAMEE   Liquid-to-Air Membrane Energy Exchanger

LD   Liquid Desiccant

LDAC   Liquid-Desiccant Air-Conditioning

RAMEE   Run-Around Membrane Energy Exchanger

Roman Symbols

A Membrane active area (m^2)

a Constant Coefficient

B Bias error

C Heat capacity rate (kJ/s K)

c_p Specific heat capacity at constant pressure (kJ/kg K)

Cr Heat capacity ratio

Cr^* Heat capacity ratio

D_{h}	Hydraulic diameter (m)
$D_{\mathrm{v\text{-}a}}$	Diffusivity coefficient of vapor into air ($\mathrm{m^2/s}$)
d	Thickness (m)
$\mathrm{d}x, \mathrm{d}y$	Small increment in x or y directions, respectively (m)
E_{T}	Slope of equilibrium humidity to temperature of solution (kg/kg K)
EEI	Energy Exchange Inequality (%)
H	Enthalpy (J/kg)
H^{*}	Operating factor
H_{ex}	Exchanger height (m)
h	Convective heat transfer coefficient ($\mathrm{W/m^2\ K}$)
h_{fg}	Enthalpy of phase change (J/kg)
h_{m}	Convective mass transfer coefficient ($\mathrm{kg/m^2\ s}$)
K	Intermediate coefficient
k	Thermal conductivity (W/m K)
k_{m}	Water vapor permeability (kg/m s)
L_{ex}	Exchanger length (m)
L_{sol}	Exchanger solution inlet length (m)
Le	Lewis number
$\dot{m}$	Mass flow rate (kg/s)
m^{*}	Mass flow rate ratio
MRR	Moisture removal rate (g/h)

NTU	Number of heat transfer units
NTU_{m}	Number of mass transfer units
Nu	Nusselt number
Q	Volume flow rate ($\mathrm{m^3/s}$)
Q''	Constant heat flux ($\mathrm{W/m^2}$)
q	Transferred energy in heat or energy exchangers (W)
R	Membrane resistance (s/m)
R_C	Solution operation ratio
Re	Reynolds number
RH	Relative humidity (%RH)
Rp	Repeatability
R_W	Moisture flux ratio
S	Standard deviation
Sh	Sherwood number
T	Temperature (K)
t	Student's distribution t-factor
U	Overall heat transfer coefficient ($\mathrm{W/m^2\ K}$)
U_{m}	Overall mass transfer coefficient ($\mathrm{kg/m^2\ s}$)
Un	Uncertainty
W	Humidity ratio ($\mathrm{kg_v/kg_{air}}$)
W_0	Constant value equal to $(W_{sol,i} - W_{air,i})$
X	Ratio of water mass to mass of pure salt ($\mathrm{kg_{water}/kg_{salt}}$)

x, y, z	Coordinates
x_0, y_0	Exchanger length and height (m)
Y	Parameter (temperature or humidity content)

Greek symbols

Δ	Differential between two quantities
δ	Membrane thickness (m)
ε	Exchanger effectiveness
ϕ	Dimensionless humidity ratio
ρ	Density (kg/m^3)
θ	Dimensionless temperature

Subscripts

air	Air
counter	Counter flow configuration
cross	Cross flow configuration
f	Fluid
full-scale	Full-scale LAMEE
i	Sensible, latent or total effectiveness
in	Inlet
lat	Latent effectiveness
lm	Log mean value
max	Maximum
mem	Membrane
min	Minimum

out	Outlet
s	Wall surface
salt	Pure salt in the solution
sen	Sensible effectiveness
small-scale	Small-scale LAMEE
sol	Salt solution
steady	Steady-state conditions
th	Theoretical
tot	Total effectiveness

CHAPTER 1

INTRODUCTION

World energy consumption has been continuously increasing with population and economic growth during the last few decades. In developed countries such as United States and Canada, residential and commercial buildings consume over 40% of the total energy. Heating, ventilating and air-conditioning (HVAC) systems in the buildings consume almost 50% of this energy (Perez-Lombard *et al.*, 2008). Also, residential and commercial buildings are a significant source of greenhouse gas (GHG) emissions, amounting to 36% of total GHG emissions in developed countries in 2006 (Perez-Lombard *et al.*, 2008). Moreover, indoor air quality (IAQ) and occupant thermal comfort affect the occupant health and productivity, since people spend almost 90% of their time inside buildings (Yu *et al.*, 2009). Different types of air-to-air or liquid-to-air energy recovery (ER) systems (i.e. air-to-air heat exchangers, air-to-air membrane energy exchangers, direct contact liquid-to-air energy exchangers and liquid to air membrane energy exchangers) have been developed and experimentally tested to reduce the energy consumption in HVAC systems and downsize heating and cooling equipment. This PhD project focuses on liquid-to-air membrane energy exchangers as a component that can be used in a HVAC system to improve the performance of the system and reduce the system energy consumption.

1.1   Flat-Plate Liquid-to-Air Membrane Energy Exchanger (LAMEE)

A flat-plate liquid-to-air membrane energy exchanger (LAMEE) is a novel energy exchanger which transfers heat and moisture between an air stream and a salt solution through a semi-permeable membrane. The membrane is permeable for water vapor, but impermeable to liquids. The flat-plate LAMEE consists of several solution panels which are placed side by side, and air spacers are used between the solution panels to create air channels in the LAMEE. The single panels are the basic units of heat and mass transfer in a LAMEE. Figure 1.1 shows a schematic view of a LAMEE with details of the air and solution channels design.
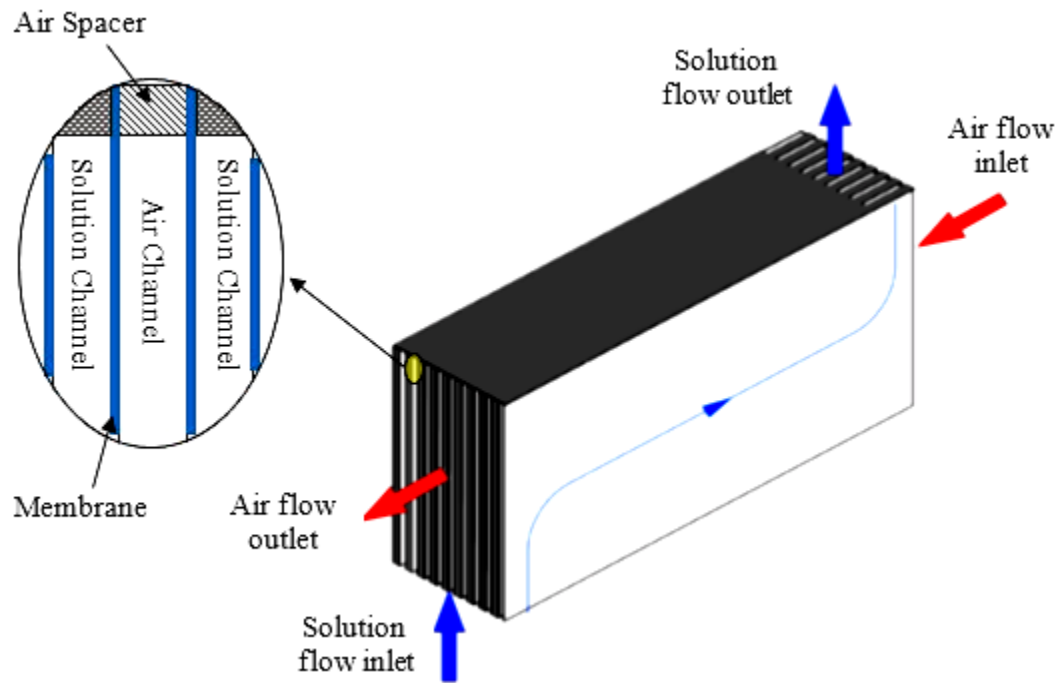
Figure 1.1 Schematic view of a flat-plate liquid-to-air membrane energy exchanger (LAMEE)

A comprehensive literature review for the flat-plate LAMEE and other types of liquid-to-air membrane energy exchangers (i.e. hollow fiber LAMEE) is presented in Chapters 2 to 6, since each chapter is a research paper, and has an introduction section

with comprehensive literature review. The main aim in the Introduction chapter of this PhD thesis is to briefly introduce the LAMEE and its application, and introduce the thesis objectives in detail.

There are few papers available directly on flat-plate LAMEEs. Namvar *et al.* (2012) experimentally investigated the steady-state and transient performance of a flat-plate LAMEE under summer and winter test conditions. They presented a time constant for the LAMEE as an important parameter for the transient behavior of the LAMEE with step change in inlet conditions, where the transient behavior of the LAMEE mainly depends on the thermal capacity of the LAMEE and the salt solution. Bergero *et al.* (2000) numerically and experimentally investigated the performance of a flat-plate LAMEE under air dehumidification test conditions. The results showed good agreement between the experimental and numerical results for the LAMEE. Also, the numerical results showed that a membrane mass resistance plays an important role on the latent effectiveness of the LAMEE. Vestrelli (2006) numerically investigated the performance of a flat-plate LAMEE used as an air humidifier and an air dehumidifier. The results showed that for the air humidifier, the moisture transfer across the membrane increased as the solution inlet temperature decreased, and for the air dehumidifier the moisture transfer across the membrane increased as the solution inlet temperature increased. Huang *et al.* (2012) numerically solved coupled heat and mass transfer equations for a cross-flow flat-plate LAMEE used as a dehumidifier. The results showed that the real thermal and concentration boundary conditions on the membrane were neither uniform value nor uniform flux boundary conditions. The fully-developed Nusselt number for the air side of the flat-plate LAMEE was between the Nusselt number under a uniform

temperature boundary condition and Nusselt number under uniform heat flux boundary condition. However, the fully developed Nusselt number for the air side of the flat-plate LAMEE was closer to the Nusselt number under a uniform temperature boundary condition.

The flat-plate LAMEE has many applications in liquid-desiccant air-conditioning (LDAC) systems. Some applications of the LAMEE are mentioned below.

1.1.1   Run-Around Membrane Energy Exchanger (RAMEE)

A RAMEE consists of two flat-plate LAMEEs, and is a LDAC system which recovers heat and moisture from an exhaust air stream and transfers the heat and moisture to a supply air stream using a closed solution loop. One LAMEE is located in the supply air stream and the other LAMEE is located in the exhaust air stream. Liquid desiccant is circulated in a closed loop between the supply and exhaust LAMEEs to transfer heat and moisture between the supply and exhaust air streams (see Figure 1.2). Much research has been done on the RAMEE, and a large fraction of the research has been conducted at the University of Saskatchewan. Fan *et al.* (2006) developed a numerical model to investigate a RAMEE system performance which consisted of two cross-flow LAMEEs at different operating conditions. Lithium bromide was used as a salt solution in the solution loop. Fan *et al.* (2006) predicted a total effectiveness of 70% for the RAMEE system. Erb (2009) built a prototype for the RAMEE system with two cross-flow LAMEEs. Erb operated this prototype with top-to-bottom and bottom-to-top solution flow configurations at summer and winter AHRI conditions (ANSI/AHRI Standard 1060, 2011) and measured a maximum steady-state total effectiveness of 36% and 43%, respectively. The results show that reversing the solution flow direction in the LAMEE

4

reduces the impact of the solution flow mal-distribution in the LAMEE. Seyed-Ahmadi (2008) developed a two-dimensional numerical simulation to investigate the steady-state and transient behavior of the RAMEE system with two cross-flow LAMEEs. According to the results, the mass of solution in the system, initial salt solution concentration and heat gain/loss from/to the surroundings have large impacts on the transient response of the RAMEE. Finally, Mahmud (2009) designed and built a new RAMEE prototype consisting of two counter-cross flow LAMEEs and presented experimental results for both summer and winter AHRI conditions using $MgCl_2$ salt solution as the coupling fluid. This prototype achieved a maximum total effectiveness of 55%, which is higher than the minimum total effectiveness (50%) required by ASHRAE standard 90.1 (ANSI/ASHRAE STANDARD 90.1, 2007).
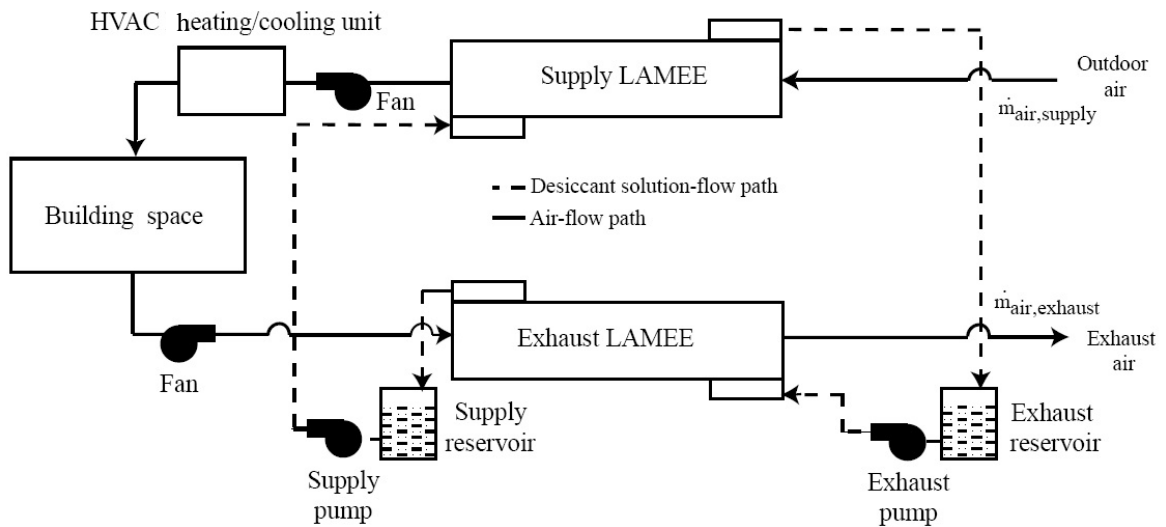
Figure 1.2 Schematic view of the run-around membrane energy exchanger (RAMEE) (Mahmud, 2009)

1.1.2   Hybrid Air-Conditioning System (HACS)

A HACS is a dehumidification system, where a LAMEE with a hygroscopic desiccant and a hydrophobic membrane is added to a direct-expansion air-conditioning

system, to increase moisture transfer and overall system performance. The HACS has the ability to humidify or dehumidify air using the membrane-desiccant energy exchanger or LAMEE. Bergero and Chiari (2011) numerically investigated the effect of air and solution mass flow rates on the steady-state performance of the HACS at summer conditions. Two cross-flow LAMEEs were used in the HACS, where one LAMEE was installed in the supply air stream and the other LAMEE was installed in the exhaust air stream. The hybrid system performance increases slightly as the solution mass flow rate increases. Also, the coefficient of performance (COP) of the HACS was significantly higher (e.g. 50% higher at certain operating conditions) than a traditional direct-expansion system. In another paper, Bergero and Chiari (2010) considered the effect of latent load and indoor and outdoor relative humidity on the steady-state behavior of the HACS at summer conditions. Results showed the percentage power saving of the HACS compared to traditional direct-expansion system increased as the indoor latent load increased, and decreased as the outdoor relative humidity increased.

1.2 Flat-Plate Small-Scale Single-Panel LAMEE

A flat-plate small-scale single-panel LAMEE consists of a single pair of neighboring air and solution channels. The single-panel LAMEE is the basic building unit of LAMEEs. The schematic of the small-scale single-panel LAMEE and a cross-sectional view of the small-scale LAMEE are shown in Figure 1.3. The small-scale LAMEE design is discussed in Chapter 2 in detail. In the small-scale LAMEE design, solution channels are grooved on two plastic side panels, and the membrane (i.e. GE^{TM} membrane) is attached on each side panel to create a half of the solution side. The other half of the solution side is made in the same way. The air flow channel is designed to be

in the middle of the single-panel LAMEE, and it is created by using air spacers in the upper and lower edges of the panel. Also, an air screen (turbulence enhancement device) is used in the air channel to enhance the heat and mass transfer properties of the air flow.
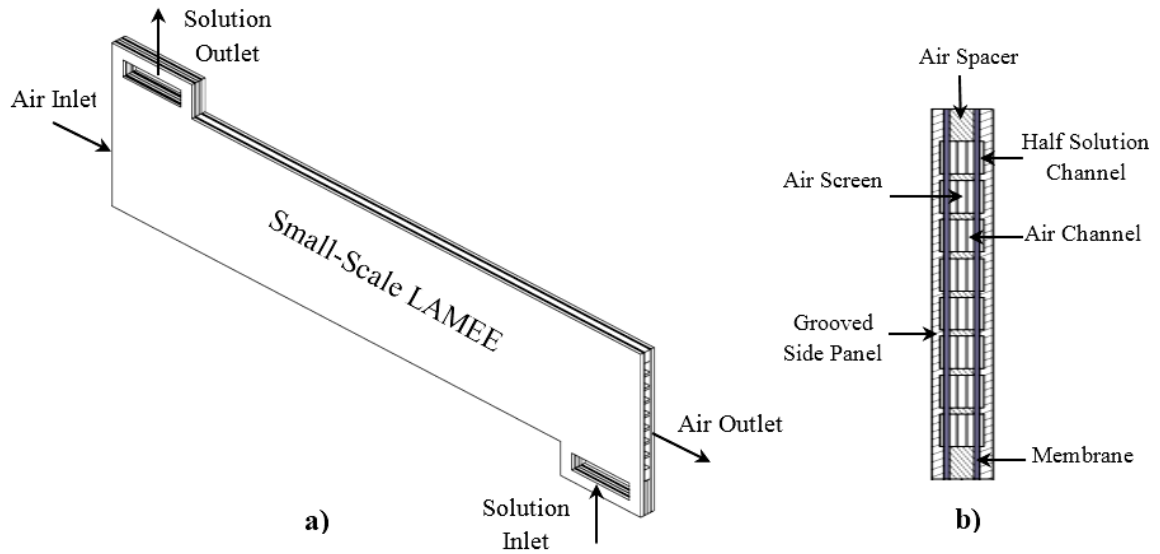
Figure 1.3 (a) Air and solution flow configuration and (b) a cross-section view of the small-scale single-panel LAMEE (Ghadiri Moghaddam *et al.*, 2013b)

There are few papers available on the flat-plate small-scale single-panel LAMEE, and almost all of them are the result of this PhD research project. Five of these papers are used here to structure this PhD thesis (one paper in each chapter). The other papers are attached in the Appendices of this thesis. A complete literature review for the small-scale LAMEEs is presented in Chapters 2 to 6. Each chapter presents a research paper, and each paper has an introduction section with comprehensive literature review.

Hollow fiber membrane contactors (hollow fiber LAMEEs) are another type of membrane based energy exchanger which are also small. Zhang (2011a, 2012) introduced a hollow fiber membrane contactor, which is a small-scale shell and tube membrane based energy exchanger where a solution passes through hollow fiber membrane tubes and heat and mass transfer occurs between the air and solution. Zhang (2011a) developed

an analytical model to investigate the steady-state performance of hollow fiber membrane contactors as a dehumidifier, and compared the analytical results with experimental data for the contactor under different operating conditions. Zhang (2011b) numerically investigated the coupled heat and mass transfer in a cross-flow hollow fiber membrane contactor for air humidification using water. The results showed that the fiber tubes packing density has a dominant effect on the performance of the hollow fiber membrane contactor. Also, Zhang *et al.* (2012a) numerically investigated the coupled heat and mass transfer in a counter-flow hollow fiber membrane contactors using a free surface model. The real boundary conditions were obtained for the hollow fiber membrane tube which were neither uniform temperature nor uniform heat flux. The results showed that the fully-developed air-side Nusselt number is between the constant temperature and constant heat flux Nusselt values, and close to constant heat flux Nusselt value for the counter-flow contactor.

1.3   Thesis Objectives and Overview

Figure 1.4 presents an overview of the objectives for this PhD project. As shown in Figure 1.4, the main focus of this PhD project is on developing, testing and modeling a small-scale single-panel LAMEE, and investigating similarity between the small-scale LAMEE and a full-scale LAMEE. The main focus of this PhD research project is shown in the large circle in the middle of Figure 1.4; the focus is the small-scale single-panel LAMEE. Before this PhD project, there was no information available in the literature about flat-plate small-scale LAMEEs and similarity between small-scale and full-scale membrane based energy exchangers. The main motivation of this PhD project is to use the small-scale LAMEE effectiveness results to predict the performance of a full-scale

LAMEE at different operating conditions, because testing a full-scale exchanger such as a LAMEE is often time consuming and expensive. Five major objectives are defined in this PhD project. These five major objectives are shown in five small circles in Figure 1.4, which are located around the center circle (the main focus of this PhD project). These five major objectives are numbered from one to five in Figure 1.4. Also, tasks which are completed during each major objectives are shown in rectangular boxes beside each of the major objectives in Figure 1.4. For each task, a chapter of the thesis and a manuscript which address that task are mentioned in the rectangular box of the task. The five major objectives which are completed during this PhD project are now discussed in separate subsections.
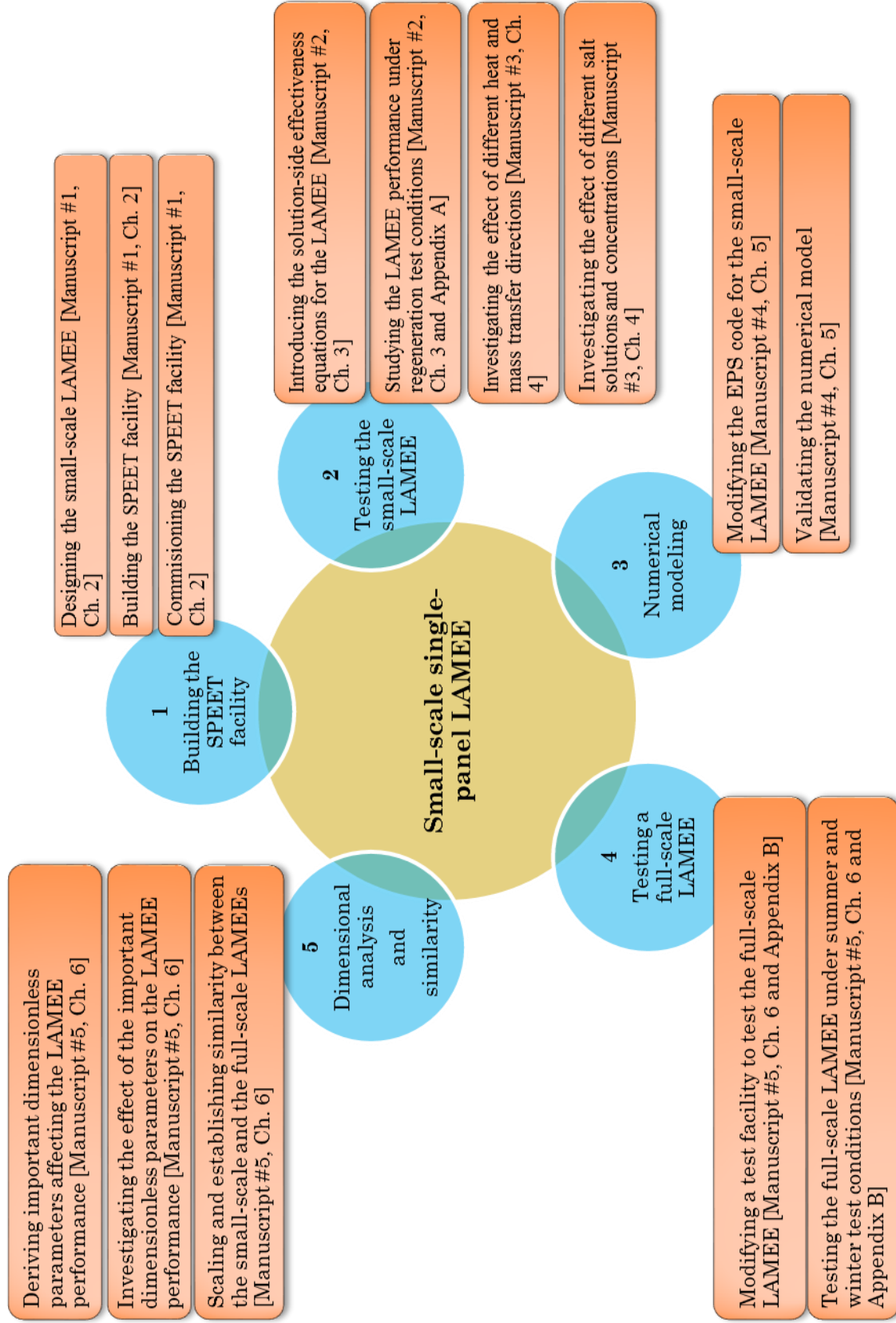
Figure 1.4 Overview of the PhD research project objectives

Small-scale single-panel LAMEE

1 Building the SPEET facility
- Designing the small-scale LAMEE [Manuscript #1, Ch. 2]
- Building the SPEET facility [Manuscript #1, Ch. 2]
- Commisioning the SPEET facility [Manuscript #1, Ch. 2]

2 Testing the small-scale LAMEE
- Introducing the solution-side effectiveness equations for the LAMEE [Manuscript #2, Ch. 3]
- Studying the LAMEE performance under regeneration test conditions [Manuscript #2, Ch. 3 and Appendix A]
- Investigating the effect of different heat and mass transfer directions [Manuscript #3, Ch. 4]
- Investigating the effect of different salt solutions and concentrations [Manuscript #3, Ch. 4]

3 Numerical modeling
- Modifying the EPS code for the small-scale LAMEE [Manuscript #4, Ch. 5]
- Validating the numerical model [Manuscript #4, Ch. 5]

4 Testing a full-scale LAMEE
- Modifying a test facility to test the full-scale LAMEE [Manuscript #5, Ch. 6 and Appendix B]
- Testing the full-scale LAMEE under summer and winter test conditions [Manuscript #5, Ch. 6 and Appendix B]

5 Dimensional analysis and similarity
- Deriving important dimensionless parameters affecting the LAMEE performance [Manuscript #5, Ch. 6]
- Investigating the effect of the important dimensionless parameters on the LAMEE performance [Manuscript #5, Ch. 6]
- Scaling and establishing similarity between the small-scale and the full-scale LAMEEs [Manuscript #5, Ch. 6]

1.3.1 Objective 1: Building a Single-Panel Energy Exchanger Test (SPEET) Facility

The first major objective of this PhD thesis is to develop, manufacture and test a novel small-scale single-panel LAMEE, and design and commission a single-panel energy exchanger test (SPEET) facility. This objective is addressed in **Manuscript #1** which forms Chapter 2 in this PhD thesis. The SPEET facility was designed and built during this PhD project to experimentally evaluate the performance of a small-scale LAMEE under different operating conditions. Also, the SPEET facility can be used to test other kinds of liquid-to-air energy exchangers. The SPEET facility provides better control in experiments on small-scale LAMEEs in comparison to full-scale LAMEE test facilities since the SPEET facility provides better control and lower uncertainty in operating parameters. Preliminarily, the small-scale LAMEE is tested under three different test cases in the SPEET facility using water as a transfer liquid. The mass and energy balance results and the preliminary test results for the small-scale LAMEE are presented in Manuscript #1 (Chapter 2).

1.3.2 Objective 2: Testing the Small-Scale LAMEE

The second major objective is to test the small-scale single-panel LAMEE under a wide range of operating conditions. The second major objective of this PhD project is addressed in two chapters of this thesis (Chapter 3 and 4):

1) The first part of the second major objective is to develop and verify new effectiveness correlations that quantify the solution-side effectiveness of LAMEEs, which is addressed in **Manuscript #2** and forms the third chapter of this PhD thesis. The LAMEE can be used as a dehumidifier to dehumidify the air

or a regenerator to regenerate (dry) the solution in LDAC systems. The air-side effectiveness has traditionally been used to evaluate the performance of liquid-to-air membrane energy exchangers used as a dehumidifier/regenerator, and is available in the literature. In a regenerator; however, the focus is on the salt solution, and the solution properties (i.e. solution outlet concentration and temperature) are important. There is no definition in the literature for the LAMEE solution-side effectiveness, and therefore they are introduced in Manuscript #2 for the first time. These effectiveness equations are used to evaluate the performance of LAMEE regenerators.

Also, it is important to study the effect of different operating parameters on the performance of a LAMEE operating as a dehumidifier/regenerator. An experimental parametric study on the performance of the LAMEE as a dehumidifier or a regenerator is presented in **Appendix A**, which is done for the first time in this research. The results of this parametric study are a helpful guide for researchers and manufacturers to estimate and understand the performance of a LAMEE that is used as a dehumidifier or a regenerator in a LDAC system.

2) The second part of the second major objective is to quantify the effect of different heat and mass transfer directions and salt solution types and concentrations on the effectiveness of a small-scale LAMEE. The results for the second part of the second major objective are presented in Chapter 4 which is **Manuscript #3**. The effect of different heat and mass transfer directions is investigated for the first time for LAMEEs in this research, and can be used by other designers and researchers to understand the effects of different heat and mass transfer directions

and salt solution types and concentrations on the performance of a LAMEE. In a LAMEE, the potential for the heat transfer is the temperature difference between the air and the solution, while the potential for the moisture transfer is the vapor pressure difference between the air and the solution. Heat and mass transfer directions in a LAMEE are defined based on the air and solution inlet conditions. The heat or moisture transfers from the air to the solution when the inlet air temperature or humidity ratio is higher than the solution inlet temperature or humidity ratio, respectively, and vice versa. There are four possible combinations for heat and moisture transfer directions. Also, there are different salt solutions which can be used with different concentrations. The results of testing different salt solution types and concentrations in the small-scale LAMEE will help researchers and manufacturers choose an appropriate salt solution and concentration for their liquid desiccant systems.

1.3.3 Objective 3: Numerical Modeling of the Small-Scale LAMEE

The third major objective is to model the small-scale LAMEE, and compare the numerical results with experimental data. The third major objective of this PhD project is addressed in **Manuscript #4**, and is presented in Chapter 5. The small-scale LAMEE numerical model eliminates the necessity of doing experiments in many cases. The coupled heat and mass transfer in the air, solution and membrane of the LAMEE are modeled to numerically evaluate the performance of the small-scale LAMEE under different test conditions. Then, the coupled heat and mass transfer equations in the air, solution and membrane of the LAMEE are nondimensionalized to derive important dimensionless parameters affecting the LAMEE performance. Also, the small-scale

LAMEE numerical effectiveness results are validated with experimental data for summer test conditions. This numerical model can be directly used or be modified by other researchers to investigate the performance of small-scale LAMEEs with the same configuration and design or different design under different operation conditions.

1.3.4 Objective 4: Testing a Full-Scale LAMEE

The fourth major objective of this PhD project is to test a full-scale LAMEE with a similar design as the small-scale LAMEE under various operating conditions. A full-scale (100 L/s) LAMEE with similar design as the small-scale LAMEE and with 10 solution panels is tested under summer and winter test conditions in this part of this PhD project. The full-scale LAMEE effectiveness results are presented in **Manuscript #5** (see Chapter 6) and **Appendix B**.

1.3.5 Objective 5: Dimensional Analysis and Similarity

The last major objective is to conduct a dimensional analysis of the small-scale LAMEE, and investigate similarity between the small-scale LAMEE and the full-scale (100 L/s) LAMEE. Testing a full-scale exchanger such as a LAMEE is often time consuming and expensive. Consequently, the small-scale LAMEE is used to predict the performance of the full-scale LAMEE at different operating conditions. The results of the last major objective will guide researchers and manufactures to test small-scale exchangers and use the results from the small-scale exchangers to predict the performance of full-scale exchangers within a certain uncertainty. The effect of important dimensionless parameters on the small-scale LAMEE steady-state effectiveness, and the comparison between the small-scale LAMEE and the full-scale LAMEE experimental and numerical effectiveness results are presented in Chapter 6 which is **Manuscript #5**.

1.3.6 Summary of Objectives

The five major objectives, which have been completed during this PhD project, were discussed in Section 1.3 and shown in Figure 1.4. These objectives also represent a <u>methodology</u> to investigate the similarity between a small-scale energy exchanger and a full-scale energy exchanger. This methodology, which is presented in this PhD thesis for LAMEEs, consists of the following steps:

(1) Manufacture a small-scale exchanger similar to a full-scale exchanger, and build a test facility to test the small-scale exchanger;

(2) Test the small-scale exchanger under various test conditions;

(3) Develop the governing heat and mass transfer equations for the exchanger, and identify important dimensionless parameters affecting the exchanger performance;

(4) Test the full-scale exchanger under various test conditions; and

(5) Study the effect of the important dimensionless parameters on the exchanger performance, and investigate the similarity between the small-scale and full-scale exchangers.

With the above methodology, which will be applied and tested in this thesis on LAMEEs, the similarity between small-scale and full-scale energy exchangers can be established. Thus, the small-scale exchanger effectiveness results can be used to predict the performance of the full-scale exchanger under different operating conditions within acceptable uncertainty bounds. Researchers and manufacturers can follow this methodology when designing and testing new energy exchangers. Manufacturing and testing a small-scale energy exchanger will facilitate new exchanger development, leading to higher performing exchangers with reduced investment in time and money.

CHAPTER 2

SINGLE-PANEL ENERGY EXCHANGER TEST FACILITY

2.1   Overview of Chapter 2

The single-panel energy exchanger test (SPEET) facility and the small-scale single-panel LAMEE are introduced in this chapter which contains Manuscript #1 (Small-scale single-panel liquid-to-air membrane energy exchanger (LAMEE) test facility development, commissioning and evaluating the steady-state performance). In this manuscript, the SPEET facility is introduced to test the small-scale LAMEE, and the mass and energy balance results for the SPEET facility are presented. The steady-state performance of the small-scale LAMEE is experimentally investigated under different test conditions using water as the transfer liquid. Finally, the experimental performance data are compared with numerical and analytical results for the small-scale LAMEE. The small-scale LAMEE numerical model, which is used in this chapter to numerically evaluate the steady-state performance of the small-scale LAMEE, is presented in detail in Chapter 5. Also, the analytical model which is used in this chapter was developed by Zhang (2011a) for hollow fiber membrane contactors. Ge *et al.* (2012) modified the Zhang's analytical model for LAMEEs. This chapter explains the first step of the methodology (see Section 1.3.6) for LAMEEs, which is manufacturing the small-scale LAMEE and building the SPEET facility to test the small-scale LAMEE under various test conditions.

References for this chapter, which contains Manuscript #1, are presented in the References section of the thesis (see page 215) which includes all the references used in this PhD thesis.

One postdoctoral fellow (Dr. Gaoming Ge) and a research fellow (Dr. Philip LePoudre) in our research group have contributed to Manuscript 1. Dr. Philip LePoudre gave useful advice to me during this project while he was in our research group from September 2010 to September 2011. He also critically reviewed Manuscript #1. He was added as the second author in Manuscript #1. Dr. Gaoming Ge developed the analytical model to evaluate the steady-state performance of LAMEEs based on Zhang's analytical model (Zhang, 2011a). The analytical results are used in Figure 2.4, Figure 2.7 and Figure 2.9. The PhD Candidate's contributions to Manuscript #1 are: (a) developing the SPEET facility to test small-scale LAMEEs, (b) manufacturing the small-scale single-panel LAMEE, (c) testing the small-scale LAMEE under different operating conditions using water as a transfer liquid, and presenting experimental effectiveness results for the small-scale LAMEE, (d) generating the numerical results for the small-scale single-panel LAMEE, and (e) writing the paper and replying to reviewers' comments.

Small-Scale Single-Panel Liquid-to-Air Membrane Energy Exchanger (LAMEE) Test

Facility Development, Commissioning and Evaluating the Steady-State Performance

(Energy and buildings, 2013, Volume 66, pp. 424-436)

Davood Ghadiri Moghaddam, Philip LePoudre, Gaoming Ge, Robert W. Besant, Carey J.

Simonson

2.2   Abstract

A new test facility was developed to assess the performance of a small-scale single-panel liquid-to-air membrane energy exchanger (LAMEE). Mass and energy balances of the exchanger were computed for each test. The steady-state performance of the small-scale LAMEE was experimentally investigated under different operating conditions. Water was used as a liquid transfer medium for the experiments and the exchanger was tested for air heating and humidifying (H&H), air cooling and humidifying (C&H), and air cooling and dehumidifying (C&D) at three different *NTU* values (2.5, 3.5 and 4.5) and $Cr^* = 7$. The experimental results were compared to results from a numerical and two analytical models. In most cases, reasonable agreement among the experimental, numerical and analytical results was achieved except for the sensible effectiveness in the H&H and latent and total effectiveness in the C&H test cases. The results showed that the effectiveness of the small-scale LAMEE always increased with *NTU* for all test conditions. Sensible and latent effectiveness contour maps of the small-scale LAMEE were generated numerically for different inlet air conditions and for *NTU* = 3.5 and $Cr^* = 7$, while the water inlet temperature was set at 22°C. Finally, the effectiveness contour maps were compared with three experimental test conditions.

Keywords: Small-scale exchanger, Liquid-to-air membrane energy exchanger, Steady-state effectiveness, *NTU*, Heat capacity ratio.

2.3 Introduction

The world energy consumption has been continuously increasing with population and economic growth during last few decades. In developed countries, over 40% of total energy is consumed in residential and commercial buildings and up to 50% of this energy is consumed by heating, ventilating and air-conditioning (HVAC) systems in buildings (Perez-Lombard *et al.*, 2008). Since people spend around 90% of their time inside buildings, occupant thermal comfort and indoor air quality (IAQ) play an important role on health and productivity (Yu *et al.*, 2009). In addition, conventional HVAC systems and refrigerants have significant effects on air pollution, amount of released greenhouse gases and global warming (Afonso, 2006).

Different types of air-to-air or liquid-to-air energy recovery (ER) systems have been developed and experimentally tested to reduce energy consumption in HVAC systems and downsize heating and cooling equipment. To select the appropriate ER technology for building HVAC systems, many parameters should be considered such as indoor and outdoor conditions, type of application, yearly weather data, installation and maintenance costs, energy recovery system design and performance (Besant and Simonson, 2000; Rasouli *et al.*, 2013; Min and Su, 2010; Min and Su, 2011). A run-around membrane energy exchanger (RAMEE) is a recent technology, which has been used to transfer both heat and moisture between supply and exhaust air streams.

A RAMEE consists of two liquid-to-air membrane energy exchangers (LAMEE). One LAMEE is located in the supply air stream and the other is located in the exhaust air

stream. Liquid desiccants, such as $MgCl_2$, LiCl or LiBr, are circulated in a closed loop between the LAMEEs to transfer heat and moisture between the supply and exhaust air streams. Several studies have been conducted on RAMEE systems. Fan *et al.* (2006) for the first time developed a numerical model to investigate the steady-state performance of a RAMEE system consisted of two cross-flow LAMEEs at different operating conditions. A total effectiveness of 70% for the RAMEE was predicted by Fan *et al.* (2006). Afterwards, the steady-state performance of a RAMEE system with cross-flow LAMEEs was investigated experimentally (Erb, 2009). The steady-state effectiveness values were reported for the RAMEE system with top-to-bottom (36%) and bottom-to-top (43%) solution flow directions, respectively. Furthermore, Seyed-Ahmadi *et al.* (2009a) developed a transient numerical model to study the transient behavior of a RAMEE system with two cross-flow LAMEEs for coupled heat and moisture transfer problems. Since the air and solution flow configuration within the energy exchangers has significant effect on the system performance, Vali *et al.* (2009) developed a two-dimensional, steady-state numerical model to study the performance of a RAMEE with two counter-cross flow LAMEEs coupled by a $MgCl_2$ solution loop. Since a counter-flow configuration is not feasible for a LAMEE (i.e. air and solution inlet and outlet cannot be at the same location), a counter-cross flow LAMEE was built and tested by Mahmud (2009). The RAMEE achieved a maximum total effectiveness of 55%, (i.e. higher than 50%, which is the minimum total effectiveness required by ASHRAE standard 90.1 (ANSI/ASHRAE STANDARD 90.1, 2007)).

Another application for LAMEE is in hybrid air-conditioning systems (HACS) (Bergero and Chiari, 2010). Bergero and Chiari (2011) studied a HACS when LAMEEs

with hygroscopic desiccant and hydrophobic membranes were added to a direct-expansion air-conditioning system to increase moisture transfer and overall system performance. Results indicated that the coefficient of performance (COP) of the HACS was significantly higher (e.g. 50% higher at certain operating conditions) compared to traditional direct-expansion air cooling and dehumidifying system. Also in another paper (Bergero and Chiari, 2011), Bergero and Chiari considered the effect of latent load, indoor and outdoor relative humidity on the steady-state behavior of the HACS performance at a summer condition.

Previous studies have investigated the RAMEE and HACS performance where a LAMEE is a part of the system, but there are less research data available for a LAMEE itself. The LAMEE consists of several panels for heat and moisture transfer between an air stream and aqueous liquid desiccant. Moisture transfer inside the LAMEE is accomplished through a semi-permeable membrane that is impermeable for liquid, but allows water vapor to transfer. Bergero *et al.* (2000) developed a numerical model and conducted an experimental test to study the performance of a LAMEE, which was used to dehumidify a supply air stream. Their results showed that moisture transfer could be increased by increasing the air flow rate, but solution flow rate did not have a significant effect, especially at lower heat capacity ratio (Cr^*) values. Recently, Namvar *et al.* (2012) experimentally investigated the steady-state and transient performance of a LAMEE at summer and winter test conditions. Their results showed that the transient effectiveness of the LAMEE increases with time, and that the thermal and moisture responses can be represented by two thermal and two moisture time constants. The thermal and moisture time constants are different and depend on the test conditions.

Several research studies have been conducted to investigate the performance of a small-scale exchanger or portion of a full-size exchanger and extrapolate the results to a full-scale exchanger. Wang *et al.* (2005) and Abe *et al.* (2006a, 2006b) investigated the transient characteristics of humidity and temperature sensors and an energy wheel during a humidity step change at constant temperature and temperature step change at constant humidity, respectively. These tests were conducted on a small portion of an energy wheel and the steady-state effectiveness values for the full-size energy wheel were predicted and showed good agreement with experimental data measured on the full-size wheel. Also, Zhang (2011a) developed an analytical solution to investigate the steady-state performance of hollow fiber membrane contactors, which were used as an air dehumidifier. The analytical results were validated by testing a small-scale hollow fiber membrane liquid-to-air energy exchanger under different operating conditions. Furthermore, there are several literature available that used water as a transfer medium in liquid-to-air energy exchangers. Zhang and Huang (2011) used water in a counter-flow hollow fiber membrane module to humidify a supply air stream. The air and water at the same inlet temperatures were used in experiments to validate a mathematical model for the air humidification module. Both membrane and liquid side resistances for heat transfer, and only liquid side resistance for mass transfer, were neglected in the mathematical model. In another paper by Zhang (2012), a rectangular cross-flow hollow fiber membrane module was used to humidify an air stream. This time air and water streams at different inlet temperatures were used in experiments. The result showed that the packing density of the hollow fiber membrane module is an important factor on the module performance.

A LAMEE is a flat-plate energy exchanger that consists of many panels. Each panel is comprised of adjacent air and solution channels which are separated with a semi-permeable membrane. A single panel is a basic building block in a LAMEE and the performance of the single panel relates to the performance of the LAMEE. Also, manufacturing and testing a full-size LAMEE is costly and time consuming, while a small-scale single-panel LAMEE is easier and less costly to manufacture and test. Furthermore, the single-panel LAMEE can be easily used to investigate the effect of mal-distribution caused by membrane bulging in the exchanger independent from mal-distribution effects due to using several panels in a LAMEE construction (Hemingson *et al.*, 2011a). Moreover, there is no numerical or experimental data available directly for single-panel LAMEEs. These reasons show the significance of doing research on small-scale single-panel LAMEEs. The main objective of this chapter is introducing and commissioning a new test facility to test small-scale single-panel LAMEEs, and presenting preliminary results for this test facility using water in the system. This chapter focuses on the steady-state performance of a small-scale single-panel LAMEE at different operating conditions. Also, different numerical and analytical models are proposed in this chapter to model the LAMEE system. The trends in the modeling results are compared with the experimental data; however validating the models is not the objective of this chapter. Finally, the effects of outdoor air conditions on the steady-state performance of the LAMEE are studied, while other important parameters (e.g. *NTU*, *Cr** and water inlet temperature) are kept constant.

2.4   Test Apparatus

A new test facility was designed and built at the University of Saskatchewan to experimentally investigate the performance of a small-scale single-panel LAMEE under different operating conditions. The single-panel energy exchanger test (SPEET) facility consists of a supply air system, an open solution loop, and a test section, where the small-scale single-panel LAMEE is located. The different parts of the SPEET facility are shown in Figure 2.1, and are introduced as follows.
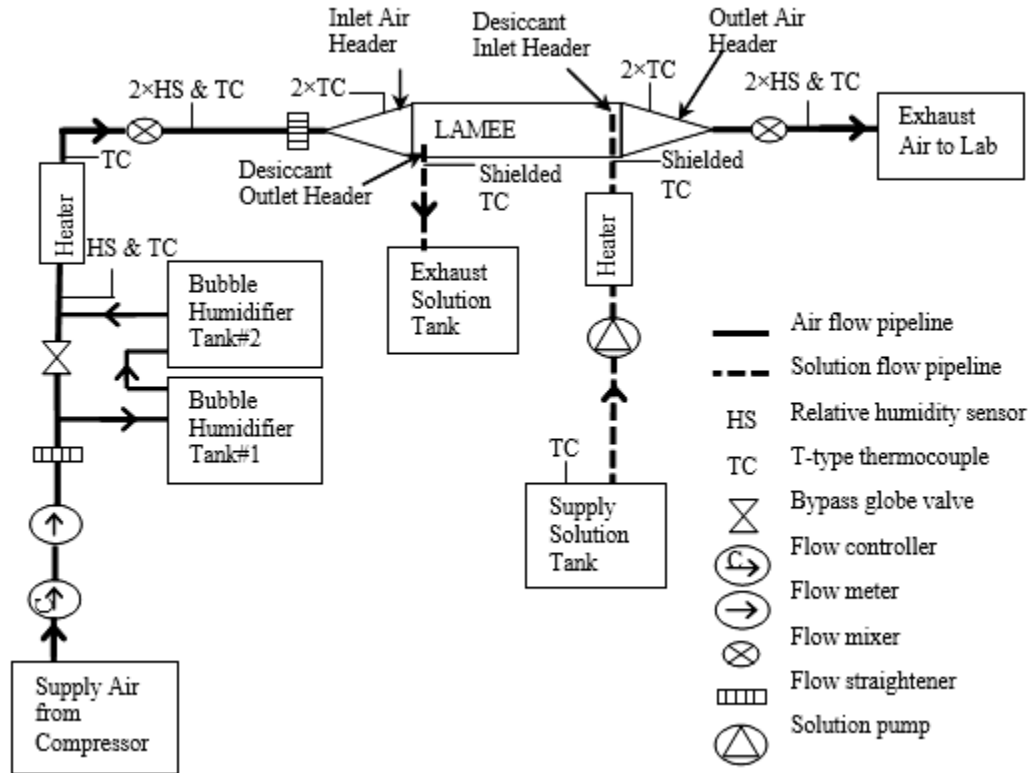
Figure 2.1 Schematic view of the SPEET facility and measurement locations

2.4.1   Supply Air System

An air compressor is used to supply the air into the test setup. A high pressure dry air (4%RH) at room temperature is supplied to the air pipeline with 25.4 mm (1 inch) inner diameter, which is made from PVC material. First, the air passes through a flow

controller (MKS-Type 1559A) to adjust the air flow rate. The capacity of the flow controller is 0 to 100 L/min, with the accuracy of 2% of the full-scale. Also, a flow meter (MKS-Type 0558A) with the same capacity as the flow controller but with an accuracy of 1% of the full-scale is used after that to provide more accurate control on the air flow rate. The flow meter is set to a selected air flow rate for each experiment. After that, two water bubble tank humidifiers are used in series to humidify the supply inlet air, and a globe valve is used in the pipeline to bypass the air into the humidifiers. Downstream of the humidifiers, a shell and tube heater is added to the system to adjust the air temperature at the inlet of the single-panel LAMEE. The PVC pipeline is replaced with a copper pipe with the same inner diameter at the heater location to increase the thermal conductivity of the pipeline, which worked as a shell for the heater system. Hot water passes through the heater tubing at a controlled rate. This heater is wound around the copper pipe to heat the supply air. The SPEET facility could adjust the air inlet temperature and humidity ratio between 15°C to 50°C and 1 to 28 g_w/kg_{air}, respectively, for the supply air velocity range of 1 to 3 m/s.

The air temperature and humidity are measured at different locations as shown in Figure 2.1. Four T-type thermocouples are used at the exchanger inlet and outlet to measure the air temperature at those locations. Also, four Honeywell humidity sensors (type HIH-4021) are used to measure the air relative humidity at the exchanger inlet and outlet. These humidity sensors are too big to be located in the exchanger inlet and outlet headers, so they are installed in the air pipeline upstream and downstream of the exchanger. Another two T-type thermocouples are also installed at the humidity sensors' locations to calculate the air humidity ratio at the exchanger inlet and outlet. Furthermore,

to provide better bulk temperature and relative humidity reading at the humidity sensor locations, two air mixers are used before the sensors to mix the flow and provide uniform properties for the air. The calculated uncertainty for the thermocouples and humidity sensors used for the air side are 0.2˚C and 2%RH, respectively. All the thermocouples are calibrated in the range of -30˚C to 40˚C by using a Hart Scientific high accuracy dry-well temperature calibrator (model 9107) with 0.1˚C uncertainty. Also, the humidity sensors are calibrated in the range of 10% to 90%RH at three different temperatures: 10, 20 and 30˚C by using a mini two-pressure humidity generator (Thunder Scientific Corporation - model 1200) with an uncertainty of 0.5%RH in the range of 10% to 95%RH.

Furthermore, two air headers are used in the test setup to direct the air flow into the LAMEE. The air inlet and outlet openings of the small-scale LAMEE are 94 mm × 5 mm. To direct the air flow from the 25.4 mm inner diameter pipeline to this narrow rectangular opening required a symmetric converging-diverging diffuser header, which converges from 25 mm to 5 mm in width, and diverges from 25 mm to 94 mm in height. There are some guidelines available to design conical diverging or converging diffusers and symmetric rectangular diffusers with converging or diverging flow (White, 2009). Since there are little data available to design a converging-diverging diffuser, it is necessary to simulate the air flow using computational fluid dynamics (CFD) software to find a proper angle for the headers to provide a uniform air flow without separation at the inlet of the single-panel LAMEE. The inlet air header in this research was simulated using FLUENT software with a 3D model. A laminar model was used in FLUENT, and an air flow with constant velocity was assumed for the inlet boundary condition. As a result, the minimum air header angle (2θ) is found to be 11.6° to provide the uniform air

flow at the exchanger inlet. Also, a 100 mm long settle down area is added to the header

to reduce any possible separation at the air header outlet and provide more uniform flow

in the LAMEE inlet opening. The CFD results show that this 100 mm length for the settle

down area is enough to provide uniform flow without any separation to the exchanger

inlet opening in the air velocity range of 0.5m/s to 3m/s. However, a fully-developed

laminar flow will happen at 170 mm to 1000 mm length from the header for that velocity

range where Reynolds number varies from 300 to 1800. The same air header is used at

the exchanger outlet. Furthermore, a flow straightener is used before the air inlet header

to supply a uniform air flow into the header.

2.4.2   Solution Loop

Water is used in this study to humidify or dehumidify the supply air. Water has

the surface relative humidity of 100%RH, and usually it is used for humidifying the air

flow (Zhang and Huang, 2011; Zhang, 2012). A peristaltic pump with the capacity of 1 to

2316 mL/min and calibration accuracy of 2% of the reading scale is used to pump the

water from a supply solution tank into the exchanger in an open loop. Also, two solution

headers, which are designed specifically for this single-panel LAMEE, are used at the

solution inlet and outlet of the exchanger to direct the solution through the exchanger and

collect it at the exchanger solution outlet, respectively. Moreover, two high-accuracy

shielded T-type thermocouples with the accuracy of 0.1˚C are used to measure the

solution temperatures at the solution inlet and outlet headers. These thermocouples were

calibrated with the same temperature calibrator as the air side thermocouples but in the

temperature range of 0 to 60˚C. Then, as shown in Figure 2.2(a), the solution is pumped

through the exchanger in the counter-cross flow configuration with respect to the air and

from bottom-to-top of the exchanger. Finally, the solution is collected in the exhaust solution tank at the exchanger solution outlet header. Also, the exchanger operates at almost constant pressure on the solution side inlet. The average static pressure at the solution side is calculated as 2.5 kPa from the friction and head loss in the solution side.
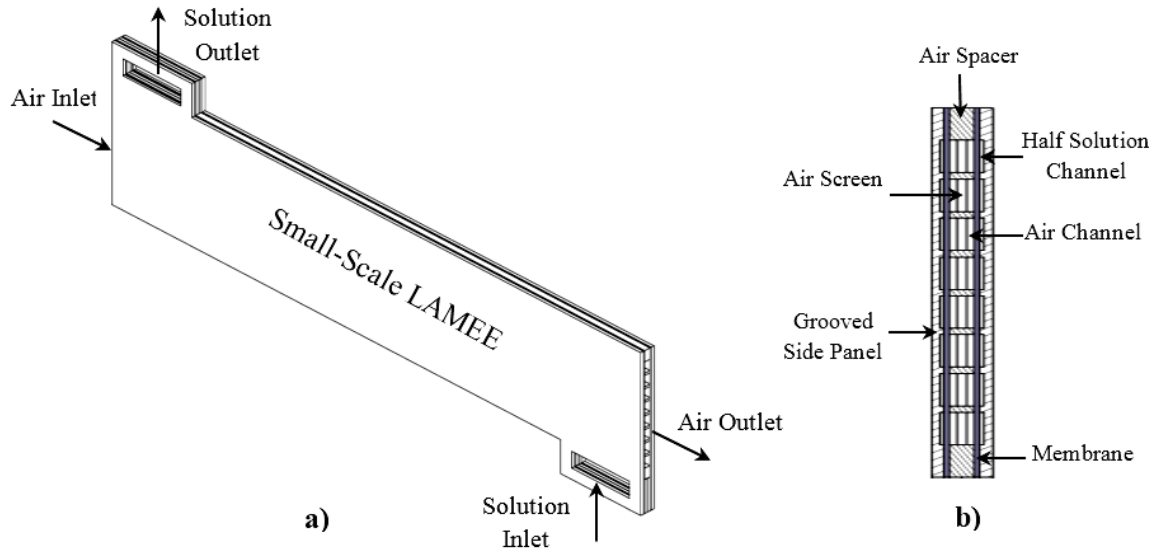
Figure 2.2 (a) Air and solution flow configuration and (b) a cross-section view of the small-scale single-panel LAMEE

Furthermore, the solution inlet temperature is conveniently adjusted by directly adding hot or cold water to the supply tank depending on the selected solution inlet temperature in the experiments. Lastly, a National Instruments data acquisition system (Type DAQ-9174) is used to acquire the data in the experiment, and a 2010 Lab View program is used to monitor and save the data during experimental tests.

2.4.3 Small-Scale Single-Panel LAMEE

A cross-section view of the small-scale flat-plate single-panel LAMEE is shown in Figure 2.2(b). The design of this novel single-panel LAMEE is improved in comparison to previous LAMEE designs to enhance the performance of the exchanger

(Mahmud, 2009). In the new design, the solution channels are grooved on two solid plastic surfaces, which are called side panels in this chapter. These side panels are made by a rapid prototype machine from FullCure850 composite material with the surface location accuracy of 0.1 mm. Afterwards, the membrane is applied on the side panels to create half-height solution side channels on each side panel. 3M Scotch ATG969 double layer adhesive tape is used to attach the membrane on the panels. The air flow channel is designed to be in the middle of the single panel exchanger and it is created by using air spacers on the upper and lower edges of the panel. Also, a turbulence enhancer device (air screen) is used in the air channel to increase the heat and mass transfer performance of the supply air. This screen is a new part which was recently added to the LAMEE. Unfortunately, right now there are not any data available for the amount of heat and mass transfer enhancement in the air channel of the LAMEE with this specific air screen. However, LePoudre *et al.* (2011) numerically modeled a rectangular air channel with the same geometry as the LAMEE's air channel, and a sinusoidal screen inside the channel. The results showed almost 100% improvement in the air convective heat transfer coefficient at *Re* ≈ 2000. Lastly, the single panel exchanger is assembled by placing two side panels side by side with the air channel in the middle. Also, the counter-cross flow configuration is chosen for the small-scale single-panel LAMEE, and the solution is pumped from the bottom-to-top through the exchanger in this research.

The main advantages of the new design for the small-scale LAMEE in comparison to the old LAMEE designs (Mahmud, 2009) are first, eliminating the solution leakage from the solution channels into the air stream. The membrane is attached directly on the edges of the side panels, which are wide enough to provide acceptable sealing

between the air and solution. Second, the solution flow mal-distribution is reduced by attaching the membrane on support walls of each solution channel. Flow mal-distribution may result from membrane deflection caused by the pressure difference between the air and the solution inside the exchanger; however, these deflections are very small in the new design. Finally, the new solution panel design uses several parallel solution channels on each side panel to provide more uniform flow across the solution panels and allows maximum membrane active area with higher heat and moisture transfer rates in comparison to previous designs. The small-scale LAMEE specifications and the measured membrane properties are presented in Table 2-1.

Table 2-1 Small-scale single-panel LAMEE specifications and membrane properties

Parameter	value
Exchanger length, L_{ex} (m)	0.49
Exchanger aspect ratio, L_{ex}/H_{ex}	5.2
Exchanger entrance ratio, L_{sol}/L_{ex}	0.11
Air gap thickness, d_{air} (mm)	5
Solution gap thickness on each side panel, $d_{sol}/2$ (mm)	0.8
Number of solution paths on each side panel	8
Mass resistance of membrane, R_{mem} (s/m)	56
Membrane thermal conductivity, k_{mem} (W/mK)	0.065
Membrane thickness, d_{mem} (mm)	0.265

2.5 Experimental Procedures

As described above, water is used as the transfer fluid in the single-panel LAMEE and the supply air state is regulated by the heater and humidifiers before entering the exchanger. The exchanger is tested at three different test conditions: air heating and humidifying (H&H), air cooling and humidifying (C&H), and air cooling and dehumidifying (C&D). The steady-state performance of the small-scale LAMEE is

evaluated at these conditions. Experiments at each condition are conducted at three different values for the number of heat transfer units (*NTU*) and constant *Cr**. The *Cr** was equal to 7 and *NTU* varied from 2.5, 3.5 and 4.5. The normal air and solution inlet conditions for each test are presented in Table 2-2; however, they are slightly different for each test case due to repeatability of the experiment at different *NTUs*. The measured air and solution inlet and outlet conditions for each experiment are reported in the results section. Also, the air and solution outlet conditions are measured at the steady-state operating condition to calculate the steady-state effectiveness of the single-panel LAMEE. The steady-state condition is determined when the temperature and relative humidity changes by time ($\frac{\mathrm{d}T}{\mathrm{d}t}$ and $\frac{\mathrm{d}(RH)}{\mathrm{d}t}$) are smaller than their uncertainties in the experiment, which are 0.1°C and 1%RH, respectively.

Afterwards, the numerical sensible and latent steady-state effectivenesses of the single-panel LAMEE at different supply air conditions are plotted on the psychrometric chart and verified with three experimental tests. The solution inlet temperature, *NTU* and *Cr** are set at 22˚C, 3.5 and 7 to generate those results. The designed air inlet and test conditions for each test are shown in Table 2-2.

Table 2-2 Normal air and solution inlet test conditions

Test Case	Air Inlet		Solution Inlet
	T,°C	W,g/kg	T,°C
H&H	22	8.5 (52%RH)	30
C&H	35	7.1 (21%RH)	22
C&D	35	19.4 (55%RH)	16
Contour map, C&H#1	28	9.2 (39%RH)	22
Contour map, C&H#2	35	7.1 (21%RH)	22
Contour map, C&D	35	21.2 (60%RH)	22

2.5.1 Test Facility Mass and Energy Balances

It is necessary to do mass and energy balances for the SPEET facility before beginning the experiments to prove that the system is working at steady-state and generating accurate experimental data within acceptable uncertainty ranges. For this purpose, the conservation of mass and energy in the system is used to check the system bias error. If the mass and energy balance are not satisfied in the system at steady-state, it means that an unaccounted bias error exists (Simonson *et al.*, 1999). Dry air and solution mass balances are checked in the energy exchanger to make sure that there is no air leakage in the system. To establish the dry air and solution mass balance the following equations should be satisfied (Simonson *et al.*, 1999):

$$\Delta \dot{m}_{air} = \left| \dot{m}_{air,in} - \dot{m}_{air,out} \right| \leq Un_{\Delta \dot{m}_{air}} \tag{2.1}$$

$$\Delta \dot{m}_{sol} = \left| \dot{m}_{sol,in} - \dot{m}_{sol,out} \right| \leq Un_{\Delta \dot{m}_{sol}} \tag{2.2}$$

where, $\dot{m}$ is the mass flow rate and subscripts *air* and *sol* refer to the air and solution (water) in the system, respectively. Also, subscripts *in* and *out* refer to the inlet and outlet of the air or solution, respectively. $Un_{\Delta \dot{m}_{air}}$ and $Un_{\Delta \dot{m}_{sol}}$ are the calculated uncertainty for measured air and solution mass flow rate differences in the system between the inlet and outlet, respectively. After establishing the dry air and solution mass balances, water vapor and energy in the system are required to be balanced to ensure valid experimental results. The water vapor and energy balances equations are provided as follow (Simonson *et al.*, 1999):

$$\Delta (\dot{m}W) = \left| \left[(\dot{m}W)_{air,in} - (\dot{m}W)_{air,out} \right] + \left[\dot{m}_{sol,in} - \dot{m}_{sol,out} \right] \right| \leq Un_{\Delta(\dot{m}W)} \tag{2.3}$$

$$\Delta (\dot{m}H) = \left| \left[(\dot{m}H)_{air,in} - (\dot{m}H)_{air,out} \right] + \left[(\dot{m}H)_{sol,in} - (\dot{m}H)_{sol,out} \right] \right| \leq Un_{\Delta(\dot{m}H)} \tag{2.4}$$

where W and H are humidity ratio and specific enthalpy, respectively. Also, $Un_{\Delta(\dot{m}W)}$ and $Un_{\Delta(\dot{m}H)}$ are the calculated uncertainties for the water vapor and energy transfer in the system based on the measured air and solution properties in Eqs. (3) and (4), respectively. In Eq. (2.3), the water vapor transfer in the solution side, which is pure water in this experiment, is the water mass flow rate difference between the solution inlet and outlet. Additionally, the energy balance of the system can be represented in terms of percentage by using the energy exchange inequality (*EEI*) in the system. The energy exchange inequality in the LAMEE is the summation of the total energy transferred to/from the air and solution in the exchanger divided by the total input energy to the system and expressed as a percentage in Eq. (2.5).

$$EEI = 100 \times \frac{\left|\left[\left(\dot{m}H\right)_{air,in} - \left(\dot{m}H\right)_{air,out}\right] + \left[\left(\dot{m}H\right)_{sol,in} - \left(\dot{m}H\right)_{sol,out}\right]\right|}{\left|\left(\dot{m}H\right)_{air,in} + \left(\dot{m}H\right)_{sol,in}\right|} \quad (2.5)$$

To verify the mass and energy balance, the small-scale LAMEE test facility is tested at a specific operating condition, where *NTU* and *Cr** are set at 3.5 and 7, respectively. The steady-state air and solution inlet and outlet conditions and flow rates for this experimental test are presented in Table 2-3. To do the dry air mass balance, a mass flow controller with the capacity of 100 L/min and 2% of full-scale accuracy is used to supply the air into the system and measure the supply inlet air flow rate. A mass flow meter with the same capacity and 1% of full-scale accuracy is installed at the end of the air pipeline to measure the outlet air flow rate. Also, during the experiment the air side pressure in the system was monitored by using a barometer on the exchanger inlet to prevent any possible damage to the test setup due to over pressurizing the system because of using the mass flow meter at the outlet. According to the mass and energy balances

results in Table 2-3, the small-scale LAMEE test setup is balanced and is operating at a steady-state condition. Also, the water vapor and energy balances of the system during the experiments are checked based on the steady-state experimental results for the three designed test cases at *NTU* and *Cr** equal to 3.5 and 7, respectively, and the results are presented in Table 2-4. The dry air and solution flow rates are assumed to be the same at the exchanger air and solution inlets and outlets for each test case. The results show that, the energy and mass are conserved within experimental uncertainties during the experiments.

Table 2-3 Air and solution properties measured at the inlet and outlet of the small-scale LAMEE to establish the mass and energy balance, and mass and energy balance results

Parameter	Unit	Value	Uncertainty
$T_{air,in}$	°C	23.1	0.2
$W_{air,in}$	g/kg	1.82	0.15
$Q_{air,in}$	L/min	28	2
$T_{air,out}$	°C	16.3	0.2
$W_{air,out}$	g/kg	7.74	0.38
$Q_{air,out}$	L/min	25.9	1
$T_{sol,in}$	°C	15.8	0.1
$Q_{sol,in}$	mL/min	55.3	2
$T_{sol,out}$	°C	13.1	0.2
$Q_{sol,out}$	mL/min	54.1	1.1
$\Delta \dot{m}_{air}$	kg/h	0.122	0.159
$\Delta \dot{m}_{sol}$	kg/h	0.079	0.172
$\Delta(\dot{m}W)$	kg/h	0.068	0.172
$\Delta(\dot{m}H)$	W	3.4	3.7
EEI	%	4.7	-

Table 2-4 Water vapor and energy balance for small-scale LAMEE at different test operating conditions at *NTU* = 3.5 and *Cr** = 7

Test case	Water vapor balance		Energy balance		*EEI*
	$\Delta(\dot{m}W)$, kg/h	$Un_{\Delta(\dot{m}W)}$, kg/h	$\Delta(\dot{m}H)$, W	$Un_{\Delta(\dot{m}H)}$, W	%
H&H	0.029	0.097	3.7	3.8	2.8
C&H	0.019	0.096	0.3	2.8	0.5
C&D	0.015	0.095	4.2	4.4	3.9

2.6 Theory of the Experiment

2.6.1 LAMEE Performance Evaluation

The performance of a LAMEE system is evaluated by sensible, latent and total effectiveness. The sensible effectiveness is due to sensible energy transfer in the LAMEE and is calculated using the following equation, for equal thermal mass capacity rates for the dry air at inlet and outlet:

$$\varepsilon_{Sensible} = \frac{\left(T_{air,in} - T_{air,out}\right)}{\left(T_{air,in} - T_{sol,in}\right)} \tag{2.6}$$

where, ε is effectiveness and T is temperature. It is noted that this definition of effectiveness is somewhat different from the standard definition in the heat transfer literature because it does not explicitly include the thermal capacity rate ratio because it is equal to 1.

Similarly, the latent effectiveness of a LAMEE is due to moisture transfer in the energy exchanger, and is defined as latent energy transferred in the system over maximum possible latent energy transfer in the exchanger.

$$\varepsilon_{Latent} = \frac{\left(W_{air,in} - W_{air,out}\right)}{\left(W_{air,in} - W_{sol,in}\right)} \tag{2.7}$$

The solution (water) inlet equivalent humidity content, $W_{sol,in}$, is equal to the saturated air (i.e. 100%RH) humidity ratio at the same temperature as the water. Finally, the total effectiveness of the LAMEE, which is related to both sensible and latent energy transfers, is calculated from the following equation which was developed for a thermal capacity rate ratio of 1 (Simonson and Besant, 1999):

$$\varepsilon_{Total} = \frac{\varepsilon_{Sensible} + H^* \varepsilon_{Latent}}{1 + H^*} \tag{2.8}$$

where H^* is the operating factor and it is calculated based on air and solution inlet temperatures and humidity ratios in the LAMEE (Simonson and Besant, 1999).

$$H^* = \frac{\Delta H_{Latent}}{\Delta H_{Sensible}} \approx 2500 \frac{W_{air,in} - W_{sol,in}}{T_{air,in} - T_{sol,in}} \tag{2.9}$$

2.6.2   Numerical and Analytical Models

In this chapter, the experimental results are compared to three different sets of results from a numerical model and two analytical models, which are available to evaluate the performance of energy exchangers at the steady-state operating conditions. The trend in the numerical and analytical models was compared with the experimental data; however, validating the models is not the purpose of this chapter. Firstly, the experimental results are compared to the enthalpy pump system (EPS) numerical model results, which had been developed by the University of Saskatchewan RAMEE research group (Seyed-Ahmadi, 2008; Hemingson, 2010). The EPS code is modified based on the small-scale single-panel LAMEE design and the results are presented for a counter-flow LAMEE at the steady-state operating conditions. Approximately, ninety percent of the designed small-scale LAMEE is pure counter-flow. Furthermore, Akbari *et al.* (2012a)

showed that for a LAMEE system with the same aspect ratio and entrance ratio as the small-scale LAMEE, the discrepancy between the numerical LAMEE performance results for a counter-cross flow LAMEE and a pure counter-flow LAMEE is less than 1%. As a result, a counter-flow configuration is used to numerically model the small-scale LAMEE. Additionally, heat losses/gains to/from surroundings are considered during numerical modeling to provide more accurate numerical results, and water is used as a transfer media in the numerical code to model the small-scale LAMEE.

2.6.2.1 Analytical Model Based on Analogy between Heat Exchangers and LAMEEs (Shah and Sekulic, 2003)

Secondly, the experimental results for the sensible effectiveness of the small-scale LAMEE are compared to the results based on Shah and London analytical solution for heat exchangers (Shah and Sekulic, 2003). This analytical model is based on heat transfer only, and it is valid for sensible performance of a flat-plate heat exchanger at steady-state operating conditions with laminar flow for both fluids. The small-scale LAMEE is modeled with counter-cross flow configuration in this model to get better agreement between the experimental and analytical results. Shah and London presented a conclusion for sensible effectiveness of a pure cross and pure counter flow heat exchangers:

$$\varepsilon_{Sensible,Cross} = 1 - \exp\left\{\frac{NTU^{0.22}}{Cr}\left[\exp\left(-Cr\ NTU^{0.78}\right) - 1\right]\right\} \tag{2.10}$$

$$\varepsilon_{Sensible,Counter} = \frac{1 - \exp\left[-NTU\left(1 - Cr\right)\right]}{1 - Cr\exp\left[-NTU\left(1 - Cr\right)\right]} \tag{2.11}$$

where the dimensionless groups NTU and Cr are the number of heat transfer unit and heat capacity ratio, respectively, and they were calculated as follow:

$$NTU = \frac{UA}{C_{\min}} \tag{2.12}$$

$$Cr = \frac{C_{\min}}{C_{\max}} \tag{2.13}$$

where U and A are the overall convective heat transfer coefficient and the total membrane active area in the LAMEE, respectively. Also, $C_{\min}$ is the minimum heat capacity rate between the air and solution in the LAMEE that is equal to the air heat capacity rate in this study. So, Eqs. (2.12) and (2.13) can be written in the following format for LAMEEs:

$$NTU = \frac{UA}{C_{air}} = \frac{UA}{\left(\dot{m} c_p \right)_{air}} \tag{2.14}$$

$$Cr = \frac{C_{air}}{C_{sol}} = \frac{\left(\dot{m} c_p \right)_{air}}{\left(\dot{m} c_p \right)_{sol}} = \frac{1}{Cr^*} \tag{2.15}$$

In Eqs. (2.14) and (2.15), $\dot{m}$ and c_p are the mass flow rate and specific heat capacity, respectively. Also Cr^* is another dimensionless group for heat capacity ratio, which is equal to the inverse of Cr, and it is used in this chapter as a definition for heat capacity ratio. Additionally, the overall convective heat transfer coefficient for LAMEEs is calculated using the equation:

$$U = \left[\frac{1}{h_{air}} + \frac{d_{mem}}{k_{mem}} + \frac{1}{h_{sol}} \right]^{-1} \tag{2.16}$$

where h, d and k are the convective heat transfer coefficient, thickness and thermal conductivity, respectively. The subscript *mem* represents the membrane properties. In a counter-cross flow LAMEE the combined sensible effectiveness obtained from Eqs. (2.10) and (2.11) is expressed as:

$$\varepsilon_{Sensible} = \left(\frac{A_{Cross}}{A} \right) \varepsilon_{Sensible,Cross} + \left(\frac{A_{Counter}}{A} \right) \varepsilon_{Sensible,Counter} \qquad (2.17)$$

The sensible effectiveness of the counter-cross flow small-scale LAMEE is calculated from Eq. (2.17), where the pure cross and counter active areas of the exchanger are readily determined for the small-scale LAMEE geometry. Furthermore, the analytical latent effectiveness of the small-scale LAMEE is calculated based on a heat and mass transfer analogy from this analytical model (Niu and Zhang, 2001). The heat and mass transfer analogy is given by the following correlation (Niu and Zhang, 2001):

$$Sh = NuLe^{-\frac{1}{3}} \qquad (2.18)$$

where Sh, Nu and Le are the Sherwood, Nusselt and Lewis dimensionless groups. The convective heat and mass transfer coefficients are found from the Nusselt and Sherwood number definitions (Seyed-Ahmadi, 2008).

$$Nu = \frac{hD_h}{k} \qquad (2.19)$$

$$Sh = \frac{h_m D_h}{D_{v-a}} \qquad (2.20)$$

Where h_m is the convective mass transfer coefficient. D_h and D_{v-a} are the hydraulic diameter and diffusivity coefficient of vapor into air. By substituting the equations for Sherwood and Nusselt numbers into Eq. (2.18), the convective mass transfer coefficient for air and solution is found as follows:

$$h_m = \frac{h}{c_p} Le^{-\frac{1}{3}} \qquad (2.21)$$

Since there are no data available about the air flow pattern in the air channel of the LAMEE with the air screen and the amount of heat transfer enhancement in the air

side of the LAMEE, the fully-developed laminar flow regime was assumed for both the air and water flow streams in the LAMEE. The maximum Reynolds numbers on the air and water channels are 1800 and 20, respectively. Consequently, Nusselt numbers of 8.24 (for a fully-developed laminar flow between two infinite parallel plates with constant heat flux on both walls) and 5.39 (for a fully-developed laminar flow between two infinite parallel plates with constant heat flux on one wall and the other wall insulated) are used for the air and water sides of the LAMEE, respectively (Incropera and DeWitt, 1985).

Similar to the sensible effectiveness, the LAMEE latent effectiveness values for counter, cross and counter-cross flow exchangers are calculated based on the heat and mass transfer analogy from Eqs. (2.10), (2.11) and (2.17) using expressions similar to those equations (Nasif *et al.*, 2005):

$$\varepsilon_{Latent,Cross} = 1 - \exp\left\{\frac{NTU_m^{0.22}}{m^*}\left[\exp\left(-m^* NTU_m^{0.78}\right) - 1\right]\right\} \tag{2.22}$$

$$\varepsilon_{Latent,Counter} = \frac{1 - \exp\left[-NTU_m\left(1 - m^*\right)\right]}{1 - m^* \exp\left[-NTU_m\left(1 - m^*\right)\right]} \tag{2.23}$$

$$\varepsilon_{Latent} = \left(\frac{A_{Cross}}{A}\right)\varepsilon_{Latent,Cross} + \left(\frac{A_{Counter}}{A}\right)\varepsilon_{Latent,Counter} \tag{2.24}$$

where the dimensionless groups NTU_m and m^* are the number of mass transfer units and mass flow rate ratio, respectively. The heat and mass transfer problems are uncoupled in this analytical model using the heat and mass transfer analogy where the latent effectiveness is found based on sensible effectiveness correlation and substituting the NTU and Cr^* with NTU_m and m^*. NTU_m and m^* are calculated as follows for the LAMEE system:

$$NTU_m = \frac{U_m A}{\dot{m}_{\min}} = \frac{U_m A}{\dot{m}_{air}} \tag{2.25}$$

$$m^* = \frac{\dot{m}_{\min}}{\dot{m}_{\max}} = \frac{\dot{m}_{air}}{\dot{m}_{sol}} \tag{2.26}$$

where,

$$U_m = \left[\frac{1}{h_{m,air}} + R_{mem} + \frac{1}{h_{m,sol}} \right]^{-1} \tag{2.27}$$

In Eq. (2.27), U_m is the overall convective mass transfer coefficient and R_{mem} is the membrane moisture transfer resistance. Finally, the total effectiveness is calculated from sensible and latent effectiveness based on Eq. (2.8) in this analytical model.

2.6.2.2 Analytical Model for Coupled Heat and Moisture Transfers in LAMEEs

Finally, the experimental results of the small-scale LAMEE are compared to the analytical model derived by Zhang (2011a) for coupled heat and moisture transfers (Zhang, 2011a). The steady-state performance of a hollow fiber-membrane shell and tube energy exchanger with counter-flow configuration is analytically and experimentally evaluated by Zhang where the tube side is used for the solution flow and air passes through the shell side in counter-flow configuration. In order to use this analytical solution for the flat-plate small-scale LAMEE, the *NTU* and *Cr** are calculated based on the small-scale LAMEE design and specifications and they are substituted into Zhang's analytical model. Moreover, due to using pure water instead of salt solution in this system, a salt solution with very small concentration (~ 0%) is used to represent the properties of water in Zhang's analytical model. Also, it is assumed that the salt solution concentration is constant in the exchanger and the solution convective heat and mass

41

transfer coefficients are neglected in comparison to the air to calculate the overall heat and mass transfer coefficients for the LAMEE (Hemingson, 2010). Moreover, Namvar *et al.* (2012) compared the experimental results for the steady-state performance of a large-scale LAMEE at different *Cr** and *NTUs* with Zhang's analytical solution. The results show an acceptable agreement between the experimental and analytical LAMEE performance results.

2.7   Results and Discussion

In this section the experimental results for each test conditions are presented and the trends in the experimental data are compared to the numerical and analytical models results which were explained in Section 2.6.2. These results are presented for three different conditions: H&H, C&H and C&D, which are representative of a cold and dry, hot and dry, and hot and humid outdoor climate operating conditions for the small-scale LAMEE, respectively. The air and solution design conditions for these experiments are presented in Table 2-2. Afterwards, numerical sensible and latent performance contour maps of the small-scale LAMEE are depicted on the psychrometric chart for various supply air conditions, and the numerical results are verified with three experimental tests.

2.7.1   Air Heating and Humidifying (H&H)

In this test condition, the supply air is heated and humidified while it passes through the exchanger. Three experimental tests at *NTUs* equal to 2.5, 3.5 and 4.5 are conducted for this test condition. The *NTU* is changed by changing the air flow rate through the exchanger for each case. The air and solution inlet conditions are almost constant and *Cr** = 7 for all experiments. The measured air and solution inlet and outlet conditions for the H&H test case are presented in Table 2-5. Moreover, the experimental

air and solution inlet and outlet conditions for *Cr** and *NTU* equal to 7 and 3.5, respectively, are plotted on the psychrometric chart in Figure 2.3 to better portray this test condition. Afterwards, the performance of the small-scale LAMEE is evaluated at three different *NTUs* and it is compared with numerical and analytical results for the same operating conditions.

Table 2-5 Measured air and solution inlet and outlet conditions for the different test cases at *Cr = 7 and different *NTUs***

Test case	NTU	$T_{air,in}$, ℃	$W_{air,in}$, g/kg	$T_{air,out}$, ℃	$W_{air,out}$, g/kg	$T_{sol,in}$, ℃	$T_{sol,out}$, ℃
H&H	2.5	21.9	8.44	26.3	20.75	29.8	23.1
H&H	3.5	21.9	8.46	26.5	21.82	29.9	22.7
H&H	4.5	22	8.46	26.9	22.28	29.8	21
C&H	2.5	35	6.69	22	14.60	22	21.1
C&H	3.5	34.9	7.12	21.7	16.30	22	21.3
C&H	4.5	34.9	7.09	21.8	16.66	22	21.4
C&D	2.5	35	19.57	19	13.77	16	22.7
C&D	3.5	34.9	19.17	18.4	13.28	16	23.2
C&D	4.5	34.8	19.13	18.1	13.02	16.1	24.6
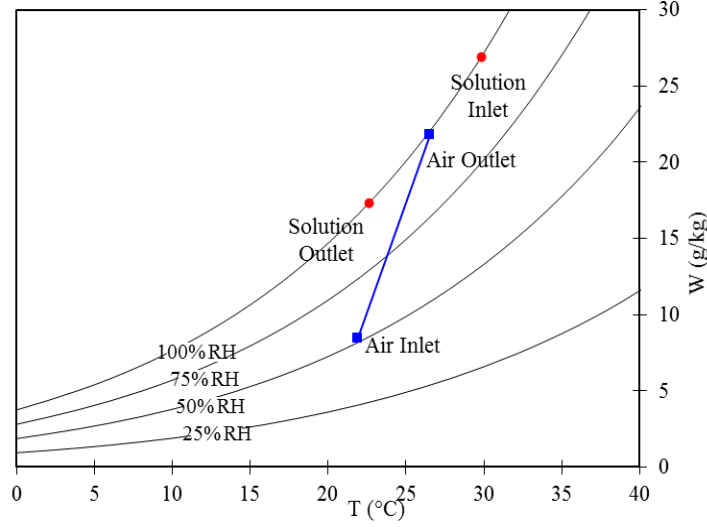
Figure 2.3 Experimental air and solution inlet and outlet conditions on the psychrometric chart for the air heating and humidifying test (*Cr** = 7 and *NTU* = 3.5)

Figure 2.4 shows the sensible, latent and total effectiveness values of the small-scale LAMEE at air H&H test conditions. The effectiveness of the small-scale LAMEE increases by almost 10% while *NTU* increases from 2.5 to 4.5. The numerical and two analytical results are presented in Figure 2.4 for the small-scale LAMEE with counter-flow configuration at the same operating conditions as the experiments. The results show that the numerical and analytical results follow the same trend as the experimental data for the LAMEE performance when *NTU* increases, but the results predict higher effectiveness for the small-scale LAMEE at this test condition. Furthermore, the agreement between the experimental, numerical and analytical results for the latent and total effectiveness is good, and the numerical and analytical results are within the uncertainty bounds for the experiments. However, discrepancy between the experimental and other results is significant for sensible effectiveness (i.e. almost 20%). The numerical and analytical models also predict higher outlet air temperatures for all three *NTUs* which cause higher sensible effectiveness values in comparison to experimental data.

44
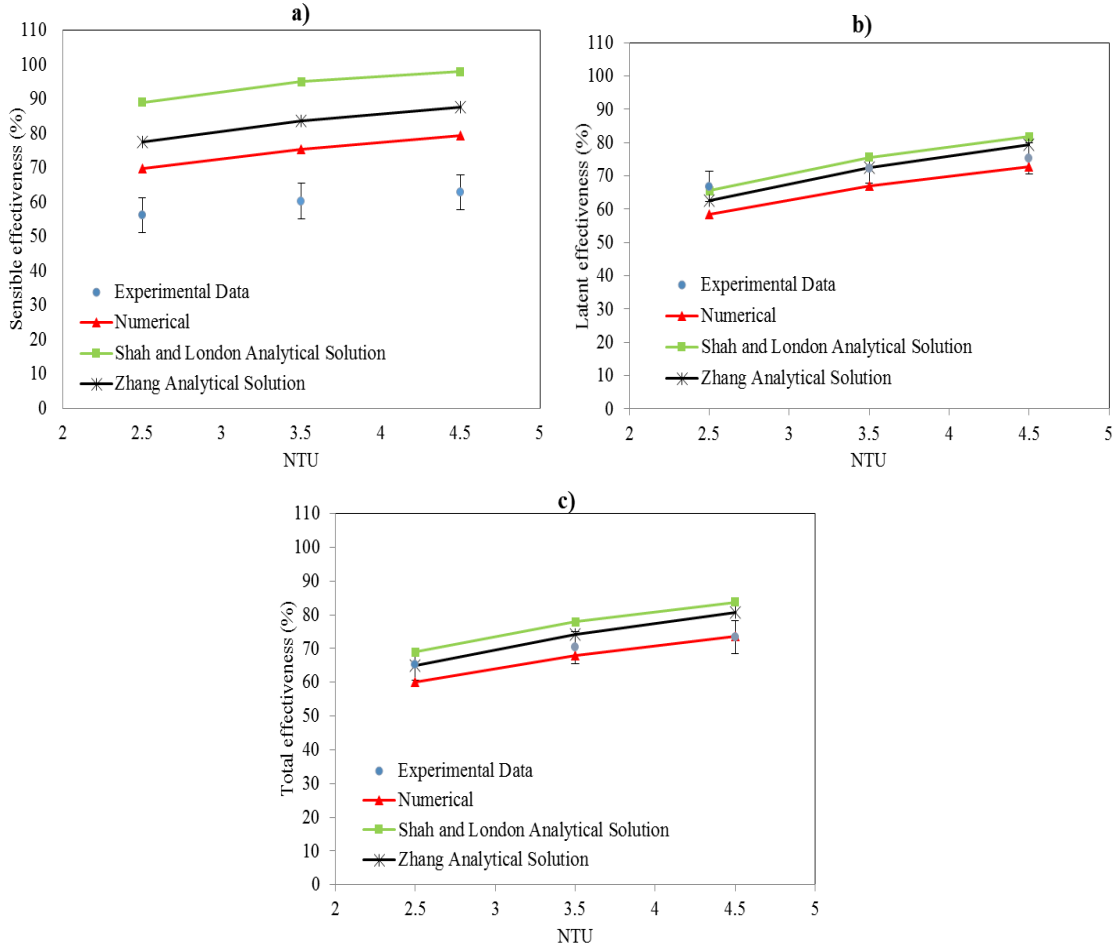
Figure 2.4 Steady-state a) sensible, b) latent and c) total effectiveness of the small-scale LAMEE versus *NTU* for the air heating and humidifying test with *Cr** = 7

Figure 2.5 shows absolute differences between the air inlet and outlet temperatures and humidity ratios at steady-state condition for both numerical and experimental results at H&H test conditions. According to Figure 2.5(a), this difference for the air temperature is 2˚C higher for the numerical results. The discrepancy between the experimental data and the numerical and analytical results may be due to the following assumptions which are made during the numerical and analytical modeling. Firstly, the membrane bulging and mal-distribution effect in the solution and air side are neglected in the numerical and analytical analysis. Also, it is assumed that there is not any solution leakage in the exchanger during numerical and analytical modeling. The

solution leakage in the small-scale LAMEE is tested and measured before the experiment and it is less than 1% of the solution flow rate inside the exchanger. Additionally, calculating the membrane properties such as membrane thickness and water vapor permeability have uncertainties, which are not considered in the numerical and analytical models, but have a significant effect on the LAMEE effectiveness results. Moreover, solving the uncoupled heat and mass transfer problems in the Shah and London analytical solution (Shah and Sekulic, 2003), and neglecting the solution heat and mass transfer convective coefficients in comparison to air while calculating the overall heat and mass transfer coefficients, in the Zhang's analytical solution can be considered as the other sources of discrepancy between the experimental and analytical results. Lastly, the laminar flow regime was assumed for the air side of the LAMEE during the modeling to calculate the air convective heat and mass transfer coefficients. The amount of heat and mass transfer enhancements caused by the air screen inside the air channel of the LAMEE are neglected in the numerical and analytical models. This assumption can be considered as an important source of discrepancy between the experimental, numerical and analytical results. The actual measured air convective heat transfer coefficient in the air channel of the small-scale LAMEE with the presence of the air screen is used in Chapter 5 to improve the accuracy of the small-scale LAMEE numerical model and calculate the small-scale LAMEE performance under different operating conditions. Also, the numerical model uncertainties are presented in Chapter 5.
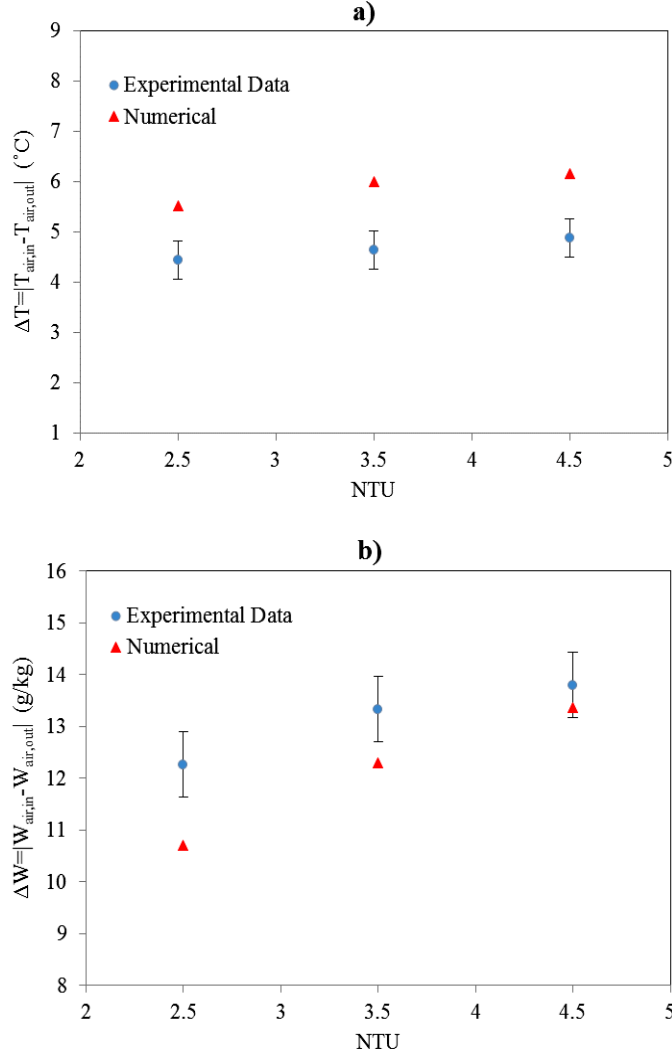
Figure 2.5 Steady-state air a) temperature and b) humidity ratio absolute difference between the air inlet and outlet of the small-scale LAMEE versus *NTU* for the air heating and humidifying test with $Cr* = 7$ ($T_{air,in}$-$T_{sol,in}$ = 7.9°C and $W_{air,in}$-$W_{sol,in}$ = 18.37 g/kg)

2.7.2 Air Cooling and Humidifying (C&H)

This test condition represents the small-scale LAMEE performance in hot and dry climates. The air is cooled and humidified while passing through the exchanger. Table 2-5 shows the measured air and solution inlet and outlet conditions for this experiment at three different *NTUs* and $Cr* = 7$ as before. Also, the experimental air and solution inlet and outlet conditions for $Cr*$ and *NTU* equal to 7 and 3.5, respectively, are shown on the

psychrometric chart in Figure 2.6. According to the data in Table 2-5 and Figure 2.6, the air outlet and the solution inlet and outlet conditions are very close together for this test case which affect the experimental uncertainty for the small-scale LAMEE effectiveness and the discrepancy between the experimental, numerical and analytical results. The air and solution inlet conditions are chosen at almost the same enthalpy line on the psychrometric chart, which causes the air and solution outlet conditions to have the same enthalpy and be very close to the solution inlet conditions.
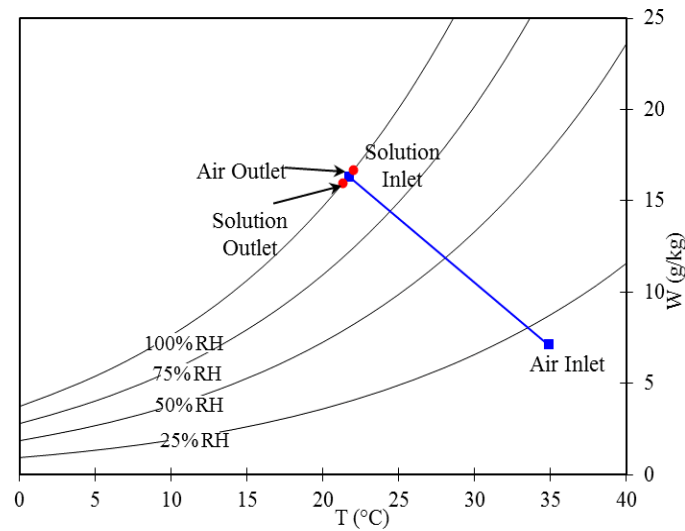
Figure 2.6 Experimental air and solution inlet and outlet conditions on the psychrometric chart for the air cooling and humidifying test ($Cr* = 7$ and $NTU = 3.5$)

Figure 2.7 shows the sensible, latent and total effectiveness of the small-scale LAMEE for the experiment and numerical and analytical analysis. Again, the sensible, latent and total effectiveness values of the LAMEE increased with NTU. The numerical and analytical solutions predict lower effectiveness for the small-scale LAMEE at this test condition. Also according to Figure 2.7(a), the experimental sensible effectiveness of the LAMEE in this case is higher than 100%, and the agreement between the experimental, numerical and analytical results is good for the sensible effectiveness.

However, the discrepancy between the results for latent and total effectiveness is significant and it can be due to choosing the air and the solution inlet conditions at almost the same enthalpy, and simplification assumptions which are made during the numerical and analytical modeling, as mentioned in Section 2.7.1 for the H&H test case.
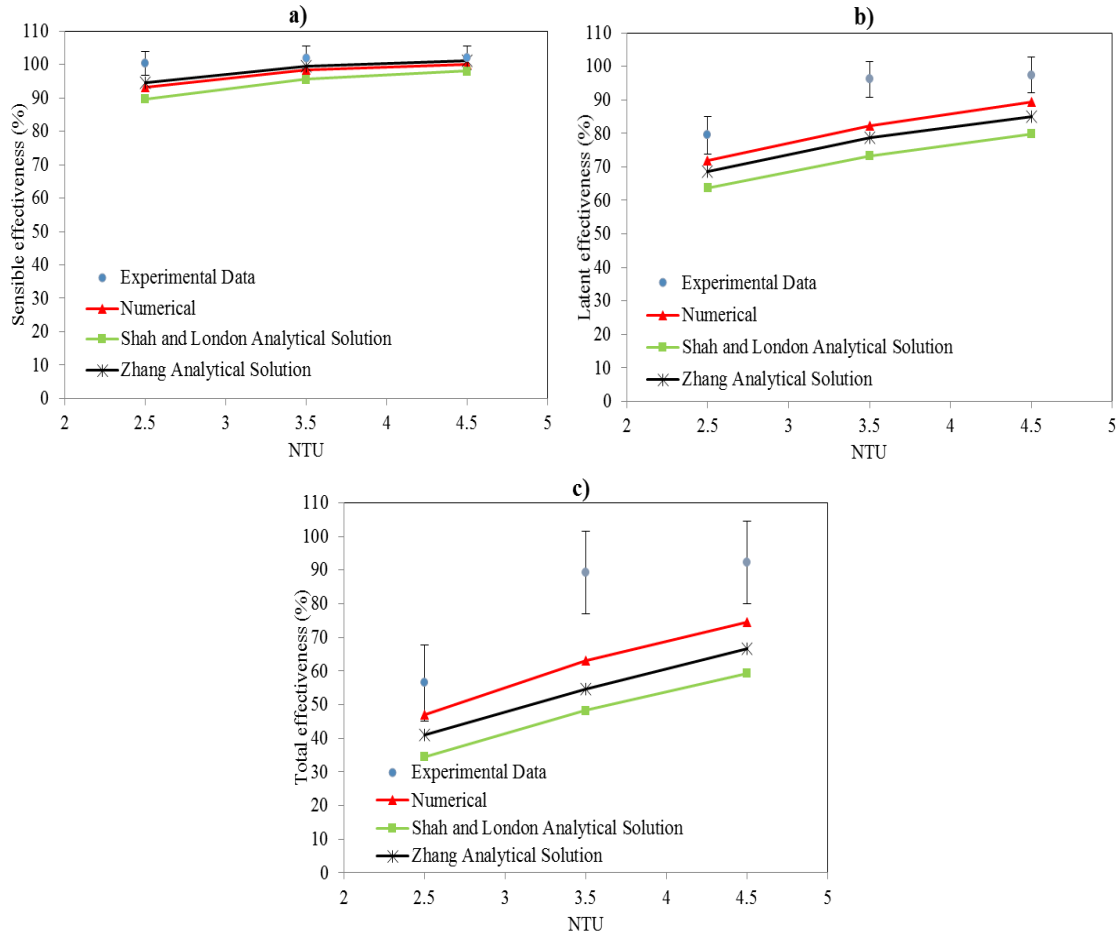
Figure 2.7 Steady-state a) sensible, b) latent and c) total effectiveness of the small-scale LAMEE versus *NTU* for the air cooling and humidifying test with *Cr* = 7*

2.7.3 Air Cooling and Dehumidifying (C&D)

For this test condition hot and humid air is supplied to the small-scale LAMEE and this air is cooled and dehumidified using 16°C water pumped through the solution channels. The measured air and solution inlet and outlet conditions are presented in Table 2-5 for three different *NTUs* the same as previous cases. Additionally, the air and solution

inlet and outlet condition for *NTU* = 3.5 and *Cr** = 7 are depicted on the psychrometric

chart in Figure 2.8 to have better understanding of the air and solution inlet and outlet

conditions in the experiment.
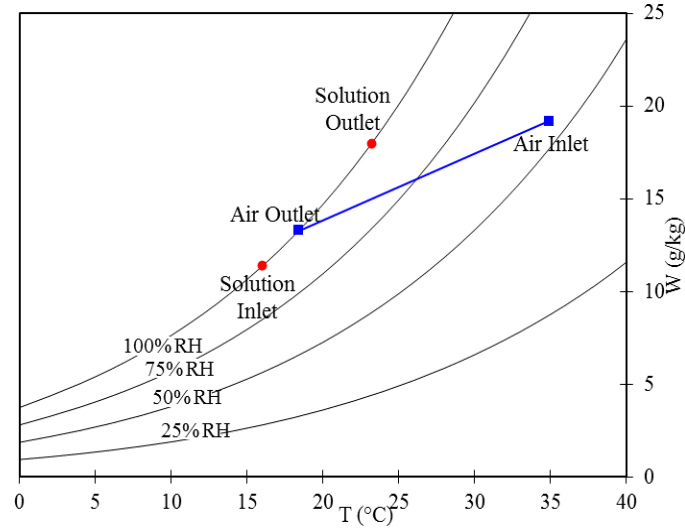
Figure 2.8 Experimental air and solution inlet and outlet conditions on the psychrometric chart for the air cooling and dehumidifying test (*Cr** = 7 and *NTU* = 3.5)

The experimental sensible, latent and total effectiveness data of the small-scale

LAMEE for three different *NTUs* and *Cr** = 7 are compared with numerical and

analytical results in Figure 2.9. The agreement among the experimental, numerical and

analytical results is good and the numerical and analytical results are within the

uncertainty bound for the experimental data especially for the latent and total

effectiveness. The maximum discrepancy between the experimental and other

effectiveness results is in Figure 2.9(a) for the sensible effectiveness which is less than

10%. The experimental sensible, latent and total effectivenesses of the LAMEE increase

with *NTU* by almost 10% in Figure 2.9. Also, as it can be seen in Figure 2.8, the good

selection of the air and water inlet conditions for the C&D test case has an effect on the

good agreement between the experimental and modeling effectiveness results of the small-scale LAMEE.
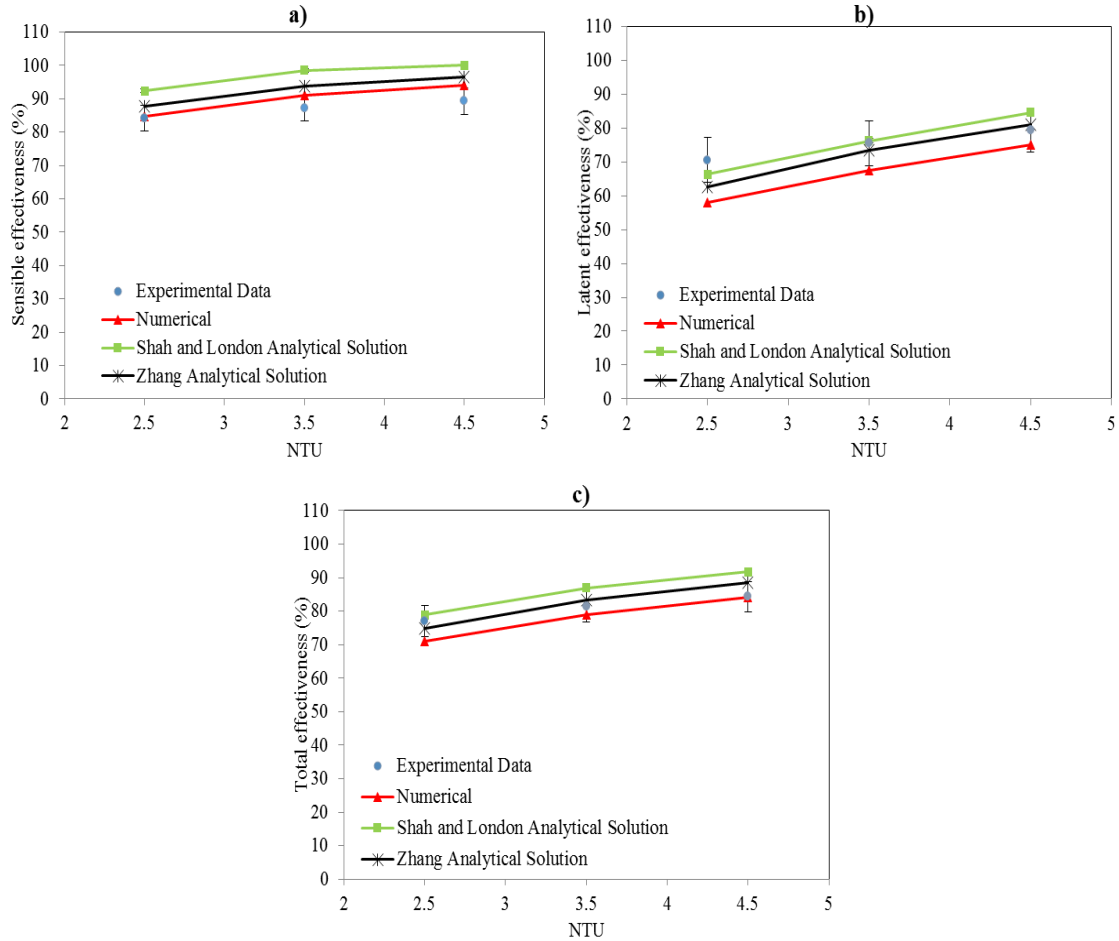
Figure 2.9 Steady-state a) sensible, b) latent and c) total effectiveness of the small-scale LAMEE versus *NTU* for the air cooling and dehumidifying test with *Cr** = 7

2.7.4 Small-Scale LAMEE Steady-State Effectiveness Contour Maps

Using the numerical model for the small-scale single-panel LAMEE with counter-flow configuration, the sensible and latent effectiveness of the small-scale LAMEE are plotted on the psychrometric chart as a contour function of the supply air conditions as shown in Figure 2.10. These performance contour maps are created with *Cr** = 7 and *NTU* = 3.5, and the water inlet temperature at 22˚C. The outdoor air condition is one of the important parameters affecting the performance of any kind of heat or energy

exchanger such as LAMEEs. Since, there are many parameters affecting the performance of the small-scale LAMEE, the other important parameters (e.g. *NTU*, *Cr** and water inlet conditions) are kept constant, and the effect of only air inlet conditions on the LAMEE performance are studied in contour maps. Finally, three different experimental tests are done to verify these performance contour maps. The measured air and solution inlet and outlet conditions for experimental tests are presented in Table 2-6. Two tests are done at C&H test conditions and one test is done at C&D test conditions, and they are included in Figure 2.10.

Table 2-6 Measured air and solution inlet and outlet conditions for the experiments that are used to verify the numerical small-scale LAMEE performance contour maps at *Cr** = 7 and *NTU* = 3.5

Test Case	$T_{air,in}$, ℃	$W_{air,in}$, g/kg	$T_{air,out}$, ℃	$W_{air,out}$, g/kg	$T_{sol,in}$, ℃	$T_{sol,out}$, ℃
C&H#1	28.1	9.16	21.8	15.53	22	20.6
C&H#2	34.9	7.12	21.7	16.3	22	21.3
C&D	35	21.19	23.2	17.68	22	25.9

In Figure 2.10, both the numerical sensible and latent effectiveness results are within the uncertainty ranges for the experimental results in most cases except for the C&H #2 test case. As a result, these contour maps can be used to predict the performance of the small-scale LAMEE at different supply air conditions with acceptable uncertainties. According to Figure 2.10(a), in the wide range of supply air conditions on the psychrometric chart, the sensible effectiveness varies between 75% and 120%. As well, the sensible effectiveness goes to infinity when the supply air temperature equals the solution inlet temperature. Additionally, it can be seen from Figure 2.10(a) that the sensible effectiveness is strongly dependent on the temperature change; however, it still depends on the supply air humidity ratio change as well. Furthermore, Figure 2.10(b) shows that the latent effectiveness goes to infinity when the supply inlet air humidity

equals the inlet solution humidity. Also, it shows that in the wide range of supply air conditions on the psychrometric chart the latent effectiveness of the small-scale LAMEE varies between 70% and 90%. The latent effectiveness of the small-scale LAMEE is strongly depending on the humidity ratio changes. These results are only an example of these kinds of contours for liquid desiccant (LD) systems such as LAMEEs, which show the effect of the outdoor air conditions on the performance of the LAMEE. The contour maps can be easily repeated using the numerical model for different *NTU*, *Cr**, and salt solution types and conditions. These kinds of results will help manufacturers and designers of LD systems such as LAMEEs to study the effect of outdoor air conditions on their designed LD systems at desired *NTU* and *Cr**.
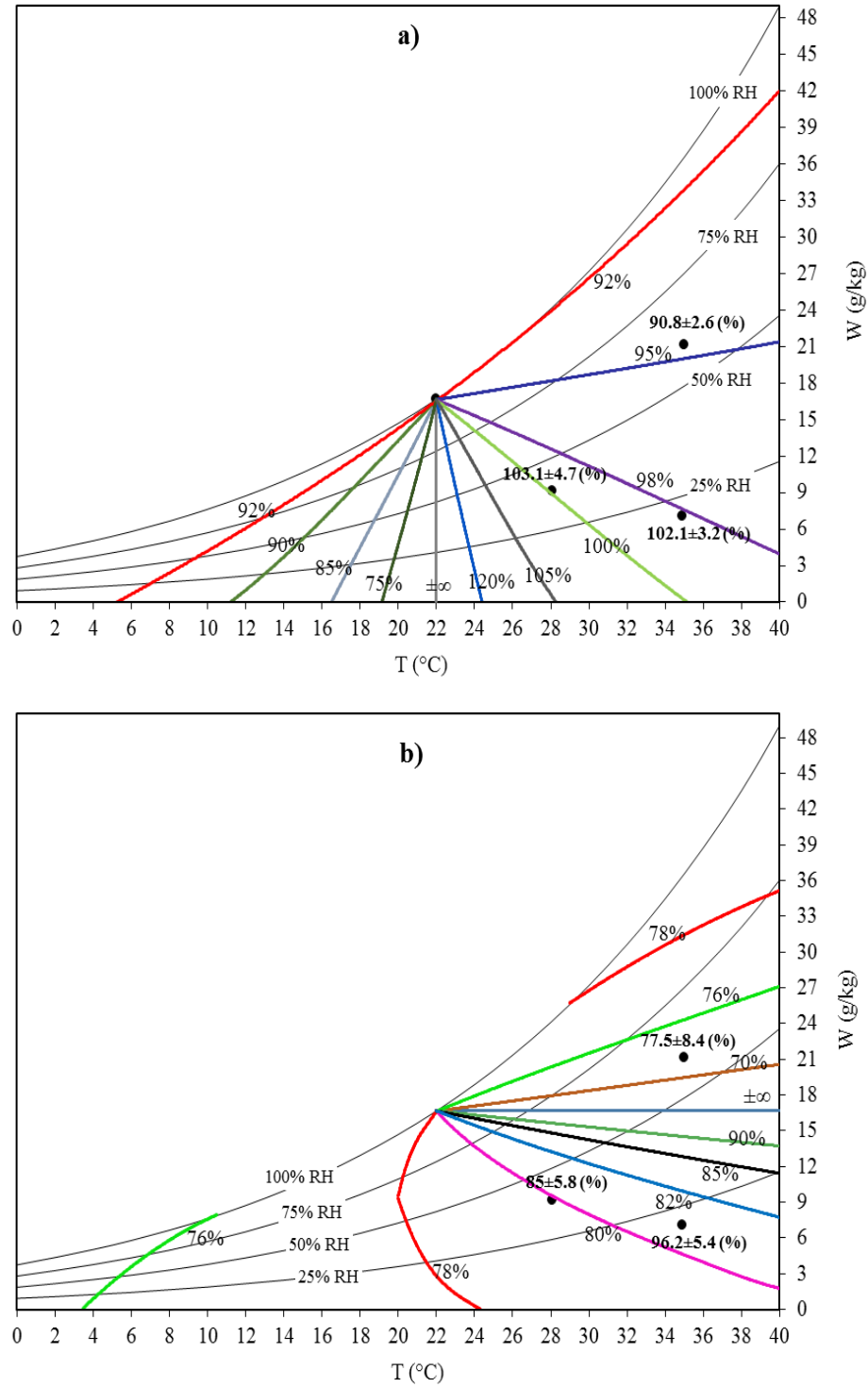
Figure 2.10 Numerical steady-state a) sensible and b) latent effectiveness contour maps of the small-scale LAMEE on the psychrometric chart at $Cr^* = 7$, NTU = 3.5 and various supply inlet air conditions ($T_{sol,in} = 22\,°C$)

2.8 Summary and Conclusions

The SPEET facility is developed to investigate the steady-state performance of a novel small-scale LAMEE at different operating conditions. The air inlet temperature and humidity ratio could be adjusted between 15°C to 50°C and 1 to 28 g_w/kg_{air}, respectively, for the supply air velocity range of 1 to 3 m/s. Mass and energy balances are maintained for each test, and the test facility energy exchange inequality is found to be maximum 5% in the worst case. Also, water is used in the experiments to evaluate the effectiveness of the LAMEE. First, the small-scale LAMEE is tested at three different test conditions: air heating and humidifying (H&H), air cooling and humidifying (C&H) and air cooling and dehumidifying (C&D) at constant $Cr* = 7$ and three different *NTUs*. The experimental effectiveness data are compared to the numerical and two analytical models which are modified for the small-scale LAMEE design and specifications with counter-flow configuration. The results show that the effectiveness of the small-scale LAMEE increased by increasing the *NTU* from 2.5 to 4.5 in all cases. The C&D test case has the best agreement between the experimental, numerical and analytical results. In most cases the numerical and analytical models predict higher effectiveness for the small-scale LAMEE except for the C&H tests where they predict lower effectiveness in comparison to experimental results. The discrepancies between the experimental, numerical and analytical results are mainly due to the simplification assumptions made during the numerical and analytical modeling which are explained in the chapter (see Section 2.7.1). In the normal operating conditions, where the air and solution inlet conditions are selected with acceptable enthalpy difference like the C&D test case, the maximum total effectiveness uncertainty is found to be ±5%.

Finally, the numerical contour maps for the sensible and latent effectiveness of the small-scale LAMEE are generated as a function of supply inlet air conditions on the psychrometric chart at $Cr^* = 7$ and $NTU = 3.5$, and constant solution temperature of 22˚C. These numerical contour maps are compared with three experimental tests. The result shows that the numerical maps have a reasonable agreement with the experimental results and numerical performances are within the uncertainty range of the experimental results in most cases. The contour maps show that, in a wide range of the inlet air temperature and humidity ratios on the psychrometric chart, the sensible and latent effectiveness varies between75% to 120%, and 70% to 90%, respectively.

CHAPTER 3

LAMEE EFFECTIVENESS EVALUATION

3.1   Overview of Chapter 3

The solution-side effectiveness of the LAMEE is discussed in this chapter which

contains Manuscript #2 (Solution-side effectiveness for a liquid-to-air membrane energy

exchanger used as a dehumidifier/regenerator). The LAMEE can been used as a

dehumidifier or a regenerator in liquid-desiccant air-conditioning (LDAC) systems. The

dehumidifier in a LDAC system conditions the supply air to a building and thus the focus

is on the air side. On the other hand, the regenerator in LDAC systems regenerates (dries)

the salt solution so that it can be reused in the dehumidifier. The air-side effectiveness has

traditionally been used to evaluate the performance of liquid-to-air energy exchangers

used as dehumidifier/regenerator. However, in the regenerators the focus is on the salt

solution, and the solution properties are important. Thus using the air-side effectiveness

to evaluate the regeneration performance of liquid-to-air energy exchangers is

questionable without some direct comparisons. In Manuscript #2, solution-side

effectiveness equations are introduced to evaluate the performance of LAMEE

regenerators using solution properties. Also, the air-side effectiveness equations to

evaluate the performance of LAMEE dehumidifiers are discussed in Manuscript #2. This

chapter provides the effectiveness equations which should be used in the methodology

(see Section 1.3.6) for LAMEEs to evaluate the experimental and numerical performance of a LAMEE under various test conditions.

References for this chapter, which contains Manuscript #2, are presented in the reference section of the thesis (see page 215) which includes all the references used in this PhD thesis.

Ge *et al.* (2014) experimentally and analytically investigated the effects of different operating parameters (i.e. air inlet temperature and humidity ratio, air and solution inlet flow rates and solution inlet temperature and concentration) on the moisture removal rate and performance of the small-scale LAMEE used as a dehumidifier and regenerator. Reference (Ge *et al.*, 2014) shows the application of the LAMEE as a dehumidifier and regenerator, where the air-side and solution-side effectiveness equations can be used to evaluate the performance of the LAMEE as the dehumidifier and the regenerator, respectively. This paper (Ge *et al.*, 2014) is presented in Appendix B. Part of the experimental results which are presented in Ref. (Ge *et al.*, 2014) are used in Manuscript #2 to show the application of the solution-side effectiveness equations for the small-scale LAMEE.

The PhD candidate's contributions to Manuscript #2 are (a) developing and introducing the solution-side effectiveness equations, (b) using the solution-side effectiveness equations to evaluate the performance of the small-scale single-panel LAMEE tested under different test conditions and (c) writing the paper and replying to reviewers' comments.

Solution-Side Effectiveness for a Liquid-to-Air Membrane Energy Exchanger used as a

Dehumidifier/Regenerator

Davood Ghadiri Moghaddam, Robert W. Besant, Carey J. Simonson

3.2   Abstract

A liquid-to-air membrane energy exchanger (LAMEE) is an energy exchange device that transfers heat and moisture between air and salt solution streams through a semi-permeable membrane which is permeable for water vapor but impermeable for liquid water. LAMEEs have been used as a dehumidifier/regenerator in air-conditioning systems. In this chapter, the solution-side effectiveness is presented for a small-scale single-panel LAMEE when it is used to regenerate the solution flow. The solution-side effectiveness is very important in regenerators where the main focus is on the salt solution, and the solution properties (i.e. solution outlet concentration) are important. The small-scale LAMEE is tested under air dehumidification and solution regeneration test conditions using a LiCl solution at one NTU (i.e. $NTU = 5$) and three different Cr^* values ($Cr^* = 2$, 4 and 6). The results show that both the air-side and solution-side effectiveness of the LAMEE increase with Cr^*. The solution-side latent effectiveness is lower for the regenerator in comparison to the dehumidifier (e.g. 43% lower at $Cr^* = 6$). Also, the numerical results for a small-scale LAMEE which were presented in the literature are used in this chapter to evaluate the solution-side effectiveness of the LAMEE under different test conditions. The numerical results show that the difference between the air-side and solution-side latent effectivenesses are negligible. Therefore, the air-side latent effectiveness can be used to evaluate the solution-side latent effectiveness of LAMEEs.

3.3   Introduction

There are three types of energy recovery (ER) devices available to recover both heat and moisture from an exhaust air stream in buildings; these are air-to-air membrane energy exchangers (AAMEEs), energy wheels and liquid-to-air energy exchangers used in run-around liquid desiccant coupled systems (Afonso, 2006; Besant and Simonson, 2000). In AAMEEs the heat and moisture transfer between supply and exhaust air streams through a semi-permeable membrane. The effectiveness of the AAMEE has been calculated for both supply and exhaust air streams using ANSI/AHRI Standard 1060 (2011). This standard can be used to calculate the effectiveness of energy wheels for the supply and exhaust air streams. Also, the effectiveness-*NTU* method, which was developed for heat exchangers (Shah and Sekulic, 2003), can be used to predict the performance of the AAMEEs and energy wheels. Simonson and Besant (1999) introduced an operating condition factor (*H**) parameter for energy wheels to calculate the total performance of the energy wheels directly from sensible and latent effectiveness. This method can be used to calculate the total effectiveness of liquid-to-air energy exchangers (Namvar *et al.*, 2012).

Liquid-to-air energy exchangers have been used to transfer heat and moisture in liquid-desiccant (LD) air-conditioning systems. In liquid-to-air energy exchangers, a salt solution and air can be in direct contact, such as packed beds (Ren, 2008), or indirect contact, such as hollow fiber membrane contactors (Zhang, 2011a) and liquid-to-air membrane energy exchangers (LAMEEs) (Namvar *et al.*, 2012). In LAMEEs, the heat and moisture transfer between the salt solution and the air stream occurs through a semi-

permeable membrane. This membrane is permeable for water vapor but impermeable for liquid water. The membrane is an important part in membrane based energy exchangers, and it is important to evaluate its properties in terms of health issues. Alkhudhiri *et al.* (2012) and Alklaibi and Lior (2004) did a comprehensive review on membrane fouling and bio-fouling which have been used in membrane-based desalination systems. The properties of those membranes are similar to membranes which have been used in LD systems. Alkhudhiri *et al.* (2012) presented a few strategies for pre-treatment and membrane cleaning due to membrane fouling in the liquid side of the membrane such as solution pretreatment by microfiltration, ultrasonic irradiation technique and fouling control by operating at low temperature and high flow rate. Alklaibi and Lior (2004) reviewed previous works on membrane fouling and bio-fouling, and concluded that problems resulting from bio-fouling such as bacterial and microbial growth were significantly lower than fouling encountered in other membrane processes.

Liquid-to-air energy exchangers have been used as a dehumidifier and regenerator in LD air-conditioning systems (Liu *et al.*, 2007a; Yin *et al.*, 2009; Abdel-Salam *et al.*, 2013). Figure 3.1 shows a schematic of a run-around membrane energy exchanger (RAMEE) system as a LD air-conditioning system. The RAMEE consists of two LAMEEs, one in the supply and another in the exhaust air streams where the heat and moisture transfers between these two air streams using a closed solution loop (Mahmud, 2009). In humid climates, the supply LAMEE acts as a dehumidifier to dehumidify the supply air and the exhaust LAMEE acts as a regenerator to regenerate the salt solution. The dehumidifier conditions the supply air to a building and thus the focus is on the air side (i.e. the air outlet conditions are the control variable that must be satisfied). The

regenerator is used in the exhaust air stream to recover waste energy from the building's exhaust air, and regenerate the salt solution concentration to reuse it in the dehumidifier. In the regenerator, the main focus is on the solution side since the solution properties are very important (Ge *et al.*, 2014). The solution properties (i.e. solution concentration) must be regenerated (dried) in the regenerator to adequately remove moisture from the supply air in the dehumidifier.
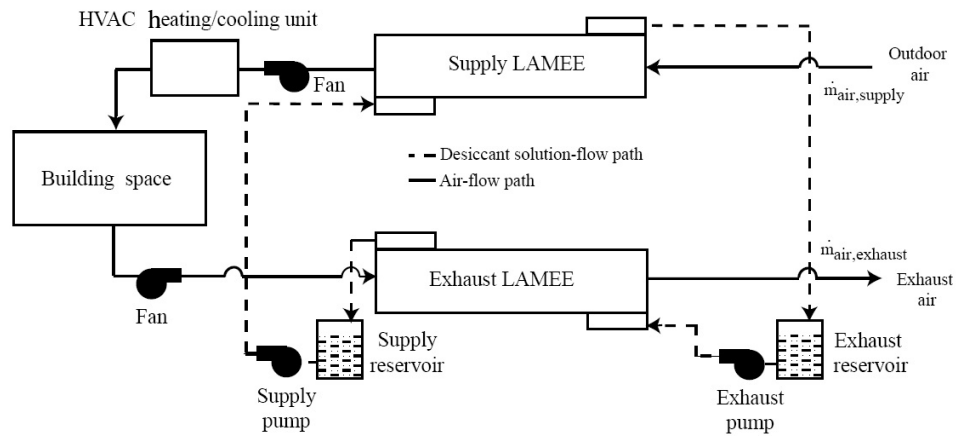
Figure 3.1 Schematic view of a run-around membrane energy exchanger (RAMEE) system (Mahmud, 2009)

There are few papers in the literature on the economic and environmental performances of membrane liquid desiccant air conditioning (M-LDAC) systems (Abdel-Salam and Simonson, 2013; Patel *et al.*, 2010). Abdel-Salam *et al.* (2013) evaluated the economic performance and emissions production of a M-LDAC system using the TRNSYS software, and compared the M-LDAC system with a conventional air conditioning (CAC) system. The M-LDAC system consists of two LAMEEs, which were used as a dehumidifier and a regenerator. A cooling coil was used in the CAC system to dehumidify the supply air. The results showed that the annual energy consumption and life cycle cost of the M-LDAC system are 19% and 12% lower than the CAC system, respectively. The annual emission of CO_2 decreased by 19% when the M-LDAC system

was used in comparison with the CAC system. Also, Patel *et al.* (2010) studied volatile organic compounds (VOCs) transfer in RAMEE systems between supply and exhaust air streams through a salt solution loop, which are an important class of indoor air contaminants which can cause severe health damage. Toluene (C_7H_8) and formaldehyde (HCHO) were used as the VOCs in their study. The results showed that transfer of VOCs in a RAMEE system is negligible for VOCs with low solubility in water and small for VOCs with high solubility in water.

In the literature and practice, liquid-desiccant packed beds are the most common air dehumidifiers and the solution regenerators, and the air-side effectiveness is exclusively used to evaluate the dehumidification and regeneration performance of the packed beds (Babakhani and Soleymani, 2009; Ren *et al.*, 2006; Liu *et al.*, 2007c; Elsayed *et al.*, 1993). Liu *et al.* (2007b) tested a cross flow packed bed with a LiBr salt solution in an LD air-conditioning system as a regenerator. They investigated the impact of the air and solution inlet parameters on the regeneration performance of the bed using air-side effectiveness definitions. In another paper (Liu *et al.*, 2007a), they analytically investigated the coupled heat and mass transfer in dehumidifier/regenerator packed beds with parallel, cross and counter flow configurations for the air and salt solution using the air-side effectiveness. This analytical model can be used for the optimal design of dehumidifier and regenerator packed beds. Yin *et al.* (2009) developed a model to evaluate the performance (based on air-side effectiveness) of a dehumidifier/regenerator packed bed which is equipped with an internal cooling/heating water loop. The results showed that the internally cooled/heated equipment, which is added to the traditional packed bed, improves the dehumidification and regeneration performance of the packed

bed. In these papers on packed beds, the air-side effectiveness definitions were used to evaluate the regeneration performance of liquid desiccant packed beds even though the focus should be on the solution properties in regenerators. Therefore, this chapter focuses on the solution-side effectiveness of regenerators but comparisons are made with the air side.

Liquid-to-air membrane energy exchangers (LAMEEs) and hollow fiber membrane contactors are other types of the liquid-to-air energy exchangers where the salt solution and the air are in indirect contact. In the LAMEE, the heat and mass transfer occurs through a semi-permeable membrane which is impermeable to liquid water but allows water vapor to transfer between the air and salt solution. LAMEEs and hollow fiber membrane contactors have been tested under air dehumidification and solution regeneration test conditions. Zhang *et al.* (2012a; 2012b) introduce the hollow fiber membrane contactors where the salt solution passes through hollow fiber tubes and the air passes on the tubes in the shell of the contactor. The air-side effectiveness equations were used to evaluate the performance of hollow fiber contactors under different test conditions. In another paper, Zhang (2011a) introduced an analytical model to simulate the performance of hollow fiber membrane contactors under different operating conditions. He compared the analytical air-side effectiveness results with experimental data for hollow fiber membrane contactors under air cooling and dehumidification test conditions. This analytical model is fast, and can be modified for other types of liquid-to-air membrane energy exchangers.

LAMEEs have been tested as a dehumidifier and regenerator (Namvar *et al.*, 2012; Ghadiri Moghaddam *et al.*, 2013a). Ghadiri Moghaddam *et al.* (2013a) tested a

small-scale single-panel LAMEE under different test conditions including air dehumidification and solution regeneration conditions. The effect of different heat and mass transfer directions and different salt solution types and concentrations on the air-side effectiveness of the LAMEE were investigated for all test cases. Ge *et al.* (2014) analytically and experimentally studied the effect of different operating parameters such as: air and solution mass flow rates, air and solution inlet temperatures, air inlet humidity ratio and solution inlet concentration on the performance of a small-scale LAMEE used as a dehumidifier and regenerator. Again, the air-side effectiveness was used to evaluate the performance of the dehumidifier and the regenerator. Also, Ge *et al.* (2012) modified the analytical model, which was introduced by Zhang (2011a), for LAMEEs. They evaluated the air-side effectiveness of a small-scale LAMEE under air cooling and dehumidification and air heating and humidification test conditions using the modified analytical model. The analytical results were compared with numerical results and experimental data for the small-scale LAMEE for those test conditions. The results showed that the modified analytical model is reliable to evaluate the performance of LAMEEs under certain operating conditions.

The air-side effectiveness has traditionally been used to evaluate the performance of liquid-to-air energy exchangers used as a dehumidifier/regenerator. In the regenerators; however, the focus is on the salt solution, and the solution properties (i.e. solution outlet concentration and temperature) are important. Thus using the air-side effectiveness to evaluate the regeneration performance of liquid-to-air energy exchangers is questionable without some direct comparisons. In this chapter, solution-side effectiveness equations are introduced to evaluate the performance of LAMEE

65

regenerators using solution properties. The proposed effectiveness equations can be used for any kind of indirect contact liquid-to-air energy exchangers such as LAMEEs and hollow fiber membrane contactors.

3.4   Experimental Data

The single-panel energy exchanger test (SPEET) facility is used to produce the experimental data in this chapter (Ghadiri Moghaddam *et al.*, 2013a; Ghadiri Moghaddam *et al.*, 2013b) (see Figure 3.2). The SPEET facility can be divided in three main sections: supply air system, open solution loop and the test section (i.e. a small-scale single-panel LAMEE). In the supply air system, a compressor is used to supply pressurized dry air (~ 4%RH) to the test facility. A flow controller and a flow meter are used to set and measure the supply air flow rate during the tests. Two bubble tank air humidifiers and a heater are used in the supply air system to control the air humidity and temperature at the desired test conditions. Then the supply air passes through the small-scale LAMEE where heat and moisture are transferred between the air and a salt solution. T-type thermocouples and relative humidity (RH) sensors are used to measure the air temperature and relative humidity at different locations in the test facility. At the end of the supply air system, the air is exhausted to the Lab. The schematic of the SPEET facility and the locations of the measurement instruments are shown in Figure 3.2. The calibration ranges and uncertainties of the measurement instruments, which are used in the SPEET facility, are presented in Table 3-1. The ASME standard PTC 19.1 (2005) is used to calculate the uncertainty for each measurement instrument based on the 95% confidence intervals (Figliola and Beasley, 2006). The details of the measurement instruments calibration methods are presented in (Ghadiri Moghaddam *et al.*, 2013a;

Ghadiri Moghaddam *et al.*, 2013b). The measurement instrument uncertainties are used to calculate the uncertainty of the small-scale LAMEE effectiveness. The method of propagation of errors is used to calculate LAMEE effectiveness uncertainties in all cases (Figliola and Beasley, 2006).

Table 3-1 The capacity, calibration range and accuracy of the measurement instruments used in the SPEET facility

Measurement Instruments	Capacity/Calibration range	95% Uncertainty
Air flow controller (L/min)	0~100	2% of full-scale
Air flow meter (L/min)	0~100	1% of full-scale
Air humidity sensors (%RH)	10~90	1.5
Air side T-type thermocouples (˚C)	-30~40	0.2
Solution side shielded T-type thermocouples (˚C)	0~60	0.1
Solution peristaltic pump (mL/min)	1~2316	2% of reading-scale
Salt solution concentration (%)	30-35	Less than 0.02%
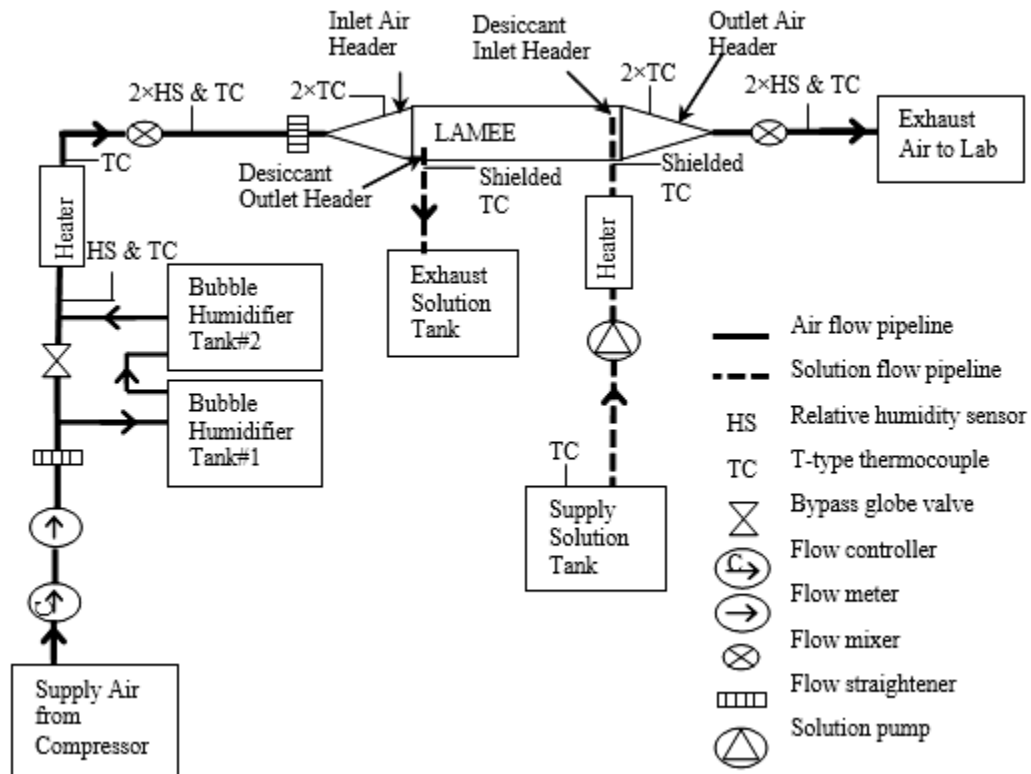
Figure 3.2 Schematic of the single-panel energy exchanger test (SPEET) facility (Ghadiri Moghaddam *et al.*, 2013b)

In the open solution loop, a LiCl salt solution is pumped into the small-scale LAMEE using a peristaltic pump from a large supply solution tank. The salt solution passes through the LAMEE, and exhausts into an exhaust solution tank. The salt solution inlet and outlet temperature and concentration are measured using shielded T-type thermocouples and a density meter device (Anton Paar-DMA 4500M) (Ghadiri Moghaddam *et al.*, 2013a) at the solution inlet and outlet headers, respectively. The salt solution inlet and outlet concentrations are measured 4 to 6 times at each location using the density meter device for each experiment, and the average absolute value and the solution concentration uncertainties are calculated based on these measurements using 95% confidence intervals. The calibration ranges and uncertainties of the solution-side measurement instruments are also presented in Table 3-1.

The small-scale single-panel LAMEE is located in the test section of the SPEET facility, where the heat and moisture transfer between the air and the salt solution through a semi-permeable membrane. The detail design of the small-scale LAMEE is given in (Ghadiri Moghaddam *et al.*, 2013a; Ghadiri Moghaddam *et al.*, 2013b). The counter-cross flow configuration is used in the small-scale LAMEE for the air and salt solution. The air and solution flow configuration and a cross section view of the small-scale LAMEE are presented in Figure 3-3. In application, a LAMEE consists of many layers of air and solution panels which are located side by side to create air and solution channels in the LAMEE. In the small-scale LAMEE, solution sub-channels are grooved on two plastic panels, and a GE^{TM} membrane is attached to the panels to create two half solution panels for the small-scale LAMEE. The solution channel thickness in these two panels is half of the normal solution channel thickness (i.e. 2.4 mm) of a full-scale LAMEE. These

two half solution side panels are placed side by side using two air spacers in the middle and on the top and bottom of the panels to create the air channel in the middle of the small-scale LAMEE. An eddy promoter air screen is used in the air channel to enhance the heat and mass transfer performance in the air side of the LAMEE (Oghabi *et al.*, 2013; LePoudre *et al.*, 2011; Ghadiri Moghaddam *et al.*, 2013c). The small-scale single-panel LAMEE specification and membrane properties are presented in Table 3-2.

Table 3-2 The small-scale single-panel LAMEE specifications and the membrane properties

Parameter	value
Exchanger length, L_{ex} (m)	0.99
Exchanger aspect ratio, L_{ex} /H_{ex}	10.5
Exchanger entrance ratio, L_{sol}/ L_{ex}	0.025
Air gap thickness, δ_{air} (mm)	5
Solution gap thickness on each side panel (mm)	1.2
Number of solution paths on each side panel	5
Mass resistance of membrane, R_{mem} (s/m)	24
Membrane thermal conductivity, k_{mem} (W/mK)	0.065
Membrane thickness, δ_{mem} (mm)	0.265
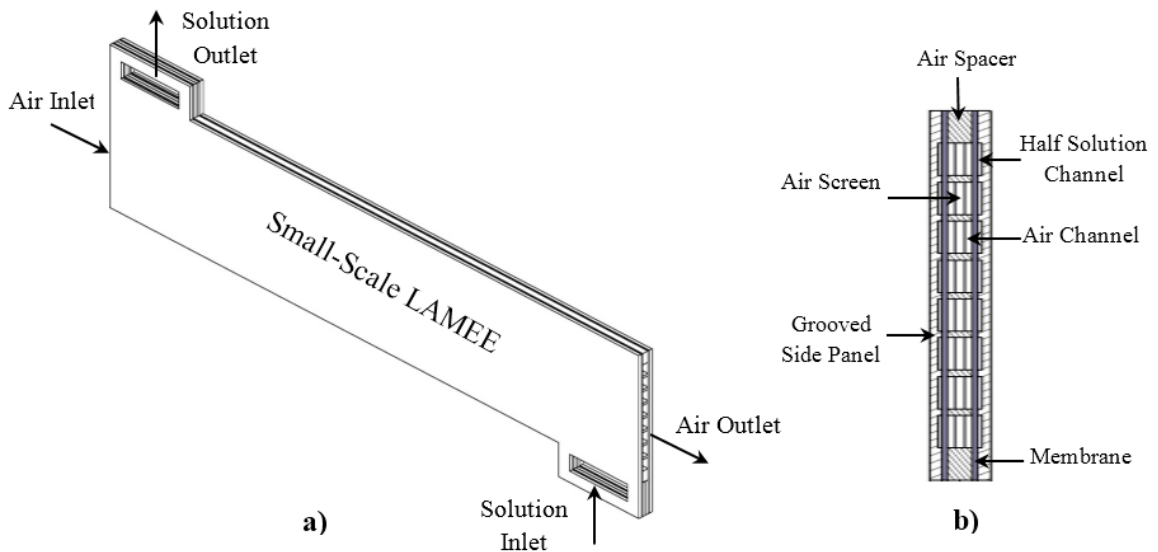
Figure 3.3 The small-scale single-panel LAMEE (a) air and solution flow configurations, and, (b) cross-section detailed view (Ghadiri Moghaddam *et al.*, 2013b)

The small-scale single-panel LAMEE is tested using the SPEET facility as a dehumidifier and a regenerator at two different test conditions. The average measured air and LiCl solution inlet and outlet conditions over time for air dehumidification (i.e. air cooling and dehumidification test conditions) and solution regeneration (i.e. air heating and humidification test conditions) test cases at steady-state conditions are presented in Table 3-3. The steady-state condition is determined when the temperature and relative humidity changes by time ($\frac{\mathrm{d}T}{\mathrm{d}t}$ and $\frac{\mathrm{d}RH}{\mathrm{d}t}$) are smaller than their uncertainties in the experiment, which are 0.1°C and 1.5%RH, respectively. The small-scale LAMEE is tested at constant number of heat transfer units ($NTU = 5$) and three different thermal capacity ratios ($Cr^* = 2$, 4 and 6). NTU and Cr^* are calculated as follows for a LAMEE:

$$NTU = \frac{UA}{\left(\dot{m}c_P\right)_{\min}} \tag{3.1}$$

$$Cr^* = \frac{\left(\dot{m}c_P\right)_{\max}}{\left(\dot{m}c_P\right)_{\min}} \tag{3.2}$$

where U is the overall heat transfer coefficient in Eq. (3.1), and calculated as follow:

$$U = \left[\frac{1}{h_{air}} + \frac{\delta_{mem}}{k_{mem}} + \frac{1}{h_{sol}}\right]^{-1} \tag{3.3}$$

where h, δ and k are the convective heat transfer coefficient, thickness and thermal conductivity. Subscripts *air*, *mem* and *sol* refer to the air, membrane and salt solution properties, respectively. In Eq. (3.1) A, $\dot{m}$ and c_P are the total membrane active area for heat and mass transfer, mass flow rate and specific heat capacity. Subscripts *min* and *max* refer to the minimum and maximum values. The *Cr** definition has been used as

the heat capacity ratio in LAMEEs (Namvar *et al.*, 2012). The air flow has the minimum heat capacity rate when Cr^* values are greater than 1. The air screen in the air channel of the small-scale LAMEE enhances the air-side heat transfer performance (Oghabi *et al.*, 2013; LePoudre *et al.*, 2011; Ghadiri Moghaddam *et al.*, 2013c). Ghadiri Moghaddam *et al.* (2013c) showed that the actual air-side convective heat transfer coefficient in the air-channel of the small-scale LAMEE is different than the traditional value which is calculated from $Nu_{air} = 8.24$ (for two infinite parallel plates with constant heat flux on both walls). A wind tunnel energy exchanger insert test (WEIT) facility (Oghabi *et al.*, 2013) was used to measure the actual air-side convective heat transfer coefficient in the air-channel of the small-scale LAMEE. The enhanced air-side convective heat transfer coefficient was used in Ghadiri Moghaddam *et al.* (2013c) to numerically evaluate the performance of the small-scale LAMEE under different test conditions. The results showed that the small-scale LAMEE sensible, latent and total air-side effectivenesses increase by 10% at $Re_{air} = 1550$ when the air-side Nusselt number enhances to $Nu_{air} = 20$ (Ghadiri Moghaddam *et al.*, 2013c) in the air channel of the small-scale LAMEE with the air screen. The measured enhanced air-side convective heat transfer coefficient from Ghadiri Moghaddam *et al.* (2013c) is used in Eq. (3.3).

Table 3-3 The average measured air and solution inlet and outlet conditions for the air dehumidification (D) and solution regeneration (R) test cases at *NTU* = 5 and different *Cr** with LiCl salt solution

Test Case	Cr^*	Inlet Conditions					Outlet Conditions				
		$T_{air,in}$	$W_{air,in}$	$T_{sol,in}$	$C_{sol,in}$	$W_{sol,in}$	$T_{air,out}$	$W_{air,out}$	$T_{sol,out}$	$C_{sol,out}$	$W_{sol,out}$
		(˚C)	(g/kg)	(˚C)	(%)	(g/kg)	(˚C)	(g/kg)	(˚C)	(%)	(g/kg)
D1	2	30.0	14.5	24.0	32.12	6.7	26.4	8.7	30.5	31.85	10.3
D2	4	30.1	14.3	24.0	32.07	6.7	24.9	7.9	28.6	31.93	9.1
D3	6	30.0	14.2	24.0	32.13	6.7	24.6	7.3	27.0	32.04	8.2
R1	2	29.9	13.8	55.0	32.00	41.1	43.7	23.3	41.8	32.30	19.4
R2	4	30.0	14.6	55.1	32.16	40.8	47.5	26.9	45.9	32.37	24.4
R3	6	30.0	13.8	55.0	32.00	41.1	48.3	28.6	50.5	32.18	31.8

3.5 Liquid-to-Air Membrane Energy Exchangers Performance Evaluation

A liquid-to-air membrane energy exchanger's (i.e. LAMEEs and hollow fiber membrane contactors) effectiveness can be calculated for air or solution sides depending on the application of the LAMEE. When the LAMEE is used as a dehumidifier in a LD air-conditioning system, the main focus is on the air side and the LAMEE effectiveness values are calculated based on the air properties. However, when the LAMEE is used as a solution regenerator in a LD air-conditioning system, the main focus is on the solution side and the salt solution properties (i.e. solution outlet concentration) are important. Thus, the regenerator effectiveness should be calculated based on the solution side of the LAMEE using the salt solution properties.

3.5.1 LAMEE Air-Side Effectiveness

LAMEE air-side effectiveness definitions are used to evaluate the performance of dehumidifiers. The LAMEE performance for the air side is evaluated with three types of effectiveness; sensible, latent and total effectiveness (Ghadiri Moghaddam *et al.*, 2013a).

Heat or energy exchangers effectiveness are defined using Eq. (3.4), where the exchanger effectiveness equals to the actual energy transfer rate in the exchanger over the maximum possible energy transfer rate in the exchanger (Parkash Narayan *et al.*, 2010):

$$\varepsilon = \frac{q}{q_{max}}.$$ (3.4)

The sensible effectiveness quantifies the heat (sensible energy) transfer rate for the air in the system, and is defined as heat transfer rate to/from the air over the maximum possible heat transfer rate in the exchanger.

$$\varepsilon_{air,sen} = \frac{\left(\dot{m}c_p \right)_{air} \left(T_{air,in} - T_{air,out} \right)}{\left(\dot{m}c_p \right)_{min} \left(T_{air,in} - T_{sol,in} \right)}$$ (3.5)

In this equation, ε and T are the effectiveness and temperature, respectively, and subscript *sen* refers to the sensible effectiveness. Also, subscripts *in* and *out* refer to the inlet and outlet properties. In the LAMEE, the minimum heat capacity rate is always related to the air side for $Cr^*{\geq}1$. As a result, Eq. (3.5) can be written in the following format for the experiments in this chapter.

$$\varepsilon_{air,sen} = \frac{\left(T_{air,in} - T_{air,out} \right)}{\left(T_{air,in} - T_{sol,in} \right)}$$ (3.6)

In evaporative coolers (i.e. LAMEE or hollow fiber membrane contactors when water is used as a liquid media), when the inlet temperature of the air and water are the same, the wet bulb temperature of the inlet air is the lower limit for the air outlet temperature, and the air inlet wet bulb temperature should be used instead of the solution (i.e. water) inlet temperature, $T_{sol,in}$, in the air-side sensible effectiveness (see Eq. (3.6)) (Jaber and Webb, 1989; Zhang and Huang, 2011). Otherwise, when the air and water

inlet temperatures are not the same, the lower limit for the air outlet temperature is the solution (i.e. water) inlet temperature.

Likewise, the air-side latent effectiveness shows the latent energy transfer rate to/from the air in the system, and is due to only moisture transfer in the LAMEE.

$$\varepsilon_{air,lat} = \frac{\left(W_{air,in} - W_{air,out}\right)}{\left(W_{air,in} - W_{sol,in}\right)} \tag{3.7}$$

In Eq. (3.7), W is the humidity ratio, and subscript *lat* refers to the latent effectiveness. Finally, the air-side total effectiveness of the LAMEE, which is related to both heat and moisture transfers to/from the air in the system, is calculated from the following equation (Simonson and Besant, 1999).

$$\varepsilon_{air,lat} = \frac{\left(H_{air,in} - H_{air,out}\right)}{\left(H_{air,in} - H_{sol,in}\right)} \tag{3.8}$$

In Eq. (3.8), H is the specific enthalpy, and subscript *tot* refers to the total effectiveness of the LAMEE. The only problem with the total effectiveness equation (Eq. (3.8)) is in the denominator of this equation, where solution inlet enthalpy is subtracted from the air inlet enthalpy. The reference points to calculate the air and solution enthalpies are different, and it is not possible to simply subtract them from each other without adjusting the reference temperature for air and the solution. As a result, the equation which was introduced by Simonson and Besant (1999) to calculate the total effectiveness of energy wheels has been used to calculate the total effectiveness of indirect contact liquid-to-air energy exchangers (Namvar *et al.*, 2012; Ghadiri Moghaddam *et al.*, 2013a) (i.e. LAMEEs and hollow fiber membrane contactors) from the air-side sensible and latent effectiveness:

$$\varepsilon_{air,tot} = \frac{\varepsilon_{air,sen} + H^* \varepsilon_{air,lat}}{1 + H^*} \qquad (3.9)$$

In Eq. (3.9), H^* is known as the LAMEE operating condition factor and it is calculated based on the air and solution inlet temperatures and humidity ratios in the system (Simonson and Besant, 1999).

$$H^* = \frac{\Delta H_{lat}}{\Delta H_{sen}} \approx 2500 \frac{W_{air,in} - W_{sol,in}}{T_{air,in} - T_{sol,in}} \qquad (3.10)$$

3.5.2 LAMEE Solution-Side Effectiveness

There are no definitions in the literature for the LAMEE solution-side effectiveness, and therefore they are introduced in this chapter for the first time. These effectiveness values are used to evaluate the performance of LAMEE regenerators. The general definition for the exchanger's effectiveness (see Eq. (3.4)) is used in this chapter to develop the solution-side effectiveness for LAMEEs. The solution-side sensible effectiveness is defined as a heat transfer rate to/from the solution over the maximum possible heat transfer rate in the exchanger. The heat transfer rate to/from the solution is calculated form the total and latent energy transfer rates to/from the solution. The heat transfer rate is equal to the total energy transfer rate to/from the solution, which is calculated from the solution enthalpy difference (i.e. $\Delta H_{sol} = (c_P T)_{sol,out} - (c_P T)_{sol,in}$), subtracted by the latent energy transfer rate to/from the solution, which is calculated from the water vapor phase change energy on the solution side. The solution-side sensible effectiveness is calculated as follows:

$$\varepsilon_{sol,sen} = \frac{(\dot{m}c_P)_{sol}(T_{sol,out} - T_{sol,in}) - \dot{m}_{salt} h_{fg}(X_{sol,out} - X_{sol,in})}{(\dot{m}c_P)_{min}(T_{air,in} - T_{sol,in})}, \qquad (3.11)$$

where X and h_{fg} are the solution mass fraction and enthalpy of phase change for saturated water. Subscript $salt$ refers to the salt properties (i.e. LiCl). Constant specific heat capacity is assumed for the salt solution in Eq. (3.11). In Eq. (3.11), the first term in the numerator of the solution-side sensible effectiveness represents the total energy transfer rate to/from the solution in a LAMEE where $H_{sol} = (c_P T)_{sol}$. The second term in the numerator represents the latent energy transfer rate to/from the solution in the LAMEE which is due to water evaporation in the solution side (i.e. air humidification). Consequently, the result of the numerator of the solution-side sensible effectiveness is the sensible energy transfer rate to/from the solution where the total energy transfer rate subtracted by the latent energy transfer rate to/from the solution. The denominator in Eq. (3.11) represents the maximum possible sensible energy transferred in the LAMEE. In the LAMEE, the maximum sensible energy transfer rate to/from the solution is the same as the maximum energy transfer rate to/from the air (see Eqs. (3.5) and (3.11)). Also, the absorption energy in the solution is neglected in Eq. (3.11) since the solution concentration change in the LAMEE is small (e.g. less than 1%), and this energy is negligible in comparison to the water phase change energy transfer to/from the salt solution in the LAMEE (Afshin, 2010). Moreover, as it was mentioned before, the minimum heat capacity rate in the LAMEE is always related to the air side for $Cr^* \geq 1$ (i.e. $(\dot{m}c_p)_{min} = (\dot{m}c_p)_{air}$). The solution mass fraction and the salt mass flow rate are calculated as follows:

$$X_{sol} = \frac{\text{mass of water}}{\text{mass of salt}} \tag{3.12}$$

$$\dot{m}_{salt} = \frac{\dot{m}_{sol}}{1 + X_{sol}} \tag{3.13}$$

The solution mass fraction can be calculated from the salt solution concentration which is measured during the experiments:

$$X_{sol} = \frac{1 - C_{sol}}{C_{sol}} \qquad (3.14)$$

The LAMEE solution-side latent effectiveness is the latent energy transfer rate to/from the solution over the maximum possible latent energy transfer rate in the solution side, and is calculated from Eq. (3.15).

$$\varepsilon_{sol,lat} = \frac{\dot{m}_{salt} h_{fg} \left(X_{sol,out} - X_{sol,in} \right)}{\dot{m}_{min} h_{fg} \left(W_{air,in} - W_{sol,in} \right)} \qquad (3.15)$$

In Eq. (3.15), the denominator is the maximum possible latent energy transfer rate for the solution side of the LAMEE, when the minimum mass flow rate is related to the air side of the LAMEE for $Cr^* \geq 0.3$ (i.e. $\dot{m}_{min} = \dot{m}_{air}$).

The solution-side total effectiveness of the LAMEE is the total (i.e. sensible + latent) energy transfer rate to/from the solution over maximum possible total energy transfer rate for the solution side of the LAMEE.

$$\varepsilon_{sol,tot} = \frac{\left(\dot{m} c_P \right)_{sol} \left(T_{sol,out} - T_{sol,in} \right)}{\left(\dot{m} c_P \right)_{air} \left(T_{air,in} - T_{sol,in} \right) + \dot{m}_{air} h_{fg} \left(W_{air,in} - W_{sol,in} \right)} \qquad (3.16)$$

In Eq. (3.16), the numerator of the solution total effectiveness is equal to the enthalpy change in the solution side of the LAMEE where $H_{sol} = (c_P T)_{sol}$, and the denominator of this effectiveness is the sum of the maximum possible sensible and latent energy transfer rates for the solution side of the LAMEE. The solution-side sensible, latent and total effectivenesses are applicable when the minimum heat capacity rate and minimum mass flow rate are related to the air side of the LAMEE (i.e. $(\dot{m} c_p)_{min} = (\dot{m} c_p)_{air}$ for $Cr^* \geq 1$ and $\dot{m}_{min} = \dot{m}_{air}$ for $Cr^* \geq 0.3$).

3.6   Results and Discussion

The small-scale LAMEE was tested under dehumidifier (i.e. air cooling and dehumidification test conditions) and regenerator (i.e. salt solution regeneration test conditions) applications using the LiCl salt solution at $NTU = 5$ and three different Cr^* ($Cr^* = $ 2, 4 and 6). The air-side and solution-side effectiveness and their uncertainty bounds are calculated for both the dehumidifier and the regenerator using the method of propagation of errors.

3.6.1   LAMEE as a Dehumidifier

To simulate the dehumidifier application of a LAMEE, the small-scale LAMEE is tested under air cooling and dehumidification test conditions. Figure 3.4 shows the measured air and solution inlet and outlet conditions for the small-scale LAMEE used as a dehumidifier on the psychrometric chart at $NTU = 5$ and $Cr^* = 4$ to provide better understanding for the air and solution process lines in the LAMEE at this test case. The air-side and solution-side effectiveness (i.e. sensible, latent and total effectiveness) of the dehumidifier are presented in Figure 3.5 at $NTU = 5$ and three different $Cr^* = $ 2, 4 and 6. The results show that both air and solution-side effectiveness of the dehumidifier increase with Cr^*. The air-side and solution-side effectiveness are almost equal for all the tests and agree within their uncertainty bounds. The maximum air and solution side total effectiveness of the small-scale LAMEE as a dehumidifier are 91% and 90%, respectively, at $Cr^* = 6$. The solution-side sensible effectiveness equation results in higher uncertainty for the sensible effectiveness (e.g. $\varepsilon_{sol,sen} = 94\%$ with 21% uncertainty at $Cr^* = 6$) which is mainly due to the uncertainty in the solution mass fraction, X, which is in the solution-side sensible effectiveness equation (see Eq. (3.11)). Change in the salt

solution concentration as it passes through the small-scale LAMEE is small, especially for high *Cr** values (see Table 3-3 and Figure 3-3), which results in a high uncertainty for solution-side sensible effectiveness. The solution-side sensible and latent effectivenesses are highly sensitive to the measured salt solution concentration values during the experiments. Consequently, the measurement uncertainty of the salt solution concentration has a significant impact on the uncertainty in the solution side sensible and latent effectivenesses which are calculated using Eqs. (3.11) and (3.15).
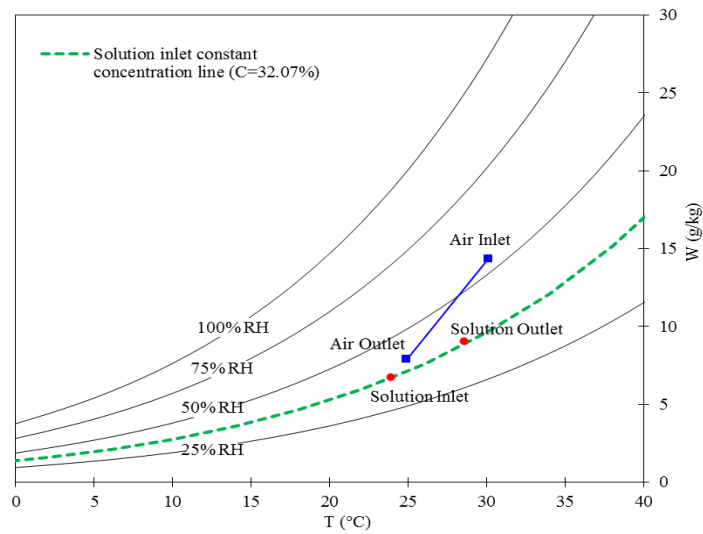
Figure 3.4 Measured air and solution inlet and outlet conditions for the small-scale LAMEE dehumidifier (i.e. air cooling and dehumidification test conditions) using LiCl salt solution at *NTU* = 5 and *Cr** = 4
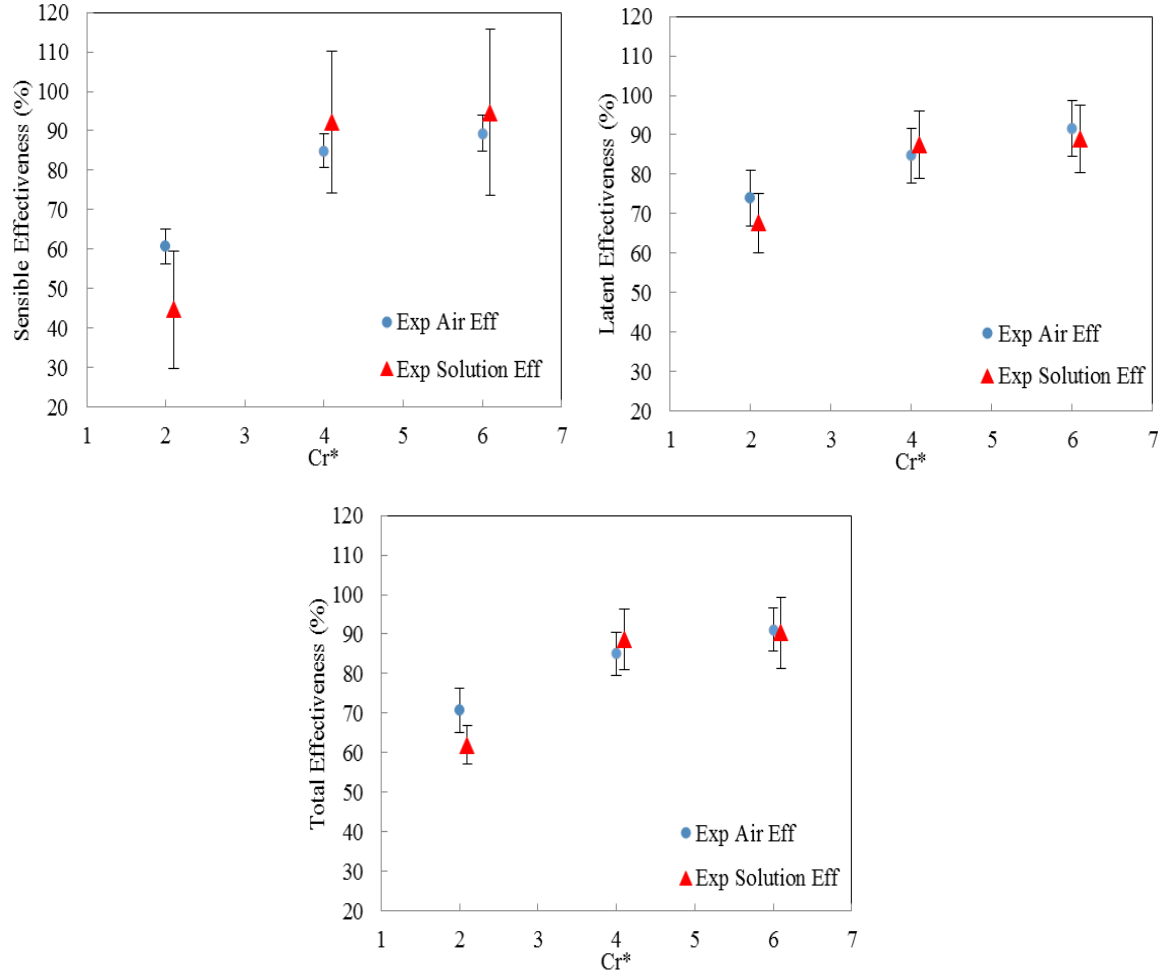
Figure 3.5 The small-scale LAMEE dehumidifier air and solution sides effectiveness under air cooling and dehumidification test conditions using LiCl solution at *NTU* = 5 and different *Cr*

3.6.2 LAMEE as a Regenerator

In this section, the small-scale LAMEE is used as a regenerator and tested under test conditions where the solution is regenerated by cool dry air (see Table 3-3). Figure 3.6 shows the measured air and solution inlet and outlet conditions during the regeneration test with *NTU* = 5 and *Cr** = 4 on the psychrometric chart. Figure 3.6 shows that the LiCl solution enters the small-scale LAMEE at 55˚C temperature and humidity ratio of 41 g/kg, and the solution is cooled and dehumidified to 46˚C and 24 g/kg at the LAMEE solution outlet for the test at *NTU* = 5 and *Cr** = 4. The air-side and solution-

side sensible, latent and total effectiveness of the regenerator are shown in Figure 3.7 at $NTU = 5$ and three different values of $Cr* = 2$, 4 and 6. The results show both the air-side and solution-side effectivenesses increase with $Cr*$. Also, the results show that the solution-side sensible effectiveness is higher than the air-side sensible effectiveness for the regeneration process (e.g. 11% higher at $Cr* = 6$), while the solution-side latent and total effectivenesses show lower effectiveness in comparison to the air-side latent and total effectiveness (e.g. 10% and 7% lower latent and total effectiveness at $Cr* = 2$, respectively). Nevertheless, the air-side and solution-side effectiveness values almost always agree within their uncertainty bounds. The reason for the high uncertainty in the solution-side sensible effectiveness are described in Subsection 3.6.1. The maximum solution-side sensible, latent and total effectiveness are 84%, 46% and 57% at $Cr* = 6$ for the regenerator. The solution latent effectiveness is very important in regenerators since it shows the ability of the LAMEE to regenerate the solution. The results show that the small-scale LAMEE has lower solution-side latent and total effectivenesses for the regenerator application in comparison to the dehumidifier application. The solution latent effectiveness for the small-scale LAMEE regenerator is 43% lower than the dehumidifier at $Cr* = 6$.
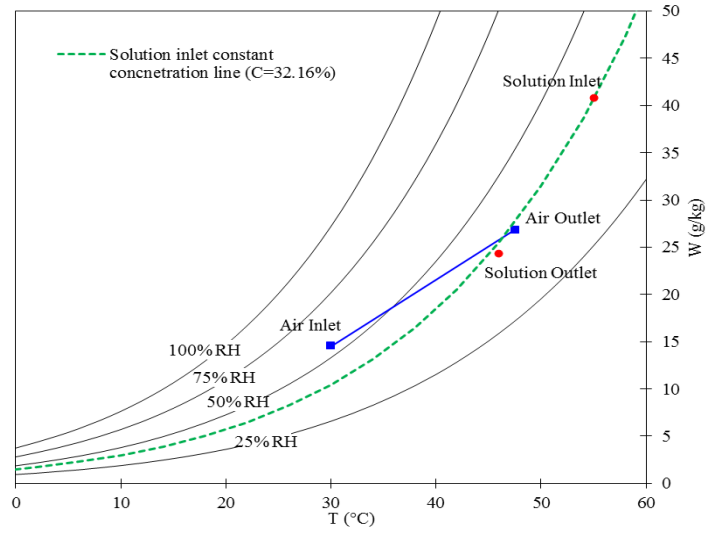
Figure 3.6 Measured air and solution inlet and outlet conditions for small-scale LAMEE regenerator (i.e. salt solution regeneration test conditions) using LiCl solution at *NTU* = 5 and *Cr** = 4
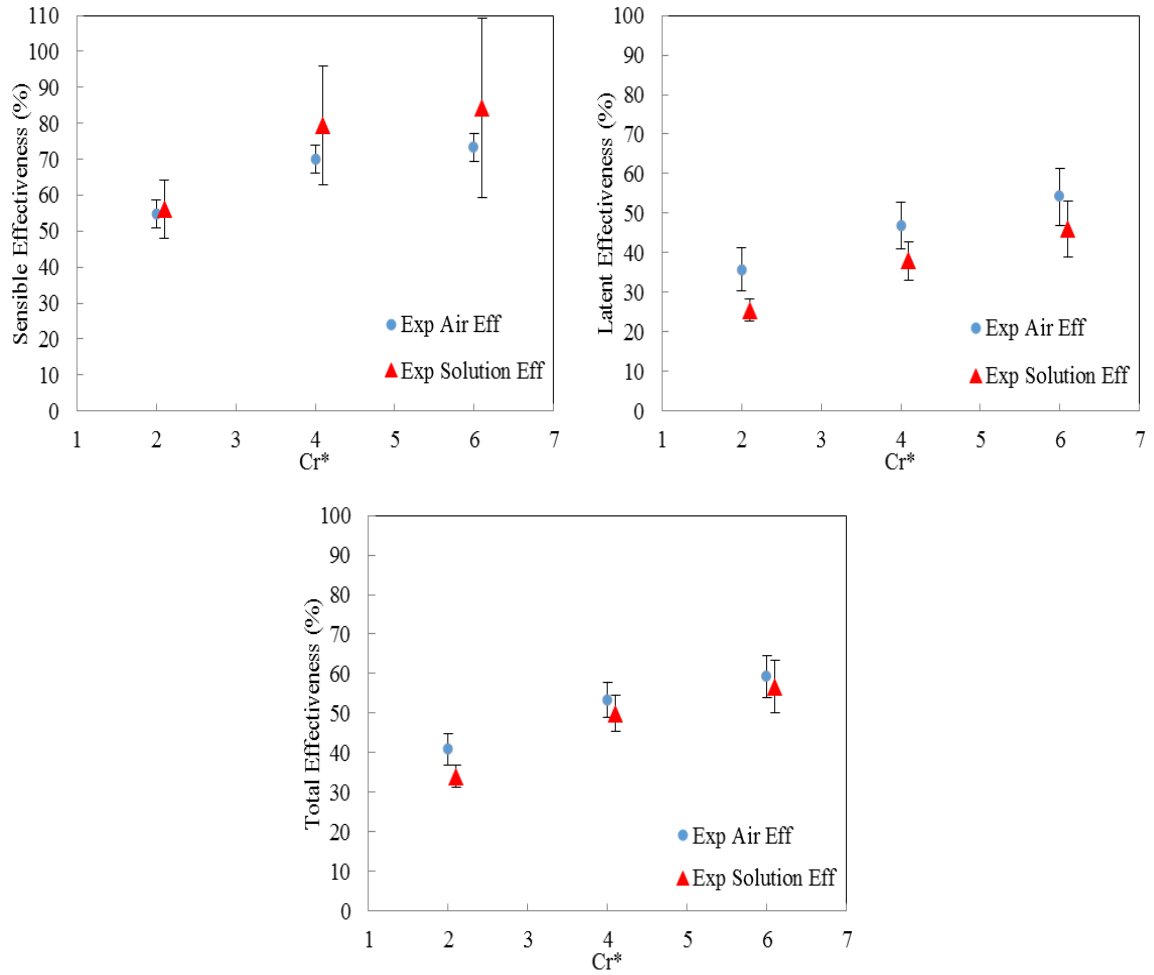
Figure 3.7 The small-scale LAMEE regenerator's air and solution sides effectiveness under salt solution regeneration test conditions using LiCl solution at *NTU* = 5 and different *Cr**

3.6.3 Application of the Solution-Side Effectiveness

In this section the solution-side effectiveness is applied to the experimental and numerical results for a small-scale single-panel LAMEE which are presented in Ghadiri Moghaddam *et al.* (2013a) and Ghadiri Moghaddam *et al.* (2013c). Ghadiri Moghaddam *et al.* (2013a) tested the small-scale LAMEE at four different test conditions: air cooling and dehumidifying (C&D), air cooling and humidifying (C&H), air heating and dehumidifying (H&D) and air heating and humidifying (H&H). LiCl solution was used as a transfer liquid in the small-scale LAMEE, and the LAMEE was tested at $NTU = 3.8$ and four different $Cr*$ ($Cr* = 1, 3, 5$ and 7). An enthalpy pump system (EPS) code (Ghadiri Moghaddam *et al.*, 2013a; Ghadiri Moghaddam *et al.*, 2013c) has been used to simulate the steady-state performance of LAMEEs in the RAMEE research group at the University of Saskatchewan. Ghadiri Moghaddam *et al.* (2013c) modified the EPS code for the small-scale LAMEE, and validated the numerical results with the experimental data presented by Ghadiri Moghaddam *et al.* (2013a). In Ghadiri Moghaddam *et al.* (2013c) coupled heat and mass transfer in liquid-to-air membrane energy exchangers is modeled for the air flow, salt solution flow and the membrane to calculate the steady-state performance of the small-scale LAMEE under different air and solution conditions. The numerical model which was introduced in Ghadiri Moghaddam *et al.* (2013c) is used in the current chapter to evaluate the numerical air-side and solution-side effectivenesses of the small-scale LAMEE. Also, Ge *et al.* (2012) showed that if the modified analytical model for the small-scale LAMEE, which was first introduced by Zhang (2011a) for hollow fiber membrane contactors, was used to evaluate the air-side effectiveness of the small-scale LAMEE, the analytical and numerical results would agree within their

uncertainty ranges. Thus, the modified numerical model is used in this section to evaluate the small-scale LAMEE performance.

Figure 3.8 shows the difference between the numerical air-side and solution-side effectiveness ($\Delta \varepsilon_i = \varepsilon_{air,i} - \varepsilon_{sol,i}$) of the small-scale LAMEE using the modified EPS code, where subscript i indicates the sensible, latent or total effectiveness. Figure 3.8 includes the numerical results for the experiments which are done for this chapter (the air dehumidification and the solution regeneration test cases), and the numerical results that are presented in Ghadiri Moghaddam *et al.* (2013a, 2013c) for the C&D, C&H, H&D and H&H test conditions. The results in Figure 3.8 show that the difference between the numerical air-side and solution-side effectiveness are negligible for the latent effectiveness while this difference is significant for the sensible and total effectiveness in most cases. This good agreement between the numerical air-side and solution-side latent effectiveness for all test cases and Cr^* values in comparison to the agreement between the experimental air-side and solution-side latent effectiveness results (see Figure 3.5 and Figure 3.7) is due to the mass and energy balance convergence criteria in the numerical model. The convergence criteria for the mass and energy balance in the EPS code is 10^{-2} (Hemingson *et al.*, 2011b); however, in the experiments the imbalance for mass and energy transfers in the small-scale LAMEE is higher than the model.

Also, Figure 3.8 shows that the sensible and total effectivenesses of the small-scale LAMEE under regeneration test conditions which are calculated using the solution-side effectiveness equations (Eqs. (3.11) and (3.16)) are higher than the sensible and total effectivenesses using the air-side effectiveness equations at the same test conditions. These results show the importance of using the sensible and total solution-side

effectiveness equations to evaluate the performance of regenerators. In dehumidifiers the difference between the air-side and solution-side sensible and total effectivenesses are smaller than for the regeneration test case. However, the air-side effectiveness equations should be used to evaluate the performance of the dehumidifiers. The air-side latent effectiveness of a LAMEE can be used as the solution-side latent effectiveness with good accuracy. The solution-side latent effectiveness shows the LAMEE performance under solution regeneration test conditions. Also, in experiments with high uncertainty for the latent effectiveness, the average value of the air-side latent effectiveness and the solution-side latent effectiveness can be used to represent the LAMEE air-side/solution-side latent effectiveness which will result in lower uncertainty for the LAMEE latent effectiveness than the air-side or the solution-side latent effectiveness. Moreover, the air-side latent effectiveness of a LAMEE can be used to calculate the solution outlet concentration using Eq. (3.15) which is also an important parameter for regenerators.
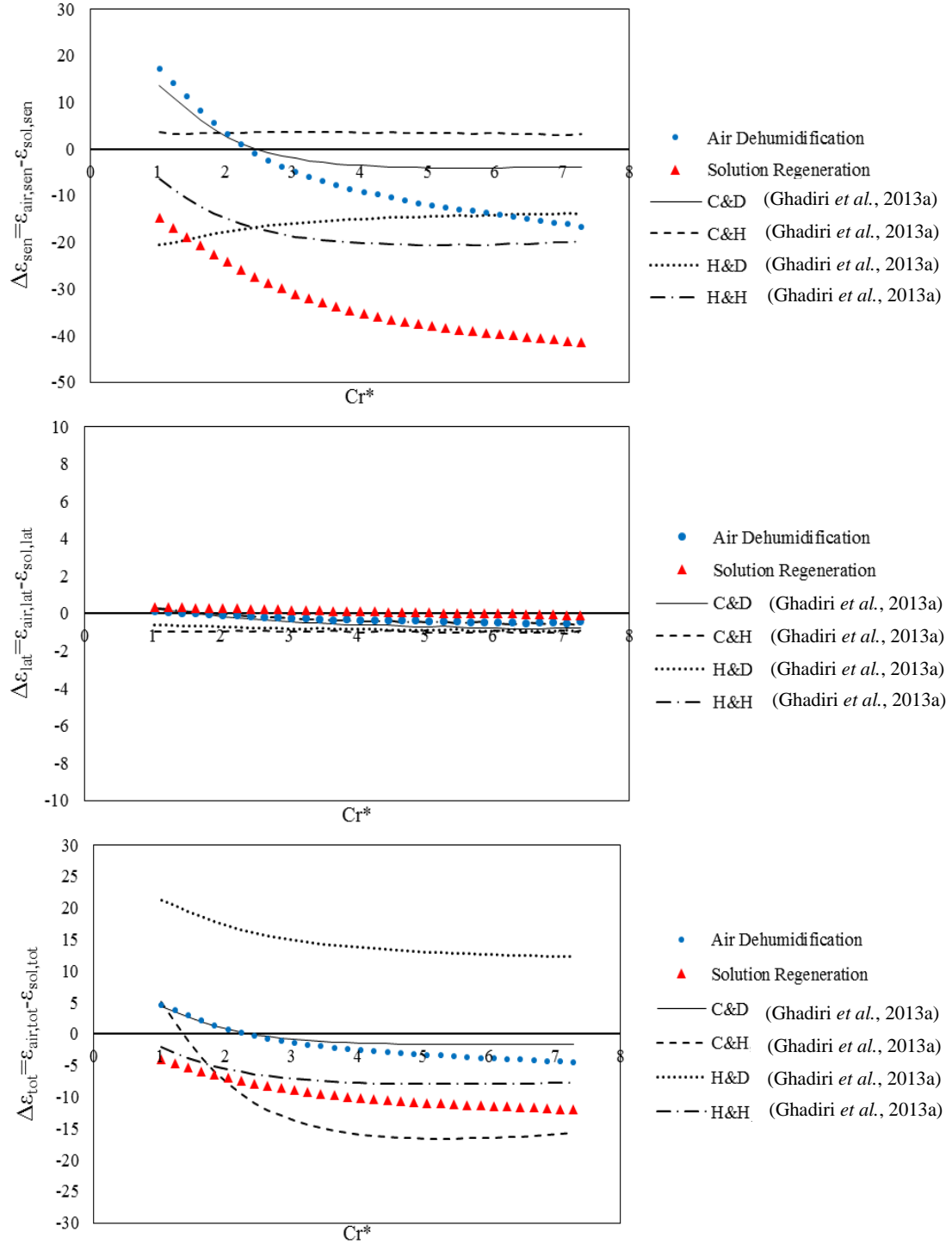
Figure 3.8 The numerical air-side and solution-side effectiveness of the small-scale LAMEE tested under different test conditions (i.e. C&D, C&H, H&D, H&H, air dehumidification and solution regeneration test cases) at different _Cr*_ with LiCl salt solution

3.7   Conclusion

In this chapter, the solution-side effectiveness for liquid-to-air membrane energy exchangers (i.e. LAMEEs and hollow fiber membrane contactors) are introduced. The solution-side effectiveness are very important for regenerators where the main focus is on the salt solution properties (i.e. solution outlet concentration). The small-scale single-panel LAMEE is tested under air dehumidification and solution regeneration test conditions using LiCl at $NTU = 5$ and three different $Cr^* = 2$, 4 and 6. For the test conditions presented, the following conclusions are made from this chapter:

- The experimental results show that the air-side and solution-side effectiveness for both the dehumidifier and the regenerator increase with Cr^*. The air-side and solution-side effectivenesses are nearly the same for the dehumidifier. However, for the regenerator, the solution-side sensible effectiveness is higher than the air-side sensible effectiveness (e.g. 11% higher at $Cr^* = 6$) while the solution-side latent and total effectiveness are slightly lower than the air-side latent and total effectiveness (e.g. 10% and 7% lower latent and total effectiveness at $Cr^* = 2$, respectively).

- The experimental results for both the dehumidifier and the regenerator show that the solution-side sensible and latent effectiveness are sensitive to the measured salt solution inlet and outlet concentrations. The accurate measuring of the salt solution concentration will result in accurate solution-side effectiveness with lower uncertainty bounds than the solution-side effectiveness results that are presented in this chapter.

- The numerical results for a small-scale LAMEE which were presented in Ghadiri Moghaddam *et al.* (2013a, 2013c) are used in this chapter to evaluate the solution-side effectiveness of the LAMEE under different test conditions (i.e. C&D, C&H, H&D and H&H test conditions). The numerical results show that the difference between the air-side and solution-side latent effectiveness are negligible. Therefore, the air-side latent effectiveness can be directly used to evaluate the solution-side latent effectiveness of LAMEEs which is an important factor to evaluate the performance of regenerators.

- For experiments with high uncertainties for the air-side and solution-side latent effectiveness, the average value of the air-side and solution-side latent effectiveness can be used as a latent effectiveness for a LAMEE which will result in lower uncertainty for the latent effectiveness than the air-side or the solution-side effectiveness.

- The air-side latent effectiveness of a LAMEE can be used to calculate the solution outlet concentration using Eq. (3.15) which is an important parameter for regenerators.

- The results show that the solution-side sensible and total effectiveness equations (see Eq. (3.11) and (3.16)) should be used to evaluate the sensible and total performance of regenerators in most cases.

CHAPTER 4

EXPERIMENTAL RESULTS

4.1   Overview of Chapter 4

The effects of different heat and mass transfer directions and different salt solution types and concentrations are experimentally investigated on the small-scale LAMEE steady-state effectiveness in this chapter which contains Manuscript #3 (Steady-state performance of a small-scale liquid-to-air membrane energy exchanger for different heat and mass transfer directions, and liquid desiccant types and concentrations: experimental and numerical data). In this manuscript, the SPEET facility is used first to investigate the effect of different heat and mass transfer directions on the steady-state performance of a LAMEE system under different operating conditions. The experimental data are compared with numerical simulation results using the small-scale LAMEE numerical model presented in Chapter 5. The results show that the performance of the LAMEE is not the same for different heat and mass transfer directions. Also, the repeatability of the experimental data for the air cooling and dehumidifying test case is studied for the first time, and repeatability results show that the experimental data are repeatable within ±2%. This chapter relates to the second step of the methodology (see Section 1.3.6) for LAMEEs which is testing the small-scale LAMEE under various test conditions.

References for this chapter, which contains Manuscript #3, are presented in the Reference section of the thesis (see page 215) which includes all the references used in this PhD thesis.

Second, the effect of different salt solution types (i.e. LiCl and $MgCl_2$) and concentrations are studied on the steady-state performance of the LAMEE under air cooling and dehumidifying test conditions. Different salt solutions with different concentrations have been used in membrane based energy exchangers such as the LAMEE. Salt solution properties are different for different desiccant types and concentrations, and they affect the performance of the system and air outlet conditions (Afshin, 2010).

Dr. Philip LePoudre, who worked as a researcher in our research group from September 2010 to September 2011, reviewed Manuscript #3 and gave useful advice and comments. Thus, He was added as the second author to Manuscript #3. The PhD candidate's contributions to Manuscript #3 are: (a) testing the small-scale single-panel LAMEE under different operating conditions using LiCl solution in the SPEET facility, (b) analyzing the experimental data and presenting the experimental effectiveness results for the small-scale LAMEE, (c) experimentally and numerically investigating the effect of different heat and mass transfer directions and different salt solution types and concentrations on the small-scale LAMEE performance, (d) presenting the numerical results for the small-scale single-panel LAMEE, and (e) writing the paper and replying to reviewers comments.

Steady-State Performance of a Small-Scale Liquid-to-Air Membrane Energy Exchanger

for Different Heat and Mass Transfer Directions, and Liquid Desiccant Types and

Concentrations: Experimental and Numerical Data

(ASME Journal of Heat Transfer, 2013, Volume 135)

Davood Ghadiri Moghaddam, Philip LePoudre, Robert W. Besant, and Carey J.

Simonson

4.2   Abstract

A liquid-to-air membrane energy exchanger (LAMEE) is an energy exchanger that allows heat and moisture transfer between air and salt solution flows through a semi-permeable membrane. For the first time, a novel small-scale single-panel LAMEE test facility is used to experimentally investigate the effect of the direction of heat and mass transfers for the air and salt solution flows, and the effect of different salt solution types and concentrations on the LAMEE effectiveness. The data for steady-state effectiveness of the LAMEE are compared to the simulation results of a numerical model. Two studies are conducted; first, a study based on different heat and mass transfer directions (four test cases), and second, a study focused on the influence of solution types and concentration on LAMEE performance. For the first study, $NTU = 3$ and four different heat capacity ratios (i.e. $Cr^* = 1, 3, 5, 7$) are used, with a LiCl salt solution in the exchanger. Mass and energy balances for all the test cases and the repeatability of the experimental data for the air cooling and dehumidifying test case show that the experimental data are repeatable and within an acceptable uncertainty range. The results show increasing effectiveness with increasing Cr^*, and good agreement between the numerical and experimental results for both air cooling and dehumidifying and air heating and humidifying test cases. In the

second study, two different salt solutions (i.e. LiCl and MgCl$_2$), and three different concentrations for the LiCl solution (i.e. 25%, 30% and 35%) are selected to investigate the effect of different salt solution types and concentrations on the performance of the LAMEE. A maximum difference of 10% is obtained for the LAMEE total effectiveness data with the different salt solution types and concentrations. The results show that both the salt solution type and concentration affect the LAMEE effectiveness, and changing the concentration is one way to control the supply air outlet humidity ratio.

Keywords: Small-scale exchangers, LAMEE, Steady-state effectiveness, Heat and mass transfer directions, Salt solution, *NTU*, Heat capacity ratio.

4.3   Introduction

There are many applications for small compact heat exchangers for electronic cooling systems, aviation and aerospace applications and medical treatment and their performance is predictable for typical geometries (Jiang et al, 2001). Testing a small-scale exchanger before manufacturing a full-size exchanger can save money and time, and will give useful data provided the operating conditions and characteristic dimensionless parameters are in the same range as that for the prototype. There is much literature available related to modeling and testing of small-scale heat exchangers (Jiang *et al.*, 2001; Long 2008; Bejan, 2002). Ozden and Tari (2010) used a commercial CFD package to numerically model a small-size shell and tube heat exchanger, and investigate the effect of the baffle spacing, baffle cut ratio and shell diameter on the heat transfer coefficient and pressure drop. Rogiers and Baelmans (2010) optimized the size of a small-scale counter flow parallel-plate heat exchanger with respect to maximum thermal power density. They considered the heat exchanger effectiveness, pressure drop and heat

transfer rate density as constraints in this design and used an asymptotic solution to downsize the heat exchanger surface area.

Few studies have been done on small-scale energy exchangers until now. Zhang (2011a) developed an analytical solution for coupled heat and mass transfer problems in a hollow fiber membrane energy exchanger used for air dehumidification with counter flow configuration for air and liquid. The analytical results compared favorably with experimental data for a small-scale shell and tube hollow fiber membrane energy exchanger. Zhang *et al.* (2012a; 2012b) numerically investigated the coupled heat and mass transfer problem in a cross flow and a counter flow hollow fiber membrane contactors. They calculated the actual Nusselt and Sherwood number for the air and solution sides of the small-scale hollow fiber membrane contactors using a free surface model. In other work, Zhang and Huang (2011) used the cross flow and counter flow hollow fiber membrane contactors for air humidification using water in the system. The performance of the small-scale hollow fiber membrane module was investigated numerically and was validated with experimental data. The results showed that the cross flow configuration has a lower pressure drop in the hollow fiber membrane contactors, and the packing density is the dominant factor influencing the performance of the cross flow contactors. Ge *et al.* (2012) used Zhang's analytical solution (Zhang, 2011a) for liquid-to-air membrane energy exchangers (LAMEE) and compared the results with experimental data for a small-scale single-panel LAMEE. Good agreement was obtained between analytical and experimental results and the maximum discrepancy in exchanger effectiveness was 10%. Abe *et al.* (2006c) and Wang *et al.* (2005) experimentally investigated the transient response of temperature and humidity sensors in the presence of

an energy wheel with step changes in temperature and no change in humidity, and step changes in humidity and no change in the inlet temperature. A new test facility had been developed for these experiments which included a small part of a stationary energy wheel in a test section. Abe *et al.* (2006d) and Abe *et al.* (2006e) used the time constants that they measured for the energy wheel to analytically predict the performance of the full-size counter-flow energy wheel and compared the results with steady-state experimental performance data for the same energy wheel.

The LAMEE is a novel membrane energy exchanger that transfers heat and moisture between air and a salt solution (Namvar *et al.*, 2012; Ghadiri Moghaddam *et al.*, 2013b). The air and liquid desiccant are separated using a semi-permeable membrane inside the LAMEE, which is permeable for water vapor, but impermeable for liquid water. The novel test apparatus used in this research was introduced in Ghadiri Moghaddam *et al.* (2013b). Some preliminary numerical and experimental results were presented for the steady-state small-scale LAMEE effectiveness, when water was used as a transfer medium in the exchanger mainly to humidify the air. Mass and energy balance results for the test facility showed that the system was balanced during the experiments. The current chapter will build on this research by using different salt solutions, rather than water in the LAMEE; investigating a wider range of test cases, including air cooling and humidifying; and will present results for the repeatability of the experiments. In previous work (Ghadiri Moghaddam *et al.*, 2013b), the authors used water which is different than salt solution especially in a numerical model.

The test facility will be used firstly to investigate the effect of different heat and mass transfer directions on the steady-state performance of a LAMEE system under

different operating conditions. Experimental data will be compared with numerical simulation results. The performance of the LAMEE is not the same for different heat and mass transfer directions. This has been shown for a run-around membrane energy exchangers (RAMEE) that the direction of heat and mass transfer are important, where the RAMEE includes two LAMEEs located one in the supply and the other in the exhaust air stream (Seyed-Ahmadi *et al.*, 2009a; Seyed-Ahmad *et al.*, 2009b). The performance of the supply and exhaust LAMEEs are not the same while operating conditions and heat and mass transfer directions are different in those two LAMEEs in the RAMEE system. Also, the effect of different heat and mass transfer directions on the performance of energy exchangers was shown by Simonson and Besant (1999) for energy wheels. In this chapter the effect of different heat and mass transfer directions on the steady-state effectiveness of the LAMEE system will be investigated for various combinations of the heat and mass transfer directions. As well, the mass and energy balances and the repeatability of the experimental data for summer AHRI test conditions (AHRI STANDARD 1060, 2005) as a standard test condition will be studied. The repeatability of the experimental data for a LAMEE will be investigated to show how much the experimental data are repeatable and trust worthy.

The second main objective of this chapter is to study the effect of different salt solution types and concentrations on the steady-state performance of the LAMEE. Different salt solutions (i.e. LiCl, LiBr and $MgCl_2$) with different concentrations have been used in membrane based energy exchangers such as the LAMEE (Fan *et al.*, 2006; Erb *et al.*, 2009). Salt solution properties are different for different desiccant types and concentrations, and they affect the performance of the system and air outlet conditions

(Afshin, 2010). The main question is - what is the effect of different salt solutions types and concentrations on the LAMEE performance? This chapter will address this question using the small-scale single-panel LAMEE test apparatus. Lithium chloride (LiCl) salt solution will be used for this purpose with three different concentrations. Moreover, Magnesium Chloride ($MgCl_2$) liquid desiccant will be used as a second option for salt solution in the system. The $MgCl_2$ inlet conditions are selected at the same temperature and humidity ratio as the 25% concentration LiCl to have better comparison between the results for these two desiccant types. There are no numerical results or experimental data available related to the second objective in literature.

4.4   Test Apparatus and Instrumentation

The single-panel energy exchanger test (SPEET) facility has been used to collect experimental data in this chapter. The SPEET facility is described in Ghadiri Moghaddam *et al.* (2013b) with more details about the LAMEE design and sensor calibration procedures. A complete description of the test facility is also given below. A full schematic of the test facility is shown in Figure 4.1. The test apparatus can be divided into three main sections: the supply air system, the salt solution loop and the small-scale single-panel LAMEE (i.e. exchanger test section).
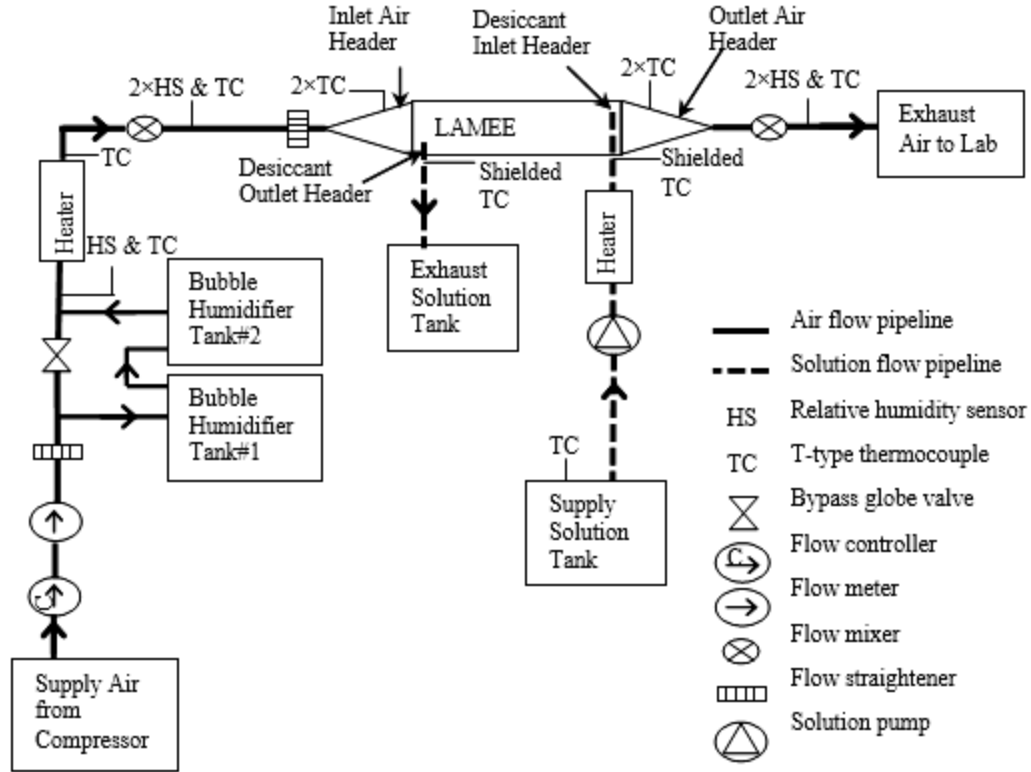
Figure 4.1 Schematic of the single-panel energy exchanger test (SPEET) facility (Ghadiri Moghaddam *et al.*, 2013b)

In the supply air system, a compressor supplies high pressure dry air (~4%RH) at room temperature to the test facility. This air passes through a 25 mm inner diameter PVC pipeline. The flow rate of the air is adjusted by using a flow controller (MKS-type 1559A). A flow meter (MKS-type 0558A) is used after the flow controller to provide more accurate control on the air flow rate. The flow meter is set to a selected air flow rate for each experiment. Furthermore, to condition the supply air, two water bubble tank humidifiers and a shell and tube heater are used in the system. A globe valve is used in the main pipeline to bypass the air into the humidifiers. The humidifiers could humidify the air up to 25 g_w/kg_{air} depend on the air temperature. After humidifying, the air passes through the heater, which can heat the air up to 50°C to adjust the supply air temperature. Finally, the air passes through a supply inlet air header to reach the test exchanger. A

converging-diverging air header (diffuser) is designed and installed at the air inlet of the exchanger to direct the air flow from a 25.4 mm diameter pipeline to the rectangular opening of the exchanger which has an outlet of 5 mm thickness and 94 mm height. The same air header is used at the air outlet of the exchanger. The detailed description of the air headers and heater designs are given in Ghadiri Moghaddam *et al.* (2013b). A flow straightener is installed before the inlet air header to provide a uniform air flow to the exchanger inlet. The temperature and humidity of the air are measured at different locations in the setup, and these locations are shown in Figure 4.1. Four T-type thermocouples are used in the inlet and outlet air headers to measure the supply air inlet and outlet temperatures. Also, four high accuracy humidity sensors (Honeywell-type HIH4012) are installed in the upstream and downstream of the exchanger in the main pipeline to measure the supply air inlet and outlet humidity. These humidity sensors are too big to be installed in the air headers close to the air inlet and outlet of the exchanger. Also, two air mixers are used before humidifiers, one at each location, to provide more accurate bulk mean flow humidity measurement. To calculate the supply air inlet and outlet humidity ratio, another two T-type thermocouples are installed in the humidity sensor locations. The measured humidity ratios in those locations are the same as at the exchanger air inlet and outlet humidity ratios; because, except for the humidifiers and the small-scale LAMEE exchanger, there is no other water vapor transfer sources or sinks in the air piping system. Finally, the air is exhausted to the laboratory room at the end of the test facility. The capacity, calibration range and accuracy of the measurement instruments are presented in Table 4-1.

Table 4-1 The air and solution side measurement instruments capacity, calibration range and accuracy

Measurement Instruments	Capacity/Calibration range	Accuracy
Air flow controller (L/min)	0~100	2% of full-scale
Air flow meter (L/min)	0~100	1% of full-scale
Air humidity sensors (%RH)	10~90	2
Air side T-type thermocouples (°C)	-30~40	0.2
Solution side shielded T-type thermocouples (°C)	0~60	0.1
Solution peristaltic pump (mL/min)	1~2316	2% of reading-scale

The LiCl salt solution is used in the test setup as a transfer liquid to both humidify or dehumidify and heat or cool the air. LiCl is pumped through the open solution loop using a peristaltic pump (OmegaFlex-FPU500) from a supply solution tank to an exhaust one. An electrical heater with 100 W maximum power dissipation is used before exchanger solution inlet to adjust the solution inlet temperature, and a variable transformer (variac) is used to regulate the heater power. After the electrical heater, the solution is pumped through the exchanger to condition the supply air. Two solution headers are designed for the exchanger solution inlet and outlet openings to distribute and collect the solution to/from the exchanger, respectively. Finally, after the solution outlet header, the liquid desiccant is collected in the exhaust solution tank. The desiccant inlet and outlet temperatures and concentrations are measured for each experiment. Two high accuracy shielded T-type thermocouple are used at the solution inlet and outlet headers to measure the solution temperatures at those locations. The inlet salt solution concentration is measured before each experiment by taking three samples from the supply solution tank and testing them in a densitometer device (Anton Paar-DMA 4500M). This device measures the salt solution density at 20°C temperature and with this information it is possible to calculate the salt solution concentration from salt solution properties

equations (Afshin, 2010). For the solution outlet, another three samples are taken from the exchanger solution outlet for each test at the steady-state condition and the outlet salt solution concentration is calculated with the same procedure as inlet salt solution. The measurement equipment locations in the solution loop are shown in Figure 4.1. Also, the calibration range and the accuracy of the solution side measurement instruments are presented in Table 4-1. Finally, all the air and solution measured properties are acquired with a National Instruments (NI-cDAQ 9174) data acquisition system, and they are monitored and saved using a 2010 LabVIEW program at steady-state conditions for each test.

The main part of this test facility is the novel small-scale single-panel LAMEE. A flat-plate liquid-to-air membrane energy exchanger consists of many panel layers, where each panel layer acts as one panel exchanger among a plurality of panel exchangers, for heat and moisture transfer (Namvar *et al.*, 2012; Afshin, 2010; Ghadiri Moghaddam *et al.*, 2013b). The heat and moisture transfers occur simultaneously through a semi-permeable membrane in each panel that is impermeable for liquid water, but allows water vapor to transfer between a supply air stream and an aqueous liquid desiccant. Since the system design is not yet finalized, future designs could differ from that tested. The main purpose of designing and manufacturing the small-scale LAMEE is to minimize the cost and time to develop a full-size LAMEE and to investigate the effect of system design and operational changes. Also, manufacturing a novel single-panel LAMEE with a new design helps in minimizing sources of errors in the system. The new small-scale single-panel design will provide better sealing between the air and solution channels to reduce the solution leakage from the solution side to the air stream (Ghadiri Moghaddam *et al.*,

2013b). Also, it reduces the membrane deflection inside the exchanger due to pressure difference between the air and solution. Consequently, it eliminates mal-distribution of flow among many flow panels and minimizes the mal-distribution effect caused by membrane deflections on the performance of the small-scale single-panel LAMEE. Therefore, a counter-cross flow flat-plate small-scale single-panel LAMEE was designed and constructed for this research. In the small-scale LAMEE, two grooved plastic panels are used on the sides of the LAMEE and two semi-permeable membranes are attached to them to form the solution channels inside the LAMEE. These two grooved side panels are placed beside each other, with an air spacer in between to form the air channel. An air screen is used inside the LAMEE to enhance the air side heat transfer performance. A cross section view of the small-scale single-panel LAMEE, and the air and solution flow configuration inside the exchanger are shown in Figure 4.2. The solution is pumped from bottom-to-top through the exchanger. The test facility and the small-scale LAMEE are well insulated to reduce heat loses/gains to/from surroundings. The exchanger geometry, specifications and membrane properties are indicated in Table 4-2. A GE™ membrane (type QL822) is used as the semi-permeable membrane in the system. The small-scale single-panel LAMEE design and manufacturing process are explained with more details in (Ghadiri Moghaddam *et al.*, 2013b).
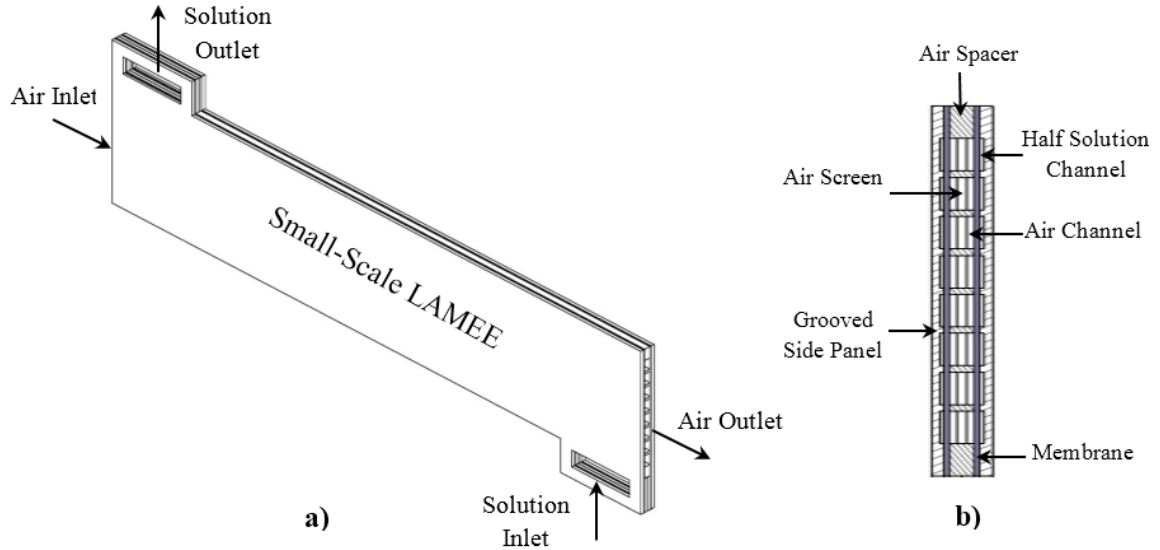
Figure 4.2 The small-scale single-panel LAMEE (a) air and solution flow configurations, and, (b) cross-section detailed view

Table 4-2 The small-scale single-panel LAMEE specifications and the membrane properties

Parameter	value
Exchanger length, L_{ex} (m)	0.49
Exchanger aspect ratio, L_{ex}/H_{ex}	5.2
Exchanger entrance ratio, L_{sol}/L_{ex}	0.11
Air gap thickness, δ_{air} (mm)	5
Solution gap thickness on each side panel, $\delta_{sol}/2$ (mm)	0.8
Number of solution paths on each side panel	8
Mass resistance of membrane, R_{mem} (s/m)	56
Membrane thermal conductivity, k_{mem} (W/mK)	0.065
Membrane thickness, δ_{mem} (mm)	0.265

4.5 Experimental Procedures

In total 44 experiments have been conducted with the small-scale LAMEE. The experimental procedure is discussed in this section.

4.5.1 Mass and Energy Balances

It is necessary to ensure that the current experimental data conserves mass and energy (Simonson *et al.*, 1999). The dry air and solution mass balances, which show the

air or solution leakages in the system, are investigated in (Ghadiri Moghaddam *et al.*, 2013b) for one specific test case and results show that the system is balanced. It was not possible to do the dry air and solution mass balances for all experiments, because for dry air mass balance it is required to use another flow meter at the air exhaust of the test facility which might over-pressurize and damage the system. Therefore, those results are trusted here for dry air and solution mass balances and the dry air and salt solution inlet flow rates are assumed to be the same as the dry air and salt solution outlet flow rates in the experiment, respectively. Afterwards, the water vapor mass and energy balances of the system are studied for all four different test cases (i.e. air cooling and dehumidifying (C&D), air cooling and humidifying (C&H), air heating and dehumidifying (H&D), and air heating and humidifying (H&H)) to ensure valid experimental data. The water vapor mass and energy balances for LAMEE systems are calculated as follows (Simonson *et al.*, 1999):

$$\Delta(\dot{m}W) = \left\| \left[(\dot{m}W)_{air,in} - (\dot{m}W)_{air,out} \right] + \left[(\dot{m}_{salt} X_{sol})_{in} - (\dot{m}_{salt} X_{sol})_{out} \right] \right\| \leq Un_{\Delta(\dot{m}W)} \quad (4.1)$$

$$\Delta(\dot{m}H) = \left\| \left[(\dot{m}H)_{air,in} - (\dot{m}H)_{air,out} \right] + \left[(\dot{m}H)_{sol,in} - (\dot{m}H)_{sol,out} \right] \right\| \leq Un_{\Delta(\dot{m}H)} \quad (4.2)$$

where $\dot{m}$, W, H and X are flow rate, humidity ratio, enthalpy and solution mass fraction, respectively. Subscripts *air, sol* and *salt* refer to the air, liquid desiccant and pure salt, respectively. Also subscripts *in* and *out* show the air or solution inlet and outlet for the test section, respectively. $Un_{\Delta(\dot{m}W)}$ and $Un_{\Delta(\dot{m}H)}$ are the calculated uncertainty for water vapor and energy transfer in the system based on the air and solution properties for each case, respectively. Moreover, the energy exchange inequality ratio (*EEI*) of the SPEET facility is presented in the results. The *EEI* presents the energy balance of the

system, and is a summation of the total energy transferred through the air and solution divided by total input energy to the system.

$$EEI = 100 \times \frac{\left|\left[\left(\dot{m}H\right)_{air,in} - \left(\dot{m}H\right)_{air,out}\right] + \left[\left(\dot{m}H\right)_{sol,in} - \left(\dot{m}H\right)_{sol,out}\right]\right|}{\left|\left(\dot{m}H\right)_{air,in} + \left(\dot{m}H\right)_{sol,in}\right|}$$ (4.3)

The test facility water vapor mass and energy balances results are presented in Table 4-3 for all test cases. Because there is more than one test in each case, the mass and energy balance results in Table 4-3 are presented for the worst case in each test condition. The mass and energy balance results show that the test facility is balanced for all experiments, and the experimental data are within acceptable uncertainty ranges. The maximum *EEI* for the C&D test case is found to be 0.02, and *EEI* is 0.04 for the worst case which is the C&H test case.

Table 4-3 The water vapor and energy balance results of the small-scale single-panel LAMEE for the worst cases at different test conditions

Test Case	Water vapor balance		Energy balance		*EEI*
	$\Delta(\dot{m}W)$, kg/h	$Un_{\Delta(\dot{m}W)}$, kg/h	$\Delta(\dot{m}H)$, W	$Un_{\Delta(\dot{m}H)}$, W	–
C&D	10.1	61.9	2.09	2.88	0.02
C&H	6.9	61.1	2.48	2.68	0.04
H&D	5.6	59.6	0.36	2.65	0.01
H&H	8.1	59.8	2.05	2.71	0.02

4.5.2 Repeatability

The repeatability results show the repeatability of the experimental data for the same test facility operating with specified ranges of inlet conditions. Thus, it is an indication of the uncertainty caused by small variations in the inlet conditions, the selection of the recording time or end time of each experiment, and the instrumentation for the SPEET facility during steady-state experiments. For this purpose, the C&D test case is repeated 20 times (5 times at each *Cr**) with the same air and solution inlet

conditions, and LiCl is used as a salt solution in the system. The repeatability is calculated based on the precision error for each set of data.

$$Rp = S \times t,$$
(4.4)

where Rp is the repeatability factor for the dependent variable (i.e. effectiveness), S is standard deviation of the data. and t is the student t factor based on 95% uncertainty bounds on both sides of the mean value (Figliola and Beasley, 2006). Also, the uncertainties of the LAMEE effectiveness for the C&D conditions are calculated based on the bias error of the measurement instruments and the precision errors, which are found from repeatability results for the measurement instruments.

$$Un = \sqrt{Rp^2 + B^2}$$
(4.5)

In Eq. (4.5), Un and B are the total and bias uncertainties, respectively. For other test conditions, the small-scale LAMEE effectiveness uncertainties are calculated based on the measurement instruments calibration results. The method of propagation of errors is used to calculate the LAMEE effectiveness uncertainties in all cases (Figliola and Beasley, 2006). The small-scale single-panel LAMEE effectiveness results for air C&D and the repeatability and uncertainty results for this test case are presented in Table 4-4. The repeatability results show that the experimental data for the LAMEE effectiveness varies between 0.8% to 1.7% for the C&D test conditions, while the LAMEE effectiveness uncertainties vary between 2.5% to 6.2%. These repeatability results show that the precision errors resulting from repeating the experiments are less than the precision errors resulting from calibrating the measurement instruments and the results are repeatable. Consequently, experiments with the small-scale LAMEE test facility are

quit repeatable, and repeating the experiments will not affect the effectiveness results and

the effectiveness results will be within the experimental uncertainty ranges.

Table 4-4 The experimental small-scale LAMEE effectiveness results with the uncertainty and the repeatability data for the C&D test case (5 measurements for each Cr^*, t = 2.571 for 95% uncertainty)

Cr^*	Sensible Effectiveness			Latent Effectiveness			Total Effectiveness		
	Value (%)	Un (%)	Rp (%)	Value (%)	Un (%)	Rp (%)	Value (%)	Un (%)	Rp (%)
1	41	3.1	1.5	52	6.2	1.2	49	4.6	0.8
3	76	2.5	1.4	77	4.9	1.1	77	3.6	1.1
5	83	2.7	1.7	82	4.8	1.7	82	3.5	1.7
7	87	2.6	1	84	4.9	1.6	85	3.6	1.6

4.5.3   Effect of Different Heat and Mass Transfer Directions

Four different test conditions are considered to investigate the effect of different

heat and mass transfer directions on the performance of the LAMEE system: air cooling

and dehumidifying (C&D), air cooling and humidifying (C&H), air heating and

dehumidifying (H&D), and air heating and humidifying (H&H). The desired air and

solution inlet set conditions for these four experiments are shown on the psychrometric

chart in Figure 4.3. The psychrometric chart can be divided in four regions according to

different heat and mass transfer directions combinations based on known salt solution

inlet conditions. The test conditions are selected based on this idea to have different heat

and mass transfer directions. LiCl is used as a liquid desiccant for these experiments. The

measured air and solution inlet conditions might be slightly different than set conditions

due to slight temperature and humidity variation during the experiments, and they are

presented in the results section with other air and solution measured properties. In

addition, the effect of thermal capacity ratio (Cr^*) on the steady-state performance of the

LAMEE is investigated for each test condition. Experiments are conducted for four

different Cr^* ($Cr^* = 1, 3, 5, 7$) and a constant number of heat transfer units ($NTU = 3$). The definitions of NTU and Cr^* are presented in Eqs. (4.6) and (4.7).
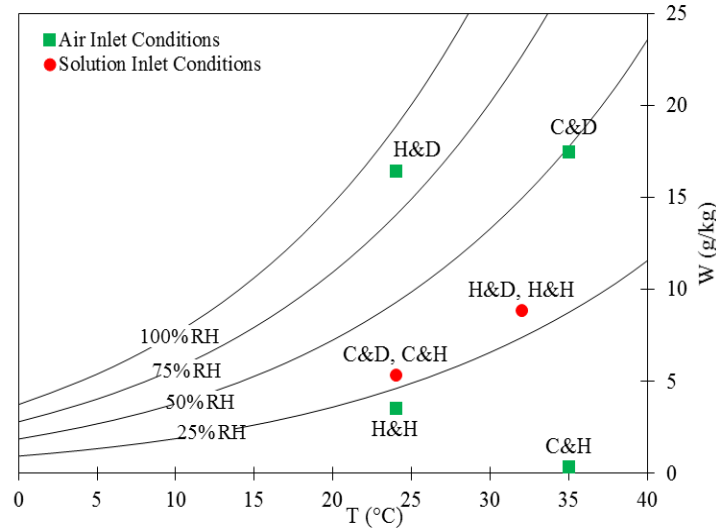
Figure 4.3 Air and salt solution (LiCl) inlet set conditions for the different heat and mass transfer directions experiments

4.5.4　Effect of Different Desiccant Types and Concentrations

Different types of salt solutions (i.e. LiCl, LiBr and $MgCl_2$) can be used in LAMEE systems. Currently, salt solution selection is based on salt properties such as saturation concentration and cost (Afshin, 2010). However, there are no experimental data available for the effect of different salt solution types and concentration on the performance of the LAMEE system. LiBr salt is expensive and less applicable in liquid to air membrane energy exchangers; however, the LiBr saturated concentration is almost 65% which reduces the risk of salt solution crystallization in the LAMEE solution side (Afshin, 2010). Thus, the effect of two salt solution types (i.e. LiCl and $MgCl_2$) is investigated. Also, to provide a better comparison between the results for these two salt solutions, the solution inlet temperatures and humidity ratios are set to be the same for both experiments. Moreover, the effect of different salt solution concentrations on the

performance of the LAMEE is studied for LiCl. Three different concentrations are selected for these experiments at the same solution inlet temperature. All tests are conducted for the air C&D test case at summer AHRI test conditions (ANSI/AHRI Standard 1060, 2011) for four different heat capacity ratios (i.e. $Cr^* = 1, 3, 5$ and 7) and $NTU = 3$. The measured air and solution inlet and outlet conditions are presented in the results section (see Table 4-6).

4.6   Numerical Modeling

An enthalpy pump system (EPS) numerical code is used to produce the numerical results in this chapter. The EPS code has been developed by University of Saskatchewan RAMEE research group and the basics and detailed formulations of this code are presented in (Seyed-Ahmadi, 2008; Hemingson, 2010). The EPS code was modified based on the small-scale single-panel LAMEE geometry and specifications by Ghadiri Moghaddam *et al.* (2013b) and numerical results were compared with experimental data in chapter 3. The same modified EPS code is used in this chapter to generate the numerical results. The numerical results are presented here to show that they follow the same trend as the experimental data in the results and in some cases they agree very well. Modifying and validating the EPS numerical code with the experimental data are planned for future work in this research project.

There are some assumptions in the numerical code which affect the numerical results. First, heat gains/losses from/to surroundings are included in the numerical code to provide more realistic numerical results. Second, a counter flow configuration for air and solution is used in the numerical code. The small-scale LAMEE has counter-cross flow configuration with 90% pure counter flow area for the air and solution (Ghadiri

Moghaddam *et al.*, 2013b). Also, Akbari *et al.* (2012a) indicated that the discrepancy in the EPS code numerical results for the counter-cross and counter flow configurations for a LAMEE system with the same aspect ratio and entrance ratio as the small-scale LAMEE is less than 1%. As a result, pure counter flow configuration is chosen for numerical modeling. Finally, the air flow inside the exchanger air channel is assumed to be laminar at the test values of channel Reynolds number. Actually, the flow is not entirely laminar because of the presence of an air screen inside the air channel, which produces regions of transitional flow in the air Channel (LePoudre *et al.*, 2011). However, there are no detailed experimental or numerical data available regarding the heat and mass transfer promotion for this specific air screen. As a result, the laminar flow regime was assumed for both the air and water flows in the LAMEE. The Reynolds numbers in the air and solution channels are 700 and 20, respectively. Nusselt numbers of 8.24 (for a fully-developed laminar flow between two infinite parallel plates with constant heat flux on both walls) and 5.39 (for a fully developed laminar flow between two infinite parallel plates with constant heat flux on one wall and the other wall insulated) are used for the air and salt solution, respectively (Incropera and DeWitt, 1985). LePoudre *et al.* (2011) showed the heat transfer enhancement for a sinusoidal air screen inside an air channel with the same thickness as the LAMEE air channels by using a CFD model. The Reynolds number was between 1370 and 2750, which is in the laminar to transitional region for the hollow rectangular channel. The results showed almost 100% improvement in the air convective heat transfer coefficient at $Re_{air} = 2000$. The effect of this novel air screen on the heat and mass transfer performance of the air, and on the LAMEE effectiveness is one of the objectives for future work. The details of

this assumption and its effect on the numerical performance of the LAMEE will be discussed in the results section (see section 4.8).

To calculate the numerical results for each test case, the *NTU* and *Cr** are used as inputs in the numerical code to have the same *NTU* and *Cr** for the experiment and numerical model. NTU_m and *m**, which are the number of mass transfer units and mass flow rate ratio, respectively, are calculated in the code to determine the LAMEE effectiveness. The *NTU* and *Cr** are important dimensionless parameters for heat and energy exchangers problems. They are calculated as follows:

$$NTU = \frac{UA}{C_{\min}} \tag{4.6}$$

$$Cr = \frac{C_{\min}}{C_{\max}} = \frac{1}{Cr^*} \tag{4.7}$$

where *U* and *A* are the overall heat transfer coefficient and total membrane active area for heat and mass transfers, respectively. Also, *C* is the heat capacity rate for an exchanger, and subscripts *min* and *max* refer to the minimum and maximum values, respectively. *Cr* and *Cr** both represent a heat capacity ratio and they have inverse values. In a LAMEE system formulation *Cr** definition has been used as a heat capacity ratio. Also, in LAMEEs, the minimum heat capacity rate is related to the air side for *Cr** values greater than 1 ($C_{\min} = (\dot{m}c_p)_{air}$ and $C_{\max} = (\dot{m}c_p)_{sol}$). c_p is the specific heat capacity. Additionally, the overall convective heat transfer coefficient for a LAMEE system is calculated using the equation:

$$U = \left[\frac{1}{h_{air}} + \frac{\delta_{mem}}{k_{mem}} + \frac{1}{h_{sol}} \right]^{-1} \tag{4.8}$$

where h, δ and k are the convective heat transfer coefficients, thickness and thermal conductivity respectively. Also, subscript *mem* refers to the membrane properties in Eq. (4.8). As it was mentioned before, the convective heat transfer coefficients for the air and solution sides are calculated for the laminar flow regime in the air and solution channels. The NTU_m and m^* are the other important dimensionless parameters for energy exchangers, which are used in the code to calculate the LAMEE performance. They are calculated as follows:

$$NTU_m = \frac{U_m A}{\dot{m}_\mathrm{min}} = \frac{U_m A}{\dot{m}_{air}} \tag{4.9}$$

$$m^* = \frac{\dot{m}_\mathrm{min}}{\dot{m}_\mathrm{max}} = \frac{\dot{m}_{air}}{\dot{m}_{sol}} \tag{4.10}$$

where U_m is the overall mass transfer coefficient and is calculated from the following equation:

$$U_m = \left[\frac{1}{h_{m,air}} + R_{mem} + \frac{1}{h_{m,sol}} \right]^{-1} \tag{4.11}$$

In Eq. (4.11), h_m and R_{mem} are the mass transfer coefficients and membrane mass resistance, respectively. The convective mass transfer coefficients for the air and solution sides are calculated based on the heat and mass transfer analogy (Niu and Zhang, 2001):

$$Sh = NuLe^{-\frac{1}{3}} \tag{4.12}$$

Where Sh and Le are the Sherwood and Lewis numbers for the air and solution, respectively. The numerical results for all test cases mentioned in the previous section are presented in the results section 4.8. Also, as it was mentioned before, the purpose of this chapter is not validating the numerical code with the experimental data. This chapter aims

to show that the LAMEE numerical steady-state effectiveness results also follow the same trend with changing *Cr** as experimental data in all cases.

4.7 LAMEE Performance Evaluation

LAMEE effectiveness definitions are used to analyze the results for both the numerical model and the experimental data. The LAMEE system performance is evaluated with three types of effectiveness: sensible, latent and total effectiveness. The sensible or latent effectiveness show how much heat (sensible energy) or latent energy are transferred in the system, respectively. The sensible or latent effectiveness is defined as heat or latent energy transferred in the system over maximum possible heat or latent energy transfer in the exchanger, respectively.

$$\varepsilon_{Sen \text{ or } Lat} = \frac{\left(\dot{m}c_p\right)_{air}\left(Y_{air,in} - Y_{air,out}\right)}{\left(\dot{m}c_p\right)_{min}\left(Y_{air,in} - Y_{sol,in}\right)} \tag{4.13}$$

In this equation, ε and Y are effectiveness and temperature (*T*) or humidity content (*W*), respectively. Subscripts *Sen* and *Lat* refer to the sensible and latent effectiveness, respectively. Also, as it was mentioned before, minimum heat capacity rate is always related to the air side in LAMEE systems for *Cr**≥1. As a result, Eq. (4.13) can be written in the following format.

$$\varepsilon_{Sen \text{ or } Lat} = \frac{\left(Y_{air,in} - Y_{air,out}\right)}{\left(Y_{air,in} - Y_{sol,in}\right)} \tag{4.14}$$

Finally, the total effectiveness of the LAMEE, which is related to both heat and moisture transfer in the system, is calculated from the following equation (Simonson and Besant, 1999).

$$\varepsilon_{Tot} = \frac{\varepsilon_{Sen} + H^{*}\varepsilon_{Lat}}{1 + H^{*}} \tag{4.15}$$

where subscript Tot refers to the total effectiveness. In Eq. (4.15), H^{*} is known as the LAMEE operating factor, and it is calculated based on the air and solution inlet temperatures and humidity ratios in the system (Simonson and Besant, 1999). However, the actual H^{*} value could be slightly different in the LAMEE system, because the specific heat capacity of the air is not constant and depends on the air inlet conditions.

$$H^{*} = \frac{\Delta H_{Latent}}{\Delta H_{Sensible}} \approx 2500 \frac{W_{air,in} - W_{sol,in}}{T_{air,in} - T_{sol,in}} \tag{4.16}$$

4.8 Results and Discussion

In total, 44 experimental tests have been designed and conducted to complete the objectives of this chapter. The experimental data of those experiments are analyzed and the results are discussed in this section. Moreover, the numerical results are presented for each test case to numerically show the effect of the different heat and mass transfer directions, and using the different salt solution types and concentrations on the steady-state performance of the LAMEE system.

4.8.1 Effect of Different Heat and Mass Transfer Directions

In this section, the effect of the different heat and mass transfer directions on the steady-state performance of the small-scale LAMEE is investigated numerically and experimentally for four different test cases: air C&D, air C&H, air H&D and air H&H. The results are presented for $NTU = 3$ and four different $Cr*$ values, and LiCl is used as a solution in the system for all cases. The air convective heat transfer coefficient and the NTU are calculated based on laminar air flow inside the air channel and it is the same for

the experiment and the numerical model. Moreover, the small-scale LAMEE effectivenesses are calculated based on the experimental data and the numerical results for each test case and they are plotted versus Cr^*. The results shows that, the small-scale LAMEE effectiveness is not the same for the different heat and mass transfer directions, and even the trend for the effectiveness graph versus Cr^* is different in some cases for the different heat and mass transfer directions.

4.8.1.1 Air Cooling and Dehumidifying (C&D)

In this test case, hot and humid air at the summer AHRI conditions is supplied to the small-scale LAMEE and it is cooled and dehumidified through the exchanger. LiCl is used as a salt solution in the system and the steady-state performance of the LAMEE is investigated for four different Cr^* values and $NTU = 3$. The repeatability of the experiment is also studied for this test case, and the results are presented in Table 4-4. Twenty experiments have been done for this test case consisting of five tests at each Cr^*. To present the results for this test case the experimental data are averaged for each Cr^*. The average measured air and solution inlet and outlet conditions are presented in Table 4-5 for different Cr^*. The sensible, latent and total effectiveness of the LAMEE for both the experimental data and the numerical results are shown in Figure 4.4. Uncertainties for the experimental effectiveness are calculated based on the measurement instruments' calibration results (see Table 4-1) and the repeatability results using the method of propagation of errors. The small-scale LAMEE effectiveness increases with Cr^* for sensible, latent and total effectiveness. Maximum total effectiveness of 85% is achieved for the small-scale LAMEE at $NTU = 3$ and $Cr^* = 7$. Also, the numerical results for the

114

small-scale LAMEE effectiveness are within the uncertainty bound of the experimental data in this test case.

Table 4-5 Average measured air and solution inlet and outlet conditions for the air C&D, air C&H, air H&D, and air H&H test cases at *NTU* = 3 and different *Cr** with LiCl salt solution

Test Case	Cr^*	Inlet Conditions					Outlet Conditions				
		$T_{air,in}$ (°C)	$W_{air,in}$ (g/kg)	$T_{sol,in}$ (°C)	$C_{sol,in}$ (%)	$W_{sol,in}$ (g/kg)	$T_{air,out}$ (°C)	$W_{air,out}$ (g/kg)	$T_{sol,out}$ (°C)	$C_{sol,out}$ (%)	$W_{sol,out}$ (g/kg)
C&D	1	35	17.28	24	34.59	5.54	30.6	11.2	39.8	33.96	15.2
	3	35	17.38	24	34.59	5.54	26.6	8.31	34.2	34.24	10.8
	5	35	17.29	24	34.59	5.53	25.8	7.71	31.1	34.36	8.83
	7	35	17.3	24	34.59	5.54	25.5	7.43	29.2	34.43	7.80
C&H	1	34.9	0.33	24	34.36	5.65	24.2	4.89	25.0	34.68	5.88
	3	35	0.31	24	34.36	5.65	24.4	5.06	24.4	34.48	5.73
	5	35	0.33	24	34.36	5.65	24.4	5.11	24.3	34.43	5.72
	7	35	0.4	24	34.36	5.65	24.5	5.19	24.4	34.40	5.32
H&D	1	23.9	16.25	32.1	34.42	9.26	31.4	10.9	33.7	33.99	10.6
	3	24	16.49	32	34.42	9.26	31.1	10.3	33.5	34.22	10.3
	5	24	16.46	32	34.42	9.26	31	10.2	33.0	34.3	9.94
	7	24	16.45	32	34.42	9.26	30.8	10.1	32.8	34.33	9.76
H&H	1	24	3.6	32	34.37	9.31	27.5	6.39	23.0	34.58	5.21
	3	24	3.58	32	34.37	9.31	29.5	7.55	27.3	34.48	6.91
	5	24	3.51	32	34.37	9.31	29.9	7.79	28.9	34.44	7.68
	7	24.1	3.55	32	34.37	9.31	30.1	8.05	30.0	34.41	8.21

The numerical results are expected to show higher performance for the small-scale LAMEE in comparison to the experimental data because of the simplification and idealization assumptions, which are made to numerically model the LAMEE system. However, they show lower values for latent and total effectiveness in Figure 4.4. There are two main assumptions in the numerical code which have significant effect on the numerical performance of the small-scale LAMEE and cause lower numerical effectiveness results in comparison to experimental data. First, as it was explained before, it is assumed that the air flow regime inside the air channel is laminar, which is not exactly the case for the small-scale LAMEE. The air screen, which is used inside the air

channel, produces a modest enhancement of the heat and mass transfer performance of the air inside the channel. As a result, the air side Nusselt number will be more than 8.24, which is based on laminar air flow between two parallel plates with constant heat flux on both walls (Incropera and DeWitt, 1985). Second, the membrane properties, which are used in the numerical code, are measured by the Permatran-W® (Model 101K) device (Larson, 2006). It has six test cells to find the water vapor transmission rate and permeability of a membrane. The geometry of the cells is not ideal for the membrane permeability test and only part of the membrane area is active inside the cell. The question is what percentage of the membrane area is active inside the test cell. This active area is very important to calculate the membrane permeability results. Larson (2006) suggested that only 52.5% of the membrane area inside the test cell is active. This value was suggested based on comparison of the Permatran results with other results from standard membrane permeability test methods, which also have high uncertainties. Therefore, there are no strong data available for the active membrane area inside the Permatran test cell. Consequently, in this chapter, it is assumed that 100% of the membrane area is active inside the test cell and the membrane properties are calculated based on this assumption, which is also not a real case for the Permatran device. CFD modeling of the test cell or modifying the Permatran test cell to find the exact active area of the membrane in the Permatran device is another objective for future studies. These two assumptions have significant effect on the small-scale LAMEE effectiveness results, and have likely caused lower numerical results in comparison to the experimental data.
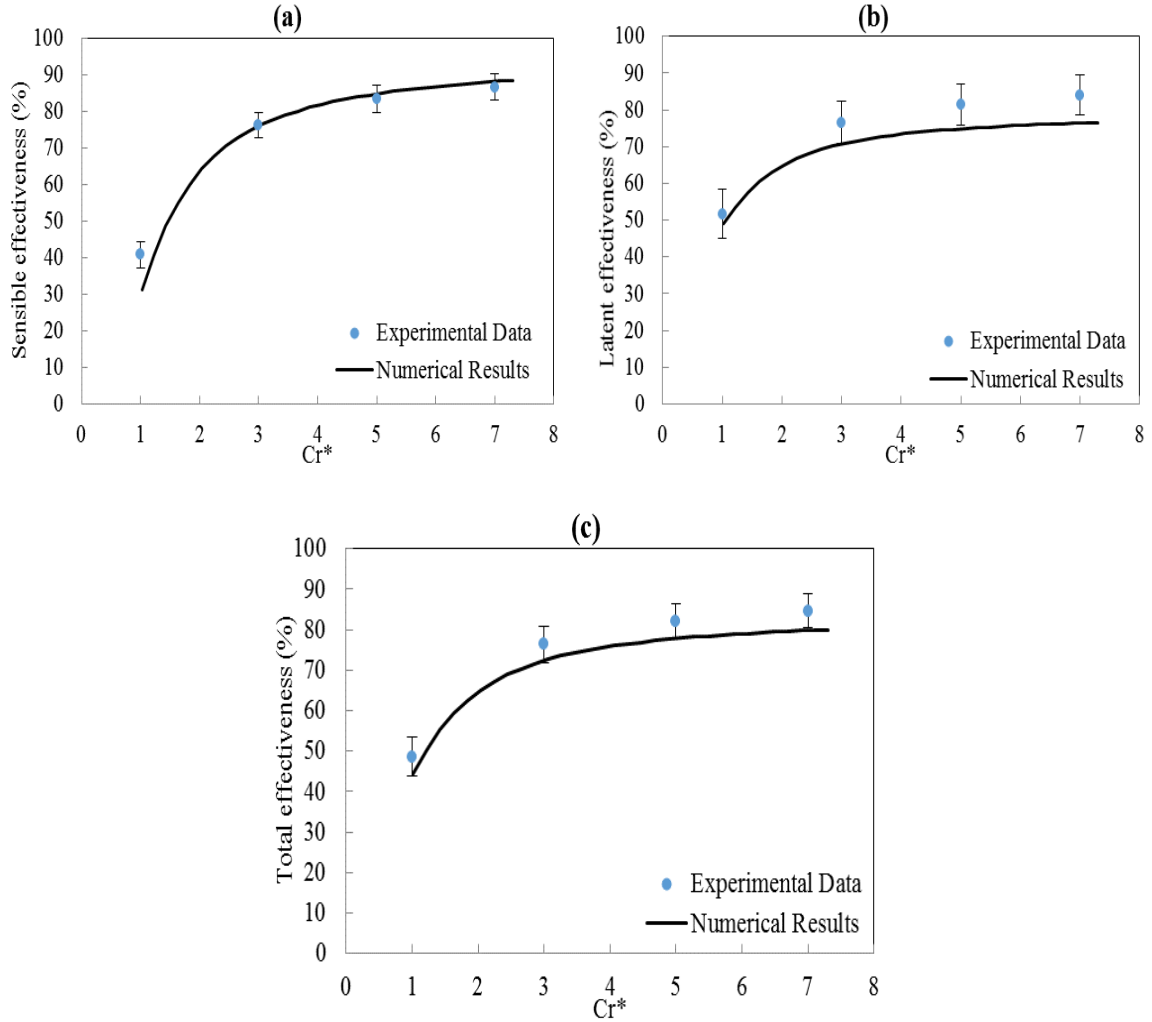
Figure 4.4 Experimental and numerical small-scale LAMEE (a) sensible, (b) latent, and (c) total effectiveness for the C&D test conditions at *NTU* = 3 and variable *Cr** with LiCl salt solution

4.8.1.2 Air Cooling and Humidifying (C&H)

This test condition represents the performance of the small-scale LAMEE in hot and dry climates. The air is cooled and humidified while passing through the exchanger. The heat transfer direction is from the air side to the solution, while moisture transfers from the solution to the air. The measured air and solution inlet and outlet conditions are presented in Table 4-5 for different *Cr** and *NTU* = 3. Also, the experimental air inlet and outlet conditions for *Cr** = 5 are shown on the psychrometric chart in Figure 4.5 to show

the air and solution process lines in the exchanger for the air C&H test case. Figure 4.6 illustrates the numerical and experimental sensible, latent and total effectiveness of the LAMEE system for the air C&H test case. In Figure 4.6-a, both numerical and experimental sensible effectiveness of the LAMEE are decrease with increasing Cr^*. Also, it shows good agreement between the numerical and experimental results for the sensible effectiveness. In the C&H test case, the heat transfer direction is from the air side to the solution side, and the mass transfer direction is opposite of the heat transfer direction. Also, the moisture transfer and the latent heat required to humidify the air causes the solution to get cold through the LAMEE. The sensible heat transfer and the latent heat transfer directions are opposite and depending on which one is dominant the LAMEE sensible effectiveness could increase or decrease. In this chapter, for the C&H test conditions the latent heat transfer is dominant and it causes the LAMEE sensible effectiveness to decrease. The same reason applies for the H&D test case in this chapter, where the LAMEE sensible effectiveness decreases while Cr^* is increasing. However, in the H&D test case, the heat transfer direction is from the solution side to the air side and the moisture transfer direction is the opposite.

The latent effectiveness in Figure 4.6-b slightly increases with Cr^*, and again, it shows lower performance for the numerical model. Finally, Figure 4.6-c shows the total effectiveness of the LAMEE for this test condition and it also increases with Cr^*. The maximum total effectiveness is 64% for this test case at $Cr^* = 7$ with more than 60% uncertainty in effectiveness. This test case represents an uncertain test condition for the LAMEE system because of the air and solution inlet conditions selections. It can be seen in Figure 4.5 that the air and solution inlets have almost the same enthalpy on a

psychrometric chart, and it caused to have air and solution outlets close to the solution inlet condition. As a result, according to the effectiveness definitions, small difference in the air or the solution outlet conditions in the experimental data or numerical results will cause big change in the effectiveness results. Also, this effect explains the discrepancies between the experimental and numerical results for latent and total effectiveness.

Furthermore, there are some other sources of errors in the experiment and the numerical model which affect the discrepancy between the experimental and numerical results. First, it is assumed that there is no solution leakage in the small-scale LAMEE exchanger and that the solution channels are completely sealed. However, according to the small-scale LAMEE leakage test, there is a small amount of leakage in the system (less than 1% of the solution flow rate), which affects the accuracy of the experimental results. Second, the heat gains/losses to/from surroundings are only considered for the exchanger exterior side walls in the numerical code, and only in one direction which is perpendicular to the air and solution flow. This effect is minor for small-scale single-panel LAMEE, and is more significant for a full-size exchanger with more channels when exterior top and bottom walls are also important for heat gain and loss. Also, in reality, for the small-scale LAMEE there are heat gains/losses from/to surroundings in some parts of the air inlet header between the air inlet thermocouples and exchanger inlet opening, and air outlet header between the exchanger outlet opening and the air outlet thermocouples. Finally, the air and solution flow configuration is assumed to be pure counter flow in the numerical model, while it is counter-cross flow with bottom-to-top direction for solution flow in the small-scale LAMEE.
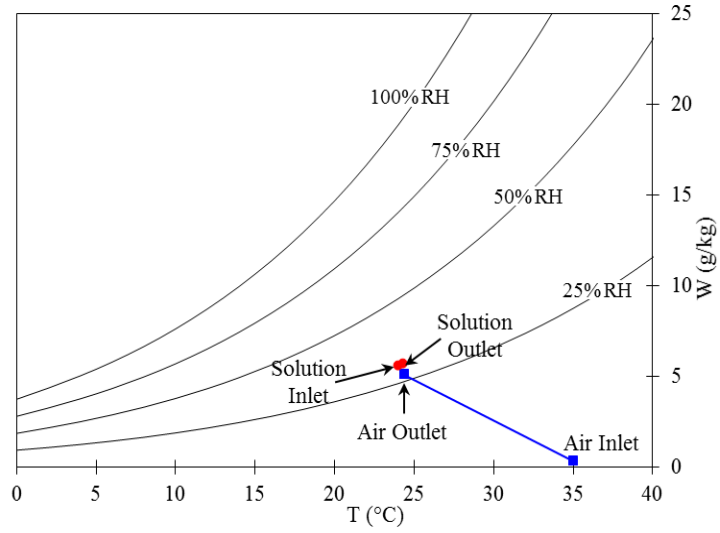
Figure 4.5 Experimental air and solution inlet and outlet conditions for the C&H test conditions at *NTU* = 3 and *Cr** = 5 with LiCl salt solution
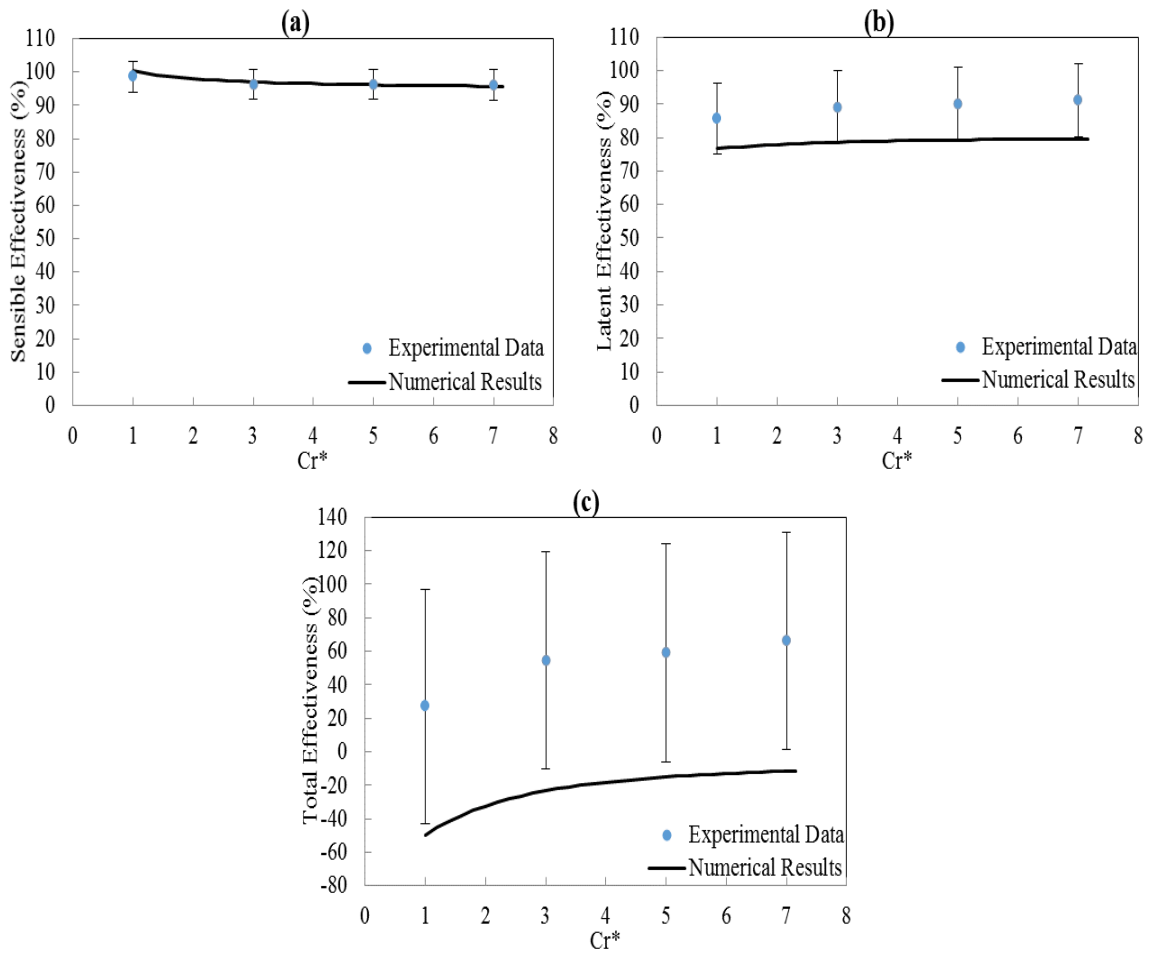
Figure 4.6 Experimental and numerical small-scale LAMEE (a) sensible, (b) latent, and (c) total effectiveness for the C&H test conditions at *NTU* = 3 and variable *Cr** with LiCl salt solution

4.8.1.3 Air Heating and Dehumidifying (H&D)

In this case, cold and humid air is supplied to the LAMEE and it is heated and dehumidified through the exchanger. It demonstrates the performance of the LAMEE in cold and humid climates, when the heat transfer direction is from the solution side to the air but, the mass transfer direction is reverse, and it is from the air to the solution side. The measured air and solution inlet and outlet conditions for different Cr^* and $NTU = 3$ are presented in Table 4-5. The results shows that the same as C&H test case, this case is almost uncertain, and again the air and solution outlet conditions are close to the solution inlet. The numerical and experimental sensible, latent and total effectiveness of the small-scale LAMEE are depicted in Figure 4.7. Figure 4.7-a shows that the LAMEE sensible effectiveness decreases with increasing Cr^* in this test conditions. Moreover, the latent and total effectiveness of the LAMEE increase with Cr^* in Figure 4.7. Also, Figure 4.7-b shows good agreement between the numerical and experimental latent effectiveness of the LAMEE. The maximum total effectiveness of 98% is reported for the small-scale LAMEE in Figure 4.7-c at $Cr^* = 7$ with 21% uncertainty in effectiveness.
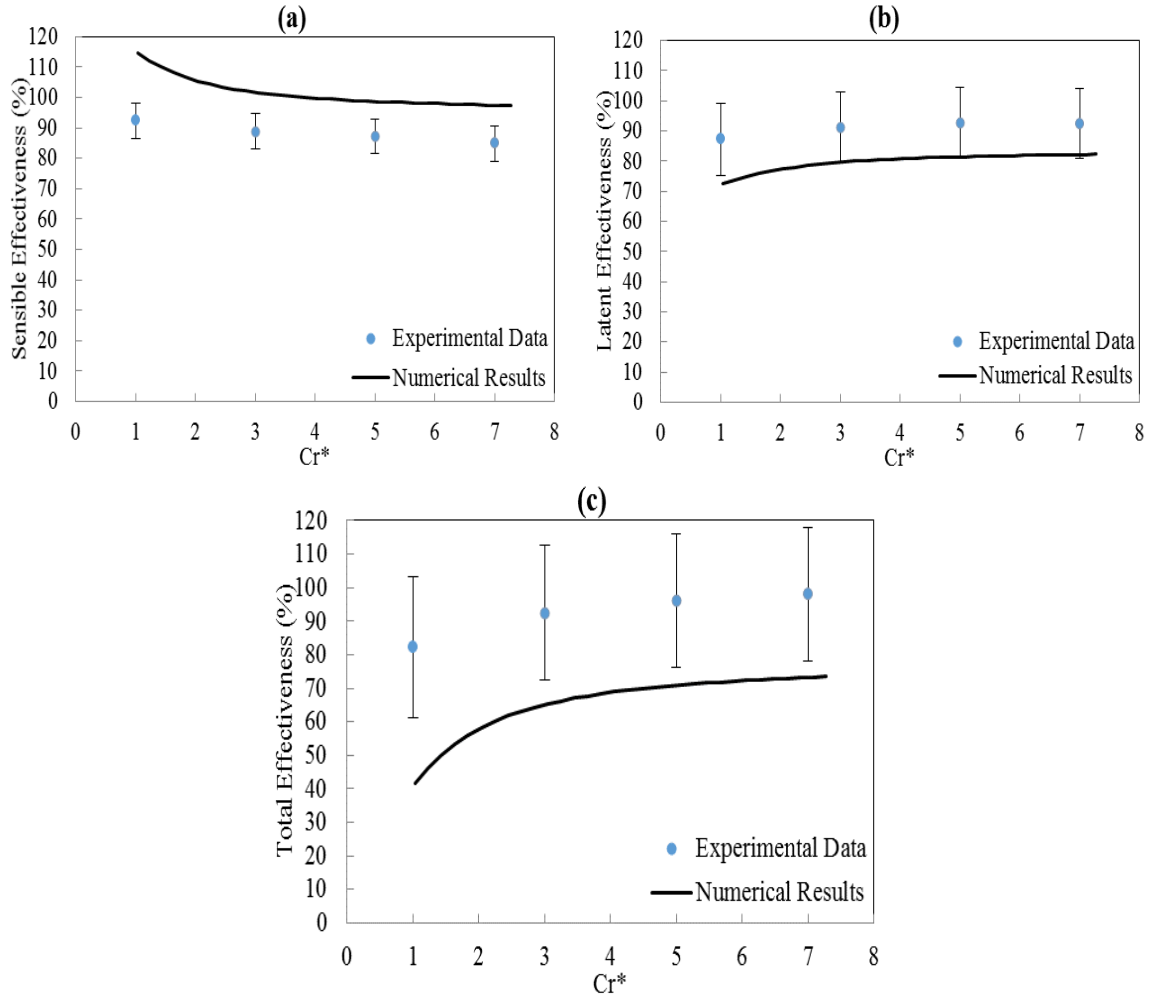
Figure 4.7 Experimental and numerical small-scale LAMEE (a) sensible, (b) latent, and (c) total effectiveness for the H&D test conditions at $NTU = 3$ and variable Cr^* with LiCl salt solution

4.8.1.4 Air Heating and Humidifying (H&H)

This test condition represents the performance of the small-scale LAMEE for cold and dry climates. The air is heated and humidified through the exchanger and both heat and mass transfer directions are from the solution side to the air. The measured air and solution inlet and outlet conditions are presented in Table 4-5. The experimental and numerical effectiveness of the LAMEE are shown in Figure 4.8. The sensible, latent and total effectiveness of the LAMEE increase with Cr^*. Also, the numerical model predicts higher performance for sensible effectiveness in comparison to the experimental data, but

122

it predicts lower performance for the LAMEE latent effectiveness. The main reasons to have lower numerical effectiveness results in comparison to the experimental data are discussed before. Also, Figure 4.8-b and Figure 4.8-c show good agreement between the numerical and experimental latent and total effectiveness results, and the maximum total effectiveness of 78% is achieved at $Cr* = 7$ with less than 10% uncertainty in total effectiveness.
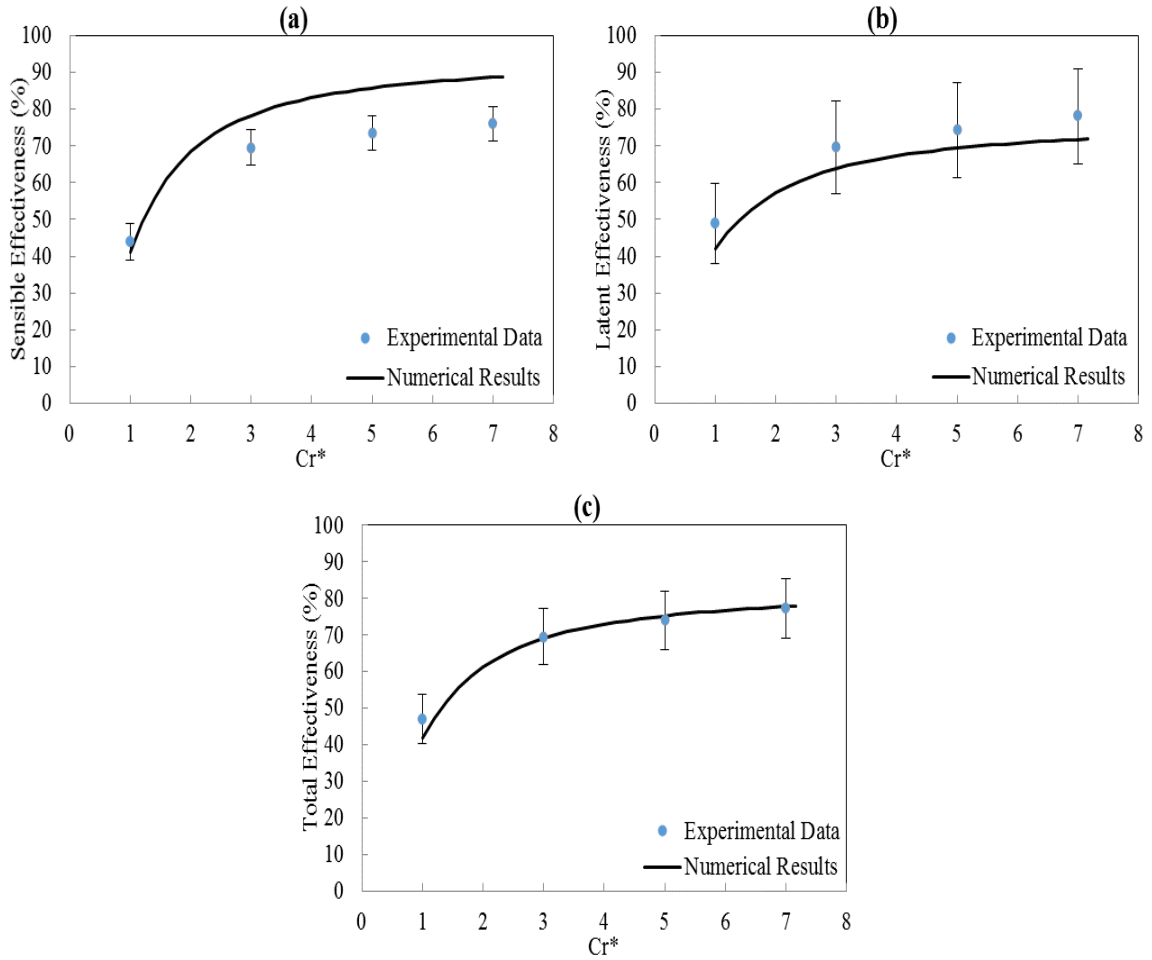
Figure 4.8 Experimental and numerical small-scale LAMEE (a) sensible, (b) latent, and (c) total effectiveness for the H&H test conditions at *NTU* = 3 and variable *Cr** with LiCl salt solution

4.8.2 Effect of Different Salt Solution Types and Concentrations

The effect of different salt solution types and concentrations is investigated for the air C&D test conditions on the steady-state performance of the small-scale LAMEE. The air inlet conditions are set at summer AHRI conditions for these experiments. The experiments are conducted at four different Cr^* and $NTU = 3$ which is the same as other cases and the small-scale LAMEE effectivenesses are plotted versus Cr^* for all tests. LiCl and $MgCl_2$ are used as salt solutions in the system and three different salt concentrations are tested for LiCl in this section. The measured solution inlet and air and solution outlet conditions for LiCl and $MgCl_2$ salt solutions are presented in Table 4-6. The air and solution outlet conditions for LiCl at 35% concentration are presented before in Table 4-5 for the C&D test case. Figure 4.9 shows the air and solution inlet and outlet conditions for all solution types and concentrations at $NTU = 3$ and $Cr^* = 5$ on the psychrometric chart. The air inlet conditions are the same for all tests (i.e. summer AHRI conditions) and the solution inlet conditions are set based on the information in Table 4-6. According to Figure 4.9, air and solution outlet conditions for different tests are almost at the same temperature, but the air and solution outlet humidity ratios increase while the salt solution concentration decreases.

Table 4-6 Measured air and solution inlet and outlet conditions for the different salt solution types and concentrations tests for the C&D test conditions at *NTU* = 3 and different *Cr**

Solution Type	Cr^*	Solution Inlet Conditions			Outlet Conditions				
		$T_{sol,in}$ (°C)	$C_{sol,in}$ (%)	$W_{sol,in}$ (g/kg)	$T_{air,out}$ (°C)	$W_{air,out}$ (g/kg)	$T_{sol,out}$ (°C)	$C_{sol,out}$ (%)	$W_{sol,out}$ (g/kg)
LiCl ($C_{sol,in}$ = 25%)	1	24	25	10.5	28.6	15.7	33.6	24.80	18.9
	3	24	25	10.5	26.4	13.3	31.0	24.88	16.1
	5	24	25	10.5	25.7	12.5	28.9	24.91	14.2
	7	24	25	10.5	25.4	12.2	27.9	24.94	13.3
LiCl ($C_{sol,in}$ = 30%)	1	24	30	7.82	30.0	13.8	36.6	29.57	17.2
	3	24	30	7.82	27.0	11.1	33.8	29.67	14.6
	5	24	30	7.82	26.0	10.2	31.0	29.78	12.2
	7	24	30	7.82	25.7	9.91	29.1	29.83	10.6
MgCl$_2$ ($C_{sol,in}$ = 35.8%)	1	24	35.8	7.81	29.5	12.5	37.3	35.36	17.8
	3	24	35.8	7.81	26.4	10.0	33.3	35.51	13.9
	5	24	35.8	7.81	25.6	9.22	30.3	35.63	11.6
	7	24	35.8	7.81	25.4	9.12	29.5	35.75	11.0
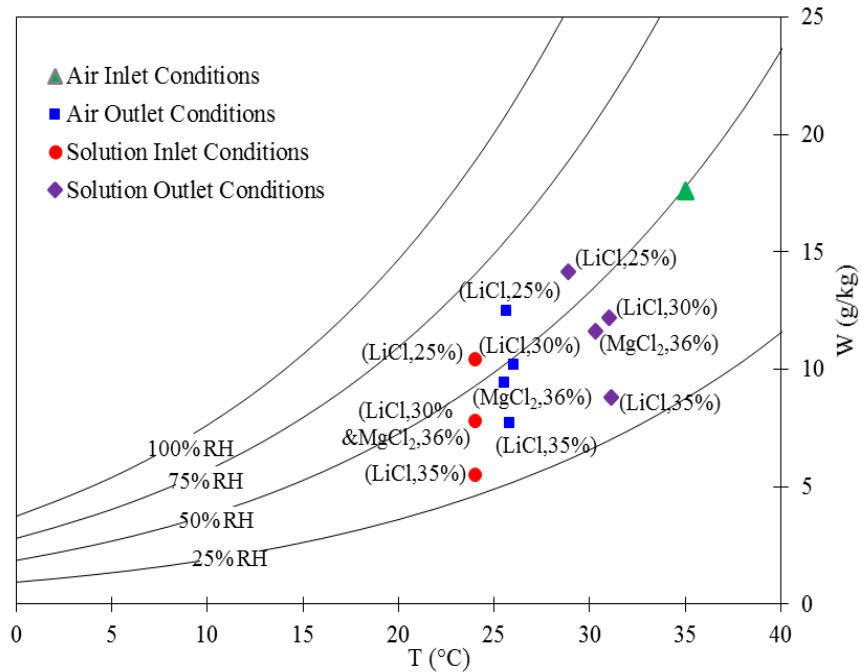
Figure 4.9 Experimental air and solution inlet and outlet conditions comparison between the different salt solution types (i.e. LiCl and MgCl₂) and concentrations for the C&D test conditions at *NTU* = 3 and *Cr** = 5

125

Figure 4.10 shows the experimental sensible, latent and total effectiveness of the small-scale LAMEE with different salt solution types and concentrations. The effectiveness uncertainties are presented only for $MgCl_2$ results, because the effectiveness uncertainties for different salt solution types and concentrations are almost the same at each $Cr*$. The LAMEE effectiveness always increase with $Cr*$ for the different solution types and concentrations at the C&D test conditions. Also, Figure 4.10-a shows that different salt solution types and concentrations do not have a significant effect on the sensible effectiveness, while the latent and total effectivenesses increase with concentration for all $Cr*$ values. There is almost 10% difference between the LAMEE total effectiveness for LiCl salt solution with 25% and 35% concentrations at $Cr* = 1$. Moreover, the experimental latent and total effectiveness of the LAMEE with $MgCl_2$ salt solution are close to the results for LiCl salt solution with 35% concentration. However, the numerical model shows good agreement between the effectiveness results for $MgCl_2$ and LiCl with 30% concentration, which has the same inlet solution temperature and humidity ratio as $MgCl_2$.

Based on the experimental results in this section, using LiCl or $MgCl_2$ at the same concentration does not have a significant effect on LAMEE effectiveness. The price of LiCl salt is slightly higher than $MgCl_2$ depending on the salt purity. However, the saturated LiCl concentration is higher than $MgCl_2$ which makes it more applicable in liquid-to-air membrane energy exchangers because of the salt solution crystallization that might happen in the solution side of the exchanger (Afshin, 2010). Moreover, using a more concentrated salt solution (i.e. 35% concentration) in the LAMEE resulted in higher latent and total effectiveness. Consequently, using more concentrated salt (i.e. 30% to

35%) is suggested in membrane based energy exchanger. However, the saturated salt solution concentration should be considered, especially for $MgCl_2$ while manufacturers want to choose the operating salt solution concentration for their exchanger to avoid any possible crystallization in the exchanger. Finally, the results in this section show that although changing the salt solution type and concentration has an effect on the steady-state LAMEE system performance, it is an effective way to control the supply air outlet humidity ratio, which is an important factor for air conditioning systems.
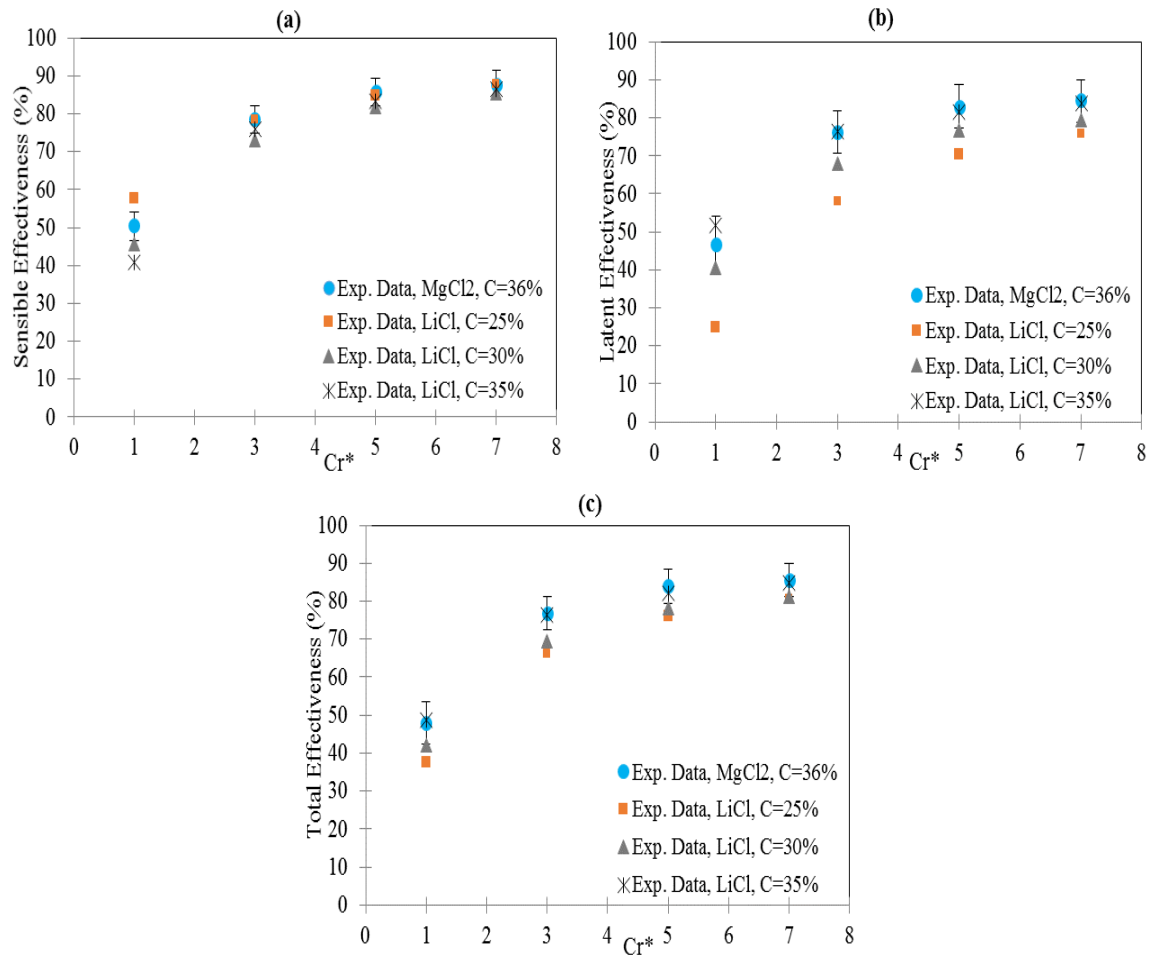
Figure 4.10 Experimental LAMEE (a) sensible, (b) latent, and (c) total effectiveness comparison between the different salt solution types and concentrations for the C&D test conditions at *NTU* = 3 and variable *Cr**

4.9 Conclusions

In chapter 4, the effect of different heat and mass transfer directions, and the effect of different salt solution types and concentrations are experimentally and numerically investigated on the steady-state performance of a LAMEE by using the SPEET facility. All the tests have been conducted at $NTU = 3$ and four different $Cr^* = 1$, 3, 5, 7. The mass and energy balances for all test cases, and the repeatability of the test facility for the air C&D test conditions are studied. The results show that the experimental data are repeatable within acceptable uncertainty range that is smaller than the effectiveness uncertainty for each test. The maximum EEI for the C&D test case is found to be 0.02, and it is 0.04 for the worst case which is the C&H test case.

The effect of different heat and mass transfer directions is investigated for four different test cases: 1) air cooling and dehumidifying (C&D), 2) air cooling and humidifying (C&H), 3) air heating and dehumidifying (H&D), and 4) air heating and humidifying (H&H). The results show good agreement between the numerical and experimental results for the C&D and H&H test cases. The C&H and H&D test cases represent greater uncertain conditions for the LAMEE system. The latent and total effectiveness of the LAMEE increases with Cr^*, while the sensible effectiveness only increases with Cr^* for the C&D and H&H test cases. For the other two test cases, the sensible effectiveness is decreasing with increasing Cr^*. Maximum total effectiveness of 98% with 21% uncertainty is obtained for the H&D test case at $NTU = 3$ and $Cr^* = 7$. Also, maximum total effectiveness of 85% is obtained for the small-scale LAMEE under summer AHRI test conditions (i.e. the C&D test case).

The effect of different salt solution types and concentrations is investigated for the steady-state performance of the small-scale LAMEE under summer AHRI conditions. LiCl and $MgCl_2$ salt solutions and three different concentrations for LiCl ($C = 25\%$, 30% and 35%) are used for this purpose. The results show that the sensible effectiveness is not sensitive to the salt solution type and concentration, but the latent and total effectiveness increase with salt solution concentration. A maximum of 10% difference is obtained for the LAMEE total effectiveness with different salt solution concentrations at $Cr* = 1$. Using different salt solution types and concentrations have effect on the LAMEE effectiveness and it is an effective method to control the supply air humidity ratio.

CHAPTER 5

NUMERICAL MODELING OF THE SMALL-SCALE LAMEE

5.1   Overview of Chapter 5

Coupled heat and mass transfer on the air-side, solution-side and in the membrane of the small-scale LAMEE are modeled in this chapter to numerically evaluate the steady-state performance of the small-scale LAMEE under different operating conditions. This chapter contains Manuscript #4 (Numerical model of a small-scale liquid-to-air membrane energy exchanger: parametric study of membrane resistance and air side convective heat transfer coefficient). The effect of membrane vapor diffusion resistance (VDR) and air-side convective heat transfer coefficient on the steady-state performance of the small-scale LAMEE under air cooling and dehumidifying test conditions are investigated in this chapter as these parameters have significant effects on the performance of LAMEEs. The membrane VDR plays an important role in the latent effectiveness of a LAMEE system. Also, there is an air screen in the air-channel of the small-scale LAMEE which is used to support the membrane, and enhance the heat and mass transfer performance in the air side of the LAMEE. Finally, the small-scale LAMEE numerical results are verified with the experimental data for summer test conditions (i.e. air cooling and dehumidifying and air cooling and humidifying test conditions), which were presented in Chapter 4, and the numerical results for the small-scale LAMEE performance are compared with the experimental data under winter test

conditions (i.e. air heating and dehumidifying and air heating and humidifying test conditions). This chapter is the third step of the methodology (see section 1.3.6) for LAMEEs which develops the coupled heat and mass transfer equations in the air, solution and membrane of a LAMEE. These equations are nondimensionalized in this chapter to derive important dimensionless parameters affecting the performance of the LAMEE. References for this chapter, which contains Manuscript #4, are presented in the reference section of the thesis (see page 215) which includes all the references used in this PhD thesis.

One Masters student (Mr. Ashkan Oghabi) and one postdoctoral fellow (Dr. Gaoming Ge) were involved in Manuscript #4. Mr. Oghabi's contribution to this paper is: testing the air-screen in a wind tunnel energy exchanger insert test (WEIT) facility at different air velocities, and calculating the enhanced air-side convective heat transfer coefficient for each case. Dr. Ge gave me useful advice during my PhD research project and critically reviewed Manuscript #4. Thus, I added him to this paper as an author to appreciate his help. My contributions to the manuscript #4 are: (a) developing the coupled heat and mass transfer equations for the air, solution and membrane of the LAMEE, and present them in a dimensionless form, (b) modify the base numerical model that we have in our research group for LAMEEs based on the small-scale LAMEE design and specifications, (c) testing different membranes in Permatran 101-K device and calculate their VDR, and comparing the VDR results for these membranes with other methods, (d) comparing the small-scale LAMEE numerical effectiveness results with the experimental data for summer and winter test conditions, and (e) writing the paper and replying to reviewers comments.

Numerical Model of a Small-Scale Liquid-to-Air Membrane Energy Exchanger:

Parametric Study of Membrane Resistance and Air Side Convective Heat Transfer

Coefficient

Davood Ghadiri Moghaddam, Ashkan Oghabi, Gaoming Ge, Robert W. Besant, Carey J.

Simonson

5.2 Abstract

A small-scale single-panel liquid-to-air membrane energy exchanger (LAMEE) is a novel membrane-based energy exchanger that allows heat and moisture transfer between a supply air stream and a salt solution flow through a semi-permeable membrane. In this chapter, the steady-state effectiveness of the small-scale single-panel LAMEE is experimentally measured and numerically modeled. The numerical model is compared with the experimental data for summer and winter test conditions. Parameters investigated using the numerical model include membrane vapor diffusion resistance (VDR) and air side convective heat transfer coefficient. The membrane VDR in the small-scale LAMEE is measured and the effect of this parameter is studied for the steady-state effectiveness. Decreasing the membrane VDR from 56 s/m to 24 s/m increases the LAMEE latent effectiveness by 11%, and as expected, it does not have any effect on the LAMEE sensible effectiveness. Enhanced convective heat transfer coefficient in the air flow of the small-scale LAMEE is calculated, and the effect of this parameter on the LAMEE effectiveness is investigated. The results show 138% improvement in the convective heat transfer coefficient in the air channel of the LAMEE with an air screen at $Re_{air} = 1570$ which results in 11% improvement in the LAMEE effectiveness. Finally, the

modified numerical model is validated by the experimental data for the steady-state effectiveness of the small-scale LAMEE under summer test conditions at four different values of the thermal capacity ratio ($Cr^* = 1, 3, 5$ and 7) and $NTU = 3.8$. Moreover, the numerical model is used for winter test conditions, and the results are compared with the experimental data. The results show that the numerical model agrees with the experimental data for the latent and total effectiveness of the LAMEE under the air heating and humidifying and air heating and dehumidifying test conditions.

Keywords: Small-scale exchangers, LAMEE, Numerical model, dimensionless parameters, membrane vapor diffusion resistance, and convective heat transfer coefficient.

5.3 Introduction

Liquid-to-air membrane energy exchangers (LAMEEs) have been investigated over the last decade (Zhang, 2011a; Bergero *et al.*, 2000; Fan *et al.* 2006; Ghadiri Moghaddam *et al.*, 2013b). Membrane energy exchangers transfer heat and moisture between an air stream and a salt solution flow through a semi-permeable membrane which is permeable for water vapor but impermeable for liquid water. The air and salt solution are in indirect contact within these exchangers which makes them useful for a wide range of applications (e.g. residential buildings, office buildings, hospitals and medical clinics). One main application of this kind of exchanger is expected to be in hot and humid climates where the supply air needs to be cooled and dehumidified. Several papers have been presented to numerically model coupled heat and mass transfer in liquid-to-air membrane energy exchangers for the air flow, salt solution flow and the membrane.

Zhang (2011a) introduced an analytical model to estimate the performance of a hollow fiber membrane contactor under air cooling and dehumidification conditions. This analytical model was based on dimensionless differential equations in the contactor and the results were validated by experimental data for selected test conditions. The results showed that the analytical model was reliable for the performance prediction of the hollow fiber membrane contactor. Also, Zhang and Huang (2011) and Zhang (2012) investigated the coupled heat and mass transfer in counter-flow and cross-flow hollow fiber membrane module for air humidification using water, respectively, using a mathematical model. In Zhang (2012), a shell and tube cross-flow contactor was used where the shell was like a rectangular box to reduce the pressure drop in hollow fiber membrane contactors. The effect of fiber tubes packing density and geometry of fiber packing arrangement were investigated on the performance of the cross-flow contactor as the main sources of air flow maldistribution in hollow fiber membrane contactors. The results showed that the fiber tubes packing density has a dominant effect on the performance of the contactor. As well, Zhang *et al.* (2012a; 2012b) used a free surface model for a single fiber tube to solve the conjugate heat and mass transfer in a counter-flow and cross-flow hollow fiber membrane contactors for air dehumidification, respectively. The air and solution convective heat and mass transfer coefficients were calculated for the air and solution sides of the hollow fiber membrane contactor and experimentally validated for selected test conditions.

Bergero *et al.* (2000) investigated the steady-state performance of a cross-flow plane-plate membrane contactor using a two dimensional theoretical model. The coupled heat and mass transfer in the exchanger was solved numerically for the air and salt

solution flows. The model results were compared with selected test conditions experimental data for this membrane contactor. Bergero and Chiari (2010; 2011) investigated a hybrid air conditioning system where a plate desiccant-to-air membrane dehumidifier coupled with a vapor-compression heat pump to replace a traditional air dehumidification system where the air is cooled below its dew-point temperature. The SIMULINK software was used to simulate the performance of this hybrid system using the same mathematical model as Bergero *et al.* (2000) to simulate the membrane contactor in the system. The results showed that the hybrid air conditioning system could save up to 50% more energy in comparison to traditional system for supply air dehumidification conditions. In Bergero *et al.* (2000), Bergero and Chiari (2010) and Bergero and Chiari (2011) the air and solution side convective heat transfer coefficients were calculated based on laminar flow in the air and solution channels of the plane-plate membrane contactor. Huang *et al.* (2012) numerically investigated the coupled heat and mass transfer in a cross-flow plane-plate liquid-to-air membrane energy exchanger used for air dehumidification. They assumed an ideal smooth channel for air and solution sides of the exchanger, while the air and solution were assumed to be hydrodynamically fully developed but thermally developing. The actual Nusselt and Sherwood numbers for the air and solution were numerically calculated for smooth channels, and the results were compared with experimental data where good agreement was achieved.

Fan *et al.* (2006) numerically simulated the steady-state performance of a run-around membrane energy exchanger (RAMEE) under AHRI summer and winter test conditions (ANSI/AHRI Standard 1060, 2011). This RAMEE had two cross-flow liquid-to-air membrane energy exchangers (LAMEEs) coupled together in a closed liquid

solution loop. A finite difference model was used to solve the dimensionless water vapor and energy transfer equations for the air and LiBr salt solution in two cross-flow LAMEEs. The overall effectiveness of 70% was obtained for this RAMEE system. Seyed-Ahmadi *et al.* (2009a; 2009b) presented a numerical model to simulate the transient performance of a similar RAMEE system using the finite difference method to solve the coupled heat and mass transfer equations for the air and solution sides of those two cross-flow LAMEEs with an implicate time discretization. Solution storage tanks volume, solution pumps and heat loss/gain to/from surroundings were also considered in this numerical model. The numerical results were compared with experimental data for the RAMEE system. The same numerical model was used by Erb *et al.* (2009), and the numerical results were compared to experimental data for a RAMEE system with two cross-flow LAMEEs using a $MgCl_2$ solution loop. Vali *et al.* (2009) developed a two dimensional numerical model to investigate the steady-state performance of a RAMEE system consist of two LAMEEs with counter-cross flow configuration for the air and salt solution. A finite difference method was used to solve the dimensionless continuity, momentum and heat and mass transfer equations for this counter-cross flow LAMEE. The results showed that the performance of the counter-cross flow LAMEE is between the counter-flow and cross-flow LAMEEs. Hemingson *et al.* (2011b) used the same numerical model to calculate the steady-state performance of a RAMEE system under a wide range of outdoor air conditions. This RAMEE system was subdivided into four cases based on the effect of heat and mass transfer on the system performance. Ge *et al.* (2012) used Zhang's analytical model (Zhang, 2011a) to evaluate the performance of a counter-flow LAMEE. These modified analytical results were compared with

experimental results for a single-panel LAMEE and a RAMEE system under different operating conditions and good agreement was obtained. The analytical model was used to evaluate the performance of a RAMEE under balanced and unbalanced air flow conditions to optimize the exchanger size and solution flow rate. Akbari *et al.* (2012a; 2012b) developed a neural network (NN) model to predict the steady-state and transient performance of a RAMEE system for a wide range of operating and design parameters. The NN model results were compared with the validated steady-state and transient numerical models (Seyed-Ahmadi *et al.*, 2009a; Seyed-Ahmadi *et al.*, 2009b; Erb *et al.*, 2009) and good agreement was obtained. The NN model is fast and easy to use and can be used to optimize the RAMEE design and operating parameters. In Fan *et al.* (2006), Seyed-Ahmadi *et al.* (2009a), Seyed-Ahmadi *et al.* (2009b), Erb *et al.* (2009) and Ge *et al.* (2012), the laminar flow was assumed for both the air and solution in air and solution channels of a LAMEE, and the air and solution convective heat transfer coefficients were calculated based on this assumption. Also, a mal-distribution due to membrane bulging in a LAMEE and high uncertainty for measured membrane vapor diffusion resistance (VDR) due to inaccurate measurement of the membrane VDR were reported as other sources of discrepancy for the numerical model in literature.

Recently, Ghadiri Moghaddam *et al.* (2013a; 2013b) used a single-panel energy exchanger test (SPEET) facility to evaluate the performance of a novel small-scale single-panel LAMEE for different operating conditions. The LAMEE numerical model which was used in the RAMEE numerical models (Seyed-Ahmadi *et al.*, 2009a; Seyed-Ahmadi *et al.*, 2009b; Erb *et al.*, 2009; Vali *et al.*, 2009) was modified based on the new small-scale LAMEE design, and the numerical results were compared with the

137

experimental data. Preliminary results for the SPEET facility were presented in Ghadiri Moghaddam *et al.* (2013b) using water as a transfer liquid in the LAMEE. Also, the effects of different heat and mass transfer directions and salt solution types and concentrations on the LAMEE effectiveness were evaluated with the SPEET facility using LiCl and $MgCl_2$ solutions (Ghadiri Moghaddam *et al.*, 2013a). Only for few cases there was agreement between the numerical and experimental results. Ge *et al.* (2014) experimentally investigated the effect of different operating parameters (i.e. air inlet temperature and humidity, solution inlet temperature and concentration, and air and solution inlet flow rates) on the performance of a small-scale LAMEE used as a dehumidifier and regenerator in an air-conditioning system. The analytical model (Ge *et al.*, 2012) was compared with the experimental data for a counter-cross flow LAMEE for both dehumidification and regeneration applications. Again, the laminar flow assumption for the air side of the small-scale LAMEE to calculate the air convective heat transfer coefficient and inaccurate measurement for the membrane VDR were reported as main sources of uncertainty for the numerical model of the small-scale LAMEE in Ghadiri Moghaddam *et al.* (2013a), Ghadiri Moghaddam *et al.* (2013b) and Ge *et al.* (2014).

In this chapter, the coupled heat and mass transfer in the air, solution and membrane of a small-scale single-panel LAMEE are numerically modeled to calculate the steady-state effectiveness of the small-scale LAMEE under different operating conditions. Also, the effects of the membrane VDR and enhanced air convective heat transfer coefficient are numerically investigated for the steady-state effectiveness of the LAMEE under air cooling and dehumidification conditions using the modified numerical model for the small-scale single-panel LAMEE. Moreover, the steady-state numerical

effectiveness of the small-scale LAMEE is validated by experimental data for summer test conditions (i.e. air cooling and dehumidification and air cooling and humidification). The same numerical model is used to simulate the effectiveness of the small-scale LAMEE under winter test conditions (i.e. air heating and dehumidifying and air heating and humidifying), and the agreement between the numerical results and experimental data are studied for these test conditions.

5.4   Experimental Data

The single-panel energy exchanger test (SPEET) facility is designed to test a small-scale LAMEE with a supply air volume flow rates up to 5 cfm with details given in Ghadiri Moghaddam *et al.* (2013b). In this test facility, a compressor and an air drier are used to supply a dry air (~4%RH) to the facility. The air passes through a flow controller, two bubble air humidifiers and a heater to adjust the air inlet flow rate, temperature and humidity to the desire test conditions. T-type thermocouples and relative humidity sensors are used to measure the air temperature and humidity in the LAMEE air inlet and air outlet headers with the uncertainties of 0.2ºC and 1.5%RH, respectively. Finally, the air passes through the LAMEE and is exhausted into the Lab. The LiCl solution flows in an open solution loop, where a peristaltic pump is used to pump the solution from a supply solution tank into the small-scale LAMEE. The inlet and outlet solution temperatures are measured using shielded T-type thermocouples at the solution inlet and outlet headers, and a density meter device is used to measure the salt solution concentration at those locations. The solution passes through the LAMEE and is collected in a solution exhaust tank. The small-scale LAMEE with the counter-cross flow configuration is located in the test section of the SPEET facility where the air and

solution pass through the LAMEE and the heat and moisture transfer through the membrane between the air and LiCl salt solution. The details of the small-scale single-panel LAMEE design, the SPEET facility schematic and the mass and energy balance results of the facility are presented in Ghadiri Moghaddam *et al.* (2013a). A schematic and the detailed cross section view of the small-scale single-panel LAMEE are presented in Figure 5.1. Table 5-1 presents membrane properties and the design specifications of the small-scale LAMEE.
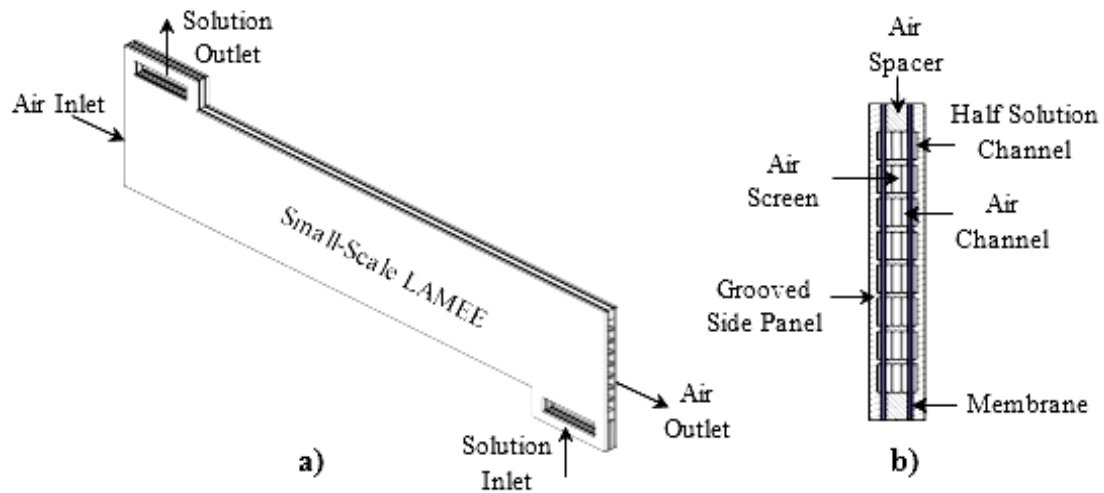
Figure 5.1 The small-scale single-panel LAMEE a) air and solution flow configuration, and b) cross-section detailed view (Ghadiri Moghaddam *et al.*, 2013b)

Experimental data which are compared to the numerical model for the steady-state performance of a counter-cross flow small-scale single-panel LAMEE are presented in Ghadiri Moghaddam *et al.* (2013a) for different operating conditions (i.e. air cooling and dehumidification (C&D), air cooling and humidification (C&H), and heating and dehumidification (H&D), and air heating and humidification (H&H)). The small-scale single-panel LAMEE was tested in the SPEET facility for four different heat capacity ratios ($Cr^* = 1, 3, 5$ and 7) and one number of heat transfer unit ($NTU = 3$). The NTU value and numerical results which are presented in Ghadiri Moghaddam *et al.* (2013a) are

based on a laminar flow regime in the air and solution channels. The experimental test data and steady-state LAMEE effectiveness results which are used in this chapter are presented in Table 5-2.

Table 5-1 The small-scale single-panel LAMEE specifications and membrane properties

Parameter	value
Exchanger length, L_{ex} (m)	0.49
Exchanger aspect ratio, L_{ex}/H_{ex}	5.2
Exchanger entrance ratio, L_{sol}/L_{ex}	0.11
Air gap thickness, d_{air} (mm)	5
Solution gap thickness on each side panel, $d_{sol}/2$ (mm)	0.8
Number of solution paths on each side panel	8
Membrane thermal conductivity, k_{mem} (W/mK)	0.065
Membrane thickness, δ_{mem} (mm)	0.265

Table 5-2 Measured air and solution inlet and outlet conditions for the small-scale LAMEE at NTU = 3 and different Cr^* with LiCl salt solution under different operating conditions

Test Case	Cr^*	Inlet Conditions					Outlet Conditions					Results		
		$T_{air,in}$ (°C)	$W_{air,in}$ (g/kg)	$T_{sol,in}$ (°C)	$C_{sol,in}$ (%)	$W_{sol,in}$ (g/kg)	$T_{air,out}$ (°C)	$W_{air,out}$ (g/kg)	$T_{sol,out}$ (°C)	$C_{sol,out}$ (%)	$W_{sol,out}$ (g/kg)	ε_{sen} (%)	ε_{lat} (%)	ε_{tot} (%)
C&D	1	35	17.3	24	34.59	5.54	30.6	11.2	39.8	33.96	15.2	40.8	51.6	48.6
	3	35	17.4	24	34.59	5.54	26.6	8.31	34.2	34.24	10.8	76.2	76.6	76.5
	5	35	17.3	24	34.59	5.53	25.8	7.71	31.1	34.36	8.83	83.3	81.5	82.0
	7	35	17.3	24	34.59	5.54	25.5	7.43	29.2	34.43	7.80	86.6	84.0	84.7
C&H	1	35	0.33	24	34.36	5.65	24.2	4.89	25.0	34.68	5.88	98.6	85.7	27.0
	3	35	0.31	24	34.36	5.65	24.4	5.06	24.4	34.48	5.73	96.3	89.1	54.4
	5	35	0.33	24	34.36	5.65	24.4	5.11	24.3	34.43	5.72	96.3	90.1	59.2
	7	35	0.40	24	34.36	5.65	24.5	5.19	24.4	34.40	5.32	96.1	91.1	66.3
H&D	1	24	16.3	32	34.42	9.26	31.4	10.9	33.7	33.99	10.6	92.4	87.3	82.3
	3	24	16.5	32	34.42	9.26	31.1	10.3	33.5	34.22	10.3	88.9	91.2	92.6
	5	24	16.5	32	34.42	9.26	31.0	10.2	33.0	34.30	9.94	87.3	92.6	96.2
	7	24	16.6	32	34.42	9.26	30.8	10.1	32.8	34.33	9.76	84.8	92.6	98.0
H&H	1	24	3.60	32	34.37	9.31	27.5	6.39	23.0	34.58	5.21	43.9	48.9	47.1
	3	24	3.58	32	34.37	9.31	29.5	7.55	27.3	34.48	6.91	69.6	69.6	69.6
	5	24	3.51	32	34.37	9.31	29.9	7.79	28.9	34.44	7.68	73.6	74.3	74.1
	7	24	3.55	32	34.37	9.31	30.1	8.05	30.0	34.41	8.21	76.0	78.1	77.4

5.5   Numerical Model

The governing equations and dimensional analysis of a counter-flow small-scale single-panel LAMEE under steady-state operating conditions are presented in this section. A schematic of the small-scale LAMEE is shown in Figure 5.2 which is used for numerical modeling. Figure 5.2 shows that air and salt solution are flowing in the counter-flow configuration through parallel air and solution flow channels. There is one air channel in the middle of the small-scale LAMEE and two half solution channels on the sides to create the single-panel LAMEE. The LAMEE enclosure is well insulated from the surroundings. The air and solution channels are separated with the semi-permeable membrane, which allows heat and water vapor transfer between the air and solution, but prevents the solution liquid from penetrating into the air channel. The differential equations for the LAMEE are for the air and salt solution. Also, the boundary conditions for those equations are discussed. The following assumptions are used to model the steady-state performance of the small-scale LAMEE:

1. The exchanger is not well insulated, thus heat losses/gains to/from surroundings are considered in the numerical model.

2. The velocity and temperature of both fluids at the inlets of the exchanger are uniform over the flow cross section in the exchanger.

3. The flows are fully developed and thermal properties and convective heat and mass transfer coefficients of both fluids and membrane properties are constant along the entire exchanger (i.e. there is no undeveloped flow or mal-distributed flow) except the temperature dependent properties like the air conductivity. The mal-distribution problem is well controlled in the small-scale LAMEE since there

is only one air channel and an air screen is used in the air channel of the LAMEE to minimize the membrane deflection.

4. The membrane exchange area in the exchanger is uniformly distributed for both fluids.

5. Fouling due to air side frosting and salt solution crystallization in the exchanger are neglected.

6. Axial conduction in the air and salt solution is neglected (i.e. *Pe*>20 in the air and solution channels (Seyed-Ahmadi *et al.*, 2009a; Vali *et al.*, 2009)).

7. Phase change energy due to water vapor evaporation or condensation at the air-liquid interface occurs in the solution side since the solution convective heat and mass transfer coefficients and solution heat capacity are significantly higher than the air side. Also, the membrane is only permeable to water vapor.

8. Heat and mass transfers in the exchanger occur normal to the membrane surface in *z*-direction (see Figure 5.2) (Seyed-Ahmadi *et al.*, 2009a).
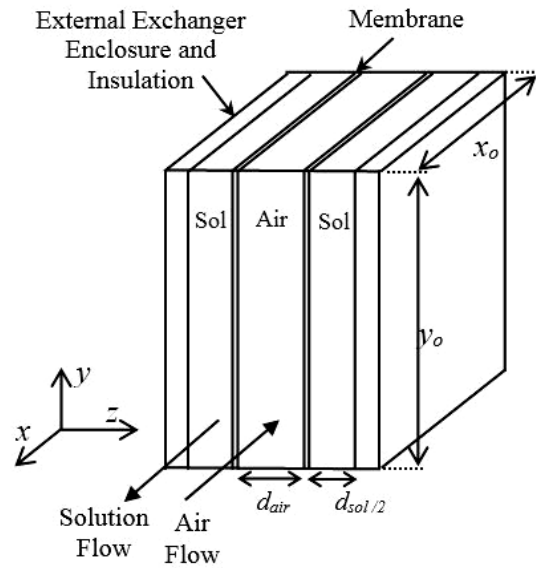
Figure 5.2 Schematic of a counter-flow small-scale single-panel LAMEE and system coordinates.

5.5.1   Solution Side Governing Equations

5.5.1.1 Mass Balance

Two half-solution channels are located on the sides of the small-scale LAMEE which are identical. Figure 5.3 shows the incremental control volume, which is used for mass balance in the solution side of the small-scale LAMEE. The following differential equation governs the mass balance of the water content in the solution channel:

$$\frac{\dot{m}_{salt}}{y_0}\frac{\mathrm{d}X_{sol}}{\mathrm{d}x}\mathrm{d}x\mathrm{d}y - U_m\left(W_{air} - W_{sol,mem}\right)\mathrm{d}x\mathrm{d}y = 0, \tag{5.1}$$

where $\dot{m}_{salt}$ and U_m are the salt mass flow rate and overall convective mass transfer coefficient, respectively and they defined as:

$$U_m = \left[\frac{1}{h_{m,air}} + \frac{\delta_{mem}}{k_{m,mem}}\right]^{-1} \tag{5.2}$$

$$\dot{m}_{salt} = \frac{\dot{m}_{sol}}{1 + X_{sol}} \tag{5.3}$$

$\dot{m}_{sol}$ is the solution flow rate in each half solution channel, and X_{sol} is the solution mass fraction and calculated as follows:

$$X_{sol} = \frac{\text{Mass of Water}}{\text{Mass of Salt}} \tag{5.4}$$

The salt solution concentration, C_{salt}, is calculated from the solution mass fraction.

$$C_{salt} = \frac{1}{1 + X_{sol}} \tag{5.5}$$

The following dimensionless parameters are used to nondimensionalize the mass balance equation in the solution side of the small-scale LAMEE:

$$\phi = \frac{W - W_{air,i}}{W_{sol,i} - W_{air,i}} \tag{5.6}$$

$$x^* = \frac{x}{x_0} \tag{5.7}$$

$$NTU_m = \frac{U_m A}{\dot{m}_{min}} = \frac{U_m A}{\dot{m}_{air}} \tag{5.8}$$

$$m^* = \frac{\dot{m}_{min}}{\dot{m}_{max}} = \frac{\dot{m}_{air}}{\dot{m}_{sol}} \tag{5.9}$$

Here ϕ and x^* are the dimensionless humidity content and dimensionless length in the LAMEE, respectively. Also, NTU_m and m^* are the number of mass transfer units and mass flow rate ratio, respectively when the thermal capacity ratio (Cr^*) is equal or greater than 1 (see Eq. (5.15)). The dimensionless form of the solution side mass balance equation is found by substituting Eqs. (5.6) to (5.9) into Eq. (5.1).

$$\frac{dX_{sol}}{dx^*} - W_0 NTU_m \, m^* \left(1 + X_{sol}\right)\left(\phi_{air} - \phi_{sol,mem}\right) = 0 \tag{5.10}$$

In Eq. (5.10), W_0 is equal to $(W_{sol,i} - W_{air,i})$.
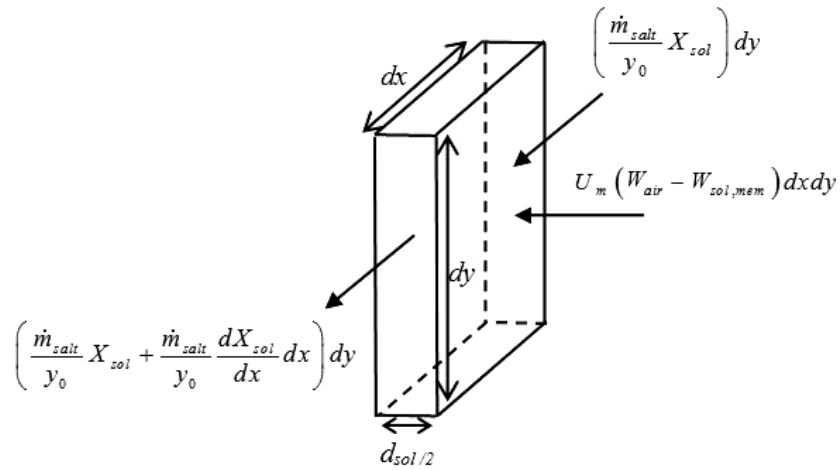
Figure 5.3 The incremental control volume used for the mass balance in the solution side of the small-scale LAMEE

145

5.5.1.2 Energy Balance

The control volume, which is used for the energy balance in the solution sides of the small-scale LAMEE, is shown in Figure 5.4. The following differential equation is governed based on the energy balance in the solution side of the small-scale LAMEE:

$$\frac{\dot{m}_{sol}}{y_0} c_{p,sol} \frac{dT_{sol}}{dx} dxdy - U_m h_{fg} \left(W_{air} - W_{sol,mem} \right) dxdy - U \left(T_{air} - T_{sol} \right) dxdy = 0 \quad (5.11)$$

The dimensionless form of Eq. (5.11) based on the dimensional analysis of the small-scale LAMEE is as follows:

$$\frac{d\theta_{sol}}{dx^*} - NTU_m H^* Cr \left(\phi_{air} - \phi_{sol,mem} \right) - NTU \; Cr \left(\theta_{air} - \theta_{sol} \right) = 0 \quad (5.12)$$

Here H^* is the operating factor, and is the ratio of maximum possible latent energy over the maximum possible sensible energy transfers between the air and salt solution in a LAMEE. Also, θ, NTU and Cr are dimensionless temperature, number of heat transfer units and thermal capacity ratio, respectively, and are determined as follows:

$$\theta = \frac{T - T_{air,i}}{T_{sol,i} - T_{air,i}} \quad (5.13)$$

$$NTU = \frac{UA}{C_{min}} = \frac{UA}{(\dot{m}c_P)_{air}} \quad (5.14)$$

$$Cr = \frac{C_{min}}{C_{max}} = \frac{(\dot{m}c_p)_{air}}{(\dot{m}c_p)_{sol}} = \frac{1}{Cr^*} \quad (5.15)$$

$$H^* = \frac{(W_{sol,i} - W_{air,i})}{(T_{sol,i} - T_{air,i})} \frac{h_{fg}}{c_{P,air}} \quad (5.16)$$

In the LAMEE the minimum heat capacity rate, C_{min}, is related to the air side of the LAMEE (Ghadiri Moghaddam *et al.*, 2013a). In Eq. (5.15), U is the overall heat transfer coefficient and defined as:

$$U = \left[\frac{1}{h_{air}} + \frac{\delta}{k_{mem}} + \frac{1}{h_{sol}} \right]^{-1} \tag{5.17}$$
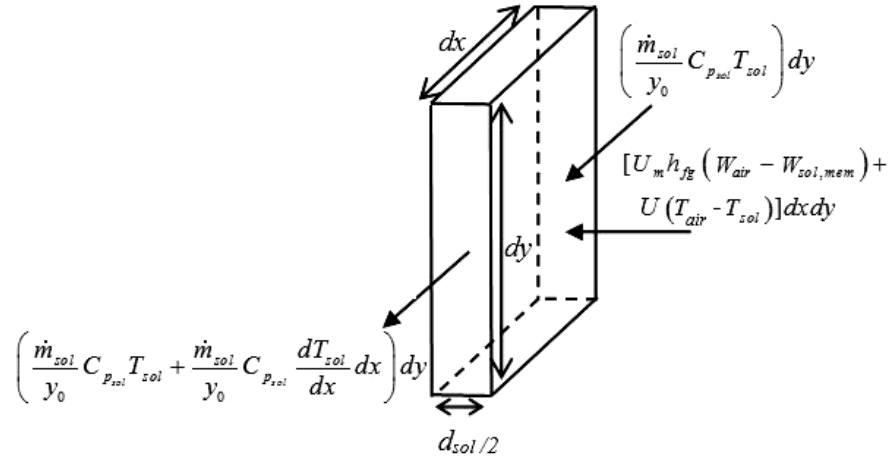
Figure 5.4 The incremental control volume used for the energy balance in the solution side of the small-scale LAMEE

5.5.2   Air Side Governing Equations

5.5.2.1 Mass Balance

The air channel is in the middle of the small-scale LAMEE and is in contact with the membrane on both sides of the channel where the heat and mass transfers occur between the air and solution. Figure 5.5 shows the incremental control volume, which is used for the water vapor mass balance in the air channel of the small-scale LAMEE. The mass diffusions in the x and y directions are neglected. The differential equation for the water vapor balance in the air side of the LAMEE is:

$$\frac{\dot{m}_{air}}{y_0} dxdy \frac{dW_{air}}{dx} + 2U_m \left(W_{air} - W_{sol,mem} \right) dxdy = 0 \tag{5.18}$$

where $W_{sol,mem}$ is the humidity content of the salt solution at the membrane-solution interface, and is calculated from the membrane mass and energy balance equations (see Section 5.5.3). Equation (5.18) is nondimensionalized by using Eqs. (5.6) to (5.8):

$$\frac{\mathrm{d}\phi_{air}}{\mathrm{d}x^*} + 2NTU_m \left(\phi_{air} - \phi_{sol,mem} \right) = 0 \tag{5.19}$$
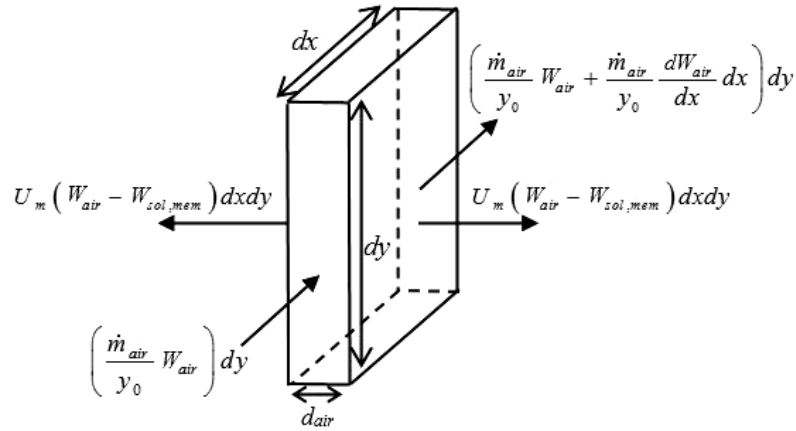
Figure 5.5 The incremental control volume used for the mass balance in the air side of the small-scale LAMEE

5.5.2.2 Energy Balance

The energy balance in the air channel of the LAMEE is presented in this section. For the air side of the LAMEE it was assumed that the heat diffusion is only in the z-direction. Figure 5.6 shows the energy transfers which occur in the air side of the small-scale LAMEE. The heat transfer differential equation for the air channel is found from the air side energy balance, and is as follows:

$$\frac{\dot{m}_{air}}{y_0} c_{p,air} \mathrm{d}x\mathrm{d}y \frac{\mathrm{d}T_{air}}{\mathrm{d}x} + 2U \left(T_{air} - T_{sol} \right) \mathrm{d}x\mathrm{d}y = 0 \tag{5.20}$$

The dimensionless form of the Eq. (5.20) is determined using Eqs. (5.7), (5.13) and (5.14):

$$\frac{\mathrm{d}\theta_{air}}{\mathrm{d}x^*} + 2NTU\left(\theta_{air} - \theta_{sol}\right) = 0 \tag{5.21}$$
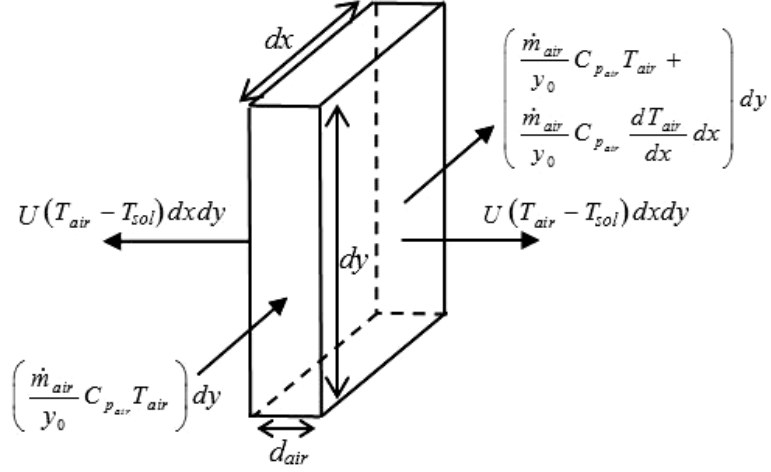
Figure 5.6 The incremental control volume used for the energy balance in the air side of the small-scale LAMEE

5.5.3 Membrane

The bulk properties of the air, solution and membrane are used to govern the differential equations for the air and salt solution in the small-scale LAMEE except the membrane humidity content ($W_{sol,mem}$) which occurs at the interface between the solution and the membrane (see Eqs. (5.10), (5.12) and (5.19)). The membrane humidity content can be calculated from the membrane temperature and solution mass fraction in the interface between the solution and the membrane ($T_{sol,mem}$ and $X_{sol,mem}$) (Cisternas and Lam, 1991). The membrane temperature and solution mass fraction on the solution side of the small-scale LAMEE are calculated from the heat and water vapor mass balance equations at the membrane-solution interface.

$$W_{sol,mem} = \text{Function}\left(T_{sol,mem}, X_{sol,mem}\right) \tag{5.22}$$

$$\frac{W_{air} - W_{sol,mem}}{\left(h_{m,air}\right)^{-1} + \left(\dfrac{k_{m,mem}}{\delta_{mem}}\right)^{-1}} = h_{m,sol}\left(\frac{1}{1+X_{sol}} - \frac{1}{1+X_{sol,mem}}\right) \qquad (5.23)$$

$$\frac{T_{air} - T_{sol,mem}}{\left(h_{air}\right)^{-1} + \left(\dfrac{k_{mem}}{\delta_{mem}}\right)^{-1}} + \frac{W_{air} - W_{sol,mem}}{\left(h_{m,air}\right)^{-1} + \left(\dfrac{k_{m,mem}}{\delta_{mem}}\right)^{-1}} h_{fg} = h_{sol}\left(T_{sol,mem} - T_{sol}\right) \qquad (5.24)$$

The dimensionless forms of the Eqs. (5.23) and (5.24) are found using Eqs. (5.5) to (5.9) and (5.13) to (5.16), and are as follows:

$$NTU_m\, W_0\left(\phi_{air} - \phi_{sol,mem}\right) = NTU_{m,sol}\left(C_{salt} - C_{salt,mem}\right) \qquad (5.25)$$

$$NTU\left(\theta_{air} - \theta_{sol,mem}\right) + NTU_m H^*\left(\phi_{air} - \phi_{sol,mem}\right) = NTU_{sol}\left(\theta_{sol,mem} - \theta_{sol}\right) \qquad (5.26)$$

Here, NTU_{sol} and $NTU_{m,sol}$ are the solution side number of heat and mass transfer units, respectively, and defined as follows:

$$NTU_{sol} = \frac{h_{sol}A}{\left(\dot{m}c_P\right)_{\min}} = \frac{h_{sol}A}{\left(\dot{m}c_P\right)_{air}} \qquad (5.27)$$

$$NTU_{m,sol} = \frac{h_{m,sol}A}{\dot{m}_{\min}} = \frac{h_{m,sol}A}{\dot{m}_{air}} \qquad (5.28)$$

Equations (5.25) and (5.26) should solve iteratively to find the solution humidity content at the membrane-solution interface.

5.5.4 Boundary Conditions

The dimensionless differential equations, those involved in the steady-state operation of the small-scale LAMEE, are Eqs. (5.10), (5.12), (5.19) and (5.21). The boundary conditions, which are required to solve the above differential equations, are determined as follows:

$$X_{sol} = X_{sol,i} \text{ at } x = 0$$
$$T_{sol} = T_{sol,i} \text{ at } x = 0$$
$$W_{air} = W_{air,i} \text{ at } x = x_0 \qquad (5.29)$$
$$T_{air} = T_{air,i} \text{ at } x = x_0$$

The dimensionless forms of the above boundary conditions are as follows, respectively:

$$X_{sol}\left(x^* = 0\right) = X_{sol,i}$$
$$\theta_{sol}\left(x^* = 0\right) = 1$$
$$\phi_{air}\left(x^* = 1\right) = 0 \qquad (5.30)$$
$$\theta_{air}\left(x^* = 1\right) = 0$$

To solve Eqs. (5.25) and (5.26) for humidity content of the solution on the membrane surface, the following conditions are be used for the initial iteration.

$$X_{sol,mem} = X_{sol,i} \text{ at } x = 0$$
$$T_{sol,mem} = T_{sol,i} \text{ at } x = 0 \qquad (5.31)$$

These are nondimensionalized to the following forms:

$$C_{salt,mem}\left(x^* = 0\right) = C_{salt,i}$$
$$\theta_{sol,mem}\left(x^* = 0\right) = 1 \qquad (5.32)$$

5.5.5 Performance Evaluation of a LAMEE

The performance of a LAMEE is evaluated by its sensible, latent and total effectiveness. Sensible and latent effectiveness are defined as sensible (heat) and latent (moisture) energy transferred in the system over the maximum possible sensible and latent energy transfer in the exchanger, respectively. Sensible and latent effectiveness are calculated for a LAMEE system by the following equation when $Cr^* \geq 1$.

$$\varepsilon_{Sens \text{ or } Lat} = \frac{\left(Y_{air,i} - Y_{air,o}\right)}{\left(Y_{air,i} - Y_{sol,i}\right)} \qquad (5.33)$$

Here, Y is temperature (T) for the sensible effectiveness, and humidity ratio (W) for the latent effectiveness. Also, the total effectiveness of the LAMEE, which is related to both sensible and latent energy transfers, is calculated by the Eq. (5.34) (Simonson and Besant, 1999).

$$\varepsilon_{Tot} = \frac{\varepsilon_{Sens} + H^* \varepsilon_{Lat}}{1 + H^*} \qquad (5.34)$$

where H^* is the operating factor (see Eq. (5.16)), and is calculated based on the air and the salt solution inlet temperatures and humidity ratios in the LAMEE (Simonson and Besant, 1999).

5.6 Results and Discussion

In this section, the effects of membrane vapor diffusion resistance and enhanced air convective heat transfer coefficient are investigated on the steady-state performance of the small-scale LAMEE under summer AHRI conditions (i.e. air cooling and dehumidification). Then, the modified numerical model is validated by the experimental data for the steady-state effectiveness of the small-scale single-panel LAMEE under summer test conditions (i.e. air cooling and dehumidification and air cooling and humidification). Finally, this numerical model is used to evaluate the effectiveness of the small-scale LAMEE under winter test conditions.

5.6.1 Membrane Vapor Diffusion Resistance (VDR)

The membrane VDR plays an important role in the latent effectiveness of a LAMEE system (Seyed-Ahmadi *et al.*, 2009a; Beriault, 2011). This resistance should not

have any effect on the sensible effectiveness of the LAMEE. The membrane which is used in the small-scale LAMEE is a GE membrane, and is tested in Permatran-W$^®$ 101K device to calculate the VDR of the membrane. In this section, the Permatran-W$^®$ 101K device is briefly introduced, and the membrane VDR result from this device is presented and verified by dynamic moisture permeation cell (DMPC) test results for the GE membrane (Larson, 2006; Gibson *et al.*, 1997; Gibson, 2000). Finally, the effect of membrane VDR on the steady-state effectiveness of the small-scale LAMEE under summer AHRI test conditions is studied.

5.6.1.1 Water Vapor Permeability Measurement

There are different devices and standards available to measure the membrane water vapor transmission rate (WVTR) (Beriault, 2011; Larson, 2006). In this chapter, the Permatran-W$^®$ 101K device (Beriault, 2011) is used to measure the WVTR of the GE membrane. This device uses a modified ASTM E96BW standard (inverted cup with a guard membrane) to measure the WVTR of a membrane (ASTM E 96-00, 2000). Then, the membrane VDR is calculated from the WVTR value for the membrane (Beriault, 2011). Permatran has six test cells to simultaneously test the membrane WVTR on six different membrane areas to reduce the precision uncertainty. A schematic of the Permatran test cell and the nitrogen gas flow pattern in the test cell are shown in Figure 5.7. There is a water reservoir on the top of the test cell which contains distilled water. A PTFE guard membrane is used on the bottom of the reservoir which allows water vapor to transfer through the guard membrane but prevents liquid water to directly contact the membrane under test. The test membrane, for which the WVTR is calculated, is located on the bottom of the PTFE guard membrane in the Permatran test cell. Dry nitrogen gas

(~ 0%RH) with constant supply pressure (~ 103 kPa) flows into the bottom of the test cell cavity, and the top of the test membrane is in contact with PTFE guard membrane and water vapor (~ 100%RH). For each cell, Permatran records the data for the nitrogen mass flow rate and outlet relative humidity (RH) of the nitrogen gas to calculate the mass flow of the water vapor through a membrane. The Permatran is used to calculate the WVTR at steady-state conditions. For this purpose, it compares the recent calculated WVTR for a cell to the previous measurement for the cell, and if they agree within the convergence criteria of 1%, the measurement for that membrane is complete and the WVTR is recorded. The outputs of the Permatran device are the test temperature in Celsius, the test membrane WVTR in $g/(m^2 \cdot day)$, the calibration WVTR in $g/(m^2 \cdot day)$, which is for the test without the test membrane (i.e. only PTFE guard membrane is used for calibration), atmospheric pressure in mmHg and the nitrogen volume flow rate in standard cubic centimeters per minute (SCCM) for each cell. The test membrane VDR, which is calculated from the calibration and membrane WVTR measured in the Permatran, is for the bare membrane since the effect of the Nitrogen flow dynamics is also considered in the calibration WVTR. The calibration VDR is subtracted from the main test VDR for each test cell to calculate the bare membrane VDR (Beriault, 2011).

Beriault (2011) reported that the membrane VDR calculated from the Permatran outputs is not accurate, and he suggested using a 52.5% correction for the result values he measured. He compared the membrane VDR calculated from the Permatran to the results of the dynamic moisture permeation cell (DMPC) method (Larson, 2006; Gibson *et al.*, 1997; Gibson, 2000) for the same membrane to find this correction factor. The discrepancy between the Permatran and DMPC results are due to the calibration method

and effects in the Permatran test cell geometry that cause a complex three-dimensional nitrogen flow pattern in the test cell which is known as edge effects (see Figure 5.7).

In the current chapter, the test method with Permatran is modified to correct the output of the Permatran device, and verify the results with DMPC method. Originally, the membrane active test area was 10 cm^2 in the Permatran test cell, and now the active test area is reduced to 1 cm^2 by using a circular aluminum mask which reduces the edge effects in the test cell. The GE membrane is tested in the Permatran with the aluminum mask, and the results are compared with the DMPC method for GE membrane in Figure 5.8. The results show that using the aluminum mask in the Permatran corrects the membrane VDR results, and the Permatran results are validated with the DMPC results for the GE membrane. The GE membrane properties are presented in Table 5-1.
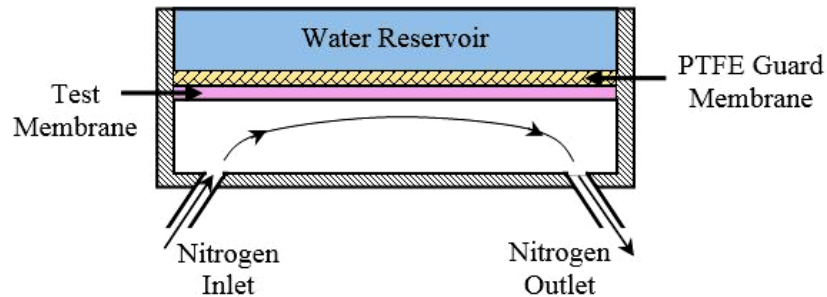
Figure 5.7 Schematic elevation view of the Permatran-W® 101K test cell showing the nitrogen gas flow pattern in the cell

5.6.1.2 Effect of the Membrane VDR on LAMEE Effectiveness

Figure 5.9 shows the effect of membrane VDR on the steady-state performance of the small-scale LAMEE under summer AHRI test conditions (air cooling and dehumidification) at $NTU = 3$ and $Cr* = 5$. Three different membrane VDR values are used for the GE membrane: 18.5 s/m from the DMPC method, 24 s/m from the modified Permatran-W 101K with the aluminum mask (i.e. 1 cm^2 membrane active area), and 56

s/m from the Permatran-W 101K without masking (i.e. 10 cm^2 membrane active area). The results show that the membrane VDR does not have any effect on the sensible effectiveness of the LAMEE. However, the latent effectiveness of the LAMEE increases with decreasing the membrane VDR. The latent effectiveness increases by 11% and 3% with decreasing membrane VDR from 56 s/m to 24 s/m and from 24 s/m to 18 s/m, respectively. The total effectiveness of the LAMEE also increases by decreasing the membrane VDR because of the increase in the latent effectiveness (see Eq. (5.34)).
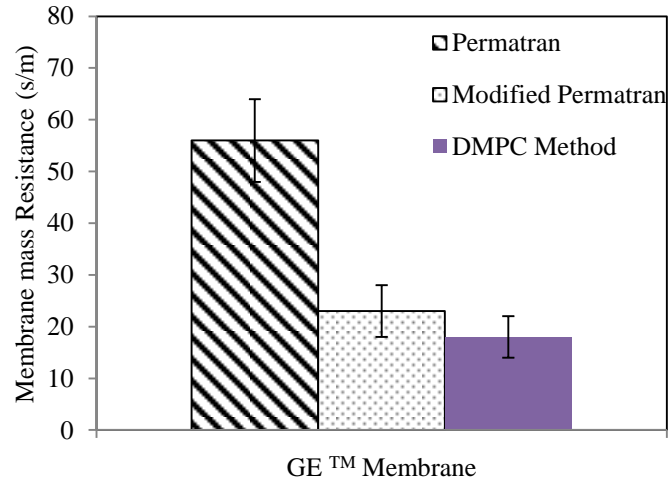
Figure 5.8 Membrane VDR data for the GE membrane using Permatran with 10 cm^2 and 1 cm^2 (with the aluminum mask) active areas, and DPMC method
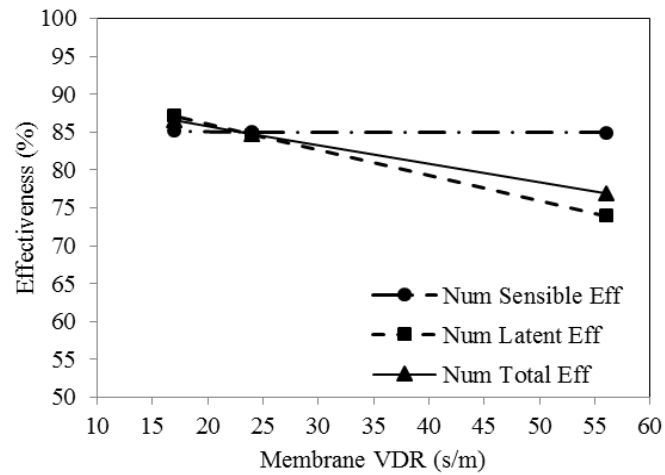
Figure 5.9 Effects of the calculated membrane VDR on the steady-state sensible, latent and total effectiveness of the LAMEE at *NTU* = 3 and *Cr** = 5 under summer AHRI test conditions

156

5.6.2 Air Side Convective Heat Transfer Coefficient

The small-scale LAMEE consists of layers of air and solution channels that are placed side by side, and separated with a semi-permeable membrane which allows heat and moisture transfer between the air and solution. The salt solution flows in the solution channel at very low Reynolds numbers (e.g. $Re_{sol} \leq 20$), and $Nu_{sol} = 5.39$ (Nusselt value for the laminar flow between two infinite parallel plates with constant heat flux on one wall and the other wall insulated) (Incropera and DeWitt, 1985) is used for the solution side of the small-scale LAMEE since the solution channels are in the sides of the LAMEE (see Figure 5.1b). In a full-size LAMEE where there are multiple air and solution channels, $Nu_{sol} = 5.39$ is used for the solution channels on the sides of the LAMEE, and $Nu_{sol} = 8.24$ (Nusselt value for the laminar flow between two infinite parallel plates with constant heat flux on both walls) (Incropera and DeWitt, 1985) is used for the solution channels in the middle of the LAMEE where each solution channel is in contact with two air channels on the sides.

In the air channel of the LAMEE, there is an air screen used to support the membrane, and enhance the heat and mass transfer performance in the air side of the LAMEE. Thus, the air side Nusselt number in the LAMEE is different than laminar air flow in an ideal smooth air channel, and needs to be calculated for the air channel of the small-scale LAMEE with the air screen.

5.6.2.1 Wind Tunnel Energy Exchanger Insert Test (WEIT) Facility

The wind tunnel energy exchanger insert test (WEIT) facility (Oghabi *et al.*, 2013) is used to determine the heat transfer enhancement by the eddy promoter air spacer

in the air channels. Figure 5.10 shows the schematic diagram of the WEIT facility in the

Mechanical Engineering Department of the University of Saskatchewan.
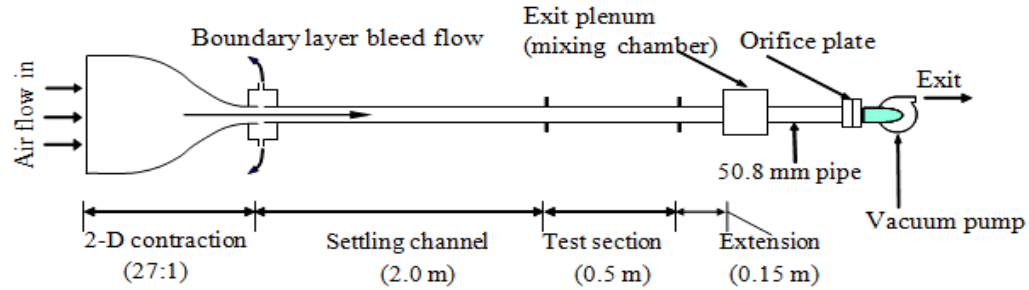
Figure 5.10 The schematic of the wind tunnel energy exchanger insert test (WEIT) facility (Oghabi *et al.*, 2013)

The WEIT facility includes four main sections: a 2-D contraction nozzle, settling

flow development channel, test section, and a mixing chamber. The channel has a

rectangular cross section with 5 mm wide by 152.4 mm high from the nozzle to the

mixing chamber which is the same geometry as the air channel in the small-scale

LAMEE. A vacuum pump located at the downstream of the test facility induces the air

through the test section. Air at room temperature (~23ºC) flows into the settling channel

to become hydrodynamically fully-developed before the test section. The side walls of

the test section are electrically heated with constant heat flux to simulate the heat transfer

in the air channel of the small-scale single-panel LAMEE. The test section walls are

completely insulated and the heater elements are installed on the air side of the test

section walls. Therefore, the heat power produced by the side wall heaters is transferred

to the air by convection. The wall surface temperatures and bulk air temperatures are

measured at the inlet and outlet of the test section using T-type thermocouples with 0.1ºC

uncertainty and are used to calculate the average convective heat transfer coefficient.

Also, the air flow rate and the pressure drop across the test section are measured by an

orifice plate downstream of the mixing chamber and static pressure probes installed along the test section wall, respectively. The heat transfer measurement results for different air screens, and mass and energy balance results for the WEIT facility are presented in Oghabi *et al.* (2013). The log mean temperature, ΔT_{lm}, is used in Eq. (5.35) to calculate the average air convective heat transfer coefficient through the test section.

$$Q'' = h_{air}\, \Delta T_{lm} \tag{5.35}$$

In Eq. (5.35), Q'' is the heat flux at the test section walls. Eq. (5.36) defines the log mean temperature difference, where T is the temperature in Celsius, and subscript s is related to the wall surface in the test section (Incropera and DeWitt, 1985).

$$\Delta T_{lm} = \frac{[(T_{(s,i)}\text{-}T_{(air,i)}) \text{-} (T_{(s,o)}\text{-}T_{(air,o)})]}{\ln\,[(T_{(s,i)}\text{-}T_{(air,i)})/(T_{(s,o)}\text{-}T_{(air,o)})]} \tag{5.36}$$

The average air Nusselt number in the test section is determined by the average air convective heat transfer coefficient as shown in Eq. (5.37) (Incropera and DeWitt, 1985). In Eq. (5.37), Nu_{air} is the average air Nusselt number, k is thermal conductivity of the air, and D_h is hydraulic diameter of the channel.

$$Nu_{air} = h_{air}\, D_h / k_{air} \tag{5.37}$$

5.6.2.2 Effect of the Air Convective Heat Transfer Coefficient on LAMEE Effectiveness

Figure 5.11 shows the schematic of the air screen which is used in the air channel of the small-scale single-panel LAMEE. This air screen is composed of cylindrical bars with 1.6 mm diameter which are axially vertical in the center of the air channel of the small-scale LAMEE (i.e. air flow is perpendicular to the bars), and horizontal plastic ribs

which are located parallel to the air flow and have rectangular holes to provide better mixing for the air. The cylindrical bars and plastic ribs are located within 90 mm and 10 mm distance apart from each other, respectively. The Reynolds number for the air in the LAMEE is depend on the operating parameters (e.g. *NTU* and *Cr**) and the size of the LAMEE, and it is usually in the laminar flow regime (i.e. $Re_{air} \leq 2200$ for a laminar air flow in a smooth rectangular duct (Incropera and DeWitt, 1985)). By using the air screen in the air channel, the air flow regime changes to transitional regime in the air channel, and the convective heat and mass transfer coefficients of the air increase in the air channel of the LAMEE. Figure 5.12 shows the measured air convective heat transfer coefficient for the air in the air channel of the small-scale LAMEE with the air screen respect to the air Reynolds number which is tested in the WEIT facility. The results show that the heat transfer enhancement increases in the air side of the LAMEE with the air screen by increasing the air Reynolds number, and significant enhancement occurs at higher Reynolds numbers. There are 37%, 67%, 138% and 177% increases in the air side convective heat transfer coefficient of the small-scale LAMEE with the air screen at Re_{air} = 620, 950, 1570 and 2170, respectively, compare to the case of no air screen. The air density and viscosity were calculated based on the air temperature and relative humidity.
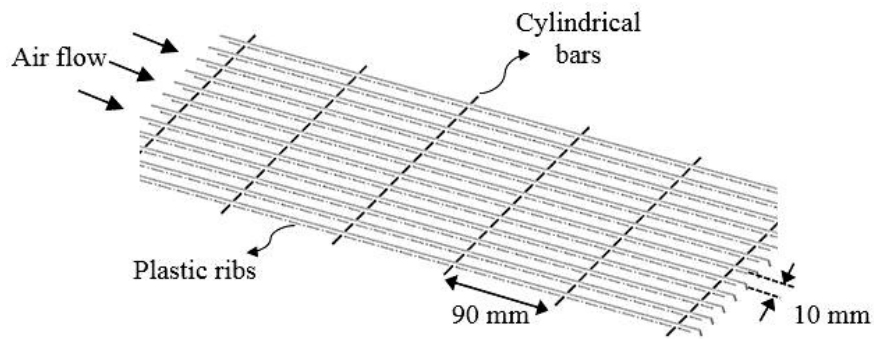
Figure 5.11 Schematic of the air screen used in the air channel of the small-scale LAMEE
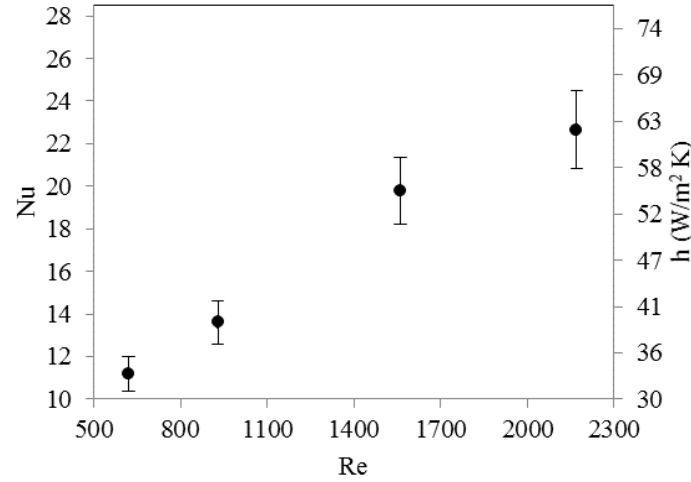
Figure 5.12 Experimental Nusselt number and air side convective heat transfer coefficient in the air channel of the small-scale single-panel LAMEE with the air screen

The improvement in the air side convective heat transfer coefficient increases the *NTU* value for the experimental and the numerical effectiveness of the small-scale LAMEE (see Eqs. (5.14) and (5.17)). Also, the air side convective mass transfer coefficient and the latent effectiveness of the LAMEE increase by using the air screen in the air channel of the LAMEE (see Eq. (5.8)). The air and solution convective mass transfer coefficients are calculated from Sherwood numbers (*Sh*) for the air and solution flows using the heat and mass transfer (Chilton-Colburn) analogy (Niu and Zhang, 2001),

$$Sh = Nu \ Le^{-\frac{1}{3}} \tag{5.38}$$

where *Le* is the Lewis number in Eq. (5.38). The Sherwood number is calculated using Eq. (5.39) for the air or solution flows.

$$Sh = \frac{h_m D_h}{D_{va}} \tag{5.39}$$

Figure 5.13 shows the effect of enhanced air convective heat transfer coefficient on the steady-state effectiveness of the small-scale LAMEE under summer AHRI test conditions at $Cr^* = 5$. The results show almost 4% improvement in the sensible, latent

and total effectiveness of the small-scale LAMEE with the air screen at the specific conditions (see Table 5-2) that the small-scale LAMEE was tested in Ghadiri Moghaddam *et al.* (2013a) (i.e. $Re_{air} = 620$ and $Nu_{air} = 11.2$) in comparison to the smooth air channel (i.e. $Nu_{air} = 8.24$). The increase in the performance of the LAMEE can be improved at higher air Reynolds numbers (e.g. 11% improvement in the LAMEE effectiveness at $Re_{air} = 1600$ and $Nu_{air} = 20$). Also, as was mentioned, the operating *NTU* increases with increasing the air convective heat transfer coefficient. Figure 5.13 shows that the *NTU* value for the tests presented in this chapter (see Table 5-2) is increased from 3 to 3.8 in the small-scale LAMEE with the air screen in the air channel.

Huang *et al.* (2012) showed that the actual heat and mass transfer convective coefficients for the air and solution in a cross-flow flat-plate hollow channel membrane energy exchanger are different than the traditional Nusselt values (i.e. $Nu_{air} = 8.24$ and $Nu_{sol} = 5.39$ in this study). The sensible, latent and total effectiveness of the small-scale LAMEE with a hollow air channel (without the air screen) using the actual air-side convective heat and mass transfer coefficients from reference (Huang *et al.*, 2012) are also shown in Figure 5.13. The ratio of the small-scale LAMEE width over the solution channel thickness, H_{ex}/d_{sol}, is 59 (see Table 5-1). Thus $Nu_{air} = 7.54$ and $Sh_{air} = 7.74$ are used for the small-scale LAMEE with a hollow air channel which are the actual air-side Nusselt and Sherwood values from Huang *et al.* (2012). The actual solution-side convective heat and mass transfer coefficients from Huang *et al.* (2012) are not applicable for the small-scale LAMEE since in the small-scale LAMEE the solution is in contact with a membrane on one side and the side wall of the exchanger on the other side, while in Huang *et al.* (2012) the solution is in contact with the membrane on both sides.

Also, the air-side convective heat and mass transfer coefficients are more important than the solution-side convective heat and mass transfer coefficients in calculating the overall convective heat and mass transfer coefficients for LAMEEs. Figure 5.13 shows that the small-scale LAMEE sensible, latent and total effectiveness with the actual air-side convective heat and mass transfer coefficients are 2% lower than the LAMEE effectiveness using the traditional values (i.e. $Nu_{air} = 8.24$).

Moreover, some literature (Zhang *et al.*, 2012a; Zhang *et al.*, 2012b) has shown that using the Chilton-Colburn analogy might be questionable for membrane based energy exchangers. Zhang *et al.* (2012a) numerically calculated the actual Nusselt and Sherwood numbers for a counter-flow hollow fiber membrane energy exchangers with different packing densities, where the boundary conditions on the membrane are numerically obtained by simultaneous solution of momentum, energy and concentration equations for the air, solution and membrane. The results showed that in all cases, the actual air-side Nusselt values for the counter-flow hollow fiber membrane energy exchanger are very close to the Nusselt values with a constant heat flux boundary condition on the membrane. The constant heat flux boundary condition on the membrane is used in the current study to experimentally measure the enhanced air-side convective heat transfer coefficient for the air side of the small-scale LAMEE with the air screen, using the WEIT facility. Also, the results of Zhang *et al.* (2012a) showed that the actual air-side Sherwood number is different than the air-side Sherwood number that is calculated from the Chilton-Colburn analogy. The actual air-side Nusselt and Sherwood number results for the counter-flow hollow fiber membrane energy exchanger are used to show the effect of deviation from the Chilton-Colburn analogy on the small-scale

163

LAMEE effectiveness. The reasons why only the air-side convective heat and mass transfer coefficients are considered in this part are mentioned in the previous paragraph. Also, since the air and solution flows in the small-scale LAMEE are mostly counter-flow, the results for the counter-flow hollow fiber membrane energy exchanger are used for this sensitivity study. The Chilton-Colburn analogy is changed to the following format based on the actual average Nusselt and Sherwood values for the counter-flow hollow fiber membrane energy exchanger in Zhang *et al.* (2012a):

$$Sh = Nu \ Le^{-(0.065 \pm 0.01)} \tag{5.40}$$

Equation (5.40) is used in Figure 5.13 to calculate the air and solution sides' convective mass transfer coefficients for the small-scale LAMEE. The experimental Nusselt values for the small-scale LAMEE with the air screen are used for the air-side of the LAMEE (see Figure 5.12), and the laminar flow Nusselt value, $Nu_{sol} = 5.39$, is used for the solution side of the small-scale LAMEE. Figure 5.13 shows that using Eq. (5.40) to calculate the air or solution side convective mas transfer coefficients has no effect on the sensible effectiveness of the small-scale LAMEE. However, the latent and total effectiveness of the small-scale LAMEE decrease by a maximum of 4% when using Eq. (5.40) to calculate the convective mass transfer coefficients, instead of the traditional Chilton-Colburn analogy.
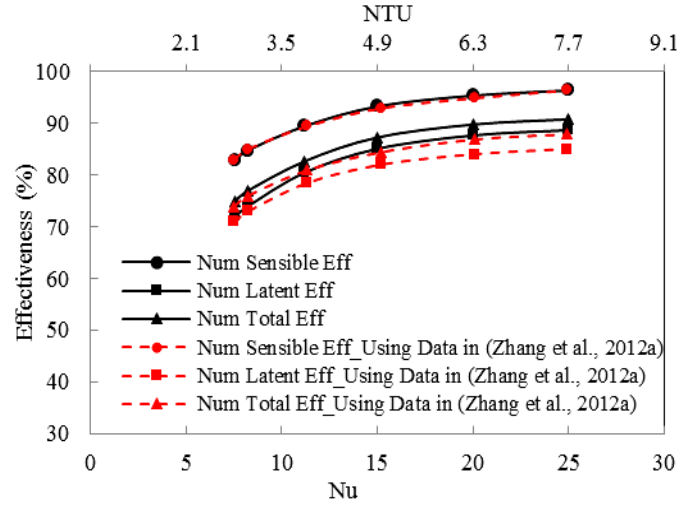
Figure 5.13 Effect of the enhanced air convective heat transfer coefficient on the steady-state sensible, latent and total effectiveness of the small-scale LAMEE at *NTU* = 3 and *Cr** = 5 under summer AHRI test conditions

5.6.3 Validating the Numerical Model for Summer Test Conditions

In this section, the numerical model is validated by the experimental data for summer test conditions (i.e. air cooling and dehumidification and air cooling and humidification test cases) which are presented in Table 5-2. The effects of the membrane VDR and the enhanced air convective heat transfer coefficient are studied for the steady-state effectiveness of the small-scale LAMEE. These two parameters are the main parameters which have significant impact on the numerical results. There are a few other parameters that slightly affect the numerical results, and they are considered in the numerical model. The first parameter is heat loss/gain to/from surroundings which is also considered in the modified numerical model for the small-scale LAMEE. The second parameter is the air and solution flow configuration in the LAMEE (e.g. cross or counter-flow configurations). The air and solution flow in the small-scale LAMEE is in the counter-cross flow configuration where 90% of the LAMEE has pure counter-flow configuration for the air and solution. Akbari *et al.* (2012a) showed that for a LAMEE

with the same entrance ratio and aspect ratio as the small-scale LAMEE, there is less than 1% discrepancy between the numerical effectiveness results for a counter-cross flow and a pure counter-flow LAMEE. Consequently, the counter flow configuration is used in the numerical model for the small-scale LAMEE.

5.6.3.1 Air Cooling and Dehumidification (C&D)

Figure 5.14 shows the experimental and numerical steady-state effectiveness of the LAMEE and their uncertainties for four different $Cr* = 1, 3, 5$ and 7 when the LiCl solution is used as a transfer liquid in the LAMEE. The small-scale single-panel LAMEE is tested under summer AHRI test conditions (ANSI/AHRI standard 1060, 2011) (i.e. air cooling and dehumidification test case) which represents hot and humid climates. The numerical results are modified based on the actual membrane VDR and enhanced air convective heat transfer coefficient. The numerical uncertainties are calculated based on the uncertainties in the measured membrane VDR and the calculated enhanced air convective heat transfer coefficient (see Figure 5.8 and Figure 5.12). The uncertainties in calculating the *NTU* and *Cr** are also considered in the uncertainty of the steady-state LAMEE effectiveness. The method of propagation of errors is used to calculate the small-scale LAMEE effectiveness uncertainties for all cases (Figliola and Beasley, 2006). The actual *NTU* for the experiments and numerical model are calculated based on the enhanced air convective heat transfer coefficient with the air screen, and $NTU = 3.8$. The results show agreement between the experimental data and numerical results, and the numerical model is validated by the experimental data during the air cooling and dehumidifying (C&D) test conditions which are presented in Table 5-2.
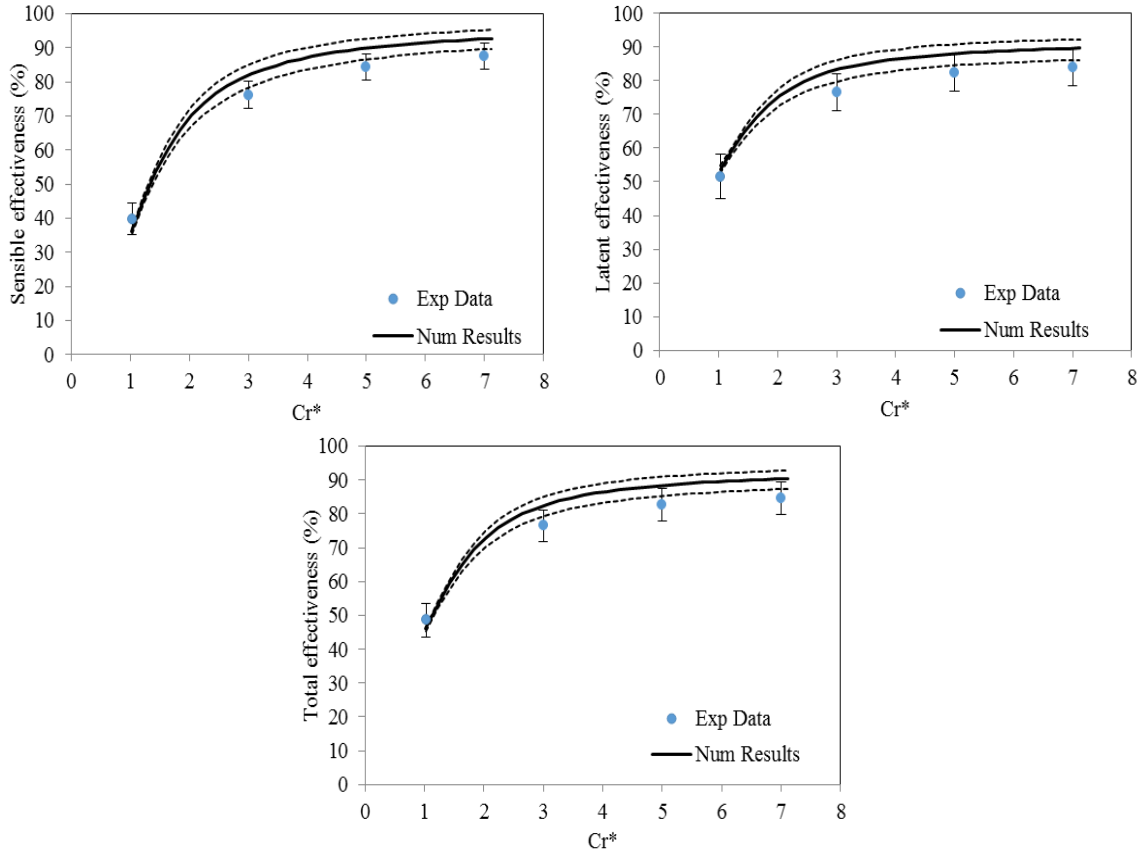
Figure 5.14 Comparison of the numerical and experimental steady-state effectiveness of the small-scale LAMEE for different *Cr** and *NTU* = 3.8 under summer AHRI test conditions (air cooling and dehumidification test case)

5.6.3.2 Air Cooling and Humidification (C&H)

Figure 5.15 shows the experimental and numerical steady-state effectiveness of the small-scale LAMEE at different *Cr** and *NTU* = 3.8 under air cooling and humidification (C&H) test conditions. The air C&H test conditions represent hot and dry climates where the supply air needs to be cooled and humidified in a LAMEE. The uncertainties of the numerical results are calculated in the same way as the results for the air C&D test conditions. The results show that the numerical model is also validated for the C&H test conditions that are presented in Table 5-2, and the experimental and numerical results are agreed within their uncertainty ranges. Also, Figure 5.15 shows

almost 60% uncertainty for the experimental total effectiveness of the small-scale LAMEE which is a high uncertainty. This is because of the air and solution inlet conditions selections for the experiments. The experimental air and solution inlet conditions for C&H tests (see Table 5-2) show that the air and solution inlets have almost the same enthalpies on a psychrometric chart, which causes to have air and solution outlets close to the solution inlet condition (Ghadiri Moghaddam *et al.*, 2013a). Consequently, according to the effectiveness definitions (see Eqs. (5.33) and (5.34)), small difference in the air or the solution outlet conditions in the numerical results or experimental data will cause a big change in the total effectiveness results.
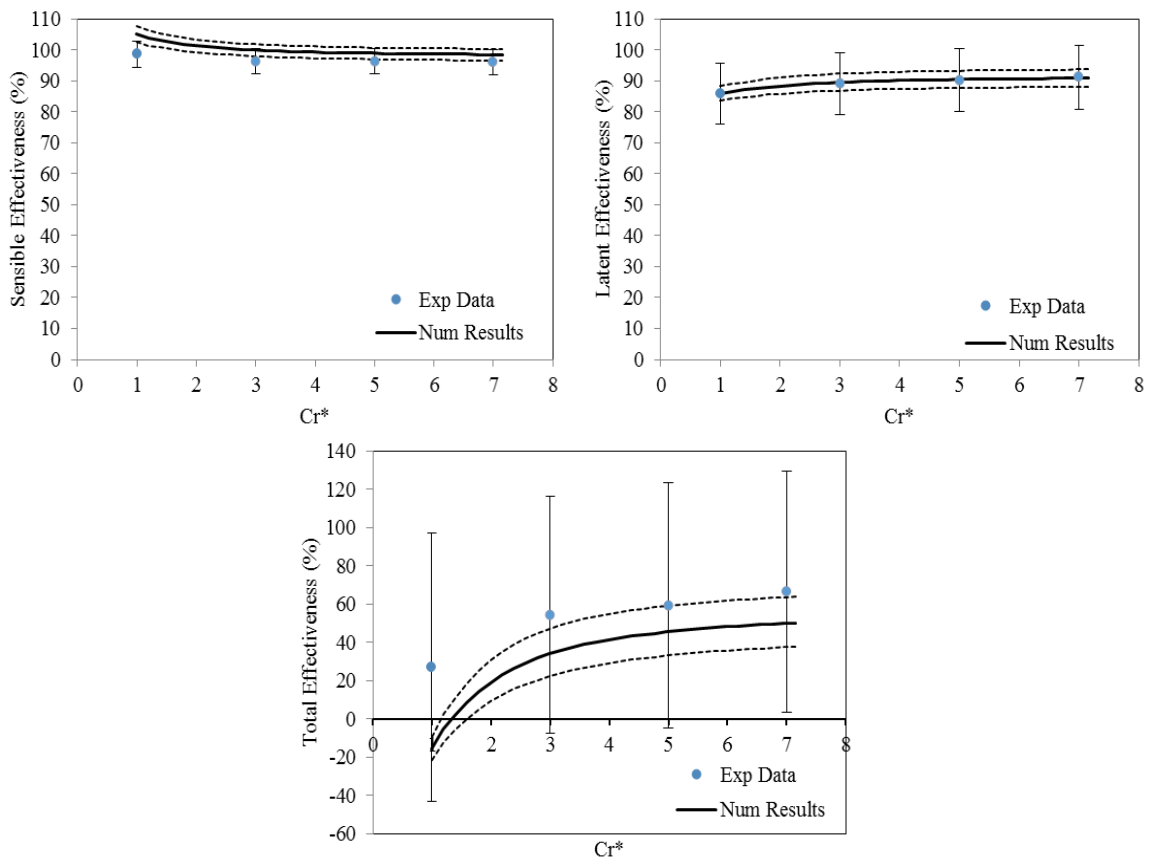
Figure 5.15 Comparison of the numerical and experimental steady-state effectiveness of the small-scale LAMEE for different *Cr** and *NTU* = 3.8 under air cooling and humidification test conditions

5.6.4 Using the Numerical Model for Winter Test Conditions

The numerical model is modified for the small-scale single-panel LAMEE, and validated for summer test conditions that are presented in Table 5-2 which is one main application of the LAMEE. In this section, the numerical model is used to simulate the performance of the small-scale LAMEE under winter test conditions which are presented in Table 5-2 (i.e. air heating and dehumidification, and air heating and humidification). In this chapter, the winter test conditions are identified based on the heat transfer direction in the LAMEE (i.e. air heating process), and are different than winter AHRI test conditions. Figure 5.16 shows the experimental and numerical steady-state sensible, latent and total effectiveness of the small-scale LAMEE under the air heating and dehumidification (H&D) test conditions at the same Cr^* and NTU as the air C&H and C&D test cases. The H&D test conditions represent the operation of the LAMEE in cold and humid climates where the supply air needs to be heated and dehumidified in a LAMEE. The results show that the numerical model is still valid for the latent and total effectiveness of the LAMEE under H&D test conditions. However, the numerical model predicts higher sensible effectiveness for the small-scale LAMEE in comparison to the experimental data. There is 5% to 10% discrepancy between the experimental and numerical sensible effectiveness of the LAMEE under H&D test conditions. This discrepancy may be due to the fact that sensible energy is not conserved in the small-scale LAMEE for H&D test cases even though the water vapor mass and total energy are conserved. The small-scale LAMEE was balanced for all the experiments that are presented in this chapter (see Ghadiri Moghaddam *et al.* (2013a) for water vapor and

energy balance results). However, the mass and energy balances show only the mass and energy conservations in the LAMEE.
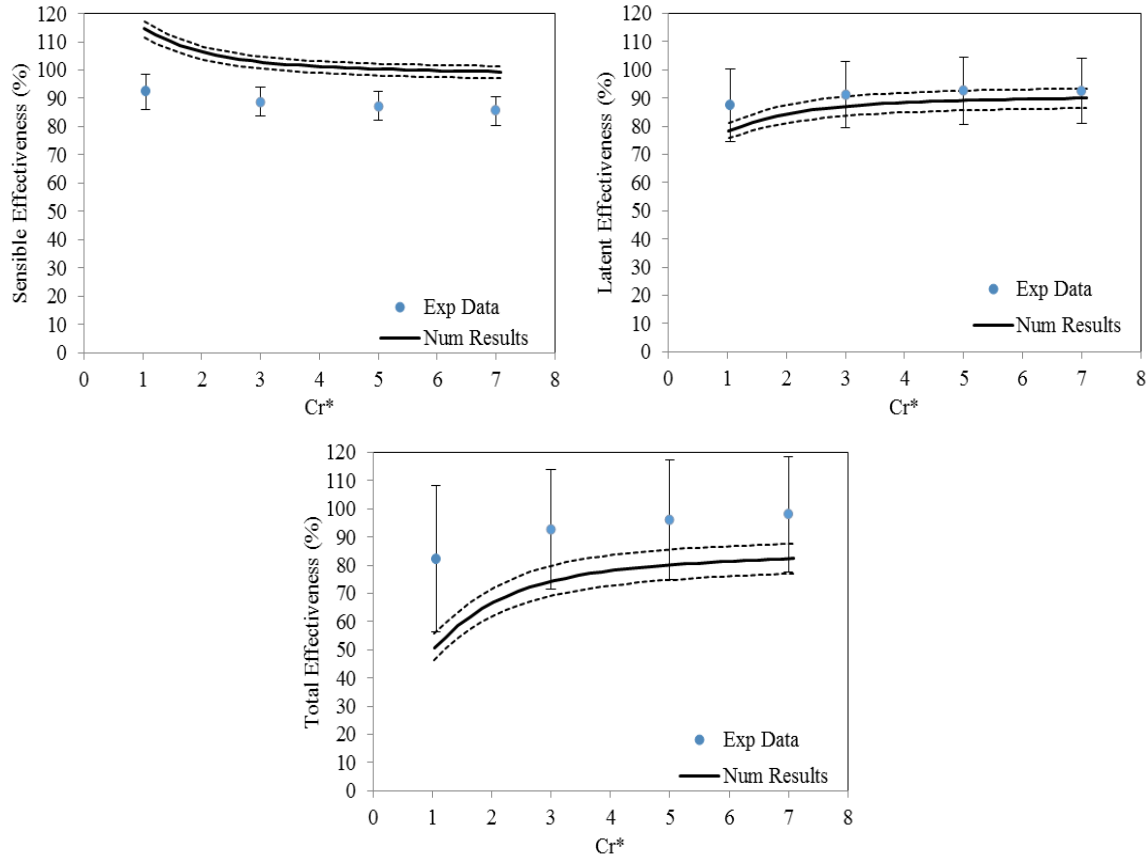
Figure 5.16 Comparison of the numerical and experimental steady-state effectiveness of the small-scale LAMEE for different *Cr** and *NTU* = 3.8 under air heating and dehumidification test conditions

Finally, the steady-state sensible, latent and total effectiveness of the small-scale LAMEE at different *Cr** and *NTU* = 3.8 under air heating and humidification test conditions (i.e. LAMEE operation in cold and dry climates) are shown in Figure 5.17. The results show that the numerical model is still valid for the latent and total effectiveness of the LAMEE with the experimental data that are presented in Table 5-2, and they agree within their uncertainty ranges. However, the same as the air H&D test case, the numerical steady-state sensible effectiveness of the small-scale LAMEE does not agree with the experimental data for the H&H test conditions at *Cr** = 3, 5, and 7.

170

Again, it is noted that the sensible energy is not conserved in the small-scale LAMEE for H&H test case. In addition, if there are any crystallization in the membrane pores, they may appear when water vapor is transferred from the solution flow to the air stream. This effect would decrease the measured effectiveness for the small-scale LAMEE (Ge *et al.*, 2014).
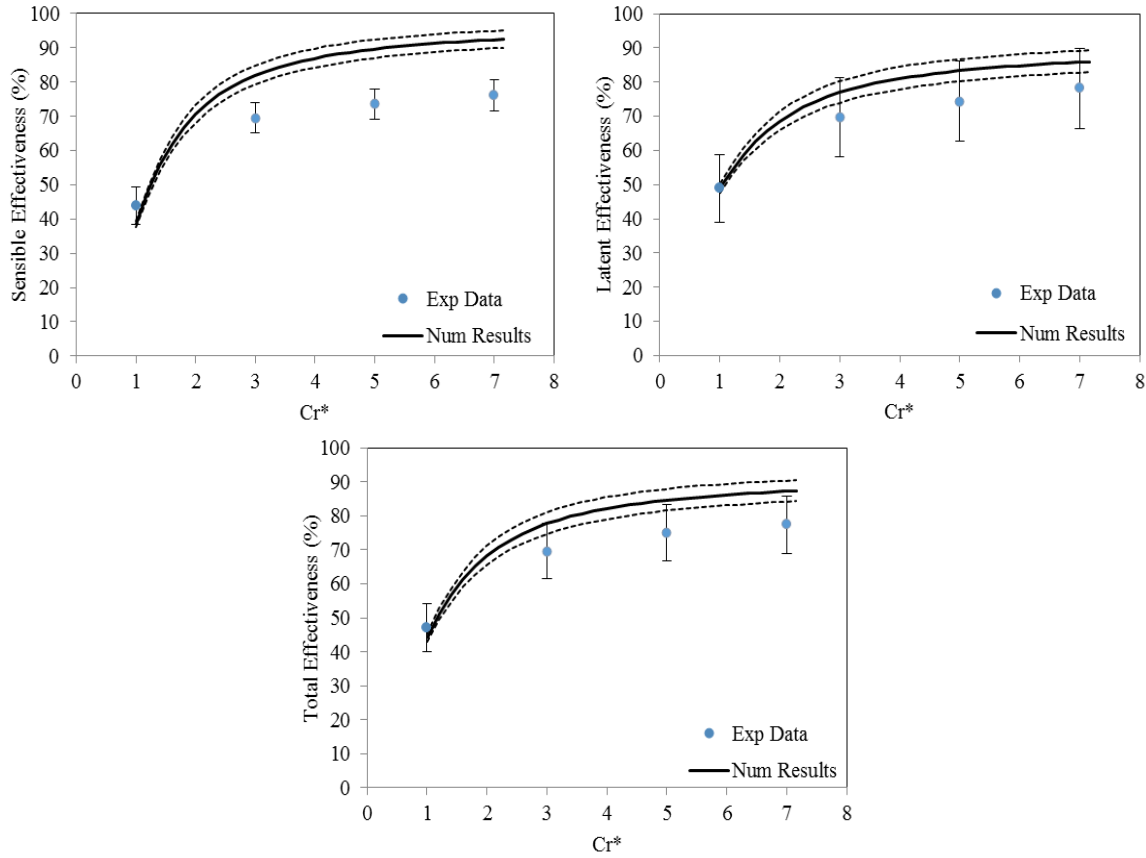
Figure 5.17 Comparison of the numerical and experimental steady-state effectiveness of the small-scale LAMEE for different *Cr** and *NTU* = 3.8 under air heating and humidification test conditions

5.7   Conclusions

In chapter 5, the steady-state effectiveness of the small-scale single-panel LAMEE is numerically simulated, and the numerical results are compared with the experimental data for summer and winter test conditions. The coupled heat and mass transfer equations in the air, salt solution and membrane and their boundary conditions

are derived and nondimensionalized for the counter-flow small-scale single-panel LAMEE. The effect of the membrane vapor diffusion resistance (VDR) and the enhanced air convective heat transfer coefficient are investigated for the performance of the small-scale LAMEE. The membrane VDR found to be 24 s/m for the GE membrane which is 57% lower than the value that had been previously used for the GE membrane in a LAMEE. The latent and total effectiveness of the small-scale LAMEE increase with decreasing the membrane VDR while the sensible effectiveness is unchanged. Also, using the air screen in the air channel of the small-scale LAMEE increases the heat and moisture performance of the air in the air channel of the LAMEE. The results show that the air side Nusselt number increases from 8.24 (for a rectangular smooth air channel with constant heat flux on both walls) to 11.2 in the small-scale LAMEE with the air screen at $Re_{air} = 620$. The sensible, latent and total effectiveness of the LAMEE increase by 4% with increasing the air convective heat transfer coefficient in the small-scale LAMEE. The numerical model is modified based on these findings for the small-scale LAMEE, and is validated by the experimental data for the summer test conditions (i.e. air cooling and dehumidification and air cooling and humidification test cases) that are presented in this chapter. Also, the model is used for winter test conditions (i.e. air heating and dehumidification (H&D) and air heating and humidification (H&H) test cases). The numerical results are compared with the experimental data for the air H&D and H&H test cases, and the latent and total effectiveness of the small-scale LAMEE are validated by the experimental data for these test cases.

CHAPTER 6

SIMILARITY BETWEEN SMALL-SCALE AND FULL-SCALE LAMEES

6.1   Overview of Chapter 6

Experimental and numerical steady-state performance results for a full-scale (100 L/s air flow rate) LAMEE tested under summer conditions, and the similarity between the small-scale LAMEE and the full-scale LAMEE, are discussed in this chapter which contains Manuscript #5 (Investigating similarity between a small-scale liquid-to-air membrane energy exchanger (LAMEE) and a full-scale (100 L/s) LAMEE: experimental and numerical results). The full-scale LAMEE is tested under four summer test conditions (i.e. air cooling and dehumidification), and the experimental and numerical effectivenesses of the full-scale LAMEE are compared together. The results show good agreement between the experimental and numerical effectiveness results for the full-scale LAMEE.

Dimensional analysis of the coupled heat and mass transfer equations in the air-side, solution-side and membrane of a LAMEE shows that there are five important dimensionless parameters affecting the performance of LAMEEs. The effects of these important dimensionless parameters on the sensible, latent and total effectivenesses of the small-scale LAMEE are numerically investigated. Finally, the similarity between the small-scale LAMEE and the full-scale LAMEE is investigated numerically and experimentally. The experimental and numerical results show that there is a similarity

between the small-scale and full-scale LAMEEs, and the small-scale LAMEE effectiveness results can be used to predict the performance of the full-scale LAMEE within an acceptable uncertainty range. This chapter represents the last step of the methodology (see Section 1.3.6) for LAMEEs, which is studying the effect of the important dimensionless parameters on the performance of the small-scale LAMEE, and investigating similarity between the small-scale and the full-scale LAMEEs.

References for this chapter, which contains Manuscript #5, are presented in the Reference section of the thesis (see page 215) which includes all the references used in this PhD thesis.

Dr. Melanie Fauchoux is a post-doctoral fellow in our research group, and is a co-author in Manuscript #5. Dr. Melanie Fauchoux's contribution to this manuscript is giving a scientific advice during writing Manuscript #5, and critically reviewing it. The PhD candidate's contributions to Manuscript #5 are (a) testing the small-scale LAMEE and the full-scale LAMEE under various test conditions, (b) analyzing the experimental data for the full-scale LAMEE, and presenting the full-scale LAMEE experimental and numerical effectiveness results under selected summer test conditions (the full-scale LAMEE numerical model was initially developed by Hemingson (2010)), (c) investigating the effects of important dimensionless parameters on the performance of the small-scale LAMEE, (d) investigating the similarity between the small-scale and full-scale LAMEEs and (e) writing the paper.

Investigating Similarity between a Small-Scale Liquid-to-Air Membrane Energy

Exchanger (LAMEE) and a Full-Scale (100 L/s) LAMEE: Experimental and Numerical

Results

Davood Ghadiri Moghaddam, Melanie Fauchoux, Robert W. Besant, Carey J. Simonson

6.2   Abstract

Liquid-to air membrane energy exchangers (LAMEEs) are novel membrane-based energy exchangers that allow simultaneous heat and moisture transfer between salt solutions and air streams. The similarity between a small-scale (2.5 L/s) LAMEE and a full-scale (100 L/s) LAMEE is investigated, both experimentally and numerically, in this chapter. Dimensional analysis of the coupled heat and mass transfer equations in the air-side, solution side and membrane of the LAMEE shows that five important dimensionless parameters affect the performance of LAMEEs: (1) number of heat transfer units, NTU, (2) thermal capacity ratio, Cr^*, (3) number of mass transfer units, NTU_m, (4) mass flow rate ratio, m^*, and (5) operating factor, H^*. The differences in the small-scale and full-scale LAMEEs effectivenesses are numerically investigated for these five important dimensionless parameters. The results show that in most cases the differences between the small-scale and full-scale LAMEE effectivenesses are less than 2%. The comparison between the experimental and numerical sensible, latent and total effectivenesses of the small-scale LAMEE and the full-scale LAMEE shows that there is a similarity between the small-scale and full-scale LAMEEs, and that the small-scale LAMEE effectiveness results can be used to predict the performance of the full-scale LAMEE.
Keywords: LAMEE; Small-scale; Full-scale; Similarity; Dimensional analysis.

6.3   Introduction

Testing a full-scale thermal system (i.e. a heat exchanger, an energy wheel or a liquid-to-air membrane energy exchanger) is often impossible or expensive to do, so a small-scale model of the thermal system, which is smaller and often simpler than the full-scale one, is often used to predict the behavior of the full-scale system under different conditions (White, 2009). For this purpose, the small-scale model should be similar to the full-scale prototype. There are common similarity rules in heat and mass transfer problems which should be satisfied for a small-scale model and a full-scale prototype of a thermal system so that the small-scale model results can be used directly to predict the behavior of the full-scale prototype (White, 2009; Shah, 1981). These similarity rules are: geometric, momentum, dynamic, thermal and mass transfer similarities (White, 2009; Incropera and DeWitt, 1985; Jaluria, 2007). Geometric similarity is generally required for most scaled models (White, 2009). For geometric similarity, all prototype dimensions in all directions should be scaled with the same linear scale ratio. For thermal systems, thermal similarity is also required. The model and prototype are thermally similar if the temperature profiles are the same for both the model and prototype at corresponding points and time (Incropera and DeWitt, 1985). The most important dimensionless parameter which should be considered during establishing the thermal similarity is the Nusselt number. Also, the model and prototype are similar in mass transfer if the concentration profiles are the same for both components at corresponding points and time in the system. The most important dimensionless parameter which should be considered during establishing the mass transfer similarity is the Sherwood number. In some cases,

the analogy between heat and mass transfer can help to find the important dimensionless parameters affecting the mass transfer similarity (Niu and Zhang, 2001).

Sometimes, it is not possible to make the small-scale model and full-scale prototype similar in all aspects; however, they could be similar in specific aspects. Thus, it is necessary to find the important dimensionless parameters in the system based on the system requirements and applications to investigate similarity between the small-scale model and the full-scale prototype. A dimensional analysis is often used to determine important dimensionless parameters that explain the behavior of a given system (White, 2009; Incropera and DeWitt, 1985). These parameters can be used to minimize the number of experiments required for the full-scale prototype or the small-scale model of the system, and to obtain the conditions for similitude (White, 2009). If complete similarity occurs between the small-scale model and the full-scale prototype, the value of the important dimensionless parameters will be the same for the model and prototype, and then the dimensionless results of the small-scale model of the thermal system such as effectiveness can be directly used to predict the performance of the full-scale thermal system.

Several studies have been conducted to investigate the performance of a small-scale exchanger or portion of a full-size exchanger and extrapolate the results to a full-scale exchanger. Wang *et al.* (2005; 2007a; 2007b) and Abe *et al.* (2006a; 2006b; 2006c) developed a test facility to investigate the transient characteristics of humidity and temperature sensors and an energy wheel during a step change in humidity and no change in temperature, and a step change in temperature and no change in humidity. They tested a small portion of the energy wheel in a test facility. They predicted the steady-state

effectiveness of the full-size energy wheel using the experimental data from the small portion of the energy wheel, and the results showed good agreement with experimental data measured on the full-size wheel. Moreover, Zhang (2011a) introduced a hollow fiber membrane contactor, which is a small-scale shell and tube membrane-based energy exchanger where a solution passes through hollow fiber membrane tubes and heat and mass transfer occurs between the air and solution. He developed an analytical model to predict the steady-state performance of a hollow fiber membrane contactor as a dehumidifier. The analytical results were compared with experimental data for a small-scale hollow fiber membrane contactor under different operating conditions. The hollow fiber membrane contactor was also used as a humidifier when water was used as a transfer liquid in the contactors (Zhang, 2011b; Zhang, 2012; Zhang and Huang, 2011). Zhang (2011b) presented a fractal model for the fluid flow and heat and mass transfer in a randomly packed hollow fiber membrane contactor, and compared the model results with experimental data for the contactor using water as a transfer liquid. Zhang (2011b) proposed correlations to estimate the friction factor and Sherwood number for the randomly packed contactor considering the degree of irregularity. The proposed correlations were also compared with available mass transfer correlations in literature. Also, Zhang *et al.* (2012a) numerically investigated the coupled heat and mass transfer in a small-scale counter-flow hollow fiber membrane contactor using a free surface model. The actual boundary conditions were obtained for the hollow fiber membrane tube which were neither uniform temperature nor uniform heat flux. The results showed that the fully developed air-side Nusselt number is between the constant temperature and constant heat

flux Nusselt numbers values, and close to constant heat flux Nusselt number value for the counter-flow contactor.

A liquid-to-air membrane energy exchanger (LAMEE) is a flat-plate membrane based energy exchanger, where the heat and moisture transfer occurs between the air and salt solution through a semi-permeable membrane which is permeable for water vapor and impermeable for liquid water. The LAMEE consists of many panels. Each panel consists of a single pair of neighboring air and liquid channels (Ghadiri Moghaddam *et al.*, 2013b). A single-panel LAMEE is a basic unit in a LAMEE and the performance of the single-panel relates to the performance of the overall LAMEE. The LAMEE can be used as a dehumidifier to condition the supply air or as a regenerator to regenerate the solution in liquid desiccant air conditioning systems (Ghadiri Moghaddam *et al.*, 2013a; Ghadiri Moghaddam *et al.*, 2014; Ge *et al.*, 2014).

Several papers are available on a small-scale single-panel LAMEE and a full-scale LAMEE with several panels. Ghadiri Moghaddam *et al.* (2013b) introduced a test facility to test a small-scale single-panel (2.5 L/s) LAMEE under different test conditions. Usually, manufacturing and testing a full-scale LAMEE is expensive and time consuming, while a small-scale single-panel LAMEE is easier and less costly to manufacture and test. Also, the small-scale LAMEE test facility provides better control in the experiments. In another study, Ghadiri Moghaddam *et al.* (2013a) experimentally and numerically investigated the performance of the small-scale LAMEE under different heat and mass transfer directions (i.e. air cooling and dehumidifying, air cooling and humidifying, air heating and dehumidifying and air heating and humidifying), and different salt solution types and concentrations. The results showed that using different

179

salt solution types and concentrations does not have a significant effect on the performance of the small-scale LAMEE. The steady-state performance of the small-scale LAMEE was numerically modeled under different test conditions, and the numerical results were verified with the experimental data for the small-scale LAMEE (Ghadiri Moghaddam *et al.*, 2013c). In addition, a full-scale (100 L/s) LAMEE, which consists of 10 single-panels, was tested under summer and winter test conditions (Ghadiri Moghaddam *et al.*, 2013d). The full-scale LAMEE has a similar design as the small-scale single-panel LAMEE. The results showed that the steady-state effectiveness of the full-scale LAMEE is almost 82% under selected summer test condition.

The similarity requirements between the small-scale LAMEE and the full-scale LAMEE are not completely satisfied in this research. The geometric similarity is not satisfied in the scaling of the small-scale LAMEE. The air and solution channels thicknesses are kept the same in the full-scale and the small-scale LAMEEs (the air and solution channels thicknesses are 5 mm and 2.4 mm, respectively, in the small-scale and full-scale LAMEEs) due to the LAMEE design constraints to minimize the pressure drop in the air and solution channels of the LAMEE (Seyed-Ahmadi *et al.*, 2009a; Seyed-Ahmadi *et al.*, 2009b; Vali *et al.*, 2009; Hemingson *et al.*, 2011b). If the air and solution channels thicknesses in the small-scale LAMEE are scaled down with the same ratio as other dimensions (i.e. exchanger length and width), some of the LAMEE's main parts such as the air screen would not be possible to be manufactured due to size limitations. However, other similarity requirements such as momentum (i.e. Reynolds number and Prandtl number), thermal (i.e. Nusselt number) and mass transfer (i.e. Sherwood number) similarities are satisfied in scaling of the small-scale LAMEE. Thus, complete similarity

was not be established between the small-scale and full-scale LAMEEs, and the small-scale LAMEE results cannot be directly used for the full-scale LAMEE. However, it is possible to predict the full-scale LAMEE performance within a certain uncertainty from the small-scale LAMEE effectiveness results using the dimensional analysis results of LAMEEs.

This chapter focuses on investigating and proving a similarity between the small-scale LAMEE and the full-scale LAMEE. The important dimensionless parameters which have significant effect on the steady-state LAMEE performance are identified, and dimensional analysis is used to investigate the effect of each important dimensionless parameter on the steady-state performance of the LAMEE. The similarity between the small-scale LAMEE and the full-scale LAMEE is investigated numerically and experimentally in this chapter. The results of this chapter will guide researchers and manufacturers to test small-scale exchangers (i.e. LAMEEs, energy wheels and hollow fiber contactors), and use their results to predict the performance of full-scale exchangers.

6.4   Test Facility

Two different test facilities are used in this research to test the small-scale single-panel LAMEE and the full-scale LAMEE. These two test facilities are introduced in this section.

6.4.1   Single Panel Energy Exchanger Test (SPEET) Facility

A single-panel energy exchanger test (SPEET) facility was designed and built to evaluate the performance of a small-scale LAMEE under different operating conditions. The SPEET facility can be used to conduct a wide range of experiments on small-scale LAMEEs and other kinds of small-scale liquid-to-air energy exchangers. Also, the

SPEET facility provides better control in experiments on small-scale LAMEEs since the SPEET facility provides less uncertainty and variation in operating parameters in comparison to a full-scale LAMEE test facility (see Section 6.4.2). A complete description of the SPEET facility is presented in Ghadiri Moghaddam *et al.* (2013a, 2013b), and is briefly introduced in this section. The SPEET facility includes three main sections: a supply air system to control the supply airflow rate, temperature and humidity content; an open solution loop to control the solution flow rate, temperature and concentration; and the small-scale LAMEE located in the test section of the facility. Figure 6.1 shows a schematic of the SPEET facility.

In the supply air system, high pressure dry air (~4%RH) provided by a compressor passes through a flow controller and a flow meter with a capacity of 100 L/min and uncertainties of ±2% and ±1% of full-scale, respectively. The flow controller and the flow meter are used to adjust and measure the supply air flow rate. The supply air then passes through two bubble tank humidifiers and a heater to achieve the desired supply air temperature and humidity. The heater and the humidifiers can adjust the air inlet temperature and humidity ratio between 15°C and 50°C, and 1 and 28 g_w/kg_{air}, respectively, when the supply air flow rate is in the range of 10 to 100 L/min. The supply air humidity ratio is measured after the heater by two humidity sensors with an uncertainty of ±1.5%RH, and a flow mixer is used before the humidity sensors to provide accurate readings for the humidity sensors. Two converging-diverging air headers are used before and after the small-scale LAMEE to supply air uniformly through the exchanger and exhaust it to the lab. Two T-type thermocouples with an uncertainty of ±0.2˚C are used in the supply air headers to measure the supply air temperature at the air

182

inlet of the LAMEE. Two T-type thermocouples are used in the exhaust air header to measure the exhaust air temperature after the small-scale LAMEE. Also, two humidity sensors and a mixer are used in the exhaust air pipeline to measure the relative humidity of the exhaust air. The locations of the instrumentation for the air and solution sides are shown in Figure 6.1.

In the open solution loop, LiCl salt solution is pumped from a supply solution tank to the small-scale LAMEE solution inlet header using a peristaltic pump. An electrical heater is used after the pump to adjust the salt solution temperature to the desired condition. Two T-type shielded thermocouples with an uncertainty of ±0.1°C are placed in the solution inlet and outlet headers to measure the solution inlet and outlet temperatures, respectively. The outlet salt solution is exhausted into a solution exhaust tank. For each test, the salt solution concentrations at the inlet and outlet of the LAMEE are measured under steady-state operating conditions, respectively.

A small-scale single-panel LAMEE with a counter-cross flow configuration for the air and solution is used in this study. A flat plate LAMEE consists of many single panels. Each single panel LAMEE consists of a single pair of neighboring air and liquid channels. The small-scale single-panel LAMEE minimizes the sources of errors in the LAMEE performance evaluation, and facilitates research and development of LAMEEs by saving the money and time required to build full-scale LAMEEs (Ghadiri Moghaddam *et al.*, 2013a; Ghadiri Moghaddam *et al.*, 2013b). The solution flows from top to bottom in the small-scale LAMEE. Figure 6.2(a) shows the air and solution flow configurations. Two grooved plastic panels are used on the sides of the LAMEE and two semi-permeable membranes are attached to them to form the solution channels inside the small-scale

183

LAMEE. These two grooved side panels are placed beside each other, with an air spacer in between to form the air channel. An air screen is used inside the LAMEE to enhance the air side heat transfer performance. The air screen and its effects on the air-side convective heat transfer coefficient and the performance of the small-scale LAMEE are discussed in detail in Ghadiri Moghaddam *et al.* (2013c). Figure 6.2(b) shows the details of the single-panel LAMEE design. The small-scale single-panel LAMEE specifications and membrane properties are presented in Table 6-1. The small-scale LAMEE design and the SPEET facility are introduced in detail in Ghadiri Moghaddam *et al.* (2013a) and Ghadiri Moghaddam *et al.* (2013b). Mass and energy balance results show that the SPEET facility is balanced and working at steady-state condition (Ghadiri Moghaddam *et al.*, 2013a, 2013b).
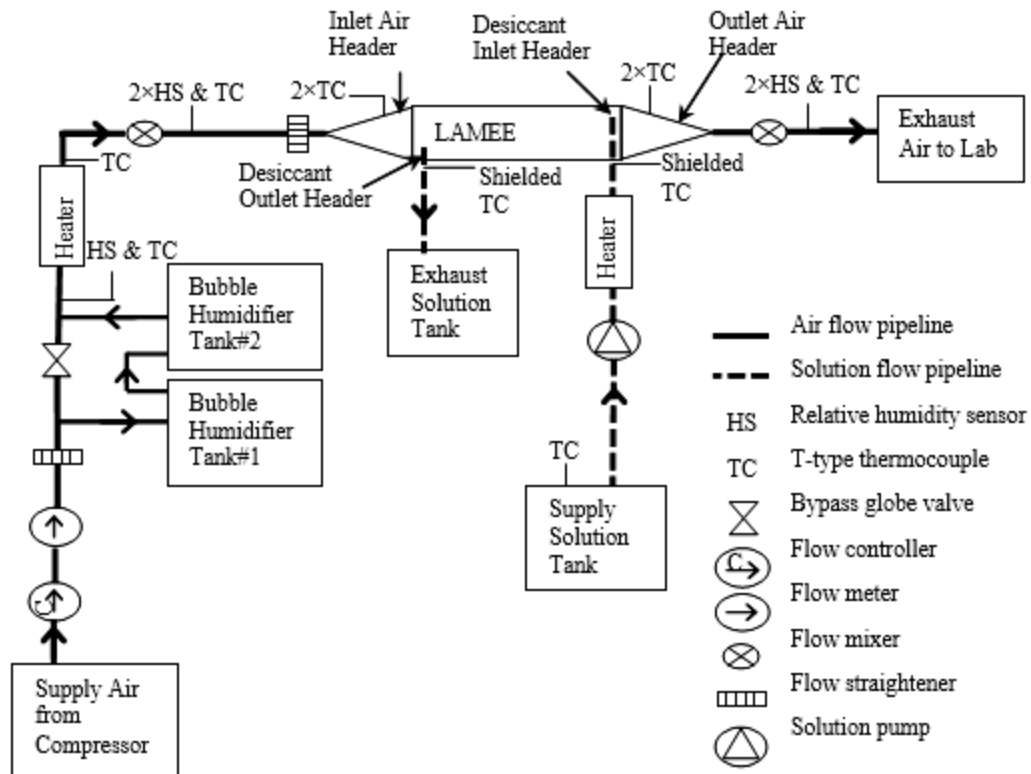
Figure 6.1 Schematic of the SPEET facility and instrumentation locations (Ghadiri Moghaddam *et al.*, 2013b)

184
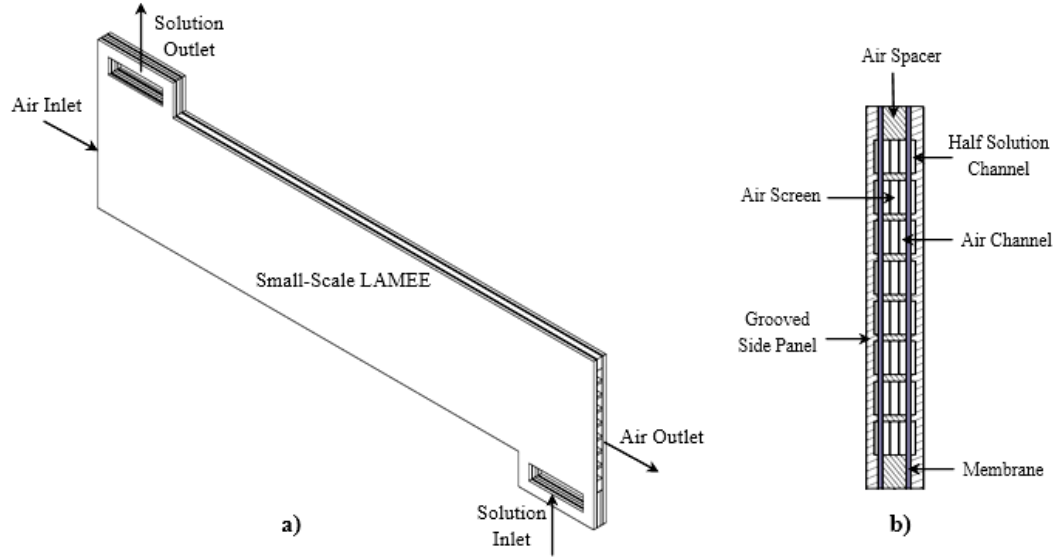
Figure 6.2 (a) Air and solution flow configurations and (b) a cross-section view of the small-scale single-panel LAMEE (Ghadiri Moghaddam *et al.*, 2013b)

Table 6-1 The small-scale single-panel LAMEE and the full-scale LAMEE specifications and the membrane properties

Parameter	Small-scale LAMEE	Full-scale LAMEE
Exchanger length, (m)	0.99	1.06
Exchanger aspect ratio (length/width)	10.5	1.4
Exchanger entrance ratio (entrance length/exchanger length)	0.025	0.01
Air gap thickness, (mm)	5	5
Solution gap thickness, (mm)	2.4	2.4
Number of solution panels in the exchanger	1	10
Maximum air flow rate capacity, (L/s)	2.5	100
Water vapor mass resistance of membrane, (s/m)	24	24
Membrane thermal conductivity, (W/mK)	0.065	0.065
Membrane thickness, (mm)	0.265	0.265
Total membrane active area, (m^2)	0.17	14.27

6.4.2   Full-Scale LAMEE Test Facility

To investigate similarity between a small-scale and a full-scale LAMEE, it is necessary to conduct experiments on a full-scale LAMEE with similar design as the small-scale LAMEE. A full-scale (100 L/s) LAMEE with similar design as the small-scale LAMEE and with 10 solution panels was tested at the University of Saskatchewan.

The detailed design and dimensions of the full-scale LAMEE are presented in Table 6-1. Figure 6.3 shows a schematic of the test facility at the University of Saskatchewan which is modified to test the full-scale LAMEE. The full-scale LAMEE and the test facility are introduced in Ghadiri Moghaddam *et al.* (2013d) in detail. Also, the mass and energy balances results for the full-scale LAMEE test facility are presented in Ghadiri Moghaddam *et al.* (2013d), and the results show that the test facility is balanced and working at steady-state condition. The full-scale LAMEE test facility consists of three sections: a supply air system, an open solution loop and the full-scale LAMEE.
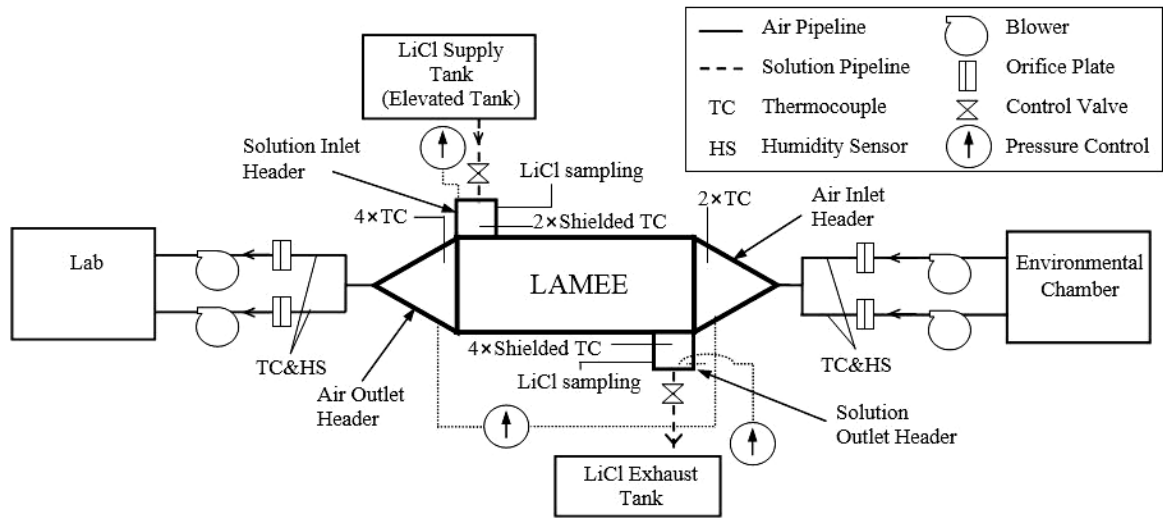
Figure 6.3 Schematic of the full-scale LAMEE test facility (Ghadiri Moghaddam *et al.*, 2013d)

An environmental chamber is used to simulate the outdoor air conditions for the supply air stream, and is able to provide air between -40˚C and +40˚C and up to 90%RH. The conditioned air is supplied in two air pipelines using two vacuum fans. The supply air passes through the exchanger, and is exhausted to the lab. In the full-scale LAMEE test facility, the air flow rate in each of the air pipelines is measured using an orifice plate. The air inlet and outlet temperatures are measured at the air inlet and outlet headers

186

using T-type thermocouples with an uncertainty of ±0.2˚C, while the air inlet and outlet relative humidities in the test facility are measured in each pipeline before and after the orifice plates using Vaisala humidity sensors (model HMP233) with an uncertainty of ±1.2%RH. The air pressure drop is measured across the full-scale LAMEE with a pressure transducer (Validyne, model P305D), which has an uncertainty of ±1.5 Pa.

In the open solution loop, the LiCl solution flows from an elevated supply solution tank through the exchanger, and is collected in a solution exhaust tank at the exchanger outlet. The solution flow rate in the full-scale LAMEE is controlled by using two control valves after the supply tank and the LAMEE, and it is measured manually. The solution inlet and outlet pressures are monitored in the full-scale LAMEE solution inlet and outlet headers, with two monometers. The solution inlet and outlet temperatures in the LAMEE solution inlet and outlet headers are measured using shielded T-type thermocouples with an uncertainty of ±0.2˚C. Also, LiCl samples from the solution inlet and outlet headers are used to measure the solution concentration at the solution inlet and outlet headers.

6.5 Experimental Data

The small-scale LAMEE and the full-scale LAMEE have been tested under various test conditions. The experimental and numerical performance of the small-scale LAMEE are presented in Ghadiri Moghaddam *et al.* (2013a) and Ge *et al.* (2014). Details of the small-scale LAMEE testing and the test conditions are presented in Ge *et al.* (2014). These experimental results, which are presented in Ge *et al.* (2014), are used in this chapter to investigate similarity between the small-scale LAMEE and the full-scale LAMEE.

The full-scale LAMEE has been tested under summer (i.e. air cooling and dehumidifying) and winter (i.e. air heating and humidifying) test conditions, and the experimental and numerical performance results for the full-scale LAMEE are presented in Ghadiri Moghaddam *et al.* (2013d). The experimental results for the full-scale LAMEE tested under summer test conditions are presented in the result section of this chapter to investigate similarity between the small-scale LAMEE and the full-scale LAMEE.

6.6   Numerical Modeling of a LAMEE

The enthalpy pump system (EPS) code (Seyed-Ahmadi *et al.*, 2009a; Seyed-Ahmadi *et al.*, 2009b; Vali *et al.*, 2009) has been developed in the LAMEE research group at the University of Saskatchewan to model the performance of LAMEEs under different test conditions. Ghadiri Moghaddam *et al.* (2013d) used the EPS code to numerically evaluate the performance of the full-scale LAMEE under summer and winter test conditions. The EPS code is used in this chapter to evaluate the effectiveness of the full-scale LAMEE under summer test conditions, and the full-scale LAMEE numerical results are validate with experimental data under certain test conditions in the result section. Also, Ghadiri Moghaddam *et al.* (2013c) modified the EPS code based on the small-scale LAMEE design, and validated the numerical results with the experimental data for the small-scale LAMEE presented in Ghadiri Moghaddam *et al.* (2013a) for the steady-state test conditions. The important modifications in the modified EPS code which affect the model are discussed in detail in Ghadiri Moghaddam *et al.* (2013c). The modified EPS code is used in this chapter to numerically model the small-scale LAMEE performance under different operating conditions. The modified EPS code is introduced in detail in Ghadiri Moghaddam *et al.* (2013c).

6.7 LAMEE Performance Evaluation

The performance of a LAMEE is evaluated by its sensible, latent and total effectivenesses. Sensible, latent and total effectivenesses are defined as sensible (heat), latent (moisture) and total (sensible + latent) energy transferred in the exchanger over the maximum possible sensible, latent and total energy transfer in the exchanger, respectively. Sensible, latent and total effectivenesses are calculated by the following equation when $Cr^* \geq 1$:

$$\varepsilon_{sensible,\ latent\ or\ total} = \frac{\left(Y_{air,in} - Y_{air,out}\right)}{\left(Y_{air,in} - Y_{sol,in}\right)} \qquad (6.1)$$

Here, Y is temperature (T) for the sensible effectiveness, humidity ratio (W) for the latent effectiveness and enthalpy (H) for the total effectiveness. Cr^* is the thermal capacity ratio, and is introduced in Eq. (6.11). For the total effectiveness, it is not possible to simply subtract the air and solution enthalpies from each other since the reference points to calculate the air and solution enthalpies are different. As a result, the total effectiveness of the LAMEE, which is related to both sensible and latent energy transfers, is calculated as follows (Simonson and Besant, 1999):

$$\varepsilon_{total} = \frac{\varepsilon_{sensible} + H^* \varepsilon_{latent}}{1 + H^*} \qquad (6.2)$$

Here, H^* is the operating condition factor, and is calculated based on the air and the salt solution inlet temperatures and humidity ratios in the LAMEE (Ghadiri Moghaddam *et al.*, 2013c; Simonson and Besant, 1999). The definition of H^* is introduced in Eq. (6.14).

6.8 Dimensional Analysis of the LAMEE

The purpose of this section is to perform a dimensional analysis of the LAMEE, and determine the important dimensionless parameters that affect its performance. The coupled heat and mass transfer in the air, solution and membrane of the LAMEE is numerically modeled in the EPS code and modified EPS code to calculate the steady-state effectiveness of the LAMEE under different operating conditions. The dimensionless heat and mass transfer equations in the air and solution sides of the LAMEE are (Ghadiri Moghaddam *et al.*, 2013c):

- Air-side:

  o Heat transfer:

$$\frac{d\theta_{air}}{dx^*} + 2NTU\left(\theta_{air} - \theta_{sol}\right) = 0 \tag{6.3}$$

  o Mass transfer:

$$\frac{d\phi_{air}}{dx^*} + 2NTU_m\left(\phi_{air} - \phi_{sol,mem}\right) = 0 \tag{6.4}$$

- Solution-side:

  o Heat transfer:

$$\frac{d\theta_{sol}}{dx^*} - NTU_m H^* Cr\left(\phi_{air} - \phi_{sol,mem}\right) - NTU\ Cr\left(\theta_{air} - \theta_{sol}\right) = 0 \tag{6.5}$$

  o Mass transfer:

$$\frac{dX_{sol}}{dx^*} - W_0 NTU_m\ m^*\left(1 + X_{sol}\right)\left(\phi_{air} - \phi_{sol,mem}\right) = 0 \tag{6.6}$$

In Eq. (6.6), W_0 is equal to $(W_{sol,in} - W_{air,in})$ and is a constant for each test condition. The following dimensionless parameters are used to nondimensionalize the coupled heat and mass transfer equations in the air and solution sides of the LAMEE (see Eqs. (6.3) to (6.6)):

$$x^* = \frac{x}{x_0} \tag{6.7}$$

$$\theta = \frac{T - T_{air,in}}{T_{sol,in} - T_{air,in}} \tag{6.8}$$

$$\phi = \frac{W - W_{air,in}}{W_{sol,in} - W_{air,in}} \tag{6.9}$$

$$NTU = \frac{UA}{C_{min}} = \frac{UA}{(\dot{m}c_P)_{air}} \tag{6.10}$$

$$Cr = \frac{C_{min}}{C_{max}} = \frac{(\dot{m}c_p)_{air}}{(\dot{m}c_p)_{sol}} = \frac{1}{Cr^*} \tag{6.11}$$

$$NTU_m = \frac{U_m A}{\dot{m}_{min}} = \frac{U_m A}{\dot{m}_{air}} \tag{6.12}$$

$$m^* = \frac{\dot{m}_{min}}{\dot{m}_{max}} = \frac{\dot{m}_{air}}{\dot{m}_{sol}} \tag{6.13}$$

$$H^* = \frac{(W_{sol,in} - W_{air,in})}{(T_{sol,in} - T_{air,in})} \frac{h_{fg}}{c_{P,air}} \tag{6.14}$$

Here, θ, ϕ and x^* are the dimensionless temperature, humidity content and length in the LAMEE, respectively. NTU and Cr are the number of heat transfer units and thermal capacity ratio. Cr^* is used in this research as the thermal capacity ratio which is the inverse of Cr for $C_{sol} > C_{air}$. NTU_m and m^* are the number of mass transfer units and mass flow rate ratio, respectively. H^* is the operating factor, and is the ratio of the maximum possible latent energy over the maximum possible sensible energy transfers between the air and salt solution in the LAMEE (Simonson and Besant, 1999). U in Eq.

(6.10) and U_m in Eq. (6.12) are the overall convective heat transfer coefficient and the overall convective mass transfer coefficient, respectively, and are calculated as follows:

$$U = \left[\frac{1}{h_{air}} + \frac{\delta}{k_{mem}} + \frac{1}{h_{sol}} \right]^{-1} \qquad (6.15)$$

$$U_m = \left[\frac{1}{h_{m,air}} + \frac{\delta}{k_{m,mem}} \right]^{-1} \qquad (6.16)$$

The air and solution sides convective heat and mass transfer coefficients are calculated from the air and solution sides Nusselt and Sherwood numbers, respectively. The air and the solution sides convective heat and mass transfer convective coefficients calculations are discussed in detail in Ghadiri Moghaddam *et al.* (2013c). The solution-side convective mass transfer coefficient has a negligible effect on the overall convective mass transfer coefficient in comparison to the air-side convective mass transfer coefficient and the membrane mass transfer resistance. Thus, the solution-side convective mass transfer coefficient is neglected in calculating the overall convective mass transfer coefficient in LAMEEs (see Eq. (6.16)). The other parameters which are used in Eqs. (6.3) to (6.16) are introduced in the nomenclature section of this chapter.

The dimensional analysis of the coupled heat and mass transfer in the LAMEE shows that the steady-state performance of a LAMEE is a function of six important dimensionless parameters.

$$\varepsilon_{total,steady} = \text{Function}\left(NTU, NTU_m, Cr^*, m^*, H^*, \text{ flow arrangment} \right) \qquad (6.17)$$

NTU and *Cr** directly affect the sensible effectiveness of the LAMEE, when the sensible effectiveness of the LAMEE is calculated from the air inlet and outlet temperatures and solution inlet temperature (see Eq. (6.1)). On the other hand, NTU_m and

*m** directly affect the latent effectiveness of the LAMEE while the latent effectiveness of the LAMEE is calculated from the air inlet and outlet humidity ratios and solution inlet equivalent humidity ratio (see Eq. (6.1)). *H** and the flow arrangement have effects on both the sensible and latent effectivenesses of the LAMEE. Equation (6.2) shows that the total effectiveness of the LAMEE is dependent on the sensible effectiveness, latent effectiveness, flow arrangement and *H**. Consequently, if similarity is established between the sensible and latent effectivenesses of the small-scale and the full-scale LAMEEs, then the small-scale LAMEE total effectiveness must also be similar to the full-scale LAMEE. Thus, this chapter mainly focuses on the similarity between the small-scale LAMEE and the full-scale LAMEE sensible and latent effectivenesses. Also, the effect of the flow arrangement on the LAMEE effectiveness is neglected in this study since the air and solution flow arrangement in both the small-scale LAMEE and the full-scale LAMEE are counter-cross flow, and a counter-cross flow arrangement is common for LAMEEs.

6.9 Results and Discussion

In the results section, the experimental and numerical effectiveness results for the full-scale LAMEE are presented under summer test conditions (i.e. air cooling and dehumidifying (C&D)). After that, the modified EPS code which was introduced in Ghadiri Moghaddam *et al.* (2013c), and was verified with the experimental data for the small-scale LAMEE under different test conditions (Ghadiri Moghaddam *et al.*, 2013c), is used to investigate the effect of the important dimensionless parameters (*NTU*, NTU_m, *Cr**, *m** and *H**), on the small-scale LAMEE sensible, latent and total effectivenesses.

Finally, the similarity between the small-scale LAMEE and the full-scale LAMEE is investigated both numerically and experimentally.

6.9.1 Full-scale LAMEE Results

The full-scale LAMEE is tested under summer test conditions (i.e. air cooling and dehumidifying). Four tests are conducted with the full-scale LAMEE under C&D conditions. LiCl is used as the transfer liquid in the LAMEE. The mass and energy balance results for these tests are presented in Ghadiri Moghaddam *et al.* (2013d). The air and solution inlet conditions and the value of the important dimensionless parameters (NTU, NTU_m, Cr^*, m^* and H^*) for the full-scale LAMEE under C&D test conditions are presented in Table 6-2. These four tests are labeled as F1, F2, F3 and F4 in Table 6-2. The air and solution inlet conditions and the operating parameters for these 4 tests are slightly different from each other due to control issues in the full-scale LAMEE test facility. Based on the data in Table 6-2, the NTU and Cr^* for these 4 summer tests vary between 5 and 5.9, and 2.8 and 4, respectively.

The experimental and numerical sensible, latent and total effectivenesses of the full-scale LAMEE under C&D test conditions are presented in Figure 6.4. The mal-distribution and buoyancy effects are neglected in the numerical modeling of the full-scale LAMEE. The results in Figure 6.4 shows good agreement between the experimental and numerical sensible, latent and total effectivenesses of the full-scale LAMEE under the C&D test conditions. The experimental and numerical effectiveness results agree within uncertainty ranges for these tests. Also, Figure 6.4 shows that the effectiveness of the full-scale LAMEE increases with both NTU from 5 to 6 at almost constant $Cr^*\approx4$ (see tests F2, F3 and F4) and Cr^* from 2.8 to 4.2 at constant $NTU = 5$ (see tests F1 and F2).

The maximum sensible, latent and total effectivenesses for the full-scale LAMEE are 86%, 87% and 87%, respectively, which occur during test F4 which has the highest *NTU* and *Cr** values.

Table 6-2 The full-scale LAMEE summer test conditions (air cooling and dehumidifying)

Test	*NTU*	*Cr**	*NTU*$_m$	*m**	*H**	$T_{air,in}$ (°C)	$W_{air,in}$ (g/kg)	$T_{sol,in}$ (°C)	$W_{sol,in}$ (g/kg)	$C_{sol,in}$ (%)
F1	5	2.8	3	0.37	3	38.8	21.4	26.7	6.8	33.6
F2	5	4.2	3	0.47	1.9	35.4	16	25.2	8.3	30.2
F3	5.5	3.9	3.2	0.45	2	36.3	17.6	23.7	7.7	30
F4	5.9	4	3.6	0.46	2.8	35.4	21	23.3	7.3	30.3
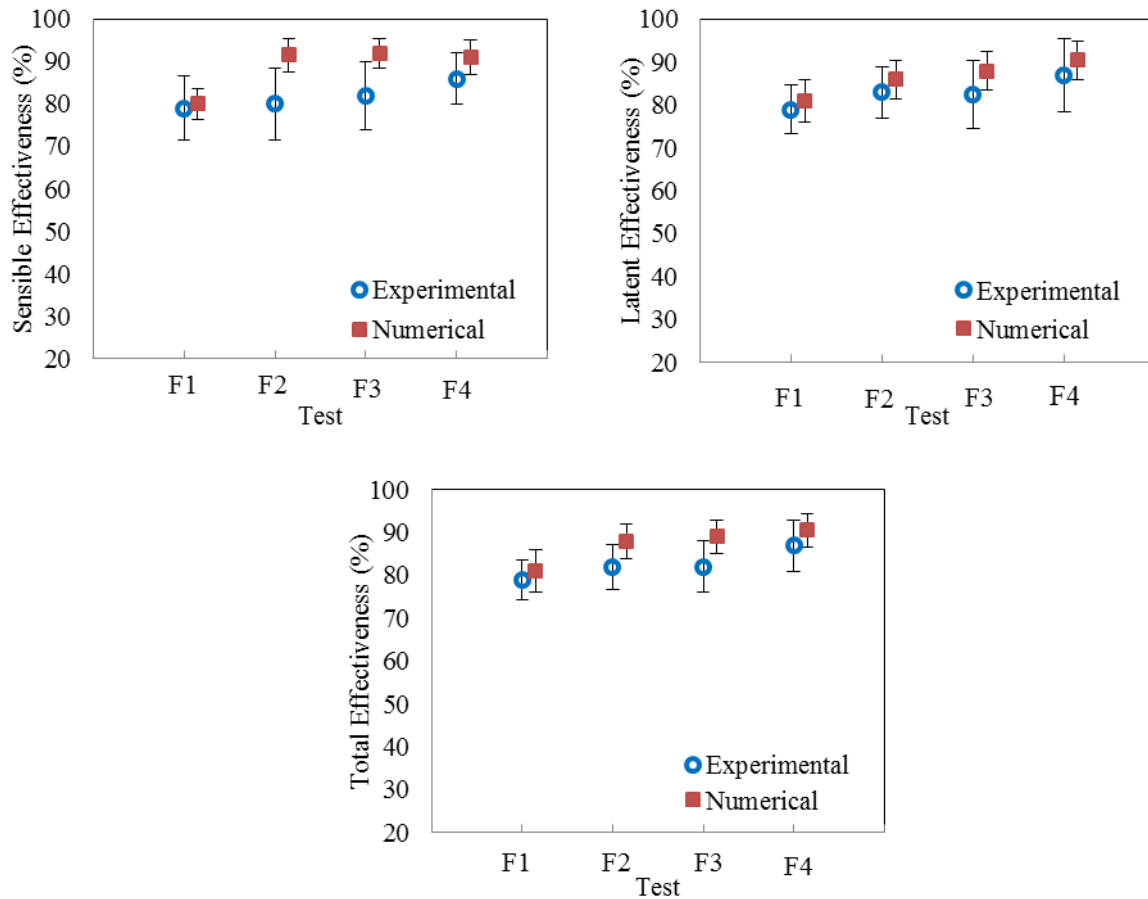
Figure 6.4 Numerical and experimental sensible, latent and total effectiveness results of the full-scale LAMEE, under summer test conditions (air cooling and dehumidifying) using LiCl solution

195

6.9.2   Effect of Important Dimensionless Parameters on a LAMEE Performance

In this section, the effect of the important dimensionless parameters presented in Section 6.8 on the sensible, latent and total effectivenesses of the small-scale LAMEE are investigated. The modified EPS code is used to simulate the performance of the small-scale LAMEE under different test conditions. These important dimensionless parameters are the (1) number of heat transfer units, NTU, (2) thermal capacity ratio, Cr^*, (3) number of mass transfer units, NTU_m, (4) mass flow rate ratio, m^*, and (5) operating factor, H^*. As mentioned in Section 6.8, NTU and Cr^* directly affect the sensible effectiveness of the LAMEE, while NTU_m and m^* directly affect the latent effectiveness of the LAMEE. H^* has effects on both the sensible and latent effectivenesses of the LAMEE.

Table 6-3 shows the reference test conditions that are selected for a parametric study of the important dimensionless parameters, and the range of study of each parameter. The air inlet conditions are set to AHRI summer conditions (ANSI/AHRI standard 1060, 2011), and the solution inlet conditions are $T_{sol,in} = 24°C$ and $C_{sol,in} = 32\%$ which represents the small-scale LAMEE under C&D conditions (these reference test conditions are also used in the next section to investigate similarity between the small-scale LAMEE and the full-scale LAMEE). In the parametric study, one dimensionless parameter is varied in the range of study shown in Table 6-3, while the other dimensionless parameters are kept constant at the reference value. Figure 6.5 shows the effect of NTU and Cr^* on the numerical sensible effectiveness of the small-scale LAMEE at steady-state conditions. The results show that the sensible effectiveness of the small-scale LAMEE increases with both NTU and Cr^*. For NTU and Cr^* values higher than 3,

NTU and *Cr** have almost the same impact on the sensible effectiveness of the small-scale LAMEE. Figure 6.5 also shows that, for *NTU* and *Cr** values higher than 5, the sensible effectiveness of the small-scale LAMEE slightly increases (i.e. the sensible effectiveness of the small-scale LAMEE increases by 5% for *NTU* and *Cr** values between 5 and 7).

Table 6-3 Reference test conditions to do the parametric study for the small-scale LAMEE, and to investigate the similarity between the small-scale LAMEE and the full-scale LAMEE

Parameter	Reference value	Range of Study
NTU	4	1~7
Cr*	4	1~7
NTU$_{m}$	2.2	1~7
m*	0.5	0.1~2.5
H*	2.5	-8~8
$T_{air,in}$ (℃)	35	-
$W_{air,in}$ (g/kg)	17.5	-
$T_{sol,in}$ (℃)	24	-
$C_{sol,in}$ (%)	32	-
Salt solution type	LiCl	-
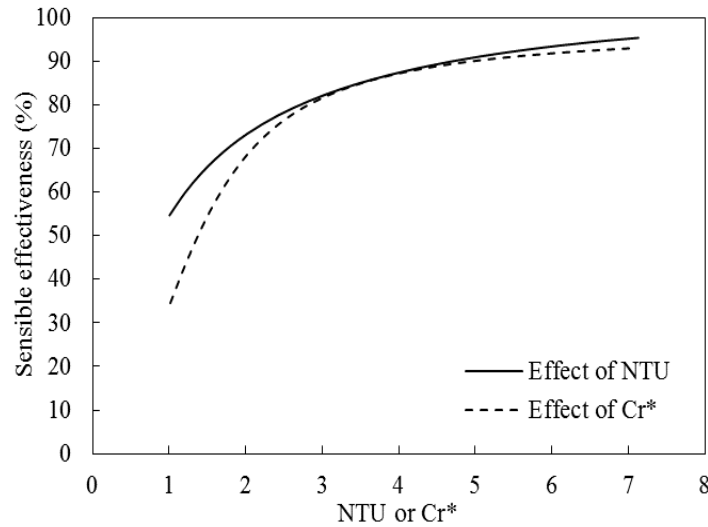
Figure 6.5 The effect of *NTU* and *Cr** on the sensible effectiveness of the small-scale LAMEE under reference test conditions

Figure 6.6 shows the effect of *NTU*$_{m}$ and *m** on the latent effectiveness of the small-scale LAMEE under summer AHRI test conditions. The effect of *NTU*$_{m}$ on the

latent effectiveness is similar to the effect of *NTU* on the sensible effectiveness of the

LAMEE. The latent effectiveness increases with NTU_m, and for NTU_m values higher than

five the effect of NTU_m on the latent effectiveness of the small-scale LAMEE is small

(i.e. less than 5%). Also, Figure 6.6 shows that the latent effectiveness of the small-scale

LAMEE increases with *m**. The effect of *m** on the latent effectiveness of the LAMEE

can be divided into two regions: (1) *m*<0.5* where a small change in the *m** value has a

significant effect on the latent effectiveness, and (2) *m*≥0.5* where the effect of *m** on

the latent effectiveness of the LAMEE is negligible.
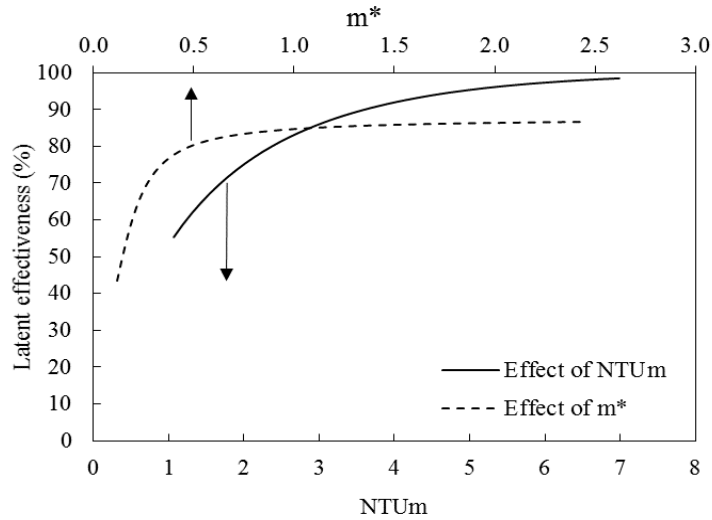
Figure 6.6 The effect of *NTU*m and *m** on the latent effectiveness of the small-scale LAMEE under reference test conditions

Figure 6.7 shows the effect of the operating factor, *H**, on the sensible, latent and

total effectivenesses of the small-scale LAMEE under summer AHRI test conditions,

when *H** varies between -8 and 8. This will cover a practical range of air and solution

inlet conditions for the LAMEE. The results in Figure 6.7 show that the sensible

effectiveness of the small-scale LAMEE linearly decreases from 125% to 68% by

increasing *H** from -8 to 8. The latent effectiveness of the small-scale LAMEE is almost

constant at 83% when *H** changes between -8 and 0. The latent effectiveness increases to

$\pm\infty$ when $H^* = 0$. This is because H^* is equal to zero when the air inlet humidity ratio and the equivalent solution inlet humidity ratio are equal, so the maximum potential moisture transfer is zero. However, due to coupled heat and mass transfer in the LAMEE, there is a small amount of moisture transfer along the exchanger when $H^* = 0$. For H^* values between 0 and 8, the latent effectiveness of the small-scale LAMEE is again almost constant, and equal to 80%. The effect of H^* on the total effectiveness of the small-scale LAMEE is similar to the effect of H^* on the latent effectiveness. The total effectiveness is almost constant when H^* increases from -8 to -1. The total effectiveness is between 72% and 75% when $-8 < H^* < -1$. The total effectiveness tends to $\pm\infty$ at $H^* = -1$ because the inlet air and solution have the same enthalpy. For the H^* values higher than -1, the
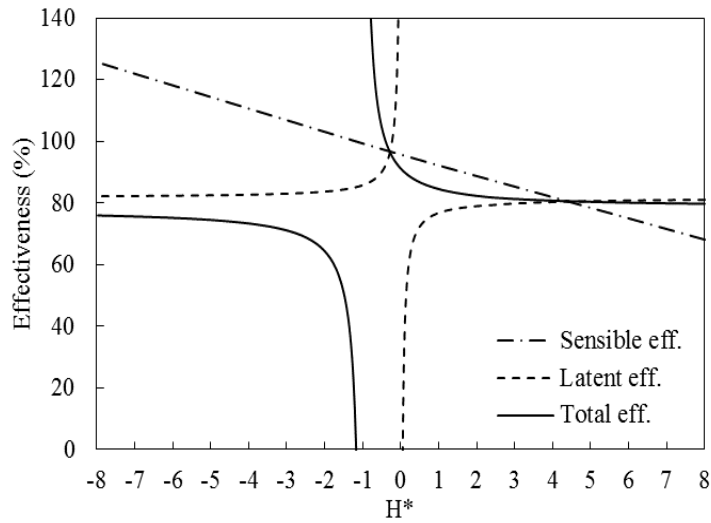
total effectiveness of the small-scale LAMEE is again almost constant and equal to 83%.

Figure 6.7 The effect of H^* on the sensible, latent and total effectivenesses of the small-scale LAMEE under reference test conditions

6.9.3 Investigating Similarity between the Small-Scale and Full-Scale LAMEEs

In this section, the experimental and numerical results are used to determine that the small-scale LAMEE and the full-scale LAMEE are similar.

6.9.3.1 Experimental Results

The experimental sensible, latent and total effectiveness results of the full-scale LAMEE for tests F2, F3 and F4, which are presented in Table 6-2, are compared with the experimental effectiveness results for the small-scale LAMEE at almost the same test conditions. The air and solution inlet conditions and the value of the important dimensionless parameters for the small-scale LAMEE under C&D test conditions are presented in Table 6-4. The LiCl solution is used as the transfer liquid in both the small-scale LAMEE and the full-scale LAMEE.

Table 6-4 The small-scale LAMEE test operating conditions under summer test conditions (air cooling and dehumidifying)

Test	NTU	Cr^*	NTU_{m}	m^*	H^*	$T_{air,in}$ (°C)	$W_{air,in}$ (g/kg)	$T_{sol,in}$ (°C)	$W_{sol,in}$ (g/kg)	$C_{sol,in}$ (%)
S1	5	4	3	0.47	3.1	30.1	14.3	24	6.7	32.1
S2	5.5	4	3.3	0.47	3.1	30.1	14.3	24.1	6.7	32.1
S3	6	4	3.5	0.47	3.1	30	14.3	24	6.8	32

Figure 6.8 compares the experimental sensible, latent and total effectivenesses of the small-scale LAMEE and the full-scale LAMEE under summer test conditions at Cr^* = 4 and NTU = 5, 5.5 and 6. Figure 6.8 shows that the small-scale LAMEE and full-scale LAMEE sensible, latent and total effectiveness results agree within the 95% uncertainty bounds. Also, the results in Figure 6.8 show that the sensible, latent and total effectivenesses increase with NTU for both the small-scale LAMEE and the full-scale LAMEE. The experimental results that are presented in Figure 6.8 prove the similarity between the small-scale LAMEE and the full-scale LAMEE for these three test cases.
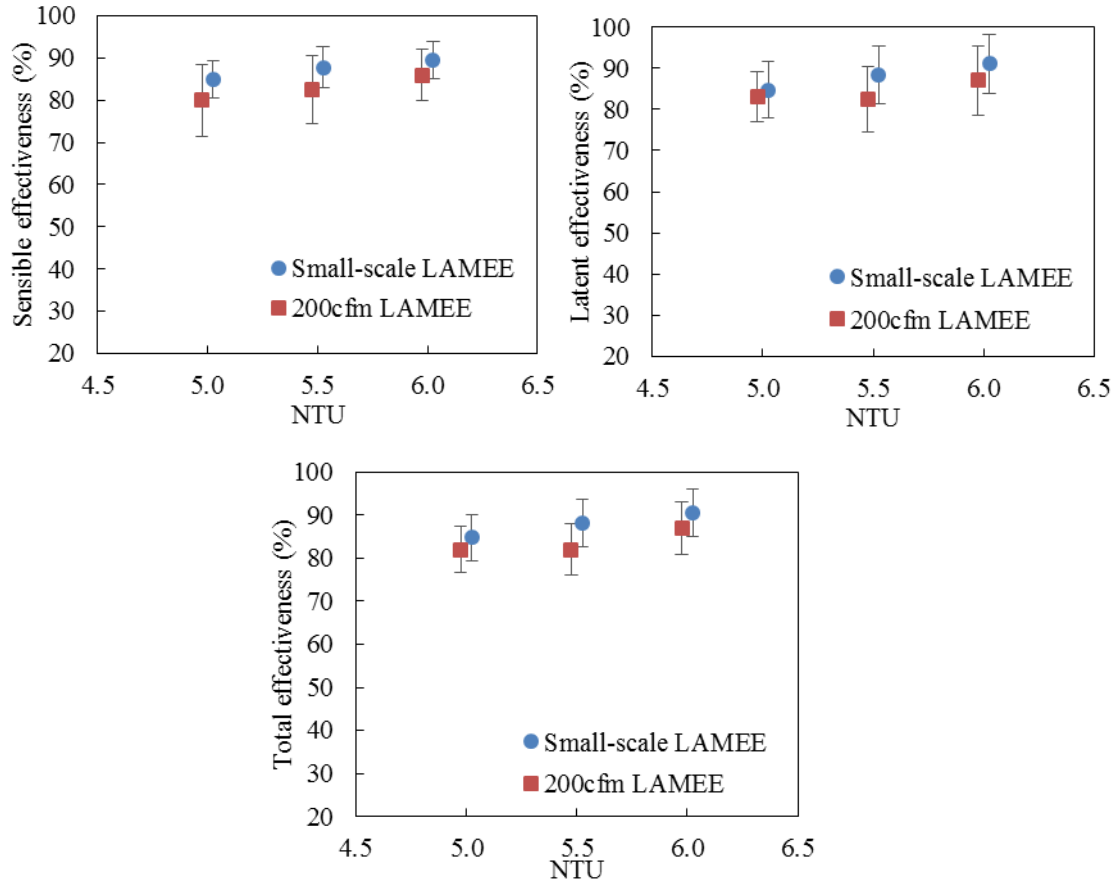
Figure 6.8 Comparison between the small-scale LAMEE and the full-scale LAMEE experimental sensible, latent and total effectiveness results under air cooling and dehumidifying test conditions at $Cr^* = 4$

6.9.3.2 Numerical Results

Since testing a LAMEE under a wide range of operating conditions is time consuming, the EPS and the modified EPS numerical models are used in this section to investigate the similarity between the small-scale and full-scale LAMEEs under wide ranges of design and operating conditions (see Table 6-3). The numerical effectiveness results of the small-scale LAMEE and the full-scale LAMEE are compared when one of the important dimensionless parameters is changing and the rest of the important dimensionless parameters are fixed at their reference values (see Table 6-3). The

201

following equation is used to compare the numerical effectiveness results for the small-scale LAMEE and the full-scale LAMEE under different test cases:

$$\Delta\varepsilon_i = \varepsilon_{i,small-scale} - \varepsilon_{i,full-scale}, \tag{6.18}$$

where, ε is the effectiveness and subscript i is the sensible, latent or total effectivenesses.

Figure 6.9 shows the difference between small-scale LAMEE and the full-scale LAMEE numerical sensible effectiveness when NTU and Cr^* vary between 1 and 7. Figure 6.9 shows that the absolute difference between the sensible effectiveness of the small-scale LAMEE and the full-scale LAMEE is less than 2% when NTU or Cr^* vary between 1 and 7. Ideally, the difference between the EPS model effectiveness results for the full-scale LAMEE and the modified EPS code effectiveness results for the small-scale LAMEE at the same test conditions should be almost zero since the heat and mass transfer governing equations for the air, solution and membrane are the same in these two numerical models, and the small-scale and full-scale LAMEEs have similar design. The small differences (see Figures 6.9, 6.10, and 6.11) between the EPS code and the modified EPS code could be because of the following reasons:

- There are different equations available in literature to calculate salt solution properties at different conditions (Afshin, 2010). Salt solution properties equations which are used in the EPS and modified EPS numerical models to calculate the solution properties (i.e. salt solution concentration and enthalpy) at different test cases are different in the EPS code and the modified EPS code. The different salt solution properties equations cause slight differences between the calculated salt solution properties in the EPS code and the

202

modified EPS code, which slightly affect the numerical effectiveness results for the small-scale and full-scale LAMEEs calculated from the modified EPS and EPS codes, respectively.

- In the full-scale LAMEE, the air channels are in the outer sides of the LAMEE, where the heat loss/gain from the surroundings occurs. However, in the small-scale LAMEE the solution channels are in the outer sides of the small-scale LAMEE (see Figure 6.2), where the heat loss/gain from the surroundings occurs. Thus, the heat loss/gain from surroundings is different in the full-scale and small-scale LAMEEs because (1) the thermal properties (i.e. thermal capacity and convective heat transfer coefficient) of the air and solution are different, and (2) the air and solution temperatures in the air and solution sides are different. Thus, the heat loss/gain from the surroundings slightly affect the difference between the small-scale full-scale LAMEEs numerical effectivenesses by almost 0.5%.

- The small-scale single-panel LAMEE consists of one air and one solution channel (the air channel is in the middle of the exchanger and there are two half solution channels on the sides of the exchanger (see Figure 6.2)), while the full-scale LAMEE is consists of 10 single-panels. When these 10 single-panels are placed side by side to create the full-scale LAMEE, they form 10 solution channels and 11 air channels in the full-scale LAMEE. Thus the air flow rate and the air-side heat and mass transfer properties in the air channels of the full-scale LAMEE are slightly different than the air channel in the small-scale LAMEE. This difference between the air flow in the air channel of

the small-scale LAMEE and the air-channels of the full-scale LAMEE has slight effect on the difference between the small-scale LAMEE and the full-scale LAMEE numerical effectivenesses.
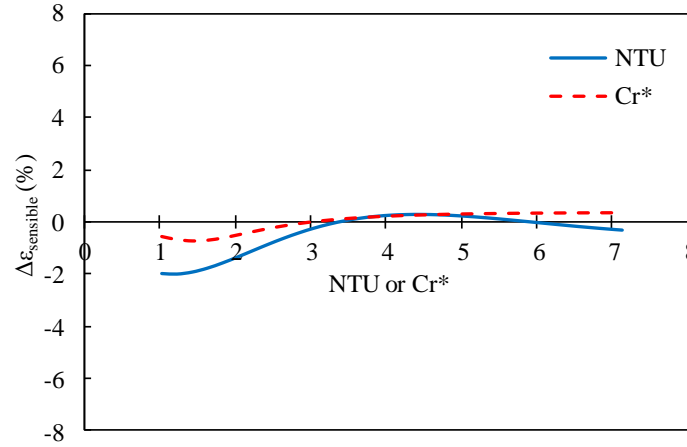
Figure 6.9 The difference in the small-scale LAMEE and full-scale LAMEE sensible effectiveness when *NTU* and *Cr** vary from 1 to 7.

Figure 6.10 shows the latent effectiveness difference between the small-scale LAMEE and the full-scale LAMEE when NTU_m varies between 1 and 7 or m^* varies between 0.1 and 2.5, and the other important parameters are fixed at their reference values (see Table 6-3). The results show that the difference between the small-scale LAMEE and the full-scale LAMEE latent effectiveness is always less than 2% when m^* varies between 0.1 and 2.5. However, the difference between the small-scale LAMEE and the full-scale LAMEE latent effectiveness is always less than 4% when NTU_m varies between 1 and 7. The difference between the small-scale and full-scale LAMEEs numerical latent effectiveness results is less than 2% when $NTU_m > 3$, which can be suggested as the operating range for NTU_m to have good agreement between the small-scale and full-scale LAMEEs numerical latent effectiveness. The reasons for discrepancy between the small-scale and full-scale LAMEEs numerical results are discussed before.
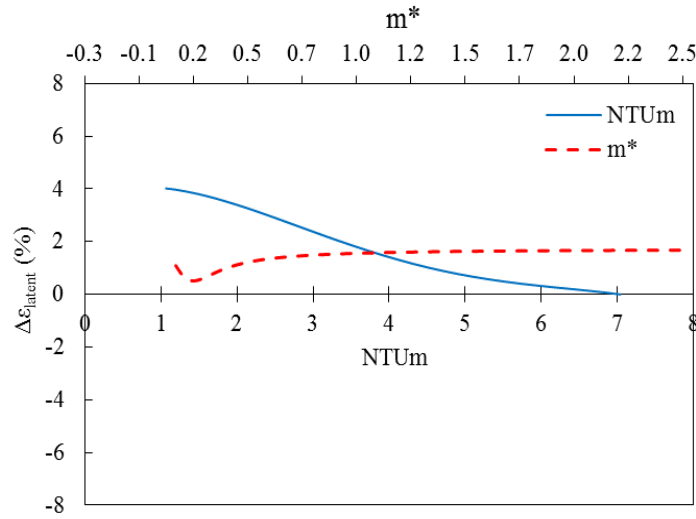
Figure 6.10 The difference in the small-scale LAMEE and full-scale LAMEE latent effectiveness when NTU_m and m^* vary from 1 to 7 and 0.1 to 2.5, respectively.

Figure 6.11 shows the difference between the small-scale LAMEE and the full-scale LAMEE sensible, latent and total effectivenesses when H^* varies between -8 and 8 and the other important dimensionless parameters are fixed at their reference values (see Table 6-3). The results show the differences between the small-scale LAMEE and the full-scale LAMEE sensible and latent effectivenesses are less than 2% when H^* varies from -8 to 8 except when H^* is close to zero for the latent effectiveness. This difference is less than 4% for the total effectiveness in the range of -8 to 8 for H^* except when H^* is close to -1. The differences between the small-scale LAMEE and the full-scale LAMEE latent and total effectivenesses tend to $\pm\infty$ at $H^* = 0$ and $H^* = -1$, respectively. The reasons for this are mentioned in Section 6.9.2, where the small-scale LAMEE sensible, latent and total effectiveness results are presented for different H^* values between -8 and 8 (see Figure 6.7). Finally, Figure 6.11 shows that for $H^* > 0$ the differences between the small-scale and full-scale LAMEEs effectivenesses are less than 2%. Thus, $H^* > 0$ can be suggested as an operating range for H^* to have good agreement between the small-scale and full-scale LAMEEs numerical effectivenesses.
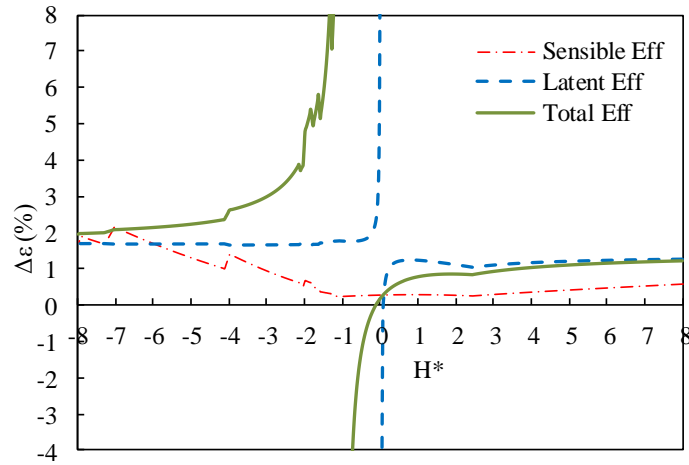
Figure 6.11 The small-scale LAMEE and full-scale LAMEE sensible, latent and total effectiveness differences when *H** is changing from -8 to 8.

The comparisons between the experimental effectiveness results in Section 6.9.3.1 and the numerical effectiveness results in Section 6.9.3.2 for the different important dimensionless parameters show that there is a similarity between the small-scale LAMEE and the full-scale LAMEE. Consequently, the small-scale LAMEE effectiveness results can be used to predict the performance of a full-scale LAMEE under different operating conditions within acceptable uncertainty (i.e. within 2% to 4% uncertainty in most cases based on comparison between the small-scale LAMEE and the full-scale LAMEE numerical effectiveness results).

6.10 Conclusion

The similarity between the small-scale LAMEE and the full-scale (100 L/s air flow rate) LAMEE is investigated numerically and experimentally in this chapter. The dimensional analysis of the coupled heat and mass transfer equations in the air, solution and membrane of a LAMEE shows that there are five important dimensionless parameters (*NTU*, NTU_m, *Cr**, *m** and *H**) that affect the performance of a LAMEE. *NTU* and *Cr** directly affect the sensible effectiveness of the LAMEE while NTU_m and

206

m* directly affect the latent effectiveness of the LAMEE. *H** affects the sensible, latent and total effectivenesses of the LAMEE. The effect of each of the important dimensionless parameters (*NTU*, *NTU*$_m$, *Cr**, *m** and *H**) on the effectiveness of the small-scale LAMEE is presented in this chapter.

The experimental and numerical effectiveness results of the full-scale LAMEE are presented under summer (i.e. air cooling and dehumidifying) test conditions. The results show good agreement between the experimental and numerical effectiveness results of the full-scale LAMEE. To investigate similarity between the small-scale and the full-scale LAMEE, first, the experimental effectiveness results of the full-scale LAMEE are compared with the experimental performance results of the small-scale LAMEE for three different tests. The results show that the experimental effectiveness of the small-scale and full-scale LAMEEs agree within their uncertainty ranges. Second, the differences between the small-scale LAMEE and the full-scale LAMEE sensible, latent and total effectiveness results are investigated numerically for each of the important dimensionless parameters. The results show that in most cases the differences between the small-scale LAMEE and the full-scale LAMEE effectiveness results is less than 2%. The experimental and numerical comparison between the small-scale LAMEE and full-scale LAMEE effectiveness results shows that there is a similarity between the small-scale LAMEE and the full-scale LAMEE, and that the small-scale LAMEE effectiveness results can be used to predict the performance of a full-scale LAMEE within 2% to 4% uncertainty in most cases based on comparison between the small-scale LAMEE and the full-scale LAMEE numerical effectiveness results.

CHAPTER 7

CONCLUSIONS

7.1 Summary and Conclusions

This PhD thesis focuses on developing, testing and modeling the small-scale single-panel liquid-to-air membrane energy exchanger (LAMEE), and extrapolating the small-scale LAMEE steady-state effectiveness results to the full-scale (100 L/s) LAMEE. A LAMEE is a novel membrane based energy exchanger where heat and moisture simultaneously transfer between air and solution streams through a semi-permeable membrane. In this thesis, a GE^{TM} membrane is used in the counter-cross flow small-scale LAMEE, and LiCl salt solution is used as the transfer liquid in most cases. This is a paper-based thesis, where each chapter of the thesis is a published (Chapters 2, 3, 4 and 5) or submitted (chapter 6) manuscript. This PhD thesis represents the methodology to investigate similarity between a small-scale and a full-scale exchangers which has five steps. Each chapter of this thesis shows one step of the methodology for LAMEEs, where the main focus is to investigate the similarity between the small-scale and full-scale LAMEEs, and use the small-scale LAMEE effectiveness results to predict the performance of the full-scale LAMEE under different operating conditions. This methodology is a helpful guide for researchers and manufacturers, and saves resources by testing small-scale exchangers. The conclusions for each chapter are presented below.

A single-panel energy exchanger test (SPEET) facility is developed and built in the University of Saskatchewan to evaluate the performance of the small-scale single-panel LAMEE under different test conditions. In Chapter 2, for the first set of experiments with the SPEET facility, water is used as a transfer liquid in the small-scale LAMEE, and the small-scale LAMEE is tested under 3 different test cases (i.e. air heating and humidifying (H&H), air cooling and humidifying (C&H) and air cooling and dehumidifying (C&D)) at constant $Cr^* = 7$ and three different $NTUs$. Mass and energy balance results are presented for each test, and the test facility energy exchange inequality is found to be a maximum of 5% in the worst case. The experimental effectiveness data are compared to data from one numerical and two analytical models which are modified based on the small-scale LAMEE design and specifications. The results show that the effectiveness of the small-scale LAMEE increases by increasing the NTU from 2.5 to 4.5 in all cases. The C&D test case has the best agreement between the experimental, numerical and analytical results.

The air-side effectiveness equations have traditionally been used to evaluate the performance of liquid-to-air energy exchangers used as dehumidifiers/regenerators. However, in regenerators the focus is on the salt solution, and using the air-side effectiveness to evaluate the regeneration performance is questionable. The solution-side effectiveness equations for liquid-to-air membrane energy exchangers are introduced in Chapter 3 for the first time in literature. The small-scale LAMEE is tested as a dehumidifier and a regenerator at $NTU = 5$ and three different $Cr^* = 2, 4$ and 6 using LiCl salt solution. The experimental results show that the air-side and solution-side effectiveness results are almost the same for the dehumidifier, but the solution-side

sensible effectiveness is higher than the air-side sensible effectiveness in the regenerator (e.g. 11% higher at $Cr^* = 6$). The numerical effectiveness results show that the air-side and solution-side latent effectivenesses are almost the same for different test cases (i.e. air heating and dehumidification (H&D), C&D, C&H, and H&H test conditions). Thus, the air-side latent effectiveness equation can be directly used to evaluate the solution-side latent effectiveness of LAMEEs.

The effects of different heat and mass transfer directions and salt solution types and concentrations are experimentally and numerically investigated in Chapter 4. To investigate the effect of different heat and mass transfer directions, the small-scale LAMEE is tested at $NTU = 3$ and four different $Cr^* = 1, 3, 5, 7$ under H&D, C&D, C&H, and H&H test conditions which represent different heat and mass transfer directions in LAMEEs. The results show that the latent and total effectiveness of the small-scale LAMEE increases with Cr^* for all test cases, while the sensible effectiveness increases with Cr^* for the C&D and H&H test cases, and decreases with increasing Cr^* for the H&D and C&H test cases. Maximum total effectiveness of 85% is obtained for the small-scale LAMEE under summer AHRI test conditions (i.e. C&D test case) at $NTU = 3$ and $Cr^* = 7$. The effect of different salt solution types and concentrations is investigated on the small-scale LAMEE effectiveness under C&D test case using LiCl and $MgCl_2$ salt solutions and three different concentrations for LiCl ($C = 25\%$, 30% and 35%). The results show that using different salt solution types and concentrations have a small effect on the LAMEE effectiveness.

The coupled heat and mass transfer in the air, solution and membrane of the small-scale single-panel LAMEE are numerically modeled to calculate the steady-state

effectiveness of the small-scale LAMEE under different operating conditions (i.e. H&D, C&D, C&H, and H&H test conditions) in Chapter 5. The effects of the membrane vapor diffusion resistance (VDR) and enhanced air convective heat and mass transfer coefficients are investigated on the small-scale LAMEE numerical effectiveness under C&D conditions using the modified numerical model for the small-scale single-panel LAMEE. Also, the steady-state numerical effectiveness of the small-scale LAMEE is validated by experimental data for summer test conditions (i.e. C&H and C&D test cases). The membrane VDR found to be 24 s/m for the GE^{TM} membrane which is 57% lower than the value that had been previously used for the GE^{TM} membrane in LAMEEs. The latent effectiveness increases by 11% with decreasing the membrane VDR from 56 s/m to 24 s/m at $NTU = 3$ and $Cr^* = 5$. However, changing the membrane VDR does not have any effect on the sensible effectiveness. Also, using an air screen in the air channel of the small-scale LAMEE enhances the heat and moisture transfers in the air channel of the LAMEE. The results show that the air side Nusselt number and the small-scale LAMEE effectiveness increase by 37% and 4%, respectively, when the air screen is used in the air channel of the small-scale LAMEE, compare to the case of no air screen at Re_{air} $= 620$.

Finally, in Chapter 6, the similarity between the small-scale and the full-scale LAMEEs is numerically and experimentally investigated. The dimensional analysis of the coupled heat and mass transfer in the air and solution sides of the LAMEE shows that the performance of a LAMEE is a function of 5 important dimensionless parameters (NTU, NTU_m, Cr^*, m^* and H^*). The effect of these important dimensionless parameters on the small-scale LAMEE effectiveness is numerically investigated. The full-scale

LAMEE is tested under summer test conditions (i.e. C&D test case), and the results show good agreement between the experimental and numerical effectiveness results of the full-scale LAMEE. The experimental results for the small-scale and full-scale LAMEEs under summer test conditions are compared for three test cases, and the results show that the experimental effectivenesses of the small-scale and full-scale LAMEEs agree within their uncertainty ranges. Also, the numerical results show that, in most cases the differences between the small-scale LAMEE and the full-scale LAMEE effectiveness results is less than 2%. These experimental and numerical results show the similarity between the small-scale and full-scale LAMEEs. The numerical results show that the small-scale LAMEE effectiveness results can be used to predict the performance of a full-scale LAMEE within 2% to 4% uncertainty in most cases.

7.2   Future Work

There are some additional topics which are related to this research project, and can be studied in the future to improve the LAMEE design and the performance of LAMEEs. Some of these topics are:

- The pressure difference between the air and solution sides of a LAMEE causes the flexible membrane to buldge in the LAMEE. This effect is known as the mal-distribution effect, which has negetive effect on the LAMEE performance. The maldistribution effect on the performance of the LAMEE should be studied experimentally and numerically to reduce the mal-distribution effects in future LAMEE designs.

- Recent studies (Zhang *et al.* 2012a; Huang *et al.*, 2012) show that the actual boundary condition on the membrane of liquid-to-air memberane energy

212

exchangers is neither uniform temperature nor uniform heat flux. The uniform heat flux boundary condition on the membrane is used in this PhD thesis to calculate the air and solution sides convective heat and mass transfer coefficients in the LAMEE, which is a reasonable assumption for counter-flow membrane based energy exchangers. The actual values for the air and solution sides convective heat and mass transfer coefficents should be calculated, and their effects on the LAMEE performance should be investigated in future.

- Recent studies (Zhang *et al.*, 2012a) show that the Chilton-Colburn analogy between the convective heat and mass transfer coefficents is not valid in lquid-to-air membrane energy exchangers due to coupled heat and mass transfer. The actual corelation between the convective heat and mass transfer coefficents should be obtained for LAMEEs. This corelation helps to calculate the convective mass transfer coefficent for the air or soultion using the air or solution side convective heat transfer coefficents, respectively, which are easier and more common to measure.

- Salt solution crystalization in the membrane and on the solution side of the LAMEE is possible under air humidification test conditions (i.e. winter test cases). The effect of salt solution crystalization on the membrane vapor diffusion resitance and the LAMEE performance should be investigated. It might be possible to define limits for LAMEE operation conditions to avoid salt solution crystalization in LAMEEs.

- Buoyancy forces decrease the LAMEE performance under specific operating conditions. The salt solution density changes when the salt solution temperature

and concentration change. The buoyancy forces are important in the solution-side of the LAMEE, when the solution flows vertically, and the solution density increases in the vertical direction (heavy solution on top). Further experimental test and numerical modeling are necessary to characterize the buoyancy forces, and quantify their impacts on the LAMEE effectiveness.

REFERENCES

Abdel-Salam, A.H., Ge, G., Simonson, C.J., 2013. Performance analysis of a membrane liquid desiccant air-conditioning system, *Energy and Buildings*, **62**, 559-569.

Abdel-Salam, A.H., Simonson, C.J., 2013, Annual evaluation of energy, environment and economic performances of a membrane liquid desiccant air conditioning system with/without ERV, Submitted to *Applied Thermal Engineering*.

Abe, O. O., Besant, R. W., Simonson, C. J., and Shang, W., 2006d. Relationship between Energy Wheel Speed and Effectiveness and Its Transient Response, Part I: Mathematical Development of the Characteristic Time Constants and Their Relationship with Effectiveness, *ASHRAE Transactions*, **112**, 89-102.

Abe, O. O., Besant, R. W., Simonson, C. J., and Shang, W., 2006e. Relationship between Energy Wheel Speed and Effectiveness and Its Transient Response, Part II: Comparison between Mathematical Model Predictions and Experimental Measurements and Uncertainty Analysis, *ASHRAE Transactions*, **112**, 103-115.

Abe, O. O., Wang, Y. H., Simonson, C. J., Besant, R. W., and Shang, W., 2006c. Transient Temperature Measurements and Characteristics for Temperature Sensors and Energy Wheels. *ASHRAE Transactions*, **112**, 76-88.

Abe, O.O., Simonson, C.J., Besant, R.W., Shang, W., 2006a. Effectiveness of energy wheels from transient measurements: Part I: Prediction of effectiveness and uncertainty, *International Journal of Heat and Mass Transfer*, **49**, 52-62.

Abe, O.O., Simonson, C.J., Besant, R.W., Shang, W., 2006b, Effectiveness of energy wheels from transient measurements: Part II: Results and Verification, *International Journal of Heat and Mass Transfer*, **49**, 63-77.

Afonso, C.F.A., 2006. Recent advances in building air conditioning systems, *Applied Thermal Engineering*, **26**, 1961-1971.

Afshin, M.J., 2010. Selection of the liquid desiccant in a run-around membrane energy exchanger, M.Sc. thesis, Department of Mechanical Engineering, University of Saskatchewan, SK, Canada.

Akbari, S., Hemingson, H.B., Beriault, D., Simonson, C.J., Besant, R.W., 2012a. Application of neural networks to predict the steady state performance of a Run-Around Membrane Energy Exchanger, *International Journal of Heat and Mass Transfer*, **55**, 1628-1641.

Akbari, S., Simonson, C. J., and Besant, R. W., 2012b. Application of Neural Networks to Predict the transient Performance of a Run-Around Membrane Energy Exchanger for yearly non-stop operation, *International Journal of Heat and Mass Transfer*, **55**, 5403-5416.

Alkhudhiri, A., Darwish, N., Hilal, N., 2012. Membrane distillation: A comprehensive review, *Desalination*, **287**, 2-18.

Alklaibi, A.M., Lior, N., 2004. Membrane-distillation desalination: status and potential, *Desalination*, **171**, 111-131.

ANSI/AHRI Standard 1060, 2011. Performance Rating for Air-to-Air Exchangers for Energy Recovery Ventilation Equipment, Arlington, VA: Air-Conditioning & Refrigeration Institute.

ANSI/ASHRAE STANDARD 90.1, 2007. Energy standards for buildings except for low-rise residential buildings, Atlanta: American Society of Heating, Refrigerating, and Air- Conditioning Engineers.

ASME Standard PTC 19.1-2005, 2005. Test Uncertainty, American Society of Mechanical Engineers (ASME), Printed in New York, NY, USA.

ASTM E 96-00, 2000. Standard Test Method for Water Vapor Transmission of Materials, ASTM International, West Conshohocken, PA.

Babakhani, D., Soleymani, M., 2009. An analytical solution for air dehumidification by liquid desiccant in a packed column, *International Communication in Heat and Mass Transfer*, **36**, 969-977.

Bejan, A., 2002. Dendritic Constructal Heat Exchanger with Small-Scale Crossflows and Larger-Scales Counterflows, *International Journal of Heat and Mass Transfer*, **45**, 4607-4620.

Bergero, S., Chiari, A., 2001. Experimental and theoretical analysis of air humidification/ dehumidification processes using hydrophobic capillary contactors, *Applied Thermal Engineering*, **21**, 1119–1135.

Bergero, S., Chiari, A., 2010. Performance analysis of a liquid desiccant and membrane contactor hybrid air-conditioning system, *Energy and Buildings*, **42**, 1976-1986.

Bergero, S., Chiari, A., 2011. On the performance of the hybrid air-conditioning system in different climate conditions, *Energy*, **36**, 5261-5273.

Bergero, S., Chiari, A., Isetti, C., 2000. On the performance of a plane plate membrane contactor for air dehumidification, *Proceedings of the 7th REHVA World Congress (CLIMA 2000)*, 15-18 September 2000, Napoli, Italy.

Beriault, D.A., 2011. Run-around membrane energy exchanger prototype 4: design and laboratory testing, MSc Thesis, University of Saskatchewan, Saskatoon, SK, Canada.

Besant, R.W., Simonson, C.J., 2000. Air-to-air energy recovery, *ASHRAE Transactions*, **42(5)**, 31-42.

Cisternas, L.A., Lam, E. J., 1991. An analytic correlation for the vapor pressure of aqueous and non-aqueous solutions of single and mixed electrolytes. Part II. Application and extension, *Fluid Phase Equilibria Journal*, **62**, 11-27.

Dai, Y.J., Wang, R.Z., Zhang, H.F., Yu, J.D., 2001. Use of liquid desiccant cooling to improve the performance of vapor compression air conditioning, *Applied Thermal Engineering,* **21**, 1185-1202.

Elsayed, M.M., Gari, H.N., Radhwan, 1993. Effectiveness of Heat and Mass Transfer in Packed Beds of Liquid Desiccant System, *Renewable Energy*, **3**, 661-668.

Erb, B., 2009. Run-around membrane energy exchanger performance and operational control strategies, MSc thesis, University of Saskatchewan, Saskatoon, SK.

Erb, B., Seyed-Ahmadi, M., Simonson, C. J., and Besant, R. W., 2009. Experimental Measurements of a Run-Around Membrane Energy Exchanger (RAMEE) with Comparison to a Numerical Model, *ASHRAE Transactions*, **115**, 689-705.

Fan, H., Simonson, C.J., Besant, R.W., Shang, W., 2006. Performance of a run-around system for HVAC heat and moisture transfer applications using cross-flow plate exchangers coupled with aqueous lithium bromide, *ASHRAE HVAC&R*, **12 (2)**, 313-336.

Figliola, R. S., and Beasley, D. E., 2006. Theory and Design for Mechanical Measurements, 4th ed., Wiley, New York.

Fumo, N., Goswami, D.Y., 2002. Study of an aqueous lithium chloride desiccant system: air dehumidification and desiccant regeneration, *Solar Energy*, **72**, 351-361.

Ge, G., Ghadiri Moghaddam, D., Abdel-Salam, A.H., Besant, R.W., Simonson, C.J., 2014. Comparison of experimental data and a model for heat and mass transfer performance of a liquid-to-air membrane energy exchanger (LAMEE) when used for air dehumidification and salt solution regeneration, *International Journal of Heat and Mass Transfer*, **68**, 119-131.

Ge, G., Ghadiri Moghaddam, D., Namvar, R., Besant, R. W., and Simonson, C. J., 2012. Analytical Model Based Performance Evaluation and Optimization of Run-Around Membrane Energy Exchanger Systems, *Energy and Buildings*, **62**, 248-257.

Ghadiri Moghaddam D., LePoudre P.P., Besant R.W., and Simonson C.J. 2013a, Evaluating the Steady-State Performance of a Small-Scale Liquid-to-Air Membrane Energy Exchanger for Different Heat and Mass Transfer Directions and Liquid Desiccant Types and Concentrations: Experimental and Numerical Data, *ASME Journal of Heat Transfer*, **135**, pp. 12002.

Ghadiri Moghaddam, D., Besant, R.W., Simonson, C.J., 2014. Solution-side effectiveness for a liquid-to-air membrane energy exchanger used as a dehumidifier/regenerator, *Applied Energy*, **113**, 872-882.

Ghadiri Moghaddam, D., LePoudre, P.P., Ge, G., Besant, R. W., and Simonson, C. J., 2013b. Small-Scale Liquid-to-Air Membrane Energy Exchanger Test Facility Development, Commissioning and Evaluating the Steady-State Performance, *Energy and Buildings*, **66**, 424-436.

Ghadiri Moghaddam, D., Mahmood, G., Ge, G., Besant, R.W., Simonson, C.J., 2013d. Steady-state performance of a prototype (200CFM) liquid-to-air membrane energy exchanger (LAMEE) under summer and winter test conditions", *Proceeding of ASME 2013 Summer Heat Transfer Conference*, 14-19 July 2013, Minneapolis, MN.

Ghadiri Moghaddam, D., Oghabi, A., Ge, G., Besant, R.W., Simonson, C.J., 2013c. Numerical Model of a Small-Scale Liquid-to-Air Membrane Energy Exchanger: Parametric Study of Membrane Resistance and Air Side Convective Heat Transfer Coefficient, *Applied Thermal Engineering*, **61(2)**, 245-258.

Gibson, P.W., 2000. Effect of temperature on water vapor transport through polymer membrane laminates, *Journal of Polymer Testing*, **19 (6)**, 673-691.

Gibson, P.W., Elsaiid, A.E., Kendrick, C.E., Rivin, D., and Charmchi, M., 1997. A test Method to Determine the Relative Humidity Dependence of the Air Permeability of Textile Materials, *Journal of Testing and Evaluation*, **25 (4)**, 416-423.

Hemingson, H.B., 2010. The impacts of outdoor air conditions and non-uniform exchanger channels on a run-around membrane energy exchanger, MSc Thesis, University of Saskatchewan, Saskatoon, SK.

Hemingson, H.B., Simonson, C.J., Besant, R.W., 2011a. Effects of non-uniform channels on the performance of a run-around membrane energy exchanger (RAMEE), *Proceedings of the 12th International Conference on Air Distribution in Rooms (ROOMVENT 2011)*, 19-22 June 2013, Trondheim, Norway.

Hemingson, H.B., Simonson, C.J., Besant, R.W., 2011b. Steady-state performance of a run-around membrane energy exchanger (RAMEE) for a range of outdoor air conditions, *International Journal of Heat and Mass Transfer*, **54**, 1814-1824.

Huang, S.M., Zhang, L.Z., Tang, K., Pei, L.X., 2012. Fluid flow and heat mass transfer in membrane parallel-plates channels used for liquid desiccant air humidification, *International Journal of Heat and Mass Transfer*, **55**, 2571-2580.

Incropera, F.P., DeWitt, D.P., 1985. Fundamental of Heat and Mass Transfer, 2nd ed, Wiley, New York.

Isetti, C., Nannei, E., Magrini, A., 1997. On the application of a membrane air-liquid contactor for air dehumidification, *Energy and Buildings*, **25**, 185-193.

Jaber, H., Webb, R.L., 1989. Design of Cooling Towers by the Effectiveness-*NTU* Method, *ASME Journal of Heat Transfer*, **111**, 837-843.

Jaluria, Y., 2007. Design and Optimization of Thermal Systems, 1st edition, CRC Press, Taylor & Francis Group.

Jiang, P. X., Fan, M. H., Si, G. S., and Ren, Z. P., 2001. Thermal-Hydraulic Performance of Small Scale Micro-Channel and Porous-Media Heat-Exchangers, *International Journal of Heat and Mass Transfer*, **44**, 1039-1051.

Kinsara, A.A., Elsayed, M.M, Al-Rabghi, O.M., 1996. Proposed energy-efficient air conditioning system using liquid desiccant, *Applied Thermal Engineering,* **16**, 791-806.

Larson, M. D., 2006. The Performance of Membrane in a Newly Proposed Run-Around Heat and Moisture Exchanger, M.Sc. Thesis, Mechanical Engineering Department, University of Saskatchewan, SK, Canada.

LePoudre, P.P., Simonson C.J., Besant, R.W., 2011. Channel Flow with Sinusoidal Screen Insert, *Proceedings of the 19th Annual Conference of the CFD Society of Canada (CFD 2011)*, 27-29 April 2011, Montreal, Canada.

Liu, X., Jiang, Y., Xia, J., Chang X., 2007a. Analytical solutions of coupled heat and mass transfer processes in liquid desiccant air dehumidifier/regenerator, *Energy Conversion and Management*, **48**, 2221-2232.

Liu, X.H., Jiang, Y., Chang, X.M., Yi, X.Q., 2007b. Experimental investigation of the heat and mass transfer between air and liquid desiccant in a cross-flow regenerator, *Renewable Energy*, **32**, 1623-1636.

Liu, X.H., Jiang, Y., Qu, K.Y., 2007c. Heat and mass transfer model of cross flow liquid desiccant air dehumidifier/regenerator, *Energy Conversion and Management*, **48**, 546-554.

Liu, X.H., Li, Z., Jiang, Y., Lin, B.R., 2006a. Annual performance of liquid desiccant based independent humidity control HVAC system, *Applied Thermal Engineering*, **26**, 1198-1207.

Liu, X.H., Zhang, Y., Qu, K.Y., Jiang, Y., 2006b. Experimental study on mass transfer performances of cross-flow dehumidifier using liquid desiccant, *Energy Conversion and Management*, **47**, 2682-2692.

Longo, G. A., 2008. Refrigerant R134a Condensation Heat Transfer and Pressure Drop Inside a Small Brazed Plate Heat Exchanger, *International Journal of Refrigeration*, **31**, 780-789.

Mahmud, K., 2009. Design and performance testing of counter-cross-flow run-around membrane energy exchanger system, MSc thesis, University of Saskatchewan, Saskatoon, SK.

Mahmud, K., Mahmood, G., Simonson, C. J., and Besant, R. W., 2010. Performance Testing of a Counter-Cross-Flow Run-Around Membrane Energy Exchanger (RAMEE) System for HVAC Applications, *Energy and Buildings*, **42**, 1139-1147.

Martin, V., Goswami, D.Y., 1999. Heat and mass transfer in packed bed liquid desiccant regenerators-an experimental investigation, *Journal of Solar Energy Engineering*, **121**, 162-170.

Min, J.C., Su, M., 2010. Performance analysis of a membrane-based energy recovery ventilator: effects of membrane spacing and thickness on the ventilator performance, *Applied Thermal Engineering*, **30 (8)**, 991-997.

Min, J.C., Su, M., 2011. Performance analysis of a membrane-based energy recovery ventilator: effects of outdoor air state, *Applied Thermal Engineering*, **31 (17)**, 4036-4043.

Monnin, C., Dubois, M., Papaiconomou, N., Simonin, J.P., 2002. Thermodynamics of the LiCl + H_2O system, *Journal of Chemical & Engineering Data*, **47**, 1331-1336.

Moon, C.G., Bansal, P.K., Jain, S., 2009. New mass transfer performance data of a cross-flow liquid desiccant dehumidification system, *International Journal of Refrigeration*, **32**, 524-533.

Namvar, R., Pyra, D., Ge, G., Simonson, C.J., Besant, R.W., 2012. Transient characteristics of a liquid-to-air membrane energy exchanger (LAMEE) experimental data with correlations, *International Journal of Heat and Mass Transfer*, **55**, 6682-6694.

Nasif, M.S., Morrison, G.L., Behnia, M., 2005. Heat and mass transfer in air to air enthalpy heat exchangers, *Proceedings of the 6th International Conference on Heat Transfer, Fluid Mechanics and Thermodynamics*, 17-21 April 2005, Matsushima, Japan.

Niu, J.L., Zhang, L.Z., 2001. Membrane-based enthalpy exchanger: material consideration and clarification of moisture resistance, *Journal of Membrane Science*, **189**, 179-191.

Oberg, V., Goswami, D.Y., 1998. Experimental study of the heat and mass transfer in a packed bed liquid desiccant air dehumidifier, *Journal of Solar Energy Engineering*, **120**, 289-297.

Oghabi, A., Ghadiri Moghaddam, D., Besant, R.W., Simonson, C.J., 2013, Measurement of Heat Transfer Enhancement and Pressure Drop Across Air Screens in a Liquid-

to-Air Membrane Energy Exchanger (LAMEE) Under Laminar Flow Regime, *Proceedings of the ASME 2013 Summer Heat Transfer Conference*, 14-19 July 2013, Minneapolis, MN, USA.

Ozden, E., and Tari, I., 2010. Shell Side CFD analysis of a Small Shell-and-Tube Heat Exchanger, *Energy Conversion and Management*, **51**, 1004-1014.

Parkash Narayan, G., Mistry, K.H., Sharqaway, M.H., Zubair, S.M., Lienhard, J.H., 2010. Energy Effectiveness of Simyltaneous Heat and Mass Exchange Devices, *Frontiers in Heat and Mass Transfer*, **1(2)**, 023001-13.

Patel, H.N., Simonson, C.J., Besant, R.W., 2010. Contaminant transfer between the supply and exhaust air streams of run-around membrane energy exchangers, *Proceedings of the 7th Int. Conference on Indoor Air Quality, Ventilation and Energy Conservation in Buildings*, 15-18 August 2010, New York, NY, USA.

Perez-Lombard, L., Ortiz, J., Pout, C., 2008. A review on buildings energy consumption information, *Energy and Buildings*, **40**, 394-398.

Rasouli, M., Akbari, S., Hemingson, H., Besant, R.W., Simonson, C.J., 2011. Application of a run-around membrane energy exchanger in an office building HVAC system, *ASHRAE Transactions*, **117**, 686-703.

Rasouli, M., Ge, G., Simonson, C.J., Besant, R.W., 2013. Uncertainties in energy and economic performance of HVAC systems and energy recovery ventilators due to uncertainties in building and HVAC parameters, *Applied Thermal Engineering*, **50**, 732-742.

Ren, C.Q., 2008. Effectiveness–*NTU* relation for packed bed liquid desiccant–air contact systems with a double film model for heat and mass transfer, *International Journal of Heat and Mass Transfer*, **51**, 1793-1803.

Ren, C.Q., Jiang, Y., Zhang, Y., 2006. Simplified analysis of coupled heat and mass transfer processes in packed bed liquid desiccant-air contact system, *Solar Energy*, **80**, 121-131.

Rogiers, F., Baelmans, M., 2010. Towards Maximal Heat Transfer Rate Densities for Small-Scale High Effectiveness Parallel-Plate Heat Exchangers, *International Journal of Heat and Mass Transfer*, **53**, 605-614.

Seyed-Ahmadi, M., 2008. Modeling the transient behavior of a run-around heat and moisture exchanger system, MSc Thesis, University of Saskatchewan, Saskatoon, SK.

Seyed-Ahmadi, M., Erb, B., Simonson, C.J., and Besant, R.W., 2009b. Transient Behavior of Run-Around Heat and Moisture Exchanger System. Part II: Sensitivity Studies for a Range of Initial Conditions, *International Journal of Heat and Mass Transfer*, **52**, 6012-6020.

Seyed-Ahmadi, M., Erb, B., Simonson, C.J., Besant, R.W., 2009a. Transient behavior of run-around heat and moisture exchanger system. Part I: Model formulation and verification, *International Journal of Heat and Mass Transfer*, **52**, 6000-6011.

Shah, R.K., 1981. The Transient Response of Heat Exchangers, in: Heat Exchangers: Thermal-Hydraulic Fundamentals and Design, Hemisphere Publications, New York.

Shah, R.K., Sekulic, D.P., 2003. Fundamental of Heat Exchanger Design, John Wiley & Sons, Hoboken, NJ, 97-164.

Simonson, C.J., Besant, R.W., 1999. Energy wheel effectiveness: Part I- Development of dimensionless groups, *International Journal of Heat and Mass Transfer*, **42**, 2161-2170.

Simonson, C.J., Ciepliski, D.L., Besant, R.W., 1999. Determining the performance of energy wheels: Part I-Experimental and numerical method, *ASHRAE Trans.*, **105 (1)**, 174-187.

Sultan, G.I., Hamed, A.M., Sultan, A.A., 2002. The effect of inlet parameters on the performance of packed tower regenerator, *Renewable Energy*, **26**, 271-283.

Tu, M., Ren, C.Q., Zhang, L.A., Shao, J.W., 2009. Simulation and analysis of a novel liquid desiccant air-conditioning system, *Applied Thermal Engineering*, **29**, 2417-2425.

Vali, A., Simonson, C.J., Besant, R.W., Mahmood, G., 2009. Numerical model and effectiveness correlations for a run-around heat recovery system with combined counter and cross flow exchangers, *International Journal of Heat and Mass Transfer*, **52**, 5827-5840.

Vestrelli F., 2006. Study on Membrane Contactors: Performances Analysis, System Simulations and Fields of Application, PhD thesis, Faculty of Engineering, University of Genoa, Genoa, Italy.

Wang, Y.H., Besant, R.W., Simonson, C.J., Shang, W., 2005. Transient humidity measurement for flow through an energy wheel. *ASHRAE Trans*actions, **111(2)**, 353-369.

Wang, Y.H., Simonson, C.J., Besant, R.W., Shang, W., 2007a. Transient humidity measurements: Part I-sensors calibration and characteristics, *IEEE Transactions on Instrumentation and Measurement*, **56(3)**, 1074-1079.

Wang, Y.H., Simonson, C.J., Besant, R.W., Shang, W., 2007b. Transient humidity measurements: Part II-determination of the characteristics of an interactive device", *IEEE Transactions on Instrumentation and Measurement*, **56(3)**, 1080-1086.

Welty, J.R., Wicks, C.E., Wilson, R.E., 2001. Fundamentals of Momentum, Heat and Mass Transfer, John Wiley & Sons Inc., New York.

White, F. M., 2009. Fluid Mechanics, 4th edition, McGraw-Hill, New York, NY.

Yin, Y., Zhang, X., Peng, D., Li, X., 2009. Model validation and case study on internally cooled/heated dehumidifier/regenerator of liquid desiccant systems, *International Journal of Heat and Mass Transfer*, **48**, 1664-1671.

Yu, B.F., Hu, Z.B., Liu, M., Yang, H.L., Kong, Q.X., Liu, Y.H., 2009. Review of research on air conditioning systems and indoor air quality control for human health, *International Journal Refrigeration*, **32**, 3-20.

Zhang, L.Z., 2011a. An analytical solution to heat and mass transfer in hollow fiber membrane contactors for liquid desiccant dehumidifier, *ASME Journal of Heat Transfer*, **133**, pp. 1-7.

Zhang, L.Z., 2011b. Heat and mass transfer in a randomly packed hollow fiber membrane module: A fractal model approach, *International Journal of Heat and Mass Transfer*, **54**, 2921-2931.

Zhang, L.Z., 2012. Coupled heat and mass transfer in an application-scale cross-flow hollow fiber membrane module for air humidification, *International Journal of Heat and Mass Transfer*, **55**, 5861-5869.

Zhang, L.Z., Huang, S.M., 2011. Coupled heat and mass transfer in a counter flow hollow fiber membrane module for air humidification, *International Journal of Heat and Mass Transfer*, **54**, 1055-1063.

Zhang, L.Z., Huang, S.M., Chi, J.H., Pei, L.X., 2012a. Conjugate heat and mass transfer in a hollow fiber membrane module for liquid desiccant air dehumidification: a free surface model approach, *International Journal of Heat and Mass Transfer*, **55**, 3789-3799.

Zhang, L.Z., Huang, S.M., Pei, L.X., 2012b. Conjugate heat and mass transfer in a cross-flow hollow fiber membrane contactor for liquid desiccant air dehumidification, *International Journal of Heat and Mass Transfer*, **55**, 8061-8072.

APENDICES

APPENDIX A

COPYRIGHT PERMISSIONS

This Appendix includes the copyright permission from the publishers of manuscripts #1, 2, 3 and 4, and appendices B and C, and co-authors who contributed in the manuscript #5.

A.1 Permission for Manuscripts #1, 2 and 4, and Appendix B

For previously published manuscripts that form a part of a thesis, written permission from the publisher (copyright holder) is required by the College of Graduate Studies and Research (CGSR). For manuscripts published by Elsevier, the authors retain the right to include their publication in a thesis without requesting a written permission:

"*As an author, you retain rights for a large number of author uses, including use by your employing institute or company. These rights are retained and permitted without the need to obtain specific permission from Elsevier. These include: the right to include the article in full or in part in a thesis or dissertation (provided that this is not to be published commercially); the right to use the article or any part thereof in a printed compilation of works of the author, such as collected writings or lecture notes (subsequent to publication of the article in the journal); and the right to prepare other derivative works, to extend the article into book-length form, or to otherwise re-use portions or excerpts in other works, with full acknowledgement of its original publication in the journal.*"

This information is available at the publisher's website at:
http://support.elsevier.com/app/answers/detail/a_id/565/session/L3RpbWUv
October 20, 2013

A.2   Permission for Manuscript #3, and Appendix C

For previously published manuscripts that form a part of a thesis, written permission from the publisher (copyright holder) is required by the College of Graduate Studies and Research (CGSR). For manuscripts published by American Society of Mechanical Engineers (ASME), the authors required a written permission from the publisher. I requested a permission to used Manuscript #3 and Appendix C in my PhD thesis, and I got a written permission for ASME by email on October 23, 2013:

"*Dear Mr. Moghaddam:*

It is our pleasure to grant you permission to use the following ASME materials:

- *Steady-State Performance of a Prototype (200CFM) Liquid-to-Air Membrane Energy Exchanger (LAMEE) Under Summer and Winter Test Conditions, by Davood Ghadiri Moghaddam, Gazi Mahmood, Gaoming Ge, John Bolster, Robert W. Besant, and Carey J. Simonson, ASME 2013 Summer Heat Transfer Conference, Paper Number HT2013-17135,*

- *Steady-State Performance of a Small-Scale Liquid-to-Air Membrane Energy Exchanger for Different Heat and Mass Transfer Directions, and Liquid Desiccant Types and Concentrations: Experimental and Numerical Data, by Davood Ghadiri Moghaddam, Philip LePoudre, Robert W. Besant, and Carey J. Simonson, Journal of Heat Transfer, Volume 135, 2013,*

as cited in your letter for inclusion in a Ph.D. thesis entitled "Small-Scale Single-Panel Liquid-to-Air Membrane Energy Exchanger (LAMEE); Developing, Testing, Modeling and Extrapolating Results to a Full-Scale LAMEE" to be published by University of Saskatchewan, SK, Canada.

Permission is granted for the specific use as stated herein and does not permit further use of the materials without proper authorization. Proper attribution must be made to the author(s) of the materials. PLEASE NOTE: if any or all of the figures and/or Tables are of another source, permission should be granted from that outside source or include the reference of the original source. ASME does not grant permission for outside source material that may be referenced in the ASME works.

As is customary, we request that you ensure full acknowledgment of this material, the author(s), source and ASME as original publisher. Acknowledgment must be retained on all pages printed and distributed.

Many thanks for your interest in ASME publications.

Sincerely,

Beth Darchi

Permissions & Copyrights

ASME, 2 Park Avenue

New York, NY 10016

T: 212-591-7700

F: 212-591-7841

E: permissions@asme.org"

A.3   Permission for Manuscript #5

For unpublished manuscripts, written permission from co-authors is required by CGSR to include the manuscript in a thesis.

Copyright Permission Request Form

I am preparing the publication of a manuscript titled:

Establishing Similarity between a Small-Scale Liquid-to-Air Membrane Energy Exchanger (LAMEE) and a Full-Scale (200cfm) LAMEE: Experimental and Numerical Results

to be published as the fifth chapter of my Ph.D. thesis, and to be submitted to the Department of Mechanical Engineering at the University of Saskatchewan. The authors contributing in the completion of this manuscript are as follows:

Davood Ghadiri Moghaddam, Melanie Fauchoux, Robert W. Besant, Carey J. Simonson

I am requesting permission to use the materials described in aforementioned manuscript in my Ph.D. thesis and all subsequent editions that may be prepared at the University of Saskatchewan. Please indicate agreement by signing below:

Yours sincerely,

Davood Ghadiri Moghaddam

October 17, 2013

Permission granted by: Melanie Fauchoux

Signature:

Date:

Copyright Permission Request Form

I am preparing the publication of a manuscript titled:

Establishing Similarity between a Small-Scale Liquid-to-Air Membrane Energy Exchanger (LAMEE) and a Full-Scale (200cfm) LAMEE: Experimental and Numerical Results

to be published as the fifth chapter of my Ph.D. thesis, and to be submitted to the Department of Mechanical Engineering at the University of Saskatchewan. The authors contributing in the completion of this manuscript are as follows:

Davood Ghadiri Moghaddam, Melanie Fauchoux, Robert W. Besant, Carey J. Simonson

I am requesting permission to use the materials described in aforementioned manuscript in my Ph.D. thesis and all subsequent editions that may be prepared at the University of Saskatchewan. Please indicate agreement by signing below:

Yours sincerely,

Davood Ghadiri Moghaddam

October 17, 2013

Permission granted by: Robert W. Besant

Signature:

Date:

Copyright Permission Request Form

I am preparing the publication of a manuscript titled:

Establishing Similarity between a Small-Scale Liquid-to-Air Membrane Energy Exchanger (LAMEE) and a Full-Scale (200cfm) LAMEE: Experimental and Numerical Results

to be published as the fifth chapter of my Ph.D. thesis, and to be submitted to the Department of Mechanical Engineering at the University of Saskatchewan. The authors contributing in the completion of this manuscript are as follows:

Davood Ghadiri Moghaddam, Melanie Fauchoux, Robert W. Besant, Carey J. Simonson

I am requesting permission to use the materials described in aforementioned manuscript in my Ph.D. thesis and all subsequent editions that may be prepared at the University of Saskatchewan. Please indicate agreement by signing below:

Yours sincerely,

Davood Ghadiri Moghaddam

October 17, 2013

Permission granted by: Carey J. Simonson

Signature:

Date:

SMALL-SCALE LAMEE AS A DEHUMIDIFER/REGENERATOR

B.1 Overview of Appendix B

The small-scale LAMEE is tested as a dehumidifier and a regenerator in the SPEET facility, and experimental and analytical steady-state performance results for the small-scale LAMEE are presented in Appendix B which contains a paper with a title of: Comparison of experimental data and a model for heat and mass transfer performance of a liquid-to-air membrane energy exchanger (LAMEE) when used for air dehumidification and salt solution regeneration. The small-scale single-panel LAMEE is introduced in detail in Chapter 2. A LAMEE can be used as a dehumidifier to dehumidify the air or a regenerator to regenerate (dry) the solution in a LDAC system. Therefore, it is important to study the effect of different operating parameters on the performance of a LAMEE when it is used as a dehumidifier or regenerator. In Appendix B, the small-scale LAMEE was tested under dehumidification and regeneration test conditions and the effects of *NTU*, *Cr**, air inlet temperature and humidity ratio, and solution inlet temperature and concentration are investigated on the performance of the small-scale LAMEE used as a dehumidifier or a regenerator. This experimental parametric study on the performance of a LAMEE when it is used as a dehumidifier or a regenerator is done for the first time in literature, and the results of this study are a helpful guide for researchers and manufactures to have an estimation of a LAMEE performance when they want to use the LAMEE in a LDAC system as a dehumidifier or a regenerator.

Mr. Gaoming Ge is the first author and Mr. Ahmed H. Abdel-Salam is a co-author in this paper which is presented in Appendix B. Mr. Gaoming Ge is a post-doctoral fellow in our research group in the University of Saskatchewan, and his contributions to this paper are: (a) planning and writing the paper, and (b) analytically evaluating the performance of the small-scale LAMEE using the LAMEE analytical model which was presented by Ge *et al.* (2012). Mr. Ahmed H. Abdel-Salam is a PhD student in our research group in the University of Saskatchewan, and he helped Mr. Gaoming Ge in

analyzing the small-scale LAMEE results which was tested as a dehumidifier and a regenerator. My contributions to Appendix B are: (a) modifying the SPEET facility to test the small-scale LAMEE under regeneration test conditions, which require heating for the solution (see Figure B.1), (b) Testing the small-scale LAMEE under dehumidification and regeneration test conditions, and (c) analyzing the experimental data and calculating the small-scale LAMEE experimental effectiveness under dehumidification and regeneration test conditions.

Comparison of experimental data and a model for heat and mass transfer performance of a liquid-to-air membrane energy exchanger (LAMEE) when used for air dehumidification and salt solution regeneration

Gaoming Ge[*], *Davood Ghadiri Moghaddam, Ahmed H. Abdel-Salam, Robert W. Besant,*

Carey J. Simonson

B.2   Abstract

Liquid-to-air membrane energy exchangers (LAMEEs) allow simultaneous heat and moisture transfer between salt solution flows and airflows. These exchangers can be used as air dehumidifiers for supply air or liquid desiccant regenerators in liquid desiccant air conditioning systems while the membrane eliminates entrainment of liquid desiccant as aerosols in air streams. In this study, the heat and mass transfer performance of a LAMEE used as dehumidifier or regenerator is experimentally and analytically investigated to determine the influences of air and desiccant solution flow rates, inlet air temperature and humidity, and inlet desiccant solution temperature and concentration. Using the experimental data, the analytical model for the counter-cross-flow LAMEEs is quantitatively validated for sensible and latent effectiveness during air dehumidification process for the inlet conditions tested, while agreement is not good for the salt solution regeneration or de-watering process. This discrepancy may be caused by the crystallization of LiCl aqueous solution within the membrane pores near the solution side of the membrane during the regeneration tests. It is implied that both the moisture flux ratio and the proximity of the solution concentration to the saturation concentration play a role for moisture transfer blockage within the membrane when the data for latent effectiveness is significantly below the theoretical values. The influences of inlet air and solution parameters on the mass transfer performances of LAMEEs used as dehumidifiers and regenerators are also compared with those of direct-contact liquid desiccant devices available in the literature.

Keywords: Liquid-to-air membrane energy exchanger; air dehumidification; solution regeneration; moisture flux ratio; latent effectiveness; crystallization

B.3   Introduction

Liquid desiccant air conditioning (LDAC) systems have been studied by several research groups over recent decades. They have shown the potential to be more energy efficient than conventional air conditioning systems for the control of indoor air humidity, especially in hot and humid climates (Kinsara *et al.*, 1996; Dai *et al.*, 2001; Liu *et al.*, 2006a; Tu *et al.*, 2009). In LDAC systems, the air dehumidification exchanger and solution regeneration exchanger are two key components. The dehumidifier is used to dehumidify the supply air while the desiccant solution absorbs moisture from airflow and becomes diluted during this process. The diluted solution is then dried or de-watered in the regenerator which is part of the closed-liquid-desiccant-loop of LDAC systems.

For conventional direct-contact liquid desiccant devices (e.g. packed towers or packed beds (Liu *et al.*, 2006a; Fumo and Goswami, 2002)) entrainment of liquid desiccant droplets into the downstream air will cause corrosion of downstream air ducts and exposed metal components. As well, particle downstream drift will negatively impact the air quality or indoor environment quality. This liquid desiccant carryover problem in this kind of exchanger largely limits direct-contact exchanger usage to a few types of commercial and industrial applications, such as health care facilities (Bergero and Chiari, 2011). Research on new liquid desiccant exchangers that prevent desiccant carryover problems is needed.

Isetti *et al.* (1997) conducted a series of experiments to investigate the performance of hydrophobic membranes suitable for use in liquid absorption air-handling processes. Results showed high vapor fluxes between a hygroscopic solution and an air stream flowing across a contactor or exchanger can be achieved by using thin and permeable membranes. Bergero and Chiari (2001) experimentally and numerically studied the air humidification/dehumidification performance of a hollow-fiber semi-permeable contactor under different air and liquid desiccant flow rate conditions. It was found that the change in the humidity ratio of the air diminished as the air flow rate increased and these findings did not depend significantly on the desiccant flow rate provided it was above the mass flow rate of air. Zhang (2011a) and Zhang and Huang (2011) investigated experimentally and theoretically the heat and mass transfer in a hollow fiber module for air dehumidification and humidification conditions. They

concluded that indirect-contact energy exchangers where semi-permeable hollow fibers or membranes were used to separate the air and the solution streams could achieve high heat and mass transfer performance and effectively overcome the liquid desiccant salt particle downstream drift problem.

A new kind of liquid-to-air membrane energy exchanger (LAMEE), which uses semi-permeable membranes to transfer heat and moisture between the air and solution flows, has been under development and investigation at the University of Saskatchewan during the past decade. The effectiveness and energy performance of run-around membrane energy exchanger (RAMEE) systems, which are mainly comprised of two LAMEEs and a closed loop of aqueous desiccant solution and used as passive energy recovery ventilators (ERV) in building air conditioning systems, have been experimentally measured and numerically investigated (Erb *et al.*, 2009; Mahmud *et al.*, 2010; Rasouli *et al.*, 2011). Early test results showed that a 55% total effectiveness could be achieved by RAMEE systems using two laboratory-constructed counter-cross-flow LAMEE exchangers for energy recovery from the exhaust air (i.e. higher than the minimum total effectiveness 50% required by ASHRAE Standard 90.1 (ANSI/ASHRAE Standard 90.1, 2007)). Steady-state and transient performance data for a LAMEE obtained under different air and desiccant flow rates for AHRI summer and winter conditions was reported (Namvar *et al.*, 2012). Steady-state results for this LAMEE revealed that the effectiveness increased as either the desiccant flow rate increased or the air flow rate decreased. However, no experimental and theoretical work has been performed for LAMEEs to study the effects of different design and operating parameters on the mass transfer performance when LAMEEs are used as active air dehumidifiers and salt solution regenerators in LDAC systems.

The purpose of this paper is then to measure and compare the LAMEE performance with a theoretical model results, with a special emphasis on the moisture transfer performance. In this study, the heat and mass transfer performances of LAMEEs used as dehumidifier and regenerator are experimentally investigated using a small laboratory test facility (Ghadiri Moghaddam *et al.*, 2013c). The main objective is to study the effects of different operating parameters, such as air and desiccant solution flow rates, inlet air temperature and humidity, and inlet desiccant solution temperature and

concentration, on moisture flux ratio and latent effectiveness of the LAMEE during air dehumidification and solution regeneration processes. These results can serve as guides for the design, control and operation of LAMEEs as air dehumidifiers and salt solution regenerators in LDAC systems. Another objective is to validate a previously developed analytical model for counter-cross-flow LAMEEs (Ge *et al.*, 2012) using a wide range of experimental data and analyze the possible reasons causing the discrepancy between the experimental and theoretical results.

B.4 Test Facility

A small-scale single-panel energy exchanger test (SPEET) facility (Ghadiri Moghaddam, 2013c) is used to conduct the experimental tests in this study. As shown in Figure B.1, the SPEET facility consists of a supply air system and an open loop solution system each with a flow rate controller and property measurement data acquisition scheme which flow at steady state conditions to a small-scale single-panel LAMEE, located in the test section. In the supply air system, high pressure dry air (~4%RH), provided by a compressor, and passes through a flow controller and a flow meter with a capacity of 100 L/min and accuracy of 2% and 1% of full-scale, respectively. The air flow controller and flow meter are used to control and measure the supply air flow rate. The supply air then passes through two bubble tank humidifiers and a heater to achieve the desired supply air temperature and humidity. Two converging-diverging air headers are used before and after the small-scale LAMEE to supply air uniformly to the exchanger inlet and exhaust it to the lab. Four T-type calibrated thermocouples with an accuracy of 0.2˚C and two calibrated humidity sensors with an accuracy of 1.5% RH are used to measure the temperatures and humidity ratios at the inlet and outlet of the LAMEE.

In the open solution loop, lithium chloride (LiCl) salt solution is pumped from a large supply solution tank to the small-scale LAMEE solution inlet header using a peristaltic pump. An electrical heater is used after the pump to adjust the solution inlet temperature to the desired condition. Two T-type shielded thermocouples with an accuracy of 0.1˚C are placed in the solution inlet and outlet headers to measure the solution inlet and outlet temperatures, respectively. The outlet salt solution flow is

discharged into the exhaust solution tank. For each test, the salt solution concentrations at the inlet and outlet of the LAMEE are calculated using the measured solution temperatures and sampled densities under steady state operating conditions.

A small-scale single-panel LAMEE with a counter-cross-flow configuration for air and solution flows is tested during dehumidification and regeneration operating conditions. The small-scale single-panel LAMEE was designed to minimize the sources of errors in LAMEE performance evaluation, and facilitate research and development of LAMEEs by saving the money and time (Ghadiri Moghaddam, 2013b). The LiCl solution flows from top to bottom in the small-scale LAMEE. Figure B.2 shows the air and solution flow configurations of the tested LAMEE. Two grooved plastic liquid-flow panels are each enclosed by a semi-permeable membrane to form two solution channels, one on each side of the air channel. An air spacer is used to form an air channel of constant thickness. The small-scale LAMEE specifications and membrane properties are presented in Table B-1.

Figure B.1 Schematic of the SPEET facility (Ghadiri Moghaddam *et al.*, 2013b).

236

Figure B.2 Air and solution flow configurations of the small-scale single-panel LAMEE (Ghadiri Moghaddam *et al.*, 2013b).

Table B-1 The small-scale single-panel LAMEE specifications and membrane properties.

Parameter	Value
Exchanger length (m)	0.99
Exchanger aspect ratio of the air-liquid contact area	10.5
Exchanger entrance ratio	0.025
Air gap thickness, (mm)	5
Solution gap thickness in each side panel, (mm)	1.2
Water vapor transmission resistance of membrane, (s/m)	24
Membrane thermal conductivity, (W/mK)	0.065
Membrane thickness, (mm)	0.265

B.5   Analytical Model for the Counter-Cross Flow LAMEE

An analytical solution developed by Zhang (2011a) for the steady-state heat and mass transfer for a hollow fiber membrane shell-and-tube energy exchanger with counter-flow configuration is used in this paper to describe the steady-state performance of the counter-cross-flow parallel-plate LAMEEs. In Zhang's analytical model, the problem is solved in one-dimension (i.e. counter flow). In addition, the axial dispersion of heat and mass, and heat and mass losses to the surroundings are assumed to be negligible. In order to use this analytical solution for flat-plate LAMEEs, the overall heat and mass transfer coefficients, U and U_m, are calculated based on the flat-plate LAMEE configuration as

shown in Eqs. (B.1) and (B.2) and these are substituted into Zhang's analytical correlations.

$$U = \left[\frac{1}{h_{c,sol}} + \frac{\delta}{k} + \frac{1}{h_{c,air}} \right]^{-1} \tag{B.1}$$

$$U_m = \left[\frac{1}{h_{m,air}} + \frac{\delta}{k_m} \right]^{-1} \tag{B.2}$$

where, U is the overall heat transfer coefficient (W/m²·K), U_m is the overall mass transfer coefficient (kg/m²·s), h_c is the convective heat transfer coefficient (W/m²·K), δ is the thickness of the membrane (m), k is the thermal conductivity of the membrane (W/m·K), h_m is the convective mass transfer coefficient (kg/m²·s), *and* k_m is the permeability of the membrane (kg/m·s). Subscripts *air* and *sol* refer to the air and solution, respectively.

The convective heat and mass transfer coefficients are calculated for each flow channel using Eqs. (B.3) and (B.4) (Welty *et al.*, 2001).

$$Nu = \frac{h_c D_h}{k_f} \tag{B.3}$$

$$h_m = \frac{h_c}{c_p} Le^{-\frac{2}{3}} \tag{B.4}$$

where, D_h is the hydraulic diameter of the flow channel (m) and is assumed to equal twice the channel spacing for flow between infinite parallel flat plates, k_f is the thermal conductivity of the fluid (W/m·K), c_p is the specific heat capacity (J/kg·K), Le is Lewis number which is defined as the ratio between the thermal to mass diffusivities.

In order to further simplify the calculations using Zhang's analytical steady-state model, the solution outlet temperature and concentration are assumed to be known to begin the calculations, and these assumptions are corrected by iterative calculations using energy balance calculations. One more assumption is made. This assumption is that moisture content change due to absorption/desorption by the salt solution in the LAMEEs can be neglected compared with the average desiccant mass flow rate. Therefore, constant liquid desiccant mass flow rate and constant solution concentration in the LAMEEs are assumed as simplifications. These assumptions are justified by

experimental data for direct-contact air dehumidification and desiccant regeneration processes (Fumo and Goswami, 2002; Liu *et al.*, 2006b), in which the solution concentration changed by 0.1~0.8% while the average salt concentration was around 34% or higher. This small percent change will also be demonstrated in the present study. Considering the properties of salt solution, the equilibrium humidity ratio of desiccant solution (W_{sol}) is solely related to solution temperature and the slope (E_T) is only affected by the iterated solution temperature in the analytical model, as shown in Eq. (B.5). The calculation of this coefficient is different from Zhang's solution (Zhang, 2011a), in which E_T is affected by both the iterated solution temperature and desiccant concentration. This model and Zhang (2011a) assume that saturation conditions do not occur for the salt solution.

$$E_T = \frac{dW_{sol}}{dT_{sol}} \tag{B.5}$$

Several dimensionless parameters are defined as follows for convenience:

$$T^* = \frac{T - T_{air,in}}{T_{sol,in} - T_{air,in}} \tag{B.6}$$

$$W^* = \frac{W - W_{air,in}}{W_{sol,in} - W_{air,in}} \tag{B.7}$$

$$x^* = \frac{x}{L} \tag{B.8}$$

$$H^* = 2500 \frac{W_{sol,in} - W_{air,in}}{T_{sol,in} - T_{air,in}} \tag{B.9}$$

$$NTU = Max\left\{\frac{UA}{C_{air}}, \frac{UA}{C_{sol}}\right\} \tag{B.10}$$

$$Cr* = \frac{C_{sol}}{C_{air}} \tag{B.11}$$

Where, T is the temperature (^oC), W is the humidity ratio (g/kg), L is the length of the LAMEE (m) and H^* is an operating condition factor which is defined as the ratio between the potential for mass transfer to that for heat transfer (Simonson and Besant, 1999). A is the total effective membrane area (m^2) and C is the thermal capacity (W/K).

With above parameters, the normalized governing equations for heat and moisture conservation in the air and solution flows are:

$$\frac{dT_{air}^*}{dx^*} = NTU(T_{sol}^* - T_{air}^*) \tag{B.12}$$

$$\frac{dT_{sol}^*}{dx^*} = \frac{NTU}{Cr^*}(T_{sol}^* - T_{air}^*) + \frac{H^*}{Cr^* \cdot c_{p,air}} \cdot \frac{dW_{air}^*}{dx^*} \tag{B.13}$$

$$\frac{dW_{air}^*}{dx^*} = NTU_m(W_{sol}^* - W_{air}^*) \tag{B.14}$$

$$\frac{dW_{sol}^*}{dx^*} = 2500 \frac{E_T}{H^*} \cdot \frac{dT_{sol}^*}{dx^*} \tag{B.15}$$

In order to simplify these equations further, we define

$$\xi = T_{sol}^* - T_{air}^* \tag{B.16}$$

$$\psi = W_{sol}^* - W_{air}^* \tag{B.17}$$

The governing differential equations (B.12) to (B.15) can be rewritten as

$$\frac{d\xi}{dx^*} = a_{11}\xi + a_{12}\psi \tag{B.18}$$

$$\frac{d\psi}{dx^*} = a_{21}\xi + a_{22}\psi \tag{B.19}$$

The sensible and latent effectiveness of the counter-cross-flow exchanger can be calculated by using the following equations.

$$\varepsilon_{Sen} = 1 - C_1 e^{\lambda_1} - C_2 e^{\lambda_2} \tag{B.20}$$

$$\varepsilon_{Lat} = 1 + K_1 C_1 e^{\lambda_1} - K_2 C_2 e^{\lambda_2} \tag{B.21}$$

Where, C_1 and C_2 are functions of $a_{11} \sim a_{22}$ and are constant coefficients, $\lambda_{1,2}$ are the roots of the characteristic equations of (B.18) and (B.19), and K_1 and K_2 are the intermediate coefficients of the analytical solution. More detailed calculations of these coefficients can be referred to Zhang (2011a).

It is worth mentioning that the results obtained from the above modified steady-state analytical solution were partly validated using experimental data for several test conditions in a previous study, and the analytical model was found to fit the measured data for the LAMEE performance (Ge *et al.*, 2012).

B.6 Results and Discussion

Experimental measurements for air dehumidification and desiccant regeneration processes using LiCl salt solution in the small-scale LAMEE were conducted. The results are presented in this section. In addition, an analytical analysis is carried out to study the influences of different air and desiccant solution inlet parameters affecting the heat and mass transfer performance of the dehumidifier and regenerator by using the analytical model.

In order to analyze the heat and mass transfer performance of the LAMEE during dehumidifier and regenerator operating conditions, three important indexes (i.e. the moisture flux ratio (R_W), the sensible (ε_S) and latent (ε_L) effectiveness) in the dehumidification and regeneration processes are evaluated. The dimensionless moisture flux ratio is firstly proposed in the study, as shown in Eq. (B.22), to evaluate the moisture transfer potential of the liquid desiccant exchanger under the tested inlet condition. It is the ratio between the actual moisture removal rate (MRR) with respect to the membrane overall mass transfer conductance. This index is proposed here rather than using the moisture removal rate in previous publications (Fumo and Goswami, 2002; Liu *et al.*, 2006b), since it would not depend on the size of the exchanger but only depend on the inlet conditions. This index would make the results more general and useful in the literature because other researchers could do similar tests and compare the results. In the reported results it is assumed that U_m is almost constant for all tests; however, if a partial crystal blockage was to occur in the membrane its value would decrease.

$$R_W = \frac{M_{air}\left|W_{air,in} - W_{air,out}\right|}{AU_m} \tag{B.22}$$

The sensible and latent effectiveness are calculated using Eqs. (B.23) and (B.24) when $Cr^* \geq 1$. They show the ratio between the actual heat and vapor mass transfer and the maximum heat and vapor mass that could be transferred in the energy exchanger for a given set of inlet conditions.

$$\varepsilon_S = \frac{T_{air,in} - T_{air,out}}{T_{air,in} - T_{sol,in}} \tag{B.23}$$

$$\varepsilon_L = \frac{W_{air,in} - W_{air,out}}{W_{air,in} - W_{sol,in}} \tag{B.24}$$

Another parameter, named solution operation ratio (R_C), is proposed in the study to characterize the proximity of the solution concentration to the solution thermodynamic saturation conditions at the temperature of the solution. It is calculated using Eq. (B.25).

$$R_C = \frac{C_{Sat} - C}{C_{Sat}} = 1 - \frac{C}{C_{Sat}} \tag{B.25}$$

Where C is the mass fraction of desiccant salt in the solution, and the subscript *Sat* represents the saturation condition of desiccant solution.

B.6.1 Air Dehumidification

Table B-2 summarizes the experimental results (D1-D13, totally 13 groups of tests) during various air dehumidification conditions. The measured air and solution flow rates, inlet and outlet air and desiccant solution states, the operating ratios (i.e. *NTU*, *Cr** and R_C), as well as the calculated experimental and theoretical output results (i.e. ε_S, ε_L and R_W) are listed. Effects of air and desiccant inlet parameters on the air dehumidifier performance will be discussed in this section, when the reference air inlet parameters are set as 5.3 kg/h (*NTU* = 5), 30°C and 14.3 g/kg (50%RH), and desiccant inlet parameters are 8.3 kg/h (*Cr** = 4), 24°C and concentration of 32%. It is observed that the sensible effectiveness data agrees with the theoretical prediction of sensible effectiveness, and the difference is generally within 10%. In the following analysis of dehumidifier performance, we emphasize on the mass transfer performance of the LAMEE under different parameters, and only one investigated parameter is changed for each test and the other parameters are kept at the listed reference values. According to the experimental data, it is found that the variation of desiccant concentration during the air dehumidification process is very small, i.e. in the range of 0.04~0.35%.

Table B-2 Air dehumidification experimental data, operating ratios and results.

	Inlet data						Operating ratios			Outlet data				Results					
	M_{air}	T_{air}	W_{air}	M_{sol}	T_{sol}	C_{sol}	NTU	Cr^*	R_C	T_{air}	W_{air}	T_{sol}	C_{sol}	ε_S	$\varepsilon_{S,th}$	ε_L	$\varepsilon_{L,th}$	R_W	$R_{W,th}$
	(kg/h)	(°C)	(g/kg)	(kg/h)	(°C)	(%)				(°C)	(g/kg)	(°C)	(%)	(%)	(%)	(%)	(%)	(10^{-3})	(10^{-3})
D1	5.295	30.1	14.3	8.311	24.0	32.08	5	4	0.300	24.9	7.9	28.6	31.92	84.9	90.0	84.8	85.4	2.60	2.46
D2	3.668	30.0	14.3	5.643	24.0	32.00	6	4	0.302	24.7	7.5	28.3	31.85	89.5	92.4	91.0	90.7	2.09	1.98
D3	2.626	30.0	14.2	4.082	24.0	32.00	7	4	0.302	24.4	7.4	28.2	31.8	94.1	94.8	91.6	94.3	1.65	1.63
D4	5.410	25.0	14.2	8.435	24.0	31.97	5	4	0.302	24.7	7.6	27.7	31.76	30.0	51.6	89.4	86.2	2.69	2.43
D5	5.224	35.2	14.3	8.152	24.0	32.04	5	4	0.301	25.1	8.0	29.6	31.89	89.6	93.3	83.9	84.2	2.53	2.38
D6	5.313	30.0	20.2	8.356	24.0	31.97	5	4	0.302	25.5	8.3	32.6	31.73	75.3	82.9	89.1	85.3	4.83	4.46
D7	5.345	30.1	8.2	8.198	24.0	31.97	5	4	0.302	24.4	7.0	26.4	31.93	93.4	96.5	84.1	78.5	0.47	0.30
D8	5.323	30.0	14.5	4.179	24.0	32.14	5	2	0.298	26.4	8.7	30.5	31.79	60.7	70.9	73.9	73.5	2.30	2.16
D9	5.321	30.0	14.2	12.457	24.0	32.14	5	6	0.298	24.6	7.3	27.0	32.06	89.4	93.8	91.7	88.0	2.77	2.50
D10	5.330	29.9	13.8	8.216	28.0	32.07	5	4	0.305	28.4	9.4	30.9	32.01	80.1	80.6	86.9	84.6	1.80	1.59
D11	5.330	30.0	13.8	8.205	32.0	32.01	5	4	0.312	31.7	11.2	33.4	31.89	81.6	104.7	98.1	86.0	1.04	0.70
D12	5.324	30.0	14.2	8.468	24.0	37.05	5	4	0.191	25.3	5.6	30.2	36.83	79.3	87.7	88.9	87.3	3.48	3.26
D13	5.316	30.0	13.9	7.877	24.0	27.65	5	4	0.396	24.9	10.1	27.5	27.57	85.9	92.1	79.1	82.3	1.53	1.47

A complete assessment of the mass and energy balances of the experimental tests were conducted. The LAMEE water vapor mass and energy balances are calculated from the following equations (Simonson *et al.*, 1999):

$$\Delta(MW) = \left\| (MW)_{air,in} - (MW)_{air,out} \right\| + \left[(M_{salt} X_{sol})_{in} - (M_{salt} X_{sol})_{out} \right] \le Un_{\Delta(MW)} \quad \text{(B.26)}$$

$$\Delta(MH) = \left\| (MH)_{air,in} - (MH)_{air,out} \right\| + \left[(MH)_{sol,in} - (MH)_{sol,out} \right] \le Un_{\Delta(MH)} \quad \text{(B.27)}$$

Where $Un_{\Delta(MW)}$ and $Un_{\Delta(MH)}$ are the calculated uncertainties for water vapor and energy transfers during the tests, based on the air and solution properties for each test. *W*, *H* and *X* are humidity ratio, enthalpy and solution mass fraction (Namvar *et al.*, 2012), respectively. Subscripts *salt*, *in* and *out* refer to the pure salt and the air or solution inlet and outlet in the LAMEE, respectively. The water vapor mass and energy balances of all dehumidification tests in the small-scale LAMEE are evaluated and six representative dehumidification tests are presented in Table B-3. The results show that the small-scale LAMEE is balanced for all tests, and the experimental data are within acceptable uncertainty ranges.

Table B-3 Mass and energy balances for six representative dehumidification tests.

	Water vapor balance		Energy balance	
	$\Delta(MW)$, g/h	$Un_{\Delta(MW)}$, g/h	$\Delta(MH)$, W	$Un_{\Delta(MH)}$, W
D1	20.9	159.9	0.4	8.8
D2	16.4	108.7	1.5	6.0
D5	20.8	156.9	0.8	8.9
D6	26.3	161.1	5.2	9.3
D9	26.5	239.3	1.9	12.5
D12	27.4	151.0	2.5	8.9

Figures.B.3~B.9 present the experimental results (i.e. moisture flux ratio and latent effectiveness) for air dehumidification process together with the analytical modeling results. Overall uncertainties of the experimental measurements were calculated using the error propagation method (Figliola and Beasley, 2006; ASME Standard PTC 19.1, 2005), which depend on the individual uncertainties of the instruments and

measured parameters. Error bars obtained from these calculations are also shown in the figures.

Figure B.3(a) shows the moisture flux ratio, R_w, in the air dehumidifier and the corresponding experimental uncertainties, as a function of the *NTU* value for different air flow rates. The moisture flux ratio decreases significantly with the increasing of *NTU* value. According to the air dehumidification experimental results (D1-D3) presented in Table B-2, it can be found that the higher the *NTU* value, the lower the air flow rate. It means that higher moisture flux is transferred in the exchanger at higher air flow rate. Figure B.3(b) shows the experimental latent effectiveness increases as the *NTU* value increases and the air flow rate decreases. It may be explained that a lower air flow rate will remove the air stream moisture content slowly (i.e. R_w is lower) in the air channel and this makes ε_S and ε_L higher. Corresponding, the air humidity ratio at the outlet of the LAMEE decreases as the air flow rate decreases, as shown in Table B-2.

Figure B.3 Influence of inlet air flow rate (*NTU*) on dehumidification (a) moisture flux ratio and (b) latent effectiveness (D1-D3 data from Table B-2).

The influences of inlet air temperature and humidity on moisture flux ratio and latent effectiveness of the dehumidification process are shown in Figure B.4 and B.5. The moisture flux ratio decreases slightly with the inlet air temperature. The reason is that the air flow at higher temperature will heat the desiccant solution in the dehumidification process by sensible heat transfer and may reduce the mass transfer potential in the dehumidifier. Therefore the latent effectiveness decreases accordingly.

Figure B.4 Influence of inlet air temperature on dehumidification (a) moisture flux ratio and (b) latent effectiveness (D1, D4 and D5 data from Table B-2).

Figure B.5(a) reveals that the moisture flux ratio increases substantially with the inlet air humidity ratio. This happens because a higher inlet air humidity ratio implies a higher air vapor pressure and consequently a higher vapor pressure difference for mass transfer between the air and solution flows. The increase of inlet air humidity results in a negligible increase of the latent effectiveness as shown in Figure B.5(b) since both the numerator and denominator in Eq. (B.24) increase simultaneously. It can also be found that the uncertainty of latent effectiveness in the case of $W_{air,in} = 8$ g/kg is much higher than other cases, since the equilibrium humidity ratio of solution in the inlet condition ($W_{sol,in} = 6.8$ g/kg) is quite close to the inlet air humidity ratio. According to the effectiveness definition in Eq. (B.24), small measurement uncertainties of the air or solution conditions will cause higher experimental uncertainties for ε_L.
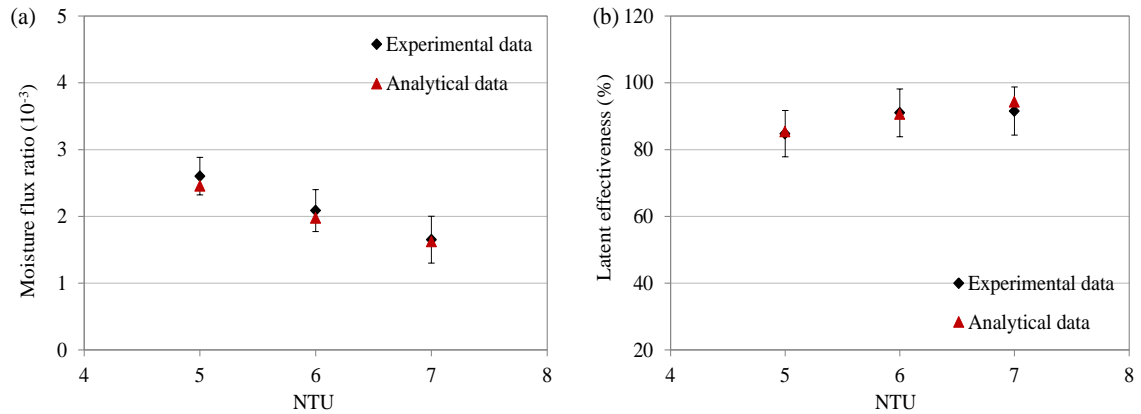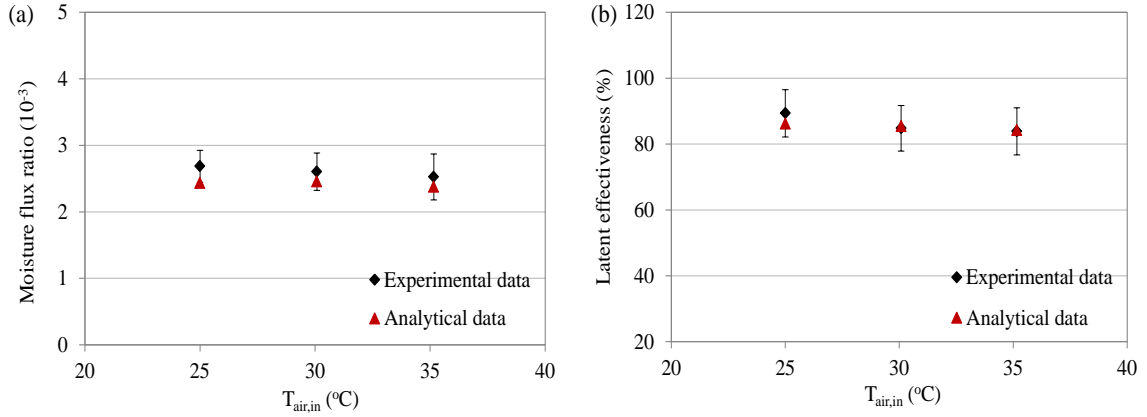
Figure B.5 Influence of inlet air humidity on dehumidification (a) moisture flux ratio and (b) latent effectiveness (D1, D6 and D7 data from Table B-2).

As the increase of solution flow rate and corresponding Cr^* value by Eq. (B.11) the moisture flux ratio increases accordingly as shown in Figure B.6(a). That is, a higher desiccant solution flow rate will increase the heat capacity rate of solution and reduce the temperature increase by absorbing the phase change heat from the moisture condensation in the air dehumidification process. Therefore, a higher humidity gradient between the air and solution flows would be maintained under higher solution flow rate conditions, since the equilibrium humidity ratio of LiCl solution is lower at lower solution temperatures and the constant desiccant concentration, as shown in Figure B.7. This will increase the average mass transfer vapor pressure difference between the air and desiccant solution flows and the latent effectiveness will increase as plotted in Figure B.6(b).

Figure B.6 Influence of inlet solution flow rate (Cr^*) on dehumidification (a) moisture flux ratio and (b) latent effectiveness (D1, D8 and D9 data from Table B-2).

247
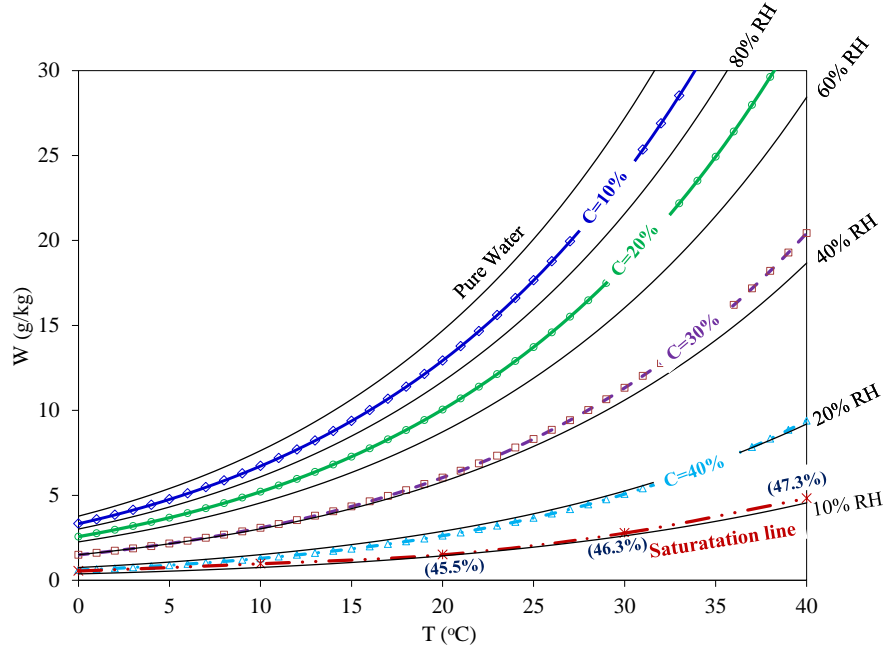
Figure B.7 Air equilibrium humidity ratio VS temperature with air relative humidity and equilibrium LiCl solution concentration as parameters.

Figure B.8 and Figure B.9 present the moisture flux ratio and latent effectiveness in the dehumidification process under various inlet solution temperature and concentration conditions. The moisture flux ratio decreases significantly from 2.6×10^{-3} to 1.0×10^{-3} as the desiccant solution temperature increases from 24°C to 32°C. The explanation is that higher desiccant temperatures produce higher water vapor pressures at constant solution concentration in the solution side, as shown in Figure B.7, and this reduces the moisture gradient between the air and solution flows, consequently resulting in a lower moisture flux in the dehumidifier. Figure B.8(b) reveals that the latent effectiveness increases since the denominator in Eq. (B.24) decreases significantly due to the increasing of inlet solution temperature. The uncertainty of effectiveness is higher (~24.6%) in the case of $T_{sol,in} = 32$°C since the equilibrium humidity ratio of solution in the inlet condition is very close to the inlet air humidity ratio and the denominator is very small.
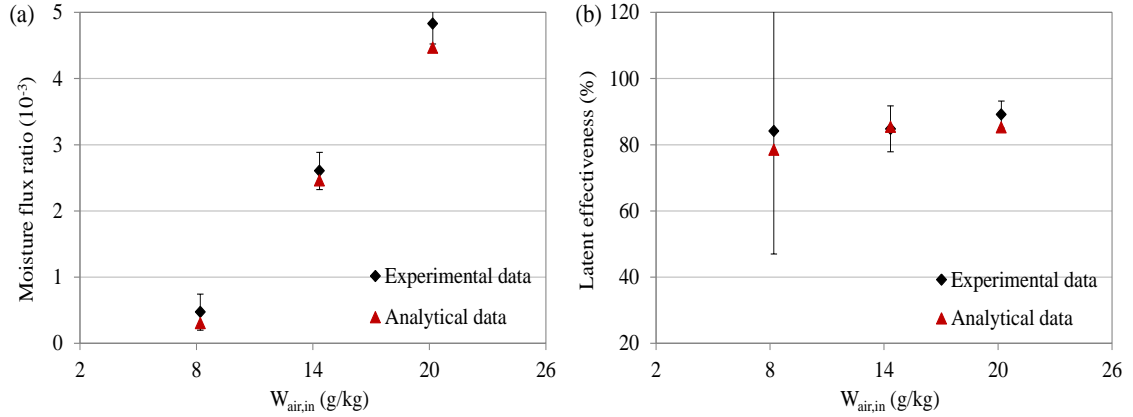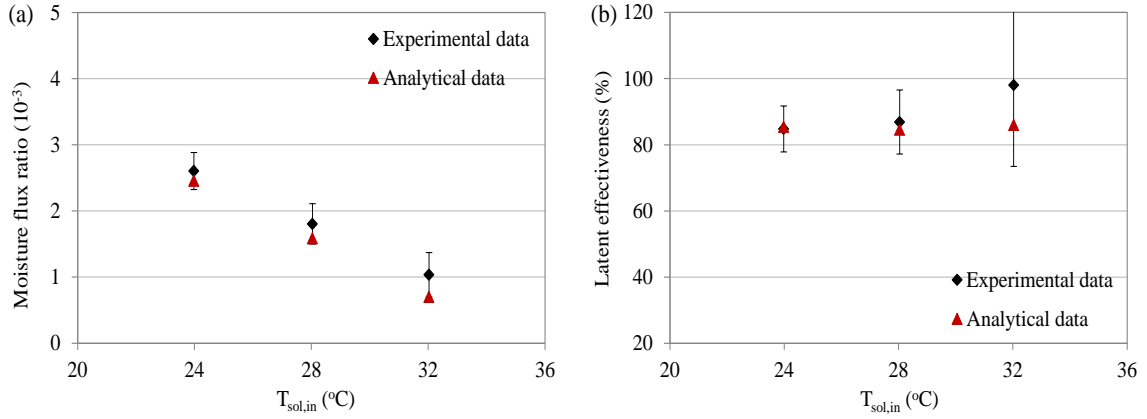
Figure B.8 Influence of inlet solution temperature on dehumidification (a) moisture flux ratio and (b) latent effectiveness (D1, D10 and D11 data from Table B-2).

Figure B.9(a) illustrates that the moisture flux ratio increases from $1.5{\times}10^{-3}$ to $3.5{\times}10^{-3}$ as the inlet desiccant concentration changes from 27% to 37%. The interpretation is that the water vapor pressure decreases with the increase of solution concentration and therefore gives a higher potential for mass transfer in the dehumidifier resulting in a greater moisture flux. Figure B.9(b) shows that the latent effectiveness increases slightly with the desiccant concentration due to the trade-off of both the denominator and numerator in Eq. (B.24).
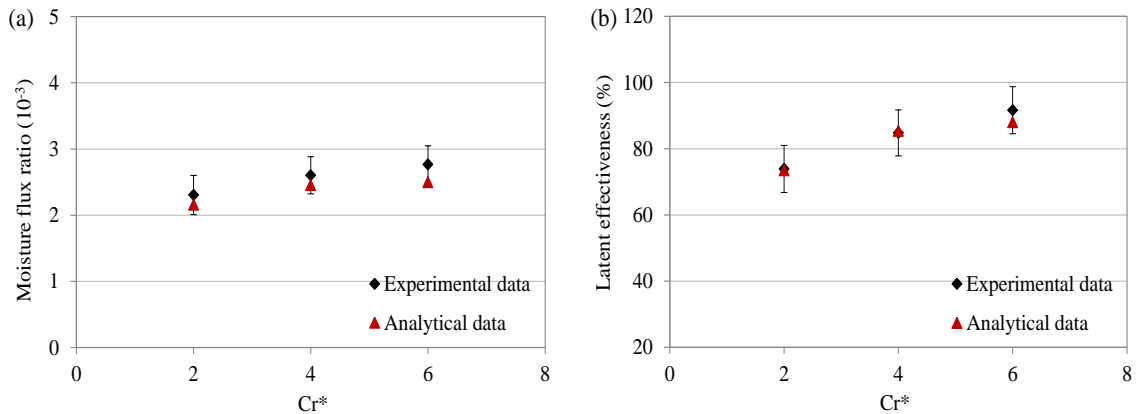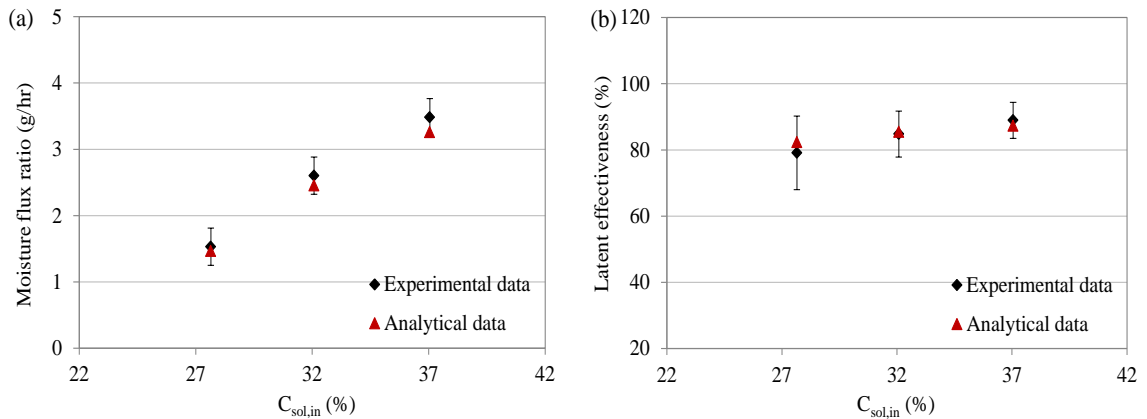

Figure B.9 Influence of inlet solution concentration on dehumidification (a) moisture flux ratio and (b) latent effectiveness (D1, D12 and D13 data from Table B-2).

In summary, the variables found to have the most significant effect on the air dehumidification moisture transfer in the LAMEE are: air flow rate, air humidity ratio, desiccant solution temperature, and solution concentration. In addition, it is seen from the Figures. B.3 to B.9 that the analytical modeling results show good agreement with the

experimental findings under the air dehumidification conditions, and the discrepancy always lies within the range of measurement uncertainty.

B.6.2 Solution Regeneration

Table B-4 presents the experimental data, operating ratios as well as calculated experimental and theoretical results (R1-R13, i.e. 13 groups of test data) for solution regeneration or de-watering process. In these tests, the average inlet air temperature and humidity ratio is around $30^{o}C$ and 14.3g/kg (50%RH) respectively, while the inlet solution temperature and concentration is around $55^{o}C$ and 32% respectively. It is found that the variation of desiccant concentration in these solution regeneration tests is within the range of 0.06~0.48%. The water vapor mass and energy balances of all regeneration tests in the small-scale LAMEE are checked and six representative regeneration tests are presented in Table B-5. The results demonstrate that the mass and energy balances are achieved for all tests in the small-scale LAMEE. Figures. B.10~B.15 show the experimental data together with the analytical results on mass transfer performance for these regeneration tests.

Table B-4 Solution regeneration (de-watering) experimental data, operating ratios and results.

	Inlet data						Operating ratios			Outlet data				Results					
	M_{air}	T_{air}	W_{air}	M_{sol}	T_{sol}	C_{sol}	NTU	Cr^*	R_C	T_{air}	W_{air}	T_{sol}	C_{sol}	ε_S	$\varepsilon_{S,th}$	ε_L	$\varepsilon_{L,th}$	R_W	$R_{W,th}$
	(kg/h)	(°C)	(g/kg)	(kg/h)	(°C)	(%)				(°C)	(g/kg)	(°C)	(%)	(%)	(%)	(%)	(%)	(10^{-3})	(10^{-3})
R1	5.326	30.0	14.6	8.056	55.1	32.16	5	4	0.344	47.5	26.9	45.9	32.36	69.9	86.7	46.9	61.7	4.96	6.39
R2	3.664	30.0	13.7	5.486	55.0	32.29	6	4	0.342	45.6	27.5	46.4	32.37	62.3	87.7	52.0	68.7	4.26	5.49
R3	2.695	30.0	14.4	4.010	55.0	32.29	7	4	0.342	45.4	30.6	46.1	32.47	61.5	88.8	62.5	73.4	3.98	4.53
R4	5.419	25.0	14.2	8.199	55.0	32.32	5	4	0.341	48.4	27.6	46.8	32.55	77.9	88.6	51.3	61.6	5.44	6.36
R5	5.239	35.0	13.5	7.915	55.0	32.32	5	4	0.341	47.7	26.1	47.1	32.54	63.5	83.8	47.3	62.8	5.05	6.56
R6	5.283	30.0	19.9	8.078	55.1	32.02	5	4	0.347	48.8	29.2	48.4	32.21	75.2	88.5	43.6	59.0	3.76	4.97
R7	5.352	30.1	8.4	7.945	55.0	32.20	5	4	0.344	47.1	25.6	45.8	32.43	68.2	84.5	53.7	64.3	6.91	8.10
R8	5.334	29.9	13.4	4.046	55.0	32.00	5	2	0.348	43.7	23.3	41.8	32.3	54.8	66.7	35.8	41.2	4.00	4.48
R9	5.333	30.0	13.8	11.974	55.0	32.00	5	6	0.348	48.3	28.6	50.5	32.18	73.3	92.0	54.2	70.5	5.97	7.54
R10	5.341	29.9	13.9	8.068	50.1	32.04	5	4	0.339	45.2	22.8	43.1	32.23	75.8	88.7	51.2	64.6	3.59	4.51
R11	5.342	30.0	14.2	8.085	45.0	32.04	5	4	0.331	42.6	19.8	40.3	32.17	84.1	91.1	59.5	66.9	2.26	2.61
R12	5.338	30.1	14.4	8.156	55.1	37.00	5	4	0.246	49.8	21.3	48.6	37.16	78.8	91.8	49.8	64.9	2.81	3.75
R13	5.328	30.0	14.3	7.695	55.0	27.00	5	4	0.450	46.5	31.7	45.6	27.35	66.1	80.1	41.8	58.0	7.01	9.31

Table B-5 Mass and energy balances for six representative regeneration tests.

	Water vapor balance		Energy balance	
	$\Delta(MW)$, g/h	$Un_{\Delta(MW)}$, g/h	$\Delta(MH)$, W	$Un_{\Delta(MH)}$, W
R1	45.4	154.6	9.1	14.2
R2	34.9	105.2	8.4	10.1
R5	32.1	151.4	8.8	14.1
R6	25.4	155.4	10.6	15.3
R9	31.8	115.3	15.5	20.7
R12	24.2	145.4	8.6	14.4

Figure B.10(a) shows that the moisture flux ratio increases from 4.0×10^{-3} to 5.0×10^{-3} as the *NTU* value decreases from 7 to 5 (i.e. the air flow rate increases from 2.7 kg/h to 5.3 kg/h). The reason for this is that, as the air flow rate increases, the change of humidity ratio is smaller (as shown in R1-R3 in Table B-4) and the relatively high water vapor pressure in the air channel would be nearly constant. Consequently, the moisture transfer between air and solution flows is enhanced, but the latent effectiveness is diminished. As a result, the latent effectiveness decreases from 62.5% to 46.9% when the *NTU* value decreases from 7 to 5 as shown in Figure B.10(b). In addition, it can be found that much of the analytical results do not agree with the experimental data for the latent effectiveness for the conditions tested. The analytical results are generally 20% higher than the experimental results. The possible reasons will be analyzed in the discussion ahead.
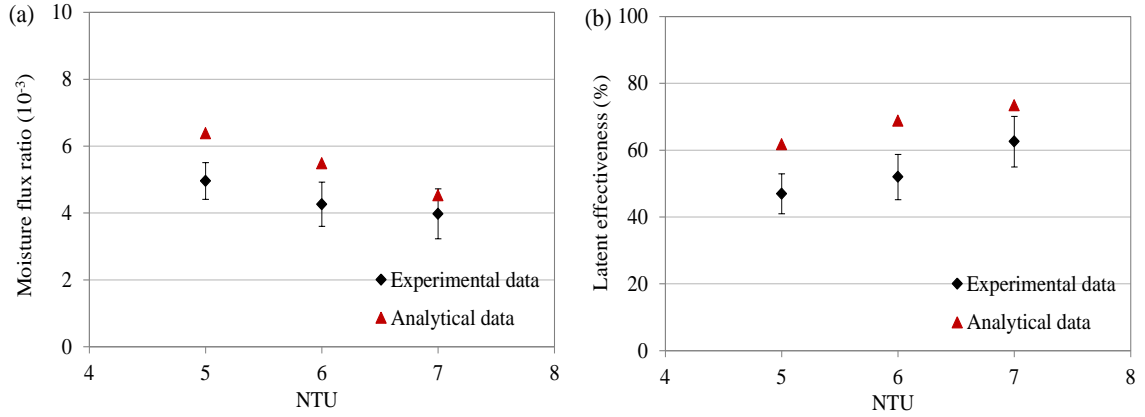
Figure B.10 Influence of air flow rate (*NTU*) on regeneration (a) moisture flux ratio and (b) latent effectiveness (R1-R3 data from Table B-4).

The influences of the regeneration air inlet temperature and humidity ratio on the moisture flux ratio and the latent effectiveness are depicted in Figure B.11 and Figure B.12. It can be seen that the inlet air temperature does not cause significant variations in the moisture flux ration and the latent effectiveness (Figure B.11). As shown in Figure B.12(a), the moisture flux ratio decreases substantially with the inlet air humidity ratio. As expected, a higher humidity ratio implies a higher water vapor pressure and consequently lower moisture gradient between the solution and air flows and hence lower potential for mass transfer during the solution regeneration process. Accordingly, it will result in a lower latent effectiveness under higher inlet air humidity condition as shown in Figure B.12(b).

Figure B.11 Influence of inlet air temperature on regeneration (a) moisture flux ratio and (b) latent effectiveness (R1, R4 and R5 data from Table B-4).

253

Figure B.12 Influence of inlet air humidity on regeneration (a) moisture flux ratio and (b) latent effectiveness (R1, R6 and R7 data from Table B-4).

Figure B.13 reveals that the moisture flux ratio, R_w, is enhanced significantly from 4.0×10^{-3} to 6.0×10^{-3} when the Cr^* value is changed from 2 to 6 and the solution flow rate is increased from 4.0 kg/h to 12.0 kg/h. The explanation is the same as the dehumidification case (i.e. the higher the solution flow rate, the higher heat capacity rate of desiccant solution). It will cause less temperature reduction of the desiccant solution during the phase change or evaporation process of liquid water in the solution channel, and maintain a high vapor pressure difference for mass transfer. The latent effectiveness increases from 35.8% to 54.2% as Cr^* increases from 2 to 6.
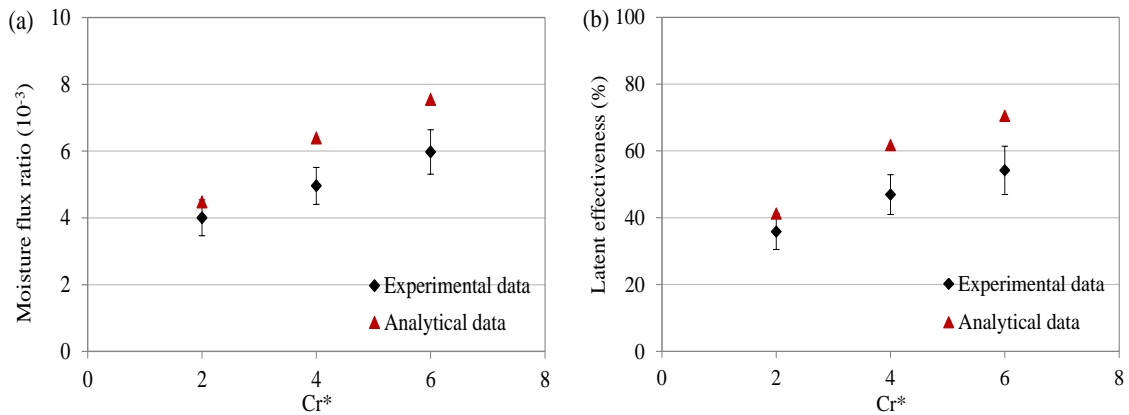
Figure B.13 Influence of solution flow rate (Cr^*) on regeneration (a) moisture flux ratio and (b) latent effectiveness (R1, R8 and R9 data from Table B-4).

The influences of solution inlet temperature and concentration on the moisture flux ratio and latent effectiveness during the solution regeneration process are presented in Figure B.14 and Figure B.15. The moisture flux ratio increases significantly with the

254

inlet solution temperature as shown in Figure B.14(a). The reason is that the water vapor pressure of desiccant solution is highly dependent on its temperature, i.e. the higher the temperature of desiccant solution, the higher the vapor pressure. Hence, the vapor pressure gradient between the solution and air streams increases as the solution temperature increases, and consequently the potential for mass transfer increases. It can also be found that the latent effectiveness decreases with the solution temperature, since the equilibrium humidity ratio of solution increases and the absolute value of the denominator of Eq. (B.24) increases significantly. In contrast to the air dehumidification process, the effect of solution temperature on the mass transfer performances in the desiccant regeneration process is opposite.

Comparing the results shown in Figure B.11 and Figure B.14, it is shown that the moisture flux ratio in the solution regeneration process is more sensitive to the change of solution inlet temperature and almost independent of the changes of air inlet temperature. Therefore, heating the desiccant solution and regulating its inlet temperature to enhance the desiccant regeneration performance in the proposed counter-cross-flow LAMEEs are more effective than heating the regeneration air flow.
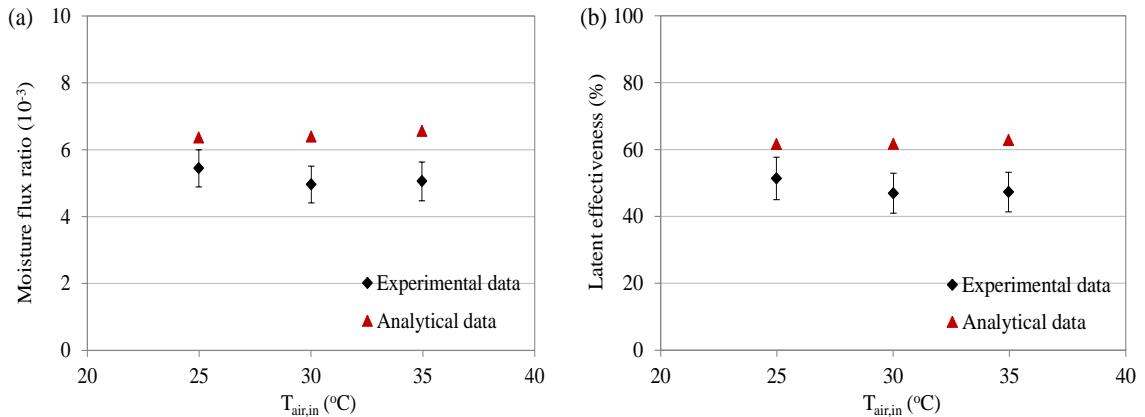

Figure B.14 Influence of solution inlet temperature on regeneration (a) moisture flux ratio and (b) latent effectiveness (R1, R10 and R11 data from Table B-4).
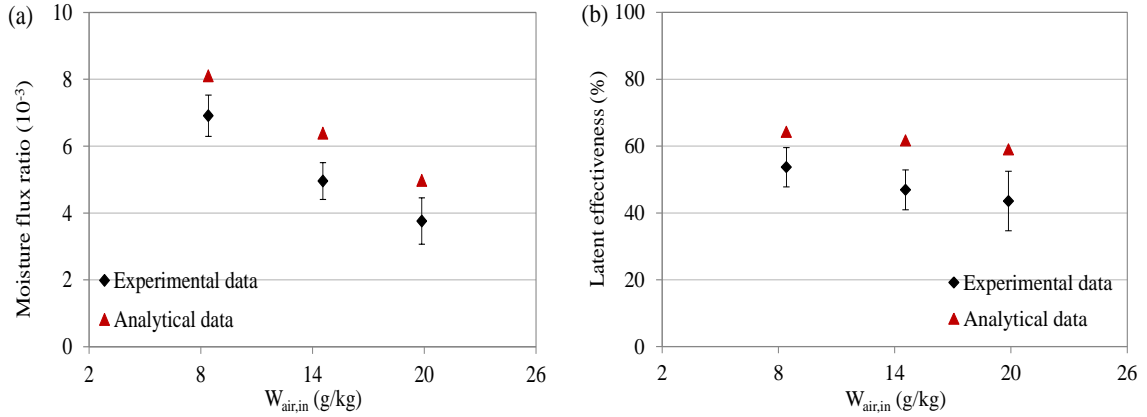
Figure B.15 shows that the moisture flux ratio significantly decreases from 7.0×10^{-3} to 2.8×10^{-3} as the inlet desiccant concentration varies from 27% to 37%. This may be interpreted from the fact that vapor pressure of the desiccant solution is a function of the concentration, as shown in Figure B.7. Therefore, the higher the concentration, the lower the vapor pressure, and consequently the lower the moisture gradient and mass

transfer potential. It can also be found that the solution concentration has a very small impact on the latent effectiveness of the regeneration process, since both the desiccant inlet equivalent humidity ratio and the air outlet humidity ratio decrease with increasing solution concentration. They offset each other and finally the latent effectiveness increases slightly.
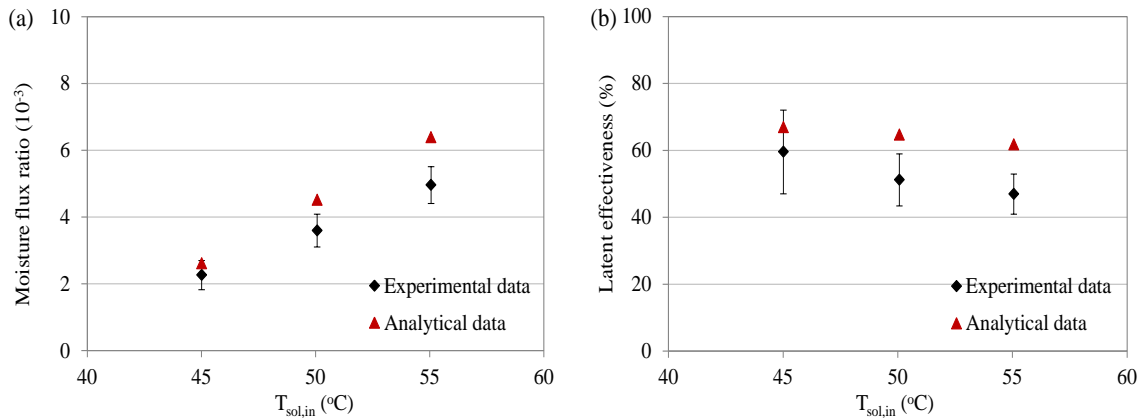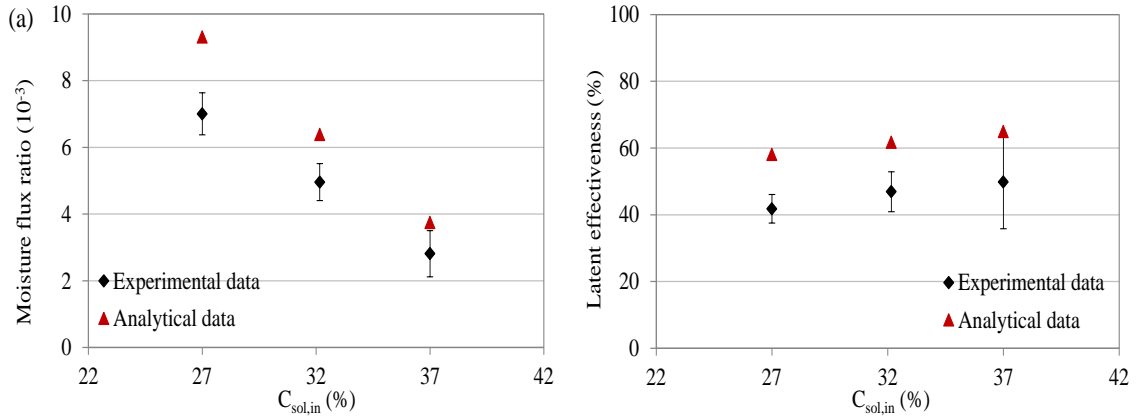

Figure B.15 Influence of inlet solution concentration on regeneration (a) moisture flux ratio and (b) latent effectiveness (R1, R12 and R13 data from Table B-4).

According to the results presented in Figures. B.10~B.15, it can be summarized that the inlet air humidity ratio, air flow rate, solution inlet temperature, solution concentration and solution flow rate have significant influences on the moisture transmission in the desiccant solution regeneration process. In addition, it appears that except for a small fraction of data the agreement between the analytical and experimental results is not good in the tested regeneration conditions, although they have almost the same variation trend as the investigated inlet parameter changes. There are two possible reasons causing this significant discrepancy between the analytical and experimental results. The first reason is that the concentration of LiCl aqueous solution near or in the membrane increases towards saturation conditions while its temperature decreases with the evaporation of liquid water in the solution channel during the de-watering regeneration process. This makes the process prone to generate LiCl·H$_2$O crystals above 20°C and LiCl·2H$_2$O crystals below 20°C (Monnin *et al.*, 2002), when the value of R_w is high and the value of R_C is small, in the membrane pores, which are close to solution side of the membrane during the regeneration tests. Any crystallization would reduce the overall moisture transfer coefficient, U_m, (defined in Eq. (B.2) and used in Eq. (B.22))

256

during the regeneration tests. Due to the evaporation of liquid water in the solution channel and the phase change energy required for the desiccant crystallization process, the solution temperature and membrane temperature will decrease and consequently the experimentally measured sensible effectiveness is lower than the theoretical results as shown in Table B-4 for the solution regeneration process. Another less likely reason is that higher membrane deflections occur in the regeneration tests due to higher solution temperature in the LAMEE, which may reduce the mass transfer performance of the exchanger (Hemingson *et al.*, 2011). According to the recorded data, we found that the measured air pressure drops during the regeneration tests were 10-15% higher than those in the corresponding dehumidification cases. But, it is noted, the air kinematic viscosity would have also increased by about 10%, so this pressure drop increase may be mostly due to viscosity changes not increased deflections.

B.7   Comparison with Results for Other Direct-Contact LD Devices

Many investigations about the heat and mass transfer performances of direct-contact liquid desiccant devices (e.g. packed towers or packed beds) have been published in the last decade, while little literature was concerned about the mass transfer performance of the membrane-based indirect-contact energy exchangers. The present experimental results for the liquid-to-air membrane energy exchanger during dehumidifier and regenerator operating conditions are then compared with those for the direct-contact energy exchanger as dehumidifier and regenerator available in the literature.

The trends of the effects of the inlet parameters on the moisture transfer (i.e. moisture flux ratio) and the latent effectiveness of the proposed indirect-contact LAMEE as dehumidifier and regenerator are summarized in Table B-6 and Table B-7, respectively, compared with the experimental results reported in the literature for direct-contact liquid desiccant devices as dehumidifiers and regenerators. It can be found that the inlet parameters generally have the same trends in affecting the performances of the indirect-contact LAMEE and the direct-contact energy exchangers. Few exceptions exist mainly caused by the differences of the operating parameter ranges, such like the air and solution flow rates (Liu *et al.*, 2007b).

Table B-6 Effects of inlet parameters on the moisture flux ratio (R_W), MRR and latent effectiveness of the indirect-contact LAMME and direct-contact exchangers as dehumidifiers.

Reference	Desiccant	Flow type	Index	M_{air}	T_{air}	W_{air}	M_{sol}	T_{sol}	C_{sol}
Present study	LiCl	Counter-cross	R_W	↑	↔	↑	↑	↓	↑
			ε_L	↓	↔	↔	↑	↑	↔
Oberg and Goswami (1998)	TEG	Counter	MRR	↑	↔	↑	↔	↓	↑
			ε_L	↓	↔	↔	↔	↔	↔
Fumo and Goswami (2002)	LiCl	Counter	MRR	↑	↔	↑	↔	↓	↑
Liu *et al.* (2006b)	LiBr	Cross	MRR	↑	↔	↑	↑	↓	↑
			ε_L	↓	↔	↔	↑	↑	↔
Moon *et al.* (2009)	CaCl₂	Cross	MRR	↑	↔	↑	↑	↓	↑
			ε_L	↓	↔	↔	↑	↑	↓
↑: Increasing trend; ↓: Decreasing trend; ↔: No significant effect.									

Table B-7 Effects of inlet parameters on the moisture flux ratio (R_W), MRR and latent effectiveness of the indirect-contact LAMME and direct-contact exchangers as regenerators.

Reference	Desiccant	Flow type	Index	M_{air}	T_{air}	W_{air}	M_{sol}	T_{sol}	C_{sol}
Present study	LiCl	Counter-cross	R_W	↑	↔	↓	↑	↑	↓
			ε_L	↓	↔	↓	↑	↓	↑
Martin and Goswami (1999)	TEG	Counter	MRR	↑	↔	↓	↑	↑	↓
			ε_L	↓	↔	↔	↑	↓	↔
Fumo and Goswami (2002)	LiCl	Counter	MRR	↑	↔	↓	↑	↑	↓
			ε_L	↓	×	×	↑	×	×
Liu *et al.* (2007b)	LiBr	Cross	MRR	↑	↔	↓	↑	↑	↓
			ε_L	↓	↔	↔	↑	↓	↑
Sultan *et al.* (2002)	CaCl₂	Counter	MRR	↑	↑	↓	↑	↑	↓
↑: Increasing trend; ↓: Decreasing trend; ↔: No significant effect; ×: Not mentioned.									

B.8   Conclusions

Experimental tests for air dehumidification and desiccant solution regeneration using lithium chloride in a liquid-to-air membrane energy exchanger (LAMEE) have been conducted. The influence of the independent operating parameters (i.e. *NTU*, *Cr**, R_C, etc.) have been investigated and they are shown to influence the resulting moisture flux ratio, R_w, and latent effectiveness, ε_L, during dehumidifier and regenerator operating conditions. During the air dehumidifying tests the theoretical predictions for the sensible and latent effectiveness agreed with the data; however, during the solution regenerator tests the agreement was not good. Results show that the most important parameters impacting the mass transfer performance of the dehumidifier are air flow rate, inlet air humidity ratio, desiccant solution inlet temperature, and solution concentration. It is also found that the parameters significantly influencing the performance of the solution regenerator are the air flow rate, inlet air humidity ratio, solution inlet temperature, solution concentration and solution flow rate. The effects of air and desiccant solution inlet parameters on the performance of the counter-cross-flow LAMEEs show similar tendency with those previously reported for direct-contact liquid desiccant devices used as dehumidifiers and regenerators. In addition, using the experimental data, the analytical model is quantitatively validated during the air dehumidification process for the inlet conditions tested, while a qualitative agreement is achieved for desiccant solution regeneration process. The discrepancy between the experimental and analytical results in regeneration tests may be mainly caused by the crystallization of LiCl aqueous solution in the membrane pores near solution side during the de-watering process.

APPENDIX C

FULL-SCALE (200 CFM) LAMEE RESULTS

C.1   Overview of Appendix C

The full-scale (200cfm) LAMEE is tested under summer and winter test conditions and the experimental and numerical steady-state performance results for the 200cfm LAMEE are presented in Appendix C which contains my paper in ASME 2013 Summer Heat Transfer Conference in Minneapolis, MN (Title: steady-state performance of a prototype (200 cfm) liquid-to-air membrane energy exchanger (LAMEE) under summer and winter test conditions). The 200cfm LAMEE design is similar to the small-scale single-panel LAMEE design which is presented in Chapter 2. The 200cfm LAMEE is tested under four summer test conditions and two winter test conditions using the LiCl salt solution.

Mr. Gazi Mahmood and Mr. John Bolster are co-authors of my paper in ASME 2013 Summer Heat Transfer Conference. Mr. Mahmood and Mr. Bolster are working in VenmarCES, Saskatoon. Mr. Mahmood helped me to prepare the experimental test facility to test the 200cfm LAMEE, and conducting tests with the full-scale LAMEE. Mr. Bolster provided me with the numerical model which I used in Appendix C to evaluate the numerical performance of the 200cfm LAMEE under summer and winter test conditions. My contributions to the manuscript #5 are: (a) preparing the test facility to test the 200cfm LAMEE, (b) testing the 200cfm LAMEE under summer and winter test conditions, and analyzing the experimental data to calculate the effectiveness of the 200cfm LAMEE under summer and winter test conditions, (c) comparing the experimental data with the numerical results for the 200cfm LAMEE effectiveness under summer and winter test conditions, and (d) writing this paper and presenting the paper in ASME 2013 Summer Heat Transfer Conference in Minneapolis, MN.

Steady-State Performance of a Prototype (200 cfm) Liquid-to-Air Membrane Energy Exchanger (LAMEE) Under Summer and Winter Test Conditions

Davood Ghadiri Moghaddam, Gazi Mahmood, Gaoming Ge, John Bolster, Robert W. Besant, Carey J. Simonson

C.2   Abstract

Liquid-to-air membrane energy exchangers (LAMEEs) are a new generation of energy exchangers in air-conditioning systems to transfer both heat and moisture. In this paper, the performance of a 200 cfm LAMEE is numerically and experimentally investigated under summer and winter test conditions when Lithium Chloride (LiCl) is used as a salt solution in the exchanger. The results show that the LAMEE has almost the same total effectiveness at summer and winter conditions, but the latent effectiveness of the LAMEE is higher at the summer conditions. Also, the agreement between the experimental and numerical results is acceptable for all the tests, and they are within their uncertainty ranges except for the latent effectiveness of the LAMEE tested under winter test conditions.

Keywords: LAMEE, effectiveness, *NTU*, *Cr**, summer and winter conditions.

C.3   Introduction

A Liquid-to-air membrane energy exchanger (LAMEE) is a novel membrane based energy exchanger which allows both heat and moisture transfer through a semi-permeable membrane between an air stream and a salt solution; since in heat exchangers only heat transfers between two flow streams. The membrane is permeable to water vapor and impermeable to liquid water. The LAMEE can be used in different air-conditioning systems such as a run-around membrane energy exchanger (RAMEE) which is composed of two LAMEE connected with a desiccant loop (Fan *et al.*, 2006; Erb, 2009), or a hybrid air-conditioning system (HACS) where a LAMEE is added to a direct expansion air-conditioning system to increase the moisture transfer and the overall system performance (Bergero and Chiari, 2010; Bergero and Chiari, 2011).

Many studies have been done on RAMEEs and HACSs. The effectiveness of different RAMEE systems with cross and counter-cross flow LAMEEs were numerically and experimentally investigated under different operating conditions using different salt solutions (Seyed-Ahmadi *et al.*, 2009a; Fan et al, 2006; Vali *et al.*, 2009). Also, Bergero and Chiari (2010, 2011) numerically investigated the effects of air and solution mass flow rates, latent load, and indoor and outdoor relative humidities on the steady-state performance of a HACS at summer condition using two cross flow LAMEEs in the supply and exhaust air streams. The results showed that the performance of the HACS compared to a traditional direct-expansion system was significantly improved (e.g. 50% higher energy saving at certain operating conditions).

Few studies have been done directly on the performance of LAMEEs. Bergero *et al.* (2000) numerically and experimentally investigated the effects of air and solution flow rates on the performance of a LAMEE at steady-state conditions. The results showed that the LAMEE latent effectiveness increased by increasing the air flow rate. Namvar *et al.* (2012) investigated the steady-state and transient performance of a LAMEE under summer and winter conditions with various air and solution mass flow rates. Also, the LAMEE's time constant at transient operating conditions was studied in (Namvar *et al.*, 2012) as an important variable which depends on the thermal capacities of the exchanger and the liquid desiccant. Recently Ghadiri Moghaddam *et al.* (2013a) presented a new test facility to experimentally investigate the performance of a small-scale LAMEE under different operating conditions with different salt solution types.

In this paper, the performance of a 200 cfm LAMEE with a unique design is experimentally investigated under summer and winter test conditions to study the effect of different outdoor air conditions (e.g. summer and winter conditions) on the effectiveness of the LAMEE. The 200 cfm LAMEE prototype is chosen as a first full-scale LAMEE prototype to perform preliminary tests on a full-scale LAMEE system with a new design under different operating conditions. Seven tests were conducted with the 200 cfm LAMEE with LiCl used as the solution in the exchanger. In addition, performance of the 200 cfm LAMEE is numerically modeled and the numerical results are compared with the experimental data for summer and winter operating conditions.

C.4 Test Facility

A LAMEE test facility was used in this research to test the 200 cfm LAMEE under summer and winter test conditions. The LAMEE test facility mainly consists of three sections: supply air system, open solution loop and a LAMEE. In the supply air system, an environmental chamber was used to simulate the summer and winter air conditions. The environmental chamber is able to provide an air temperature between -40°C and +40°C and a RH of up to 90%RH. The conditioned supply air flowed into two 2-inch-diameter piping branches by using two 5 hp vacuum fans. The supply air passed through the exchanger, and was exhausted to the lab environment by using another two 5 hp vacuum fans in the exhaust pipeline. Variable transformers were used for each fan to adjust the fan power and the air flow rate. The air flow rate was measured by using an orifice plate in each piping branch. Also, the inlet and outlet air relative humidities were measured in each branch after and before the orifice plates, respectively, while the inlet and outlet temperatures were measured at the air inlet and outlet headers, respectively. T-type thermocouples and Vaisala humidity sensors with accuracies of 0.2°C and 1.2%RH, respectively, were used in the supply air system to measure the air temperature and relative humidity. The air pressure drop across the LAMEE was measured with a pressure transducer with a capacity of 550 Pa and the accuracy of 1.5 Pa. Figure 6.1 shows the schematic of the LAMEE test facility.
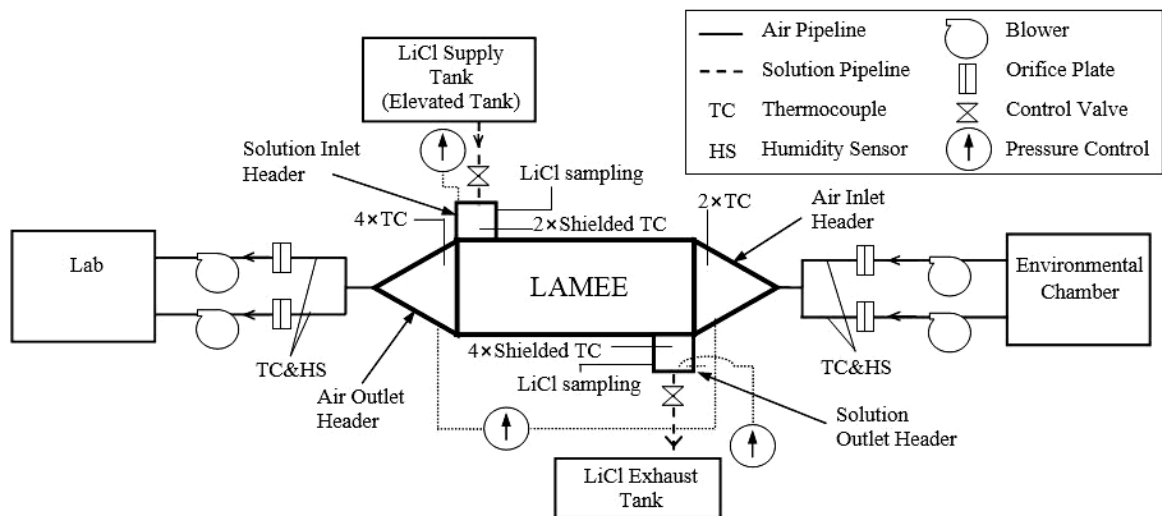

Figure C.1 Schematic of the 200cfm LAMEE test facility

The salt solution in this system ran under gravity and flowed from top-to-bottom through the exchanger. The solution flowed from an elevated supply solution tank through the exchanger, and was collected in a solution exhaust tank at the exchanger outlet. Two control valves were used after the supply tank and the LAMEE to adjust the solution flow rate. The inlet and outlet solution pressures were monitored in the LAMEE solution inlet and outlet headers, with two monometers. Shielded T-type thermocouples with an accuracy of 0.2˚C were used to measure the solution temperature in the LAMEE solution open loop. Also, LiCl samples from the solution inlet and outlet headers were used to measure the solution concentration at each location.

A 200 cfm LAMEE with a counter-cross flow configuration was used to conduct the experiments in this research. The 200 cfm LAMEE consists of 10 single-panel LAMEEs placed side by side. Each single panel LAMEE consists of a single pair of neighboring air and liquid channels (Ghadiri Moghaddam *et al.*, 2013a). Figure C.2 shows the details of a single-panel LAMEE. In the single-panel LAMEE, a semi-permeable membrane was attached to two grooved plastic panels to form a solution channel. These two plastic panels were placed side by side with an air spacer in between to create an air channel. The air and salt solution channels were separated by a semi-permeable membrane which allows heat and moisture transfer between the air and solution flows. Also, an air screen inside the LAMEE enhances the heat transfer performance in the air side. The membrane properties and specifications of the 200 cfm LAMEE are presented in Table C-1.

Table C-1 The 200 cfm LAMEE specifications and the membrane properties

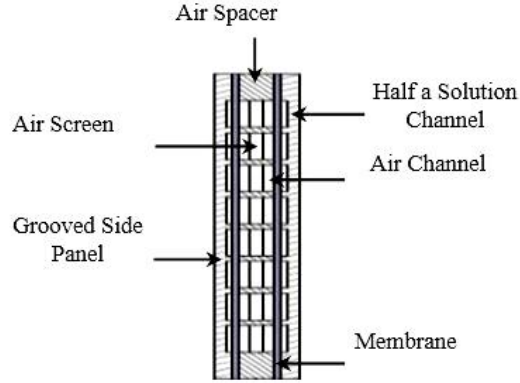| Parameter	value
Exchanger length, L_{ex} (m)	1.06
Exchanger height, H_{ex} (m)	0.8
Number of solution panels in the exchanger	10
Maximum air capacity, Q_{air} (cfm)	200
Number of heat transfer units, NTU	5-6
Heat capacity ratio, $Cr*$	2-4
Mass resistance of membrane, R_{mem} (s/m)	24
Membrane thermal conductivity, k_{mem} (W/mK)	0.065
Membrane thickness, d_{mem} (mm)	0.265

Figure C.2 The single-panel LAMEE cross-section detailed view (Ghadiri Moghaddam *et al.*, 2013b)

C.4.1 Experimental Procedure

Seven tests have been done on the 200 cfm LAMEE, 4 tests under summer (S) conditions and 3 tests under winter (W) conditions. The air and salt solution inlet and outlet conditions for each test are presented in Table C-2. The test conditions are slightly different at summer and winter conditions. Figure C.3 shows the air and solution inlet and outlet conditions of the LAMEE on a Psychrometric chart for (a) summer and (b) winter testing to have better understanding of the air and solution processes in the LAMEE. The number of heat transfer units (*NTU*) varies between 5 and 6 in the experiments, and the heat capacity ratio (*Cr**) range is from 2.8 to 4.2 and 2 to 3 for the summer and winter tests, respectively. The definitions of the *NTU* and *Cr** for a LAMEE are presented in Eq. (C.1).

$$NTU = \frac{UA}{\left(\dot{m}c_p\right)_{air}} \text{ and } Cr^* = \frac{\left(\dot{m}c_p\right)_{sol}}{\left(\dot{m}c_p\right)_{air}} \tag{C.1}$$

In Eq. (C.1), U and A are the overall heat transfer coefficient and total membrane active area for the heat and mass transfer, respectively. Also, c_p and $\dot{m}$ are the specific heat capacity and mass flow rate, respectively. The overall heat transfer coefficient in the LAMEE is calculated as follows:

$$U = \left[\frac{1}{h_{air}} + \frac{d_{mem}}{k_{mem}} + \frac{1}{h_{sol}}\right]^{-1}, \tag{C.2}$$

Where *h*, *d* and *k* are the convective heat transfer coefficient, thickness and thermal conductivity, respectively. The subscript *mem* represents the membrane properties.
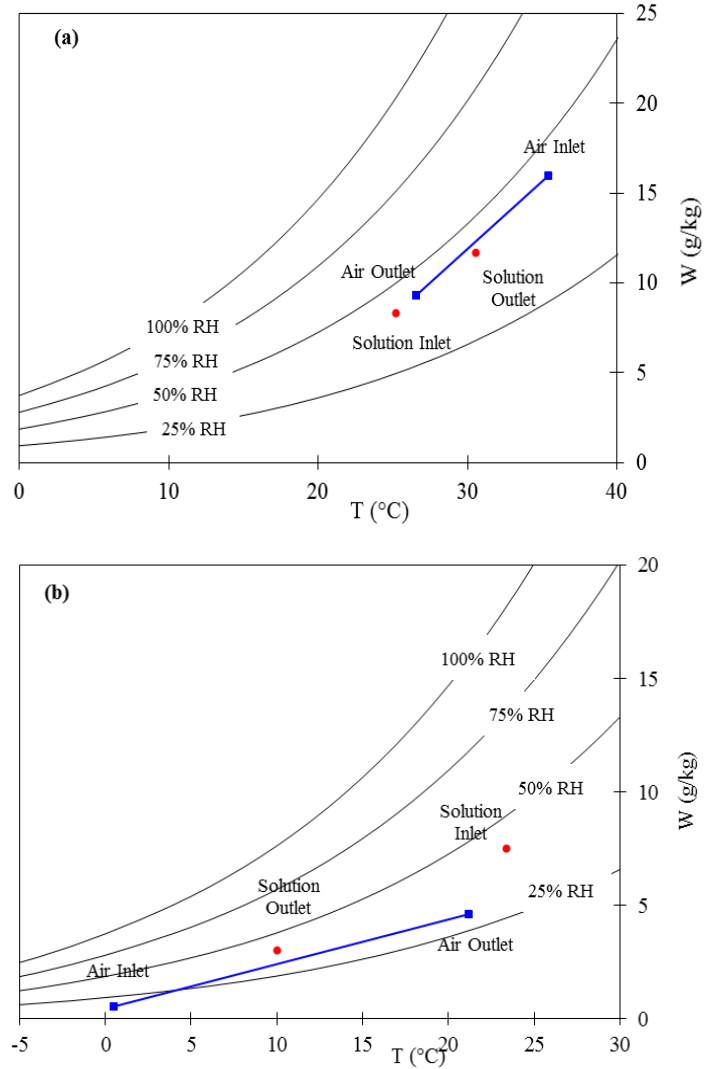

Figure C.3 The air and salt solution inlet and outlet conditions of the 200 cfm LAMEE under (a) summer (test S2) and (b) winter (test W2) conditions on a Psychrometric chart

Table C-2 The measured air and salt solution inlet and outlet conditions of the 200 cfm LAMEE under summer and winter test conditions

Test	NTU	Cr*	$T_{air,in}$ (℃)	$W_{air,in}$ (g/kg)	$T_{air,out}$ (℃)	$W_{air,out}$ (g/kg)	$T_{sol,in}$ (℃)	$W_{sol,in}$ (g/kg)	$C_{sol,in}$ (%)	$T_{sol,out}$ (℃)	$W_{sol,out}$ (g/kg)	$C_{sol,out}$ (%)
S1	5	2.8	38.8	21.4	29.3	9.8	26.7	6.8	33.6	33.6	11.2	33.2
S2	5	4.2	35.4	16	26.6	9.3	25.2	8.3	30.2	30.6	11.7	30
S3	6	4	35.4	21	25.8	9.6	23.3	7.3	30.3	32.4	13.1	30
S4	5.5	3.9	36.3	17.6	26	9.4	23.7	7.7	30	31.5	12.5	29.9
W1	5.5	3	0.95	0.6	21.2	4.8	23	7.4	29.8	10.9	3.3	30.1
W2	5.3	2.7	0.5	0.5	21.2	4.6	23.4	7.5	30	10	3	30.4
W3	5	2.2	0.36	0.6	22.4	4.8	23.9	7.5	30.4	10.5	3	30.9

C.4.1.1 LAMEE Performance Evaluation

The performance of a LAMEE system is evaluated by sensible, latent and total effectiveness. The sensible and latent effectiveness represent the amount of heat and moisture transfers in the exchanger to the maximum possible heat and moisture transfer rates, respectively. Sensible and latent effectiveness are calculated as follows for a LAMEE when $Cr^* \geq 1$:

$$\varepsilon_{Sensible \text{ or } Latent} = \frac{\left(Y_{air,in} - Y_{air,out}\right)}{\left(Y_{air,in} - Y_{sol,in}\right)} \tag{C.3}$$

In Eq. (C.3), Y can be temperature (T) or humidity ratio (W) for the sensible or latent effectiveness, respectively. Subscripts *in* and *out* refer to the air or solution inlet and outlet in the LAMEE, respectively. Subscripts *air* and *sol* refer to the air and salt solution, respectively. Also, the total effectiveness is related to both sensible and latent energy transfers in the LAMEE, and is calculated by Eq. (C.4) (Simonson and Besant, 1999).

$$\varepsilon_{Total} = \frac{\varepsilon_{Sensible} + H^* \varepsilon_{Latent}}{1 + H^*} \tag{C.4}$$

In Eq. (C.4), H^* is the operating condition factor of the LAMEE, and is calculated based on the air and the salt solution inlet temperatures and humidity ratios (Simonson and Besant, 1999).

$$H^* = \frac{\Delta H_{Latent}}{\Delta H_{Sensible}} \approx 2500 \frac{W_{air,in} - W_{sol,in}}{T_{air,in} - T_{sol,in}} \qquad (C.5)$$

C.4.1.2 Mass and Energy Balances

Mass and energy balances of the LAMEE test facility are required for each experiment to show that the LAMEE is working steady and experimental results are within their uncertainty ranges. The water vapor mass and energy balances of the LAMEE are calculated from the following equations (Simonson *et al.*, 1999):

$$\Delta(\dot{m}W) = \left|\left[(\dot{m}W)_{air,in} - (\dot{m}W)_{air,out}\right] + \left[(\dot{m}_{salt}X_{sol})_{in} - (\dot{m}_{salt}X_{sol})_{out}\right]\right| \leq Un_{\Delta(\dot{m}W)} \quad (C.6)$$

$$\Delta(\dot{m}H) = \left|\left[(\dot{m}H)_{air,in} - (\dot{m}H)_{air,out}\right] + \left[(\dot{m}H)_{sol,in} - (\dot{m}H)_{sol,out}\right]\right| \leq Un_{\Delta(\dot{m}H)} \quad (C.7)$$

Where W, H and X are humidity ratio, enthalpy and solution mass fraction (Mahmud, 2009), respectively. The subscript *salt* refers to the pure salt in the LAMEE system. Also, $Un_{\Delta(\dot{m}W)}$ and $Un_{\Delta(\dot{m}H)}$ are the calculated uncertainties for water vapor and energy transfers during the tests, based on the air and solution properties for each test. The water vapor mass and energy balances of the 200 cfm LAMEE are evaluated for each test and the results are presented in Table C-3. The results show that the 200 cfm LAMEE is balanced during all tests and the experimental data are within their uncertainty ranges.

Table C-3 Water vapor and energy balance results of the 200 cfm LAMEE under the summer and winter test conditions

Test	Water vapor balance		Energy balance	
	$\Delta(\dot{m}W)$	$Un_{\Delta(\dot{m}W)}$	$\Delta(\dot{m}H)$	$Un_{\Delta(\dot{m}H)}$
	(kg/h)	(kg/h)	(W)	(W)
S1	2.8	7.6	429	442
S2	1.8	9.8	206	464
S3	2.1	7.5	53	351
S4	2.4	8.4	73	395
W1	0.4	7.1	250	261
W2	0.5	6.8	216	222
W3	1.9	7	197	225

C.5   Numerical Modeling

An Enthalpy Pump System (EPS) numerical code, which has been developed at the RAMEE research group of the University of Saskatchewan, was used in this research to model the 200 cfm LAMEE under summer and winter test conditions (Seyed-Ahmadi *et al.*, 2009a; Vali *et al.*, 2009; Hemingson, 2010). The EPS code was recently modified by VenmarCES Inc., Saskatoon with accurate correlations to calculate the LiCl salt solution properties at different salt concentrations. A LAMEE with the counter flow configuration for the air and solution was modeled with the EPS code. The 200 cfm LAMEE is a counter-cross flow exchanger where almost 90% of the LAMEE has counter flow configuration for the air and solution. Akbari *et al.* (2012a) showed that the effectiveness difference between a counter-cross flow LAMEE with 90% counter flow configuration and a pure counter flow LAMEE was less than 2%. Thus, the counter flow configuration was used in the EPS code. The heat loss/gain to/from the surroundings was neglected during the numerical modeling. The air and salt solution inlet conditions, and the *NTU* and *Cr** from the experiments were used as an input to the EPS code.

In the numerical model, it was assumed that the air and solution flows in the LAMEE are in the laminar regime (by neglecting the effect of the air screen and membrane deflection in the air channel of the LAMEE) for all test cases ($Re_{sol,max} \approx 24$ and $Re_{air,max} \approx 1700$). Consequently, to calculate the convective heat transfer coefficients in the current paper, $Nu = 8.24$ (Nusselt value for the laminar flow between two infinite parallel plates with constant heat flux on both walls) is used for the air side, and $Nu = 5.39$ (Nusselt value for the laminar flow between two infinite parallel plates with constant heat flux on one wall and the other wall insulated) is used for the solution side of the LAMEE (Incropera and DeWitt, 1985). The convective heat transfer coefficient is calculated as follow:

$$h = \frac{Nu \times k}{D_h} \tag{C.8}$$

Where, *Nu* and D_h are Nusselt number and the hydraulic diameter of the air or solution channels, respectively. Moreover, the air and solution convective mass transfer coefficients are calculated using the heat and mass transfer analogy (Niu and Zhang, 2001):

$$Sh = Nu.Le^{-\frac{1}{3}} \qquad (C.9)$$

In Eq. (C.9), *Sh* and *Le* are Sherwood and Lewis numbers, respectively. Lewis number is calculated as follows for the air and solution:

$$Le = \frac{k}{\rho c_p D} \quad Le = \frac{k}{\rho c_P D_h} \qquad (C.10)$$

Where ρ and D are the density and binary diffusion coefficient of water in air or solution, respectively.

This is the summary of how the air and solution convective heat and mass transfer coefficients are calculated in the current paper for the 200 cfm LAMEE. However, the convective heat and mass transfer coefficients in the air side of the LAMEE are different than flat-plate exchangers with hollow channels because of the air screen in the air channel which will promote the heat and mass transfer performance in the air side of the LAMEE.

C.6   Results and Discussions

The performance results of the 200 cfm LAMEE are presented in this section. Seven tests were conducted with the LAMEE under summer and winter conditions when LiCl was used in the exchanger as a salt solution. Also, the EPS code was used to numerically model the LAMEE under the same condition as the experiments. The experimental air and salt solution inlet and outlet conditions of the LAMEE are presented in Table C-2. As it can be seen in Table C-2, the air and solution inlet conditions are not the same for all the summer tests as well as the winter tests, so, the LAMEE effectiveness results are presented for each test separately in graphs. Figure C.4 shows the experimental and numerical sensible, latent and total effectiveness of the LAMEE under the summer and winter conditions. The results in Figure C.4(a) shows that the experimental sensible effectiveness of the LAMEE is between 80% to 95% in both summer and winter conditions while the average experimental sensible effectiveness of the LAMEE in winter is almost 10% higher than in the summer. This could be caused by the higher potential for the heat transfer ($\left|T_{air,in} - T_{sol,in}\right|$) during the winter testing (see

270

Table C-2). Also, the agreement between the experimental and numerical LAMEE sensible effectiveness is acceptable and they agree within their uncertainty ranges.
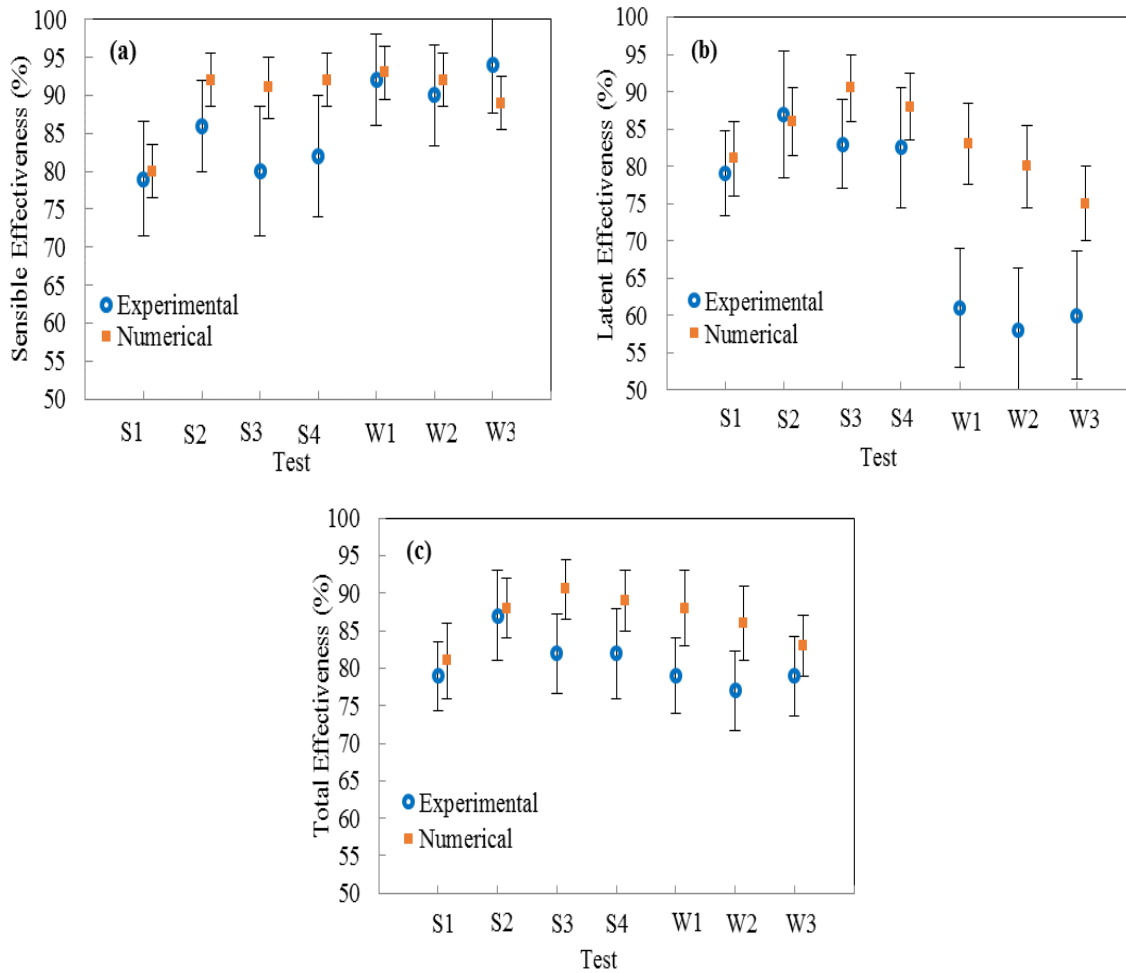

Figure C.4 The 200 cfm LAMEE (a) sensible, (b) latent, and (c) total effectiveness under summer and winter test conditions

Figure C.4(b) shows the latent effectiveness of the LAMEE under summer and winter test conditions. The results in Figure C.4(b) show that, firstly, the latent effectiveness of the LAMEE is generally lower than the sensible effectiveness which is due to higher mass transfer resistance in the LAMEE in comparison to the heat transfer resistance (Zhang, 2011a). Secondly, the experimental latent effectiveness of the LAMEE under summer conditions (e.g. ~85%) is significantly higher than the results for winter conditions (e.g. ~60%). This discrepancy can be explained by the following reasons:

1. The potential of the moisture transfer in the LAMEE is higher in summer than winter. The solution conditions are almost the same for both summer and winter

271

testing (see Table C-2), but the difference in the air humidity ratios is higher at summer conditions due to the higher slope of the RH line on the Psychrometric chart (see Figure C.2).

2. In the summer testing with the LAMEE, the heat and moisture transfer directions are from the air side to the solution side of the LAMEE while these directions are reverse for the winter testing, and are from the solution side to the air side. The thermal capacity ($\dot{m}c_P$) of the solution in the LAMEE is more than two times higher than of the air, which will cause a rapid increase of the air temperature and vapor pressure during winter testing. As a result, the potential of the air to receive the heat and moisture from the solution decreases in the winter which could cause lower latent effectiveness for the LAMEE in the winter tests (Abdel-Salam, *et al.*, 2013).

Figure C.4(b) shows a good agreement between the experimental and numerical latent effectiveness of the LAMEE under summer conditions. However, the experimental and numerical latent effectiveness do not agree within uncertainty ranges for the winter conditions. This discrepancy under winter conditions may be due to mal-distribution and salt solution crystallization on the membrane surface in the solution side of the LAMEE that might happen during the experiments. These two phenomena are not considered in the numerical model, and may be considered as sources of error in the EPS code. During the LAMEE winter testing, the moisture transfers from the solution side to the air side of the LAMEE (air humidification). Air humidification causes the salt solution to dehydrate on the membrane surface and in the membrane pores in the solution side of the LAMEE, and the salt solution concentration on the membrane surface increases. The salt solution concentration may exceed the salt solution saturation concentration (e.g. 44% at 10°C for LiCl (Afshin, 2010)), and the salt solution may crystallize on the membrane surface and in the membrane pores in the solution side of the LAMEE.

Figure C.4(c) shows the total effectiveness of the 200 cfm LAMEE under winter and summer test conditions. The results show that the total effectiveness of the LAMEE is almost the same for the summer and winter tests, and is between 80% and 90%. Also, the experimental and numerical total effectiveness of the LAMEE agree within their uncertainty ranges for all the summer and winter tests.

C.7 Conclusions

In this paper, the effectiveness of a novel 200 cfm LAMEE under summer and winter test conditions was studied numerically and experimentally. Seven tests were conducted (4 summer tests and 3 winter tests) with the LAMEE with LiCl used as the solution in the exchanger. The experimental results show the average LAMEE sensible, latent and total effectiveness are 81%, 82% and 82% in the summer conditions, while they are 92%, 60% and 78%, respectively, in the winter conditions. The latent effectiveness of the LAMEE is almost 20% lower under winter conditions in comparison to the summer tests. Also, the agreement between the experimental and numerical effectiveness is acceptable for all the tests except the latent effectiveness of the LAMEE under winter conditions, where the numerical model predicts higher latent effectiveness for the LAMEE system. The total effectiveness of the LAMEE for both summer and winter tests are in the same range and are almost 80%.